
Density functional theory of hard colloidal particles: From bulk to interfaces

Inaugural-Dissertation

zur Erlangung des Doktorgrades
der Mathematisch-Naturwissenschaftlichen Fakultät
der Heinrich-Heine-Universität Düsseldorf

vorgelegt von

Andreas Härtel

aus Düsseldorf-Gerresheim

Düsseldorf, Dezember 2012

aus dem Institut für Theoretische Physik II: Weiche Materie
der Heinrich-Heine-Universität Düsseldorf

Gedruckt mit der Genehmigung der
Mathematisch-Naturwissenschaftlichen Fakultät der
Heinrich-Heine-Universität Düsseldorf

Referent: Prof. Dr. Hartmut Löwen
Korreferent: Prof. Dr. Stefan U. Egelhaaf

Tag der mündlichen Prüfung: 24. Januar 2013

Preface

In June 2009 I have started working on this thesis with my supervisor Hartmut Löwen at the department for Theoretical Physics II: Soft Matter at the Heinrich Heine University Düsseldorf. As my work was supported by the DFG via SPP 1296 and SFB TR6, I have been able to visit some great conferences and workshops to present parts of this thesis, meet other scientists, and learn more about the field of soft matter and adjacent topics in physics. Here, one of the most impressive experiences certainly has been the SFB TR6 Cargèse Summer School 2010 in Corsica, where I took the pictures of the Mediterranean Sea that are shown in Fig. 5.2 of this thesis.

In 2010 and 2011 I was allowed to coordinate the proposal for the Cluster of Excellence *fi³ - fluctuations and interaction*, which has been an interesting insight into the scientific management at universities. However, my main topic has been the research which yields this thesis and four articles, which have been published in academic journals. In this context, I thank Martin Oettel, Roberto Rozas, Jürgen Horbach, Ronald Blaak, Kirill Sandomirski, Stefan Egelhaaf, Matthieu Marechal, and Hartmut Löwen for excellent collaboration.

During the last years, I met many people with whom I had interesting and stimulating discussions about my work and science. However, mentioning all those people by name would be a comprehensive but also unfair venture. For this reason I will thank my co-workers, my friends, my family, and all forgotten people for all the best.

In June 2012, I started writing this thesis. For this reason, I had a stay in the abbey St. Matthias in Trier, which have been a productive and enriching time for me - a warm thanks for your hospitality. Then, the end of the Mayan calendar moved closer (it will be tomorrow) and I found a small crowd of people, who took time to proofread my thesis and to support me, especially Christoph Härtel, Matthieu Marechal, Tim Neuhaus, Brigitte Schumann, Yvonne Seger, Alexandra Urbanietz, and Urs Zimmermann. Thanks a lot for that.

Finally, I thank my supervisor, who gave me the opportunity to apply for a doctor's degree, to work with him, and to write this thesis. I hope that many will read it and maybe someone will find an interesting topic to take it home.

Gerresheim, December 20th, 2012

List of published work

This work has been developed during the last years (since July 2009) at the department for *Theoretical Physics II: Soft Matter* at the *Heinrich Heine University Düsseldorf*. Accordingly, most results of this work have already been published in academic journals and the resulting publications are listed in the following. In addition, I give a statement about my personal contribution to every article to avoid plagiarism, because works have been written in cooperation with other scientists and departments.

Towing, breathing, splitting and overtaking in driven colloidal liquid crystals

A. Härtel, R. Blaak, and H. Löwen, Phys. Rev. E **81**, 051703 (2010).

Abstract: The nonequilibrium response of a colloidal liquid crystalline nematic phase to an external aligning field which rotates in a plane is explored by dynamical fundamental-measure density functional theory. Depending on the drive frequency, different dynamical states are found which are characterized by towing and overtaking of the nematic director by the field as well as by breathing and dynamical splitting of the orientational distribution peak. This complex response can be exploited for smart optical switching and mixing devices. ©2010 The American Physical Society.

Statement of the author: This work has been started within my diploma project, which mostly has been published in [A. Härtel and H. Löwen, J. Phys.: Condens. Matter **22**, 104112 (2010)]. Even if the topic of this work has already been discussed in parts in my diploma thesis, the detailed discussion of this work has been developed later, including the figures and the final description. In principle, I have performed all calculations and wrote most parts of this work.

Free energies, vacancy concentrations, and density distribution anisotropies in hard-sphere crystals: A combined density functional and simulation study

M. Oettel, S. Görig, A. Härtel, H. Löwen, M. Radu, and T. Schilling, Phys. Rev. E **82**, 051404 (2010).

Abstract: We perform a comparative study of the free energies and the density distributions in hard-sphere crystals using Monte Carlo simulations and density functional theory (employing Fundamental Measure functionals). Using a recently introduced technique [T. Schilling and F. Schmid, J. Chem. Phys. **131**, 231102 (2009)] we obtain crystal free energies to a high precision. The free energies from fundamental measure theory are in good agree-

ment with the simulation results and demonstrate the applicability of these functionals to the treatment of other problems involving crystallization. The agreement between fundamental measure theory and simulations on the level of the free energies is also reflected in the density distributions around single lattice sites. Overall, the peak widths and anisotropy signs for different lattice directions agree, however, it is found that fundamental measure theory gives slightly narrower peaks with more anisotropy than seen in the simulations. Among the three types of fundamental measure functionals studied, only the White Bear II functional [H. Hansen-Goos and R. Roth, *J. Phys.: Condens. Matter* **18**, 8413 (2006)] exhibits sensible results for the equilibrium vacancy concentration and a physical behavior of the chemical potential in crystals constrained by a fixed vacancy concentration. ©2010 The American Physical Society.

Statement of the author: This work is a comparative study using Monte Carlo (MC) simulations and density functional theory (DFT). All DFT calculations have been performed twice, in particular by M. Oettel and by myself, to ensure correct results. However, M. Oettel performed a more detailed investigation of the Gaussian-peak approximation than I did. Regarding the discussion about the chemical potential, ideas have been developed in close cooperation, but calculations resulting in Fig. 2 have solely been performed by M. Oettel. Similarly, the direct comparison between the MC simulation results and the DFT results has been applied by M. Oettel and T. Schilling. On the other hand, I have performed the calculations regarding the Lindemann parameter and the corresponding paragraphs have also been written by me.

Inhomogeneous fluids of colloidal hard dumbbells: Fundamental measure theory and Monte Carlo simulations

M. Marechal, H. H. Goetzke, A. Härtel, and H. Löwen, *J. Chem. Phys.* **135**, 234510 (2011).

Abstract: Recently, a density functional theory for hard particles with shape anisotropy was developed, the extended deconvolution fundamental measure theory (edFMT). We apply edFMT to hard dumbbells, arguably the simplest non-convex shape and readily available experimentally in the form of colloids. We obtain good agreement between edFMT and Monte Carlo simulations for fluids of dumbbells in a slit and for the same system under gravity. This indicates that edFMT can be successfully applied to nearly all colloidal shapes, not just for the convex shapes for which edFMT was originally derived. A theory, such as edFMT, that allows a fast and general way of mapping the phase behavior of anisotropic colloids, can act as a useful guide for the design of colloidal shapes for various applications. ©2011 American Institute of Physics.

Statement of the author: My personal contribution to this article essentially is the calculation of the weight functions, as described in Sec. 3 (of the article). The work has been started in form of the bachelor project of H. H. Goetzke in the framework of density functional theory, which I supervised together with H. Löwen. Later, M. Marechal continued the work and performed additional improvements regarding the edFMT approach. He also performed the simulations the DFT is compared to. Of course, we have discussed a lot about the theoretical part of the work.

Tension and Stiffness of the Hard Sphere Crystal-Fluid Interface

A. Härtel, M. Oettel, R. E. Rozas, S. U. Egelhaaf, J. Horbach, and H. Löwen, Phys. Rev. Lett. **108**, 226101 (2012).

Abstract: A combination of fundamental measure density functional theory and Monte Carlo computer simulation is used to determine the orientation-resolved interfacial tension and stiffness for the equilibrium hard-sphere crystal-fluid interface. Microscopic density functional theory is in quantitative agreement with simulations and predicts a tension of $0.66 k_B T / \sigma^2$ with a small anisotropy of about $0.025 k_B T$ and stiffnesses with e.g. $0.53 k_B T / \sigma^2$ for the (001) orientation and $1.03 k_B T / \sigma^2$ for the (111) orientation. Here $k_B T$ is denoting the thermal energy and σ the hard sphere diameter. We compare our results with existing experimental findings. ©2012 The American Physical Society.

Statement of the author: This work is a combined study using density functional theory (DFT) and Monte Carlo (MC) simulations. The MC simulations have been performed by R. Rozas and J. Horbach, where the DFT calculations have been performed by M. Oettel and myself. I have written most parts of the article and created Fig. 1 and Fig. 2. Furthermore, I have applied the calculations regarding the comparative fit to the interfacial tension, using the cubic-harmonic expansion in Equ. (2) (of the article).

Abstract

In this work about *density functional theory of hard colloidal particles*, spheres, spherocylinders, and dumbbells are investigated in the bulk and at interfaces. Therefore, the theoretical framework of density functional theory (DFT) and fundamental measure theory (FMT) is introduced first. Then, FMT functionals are applied to hard-sphere systems to obtain free energies and density distributions for the (fcc) crystal and the fluid phase. The free energies are in good agreement with Monte Carlo (MC) simulation results, which is also reflected in the density distributions around single lattice sites. From the studied variants of FMT only the White Bear mark II (WBII) functional shows qualitatively correct behavior, which implies that only the WBII functional is a promising candidate for further studies of problems involving crystallization.

Accordingly, accurate values for the anisotropic hard-sphere crystal-fluid surface tensions and stiffnesses have been predicted by using the WBII approach in combination with MC simulations. Quantitative agreement between FMT and simulations is found, where FMT predicts a tension of $0.66 k_B T / \sigma^2$ with a small anisotropy of about $0.025 k_B T$. The corresponding stiffnesses are determined with e.g. $0.53 k_B T / \sigma^2$ for the (001) orientation and $1.03 k_B T / \sigma^2$ for the (111) orientation of the interface, where $k_B T$ is the thermal energy and σ is the diameter of the hard spheres. However, the anisotropy in the tension is crucial for the transformation to stiffnesses, which differ up to a factor of 4. Moreover, the results from theory and simulation are compared with existing experimental findings and classical nucleation theory is discussed in the context of analyzing experimental results.

In another sense, FMT has also been applied to non-spherical particles. For this purpose, the recently developed extended deconvolution FMT (edFMT) has been applied to systems of orientationally resolved spherocylinders and dumbbells. The spherocylinders are assumed to constitute a fluid phase with the possibility of orientational ordering and are subjected to an in-plane aligning field which rotates with a frequency ω_0 . Consequently, the system is investigated by using dynamical DFT, an extension of DFT to non-equilibrium, time-dependent situations. The setup causes a complex orientational response of the colloidal liquid crystal with five different dynamical states which are characterized by towing, breathing, splitting, overtaking, and unsplit overtaking, as ω_0 increases.

Applied to hard dumbbells, inhomogeneous fluids are analyzed in a slit and under gravity. The edFMT features a free parameter ζ , which has to be nonzero, to obtain a stable nematic phase even for very elongated particles. Adjusting it has been shown to lead to unrealistically large values for ζ , presumably because the theory is not valid for non-convex particles like dumbbells. However, the theory with $\zeta = 0$ gives excellent results when compared to MC simulations for not too large packing fractions.

Finally, the highly localized density peaks in a crystal cause critical numerical behavior where local packing fractions exceed meaningful values which leads to a divergence of the FMT functional. For this reason, numerical methods are outlined in the appendix of this work to avoid such problems and to ensure the convergence of solutions.

Zusammenfassung

In der vorliegenden Dissertationsschrift werden die Eigenschaften harter kolloidaler Kugeln, Sphärozyylinder und Hanteln inmitten einer physikalischen Phase sowie an Grenzflächen mittels Dichtefunktionaltheorie (DFT) untersucht. Zunächst werden daher die DFT sowie eine notwendige weitere Theorie eingeführt, welche die Fundamentalmaße der Kolloide verwendet um im Rahmen der DFT ein benötigtes Funktional bereit zu stellen und daher FMT (fundamental measure theory) genannt wird. Mit mehreren Funktionalen dieser FMT werden dann die freien Energien und die Dichteprofile von (fcc) Kristallen harter Kugeln sowie deren flüssiger Phasen bestimmt. Ein Vergleich der Ergebnisse mit Monte Carlo (MC) Simulationen zeigt gute Übereinstimmung, auch wenn nur das *White Bear mark II* (WBII) (white bear = weißer Bär) Funktional auch qualitativ korrekte Ergebnisse liefert. Entsprechend ist für weitere Studien, welche sich mit der Kristallisation harter Kugeln beschäftigen, nur das WBII Funktional geeignet.

Im Weiteren wird dieses daher verwendet, um durch eine freie Minimierung der Grenzfläche zwischen dem (fcc) Kristall und der Flüssigkeit präzise Werte für die zugehörige anisotrope Oberflächenspannung sowie die Steifheit der Grenzfläche zu bestimmen. Ein erneuter Vergleich mit MC Simulationen zeigt auch dieses Mal quantitative Übereinstimmung. Dabei ergibt sich aus der Theorie eine mittlere Oberflächenspannung von $0.66 k_B T / \sigma^2$ mit einer geringen Anisotropie von ungefähr $0.025 k_B T$. Die zugehörigen Steifheiten sind beispielsweise $0.53 k_B T / \sigma^2$ für eine Orientierung (001) der Grenzfläche und $1.03 k_B T / \sigma^2$ für die Orientierung (111). Dabei ist $k_B T$ die thermische Energie des Systems und σ der Durchmesser der Kugeln. Die Anisotropie der Oberflächenspannung von ca. 10% beeinflusst dabei entscheidend die Umrechnung zwischen der Oberflächenspannung und der Steifheit. Natürlich werden die Ergebnisse auch mit vorhandenen experimentellen Daten verglichen, wobei insbesondere die Auswertung mittels klassischer Nukleationstheorie kritisch diskutiert wird.

Während das WBII Funktional nur harte Kugeln beschreibt, ermöglicht die kürzlich entwickelte *extended deconvolution* (extended deconvolution = erweiterte Entfaltung) FMT (edFMT) auch die Beschreibung nicht kugelförmiger Kolloide. Sie wird auf ein System harter Sphärozyylinder angewendet, welche sich in einer homogenen flüssigen Phase befinden, so dass die Eigenschaften des Systems nur von ihren jeweiligen Orientierungen abhängen. Auf letztere wirkt ein externes Feld, welches die Orientierungen in eine Richtung ausrichtet und dabei mit einer Frequenz ω_0 in einer Ebene rotiert. Das System wird mit einer dynamischen DFT beschrieben, welche als Erweiterung der statischen DFT auf Systeme außerhalb des Gleichgewichts zeitabhängig ist. Als Reaktion auf das externe Feld ergibt sich eine komplexe Orientierungsverteilung des Flüssigkristalls, wobei mit zunehmender Frequenz ω_0 fünf dynamische Zustände auftreten, welche als *towing* (Abschleppen), *breathing* (Atmen), *splitting* (Aufspalten), *overtaking* (Überholen) und *unsplitt overtaking* (nicht getrenntes Überholen) beschrieben werden können.

Die edFMT wird außerdem auf hantelförmige Kolloide angewendet, welche sich in einem

Spalt beziehungsweise einem Gravitationsfeld befinden und somit eine inhomogene flüssige Phase bilden. Der frei wählbaren Parameter ζ in der edFMT lässt sich dabei nur schlecht bestimmen, was vermutlich darauf zurück zu führen ist, dass die Theorie für nicht konvexe Teilchen wie Hanteln nicht gültig ist. Da der Parameter ζ nur für lange Teilchen von Null verschieden sein muss, um stabile nematische Phasen zu beschreiben, wird $\zeta = 0$ verwendet, was im Vergleich mit MC Simulationen bei nicht zu hoher Systemdichte auch zu sehr guten Ergebnissen führt.

Schließlich treten bei den Berechnungen der kristallinen Dichteprofile harter Kugeln numerische Probleme auf, weil die lokale Packungsdichte der Teilchen unphysikalisch hohe Werte annimmt. Dies führt zu numerisch kritischem Verhalten der FMT Funktionale. Im Anhang dieser Arbeit werden daher numerische Methoden vorgestellt, mit denen sich diese Probleme vermeiden lassen und mit welchen Konvergenz der Lösungen gewährleistet werden kann.

Contents

Preface	iii
List of published work	iv
Abstract	vii
Zusammenfassung	viii
Contents	xi
1 Introduction	1
2 Theory	5
2.1 Thermodynamics	6
2.2 Statistical physics	9
2.2.1 Classical ensembles and connection to thermodynamics	11
2.2.2 Particle densities and distributions	14
2.3 Density functional theory	15
2.3.1 Existence of the energy functional	16
2.3.2 Properties of the energy functional	18
2.3.3 Particle interactions	19
2.3.4 Several species and orientations	20
2.4 Dynamical Density Functional Theory	21
3 Particle interactions	23
3.1 Soft matter interactions	24
3.1.1 Pair potentials and the Mayer function	26
3.2 Hard spheres	28
3.2.1 The hard-core interactions	28
3.2.2 Experimental realization and simulations	29
3.2.3 Theoretical approaches	30
3.3 Interactions in density functional theory	32
3.4 Fundamental Measure Theory	34
3.4.1 Construction of FMT functionals	38
3.4.2 Functional derivatives and direct correlation functions	43
4 Bulk phases and the hard-sphere crystal	45
4.1 Crystalline structures	47
4.1.1 Crystalline lattices	48

4.1.2	Unit cells	50
4.1.3	Packing of hard spheres	51
4.1.4	Crystalline density profiles and order parameters	53
4.2	Hard-sphere phases	54
4.2.1	Historical progress	55
4.2.2	Density distributions	57
4.2.3	The crystal-fluid phase transition	63
4.2.4	Polydispersity	65
4.3	Conclusion	67
5	The crystal-fluid interface	69
5.1	Theoretical description of interfaces	70
5.2	The interface in theory and simulations	74
5.2.1	Density functional theory	75
5.2.2	Monte Carlo simulations	79
5.2.3	Classical nucleation theory and experiments	80
5.3	Interfacial tensions and stiffnesses	82
5.4	Conclusion	85
6	Anisotropic colloidal particles	87
6.1	Additional theoretical foundations	89
6.2	Driven colloidal liquid crystals	90
6.2.1	The model of hard spherocylinders	91
6.2.2	Towing, breathing, splitting, and overtaking	93
6.2.3	Conclusion	97
6.3	Inhomogeneous fluids of colloidal hard dumbbells	97
6.3.1	Model and system parameters	98
6.3.2	Application of FMT to dumbbells	99
6.3.3	Results for hard walls and gravity	102
6.3.4	Conclusion	104
7	Conclusion	107
A	Mathematics	111
A.1	Gibbs inequality	112
A.2	Functionals and its derivatives	113
A.2.1	Variations and generalized derivative	114
A.2.2	Functional derivatives	115
A.2.3	Examples for functional derivatives	116
A.3	Construction of rotated unit cells	117
A.3.1	Definition: fcc-lattice	117
A.3.2	Definition: rotation of the lattice	117
A.3.3	Theorem: irreducible coordinate vectors	118
A.3.4	Example	118

A.4 Fourier transformation and convolution	119
B Explicit terms in FMT	121
B.1 Derivative of the White Bear II functional	121
B.2 Fluid bulk limit of the White Bear II functional	125
B.3 Fourier transforms of the weight functions for hard spheres	127
B.3.1 Fourier transform of the spherical Heaviside step function	128
B.3.2 Fourier transform of the spherical Dirac function	128
B.3.3 Fourier transform of the vectorial weight function	129
B.3.4 Fourier transform of the tensorial weight function	130
B.4 Decomposition into weight functions	131
C Numerics	133
C.1 Solving the equation of state	134
C.1.1 Picard iterations	136
C.1.2 Direct inversion in iterative subspace (DIIS)	137
C.1.3 Gradient descent dynamics or simulated quenching	138
C.1.4 Dynamical DFT algorithm	139
C.1.5 Convergence of solutions	140
C.1.6 Example for a calculation	141
C.2 Discrete Fourier transformation and convolution	142
Bibliography	146



Daß ich erkenne, was die Welt
Im Innersten zusammenhält,
(To recognize what holds the world together in its inside)

(from: *Faust*, Johann Wolfgang von Goethe 1749 - 1832)

Introduction

Ever since the beginning of humanity, people have been interested in the reasons behind actions happening in nature. Thus, the ancient Greeks, Mayas, and other people already applied calculations for constructions and more. However, along with Galileo Galilei (1564-1642) Sir Isaac Newton (1643-1727) was one of the first scientists who founded physical expectations on a basic, purely mathematical concept. His most important work, the *Philosophiae Naturalis Principia Mathematica* from 1687, reflects this idea and contains his famous laws of motion of bodies that, according to legend, have come to his mind after an apple fell on his head. However, the importance of Newton's understanding of nature and his impact on people is expressed in Alexander Pope's epitaph on Newton's tombstone in Westminster Abbey in London [1]:

Nature, and Nature's Laws lay hid in Night.
God said, Let Newton be! and All was Light.

As outlined in the quotation at the top of this page, the driving force in natural science is curiosity and the basic principle is measuring, collecting expectations, and deriving and formulating predictive laws in a mathematical language. Hence, important ideas often grow from a simple but fascinating expectation. For this reason, theoretical and mathematical concepts are applied to recent topics in research in this thesis.

Humans have been using metallic alloys such as meteoric iron and bronze [2] for thousands of years to produce tools, weapons, and jewelry. Over the years, people recognized that the quality and hardness of these objects is enhanced, if certain materials are combined. Today, metals are smelted and mixed in modern production processes to obtain materials with specific properties. The final products, such as steel beams or screws, are obtained by solidification and can be found everywhere in daily life. Similarly, crystals take a considerable part in daily life. Common crystals are salt or diamonds and the latter are, as we know, in demand as jewelry. Moreover, crystals are the cores of lasers, and large defect-free crystals are needed in neutron scattering experiments or to create modern materials such as semiconductors. Similar to metallic alloys, crystals are grown by solidification from an oversaturated melt. Accordingly, fundamental knowledge of the melting and solidification process is an essential condition for working effectively with such materials.

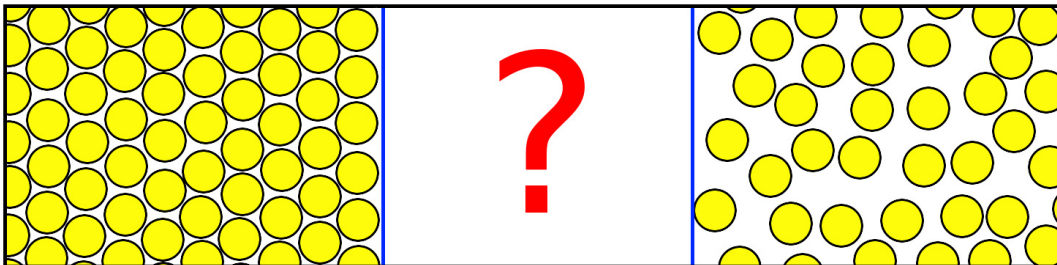


Figure 1.1: (Color) Schematic sketch of a two-dimensional hard-disk system to motivate investigations on the crystal-fluid interface. If the crystalline phase (left) and the fluid phase (right) are brought in contact with each other, an interface will constitute which separates both phases. The properties of this interface are discussed in this work.

Melting and solidification are dynamic processes involving two physical phases of a material. With respect to metallic alloys and crystals, these are a fluid and a solid (crystalline) phase, respectively (see Fig. 1.1). They are separated by an interface that stores a certain amount of energy per interface area, called the interfacial tension. For crystalline solids, this tension depends on the orientation of the interface that is related to an interfacial stiffness. Since this anisotropy controls changes of the interfacial shape, understanding the crystal-fluid interface quantitatively on a microscopic scale can help to gain deeper insight into the processes of melting and solidification as described above.

To obtain quantitative predictive results, it is useful to investigate a respectable model that can serve as a reference system. In 1991, the Nobel prize in physics was awarded to Pierre-Gilles de Gennes (1932-2007) “for discovering that methods developed for studying order phenomena in simple systems can be generalized to more complex forms of matter, in particular to liquid crystals and polymers” [3,4]. Thus, excellent model systems are available in the rich field of soft matter, where typical length scales range from about 1nm up to $10\mu\text{m}$. These mesoscopic length scales allow the observation of particles by scattering measurements with visible light. Thus, single particle trajectories can be traced in real-space measurements, which allows direct validation of theoretical approaches in experiments. Soft matter [3, 5] includes most biological and daily used materials, for example milk, honey, ink, and blood. Here, typical particles are colloids, polymers, or tensides and, in contrast to granular matter or complex plasmas [6], they are solved in microscopic solvents (i.e. blood cells in the blood plasm).¹ Moreover, the macroscopic behavior of soft matter strongly depends on the interactions between the mesoscopic (or colloidal) particles which, in principle, are tunable. They can be adjusted by screening electric forces or sterically stabilizing the colloidal particles², for instance. Accordingly, a wide set of applications arises, including tunable models and “intelligent” fluids such as

¹Neither fluid nor solid, soft matter systems are also called *complex fluids*.

²Typically, polymers are attached to colloidal surfaces, which results in additional (entropic) repulsive or attractive depletion forces, depending on the system.

those being used in liquid crystal displays.

One of the most important model systems is the hard-core model, where particles only interact when they are in contact (short-ranged interaction). Solely driven by entropic forces, hard-particle systems state ideal model, benchmark, and reference systems and are being intensely investigated over the last decades. Particle shapes are various and in principle, soft interactions can be mapped onto effective hard-core interactions [7]. Here, shapes range from simple spherical ones over rodlike, cubic, brig like, and dumbbell-like, to more complex ones [8] and even in experiments, a large set of shapes is available. Of course, the simplest shape is that of a hard sphere and for this reason, hard-sphere systems belong to the most investigated soft matter systems. Consequently, hard spheres are known to crystallize in a fcc structure, similar to metals like nickel and copper, and therefore, they constitute perfect reference systems for the investigation of interfaces. However, quantitative predictions for hard-sphere interfaces are needed to clarify apparent discrepancies found in real-space experiments of sterically-stabilized colloidal suspensions [9–12].

In general, a theoretical description of soft matter systems must include the mesoscopic particles as well as the microscopic solvent. Consequently, many-particle systems have a huge number of parameters that must be described. For example, a state of a pint of alcohol has about $10^{24} - 10^{25}$ coordinates [13], which are too many to apply calculations with actual computational resources. Thus, simple models can be defined which contain only a few macroscopic parameters, or experiments can be applied. For example, H. Ayrton describes *The Origin and Growth of Ripple-mark* in 1904 [14], motivated by curiosity about the existence of “sandy shore covered with innumerable ridges and furrows, as if combed with a giant comb”.

Now, *density functional theory* (DFT) is a theory that is based on statistical physics and describes a density distribution instead of single particles [15–18]. Developed in the context of quantum mechanics by P. Hohenberg and W. Kohn [19], it has also been extended to finite temperature [20] and classical systems [21,22]. In 1998, the Nobel prize in chemistry has been awarded to Walter Kohn³ (*1923) *for his development of density-functional theory* [23, 24]. Moreover, DFT provides a theoretical framework to obtain the (grand canonic) energy of a system in equilibrium. For this purpose, a functional is needed that depends on the local one-particle density, but which is not known in general [20]. Accordingly, a huge family of approximate functionals has been obtained over the last decades, including a family of fundamental measure theory (FMT) functionals [25–29] which perfectly describe hard-core interactions, but whose properties are not known ab initio. Consequently, they must be applied to physical models and a comparison must be drawn to experiments and/or computer simulations. However, developed from statistical physics, DFT is, in principle, a promising tool, if a reliable functional is known. In addition, DFT can also be extended to non-equilibrium situations. As the atomic motion of the microscopic solvent is much faster than the movement of the mesoscopic particles, the solvent particles can be integrated out. Then, they enter a dynamic DFT (DDFT) in

³The prize was shared by J. A. Pople.

form of thermal noise [30] or diffusion [31]. Besides, hydrodynamics can also be taken into account [32].

In this thesis, first an introduction to the theoretical framework is given in Chapter 2, resulting in a detailed description of DFT. Then, particle interactions are discussed in Chapter 3 and FMT is introduced, especially the very accurate *White Bear version mark II* (WBII) and the extended deconvolution FMT (edFMT) which are both applied to physical systems in this work. In Chapter 4, the crystal and the fluid phase of hard-sphere systems are analyzed in detail in the framework of DFT and results are carefully compared to Monte Carlo (MC) computer simulation and to available experimental data to obtain detailed knowledge about the WBII approach. On this fundament, the crystal-fluid interface in a hard-sphere system is investigated in Chapter 5. Performing free minimization of the one-particle density, the orientation-resolved interfacial tensions and stiffnesses are obtained for the equilibrated interface, supported again by MC computer simulations. The results are compared with existing experimental findings. Finally, edFMT is applied to non-spherical anisotropic spherocylinders and dumbbells in Chapter 6. As orientational order plays an important role in switching processes of liquid crystal displays, the dynamic behavior of orientational resolved spherocylinders is analyzed by DDFT, while a time-dependent external field is applied to the system that acts solely on the orientations of the particles. Moreover, the model of non-convex dumbbells is investigated in the context of edFMT to analyze the effects of non-convexity and is finally compared to computer simulations.

2

Theory

Go, wondrous creature! mount where science guides,
 Go, measure earth, weigh air, and state the tides;
 Instruct the planets in what orbs to run,
 Correct old Time, and regulate the sun;

(from: *An Essay on Man*, Alexander Pope 1688 - 1744)

The basic principle of natural science is measuring, collecting expectations, and deriving and formulating predictive laws in a mathematical language. Accentuating this concept, William Thomson (1824-1907, since 1892 Lord Kelvin) placed the above cited lines of the poem *An Essay on Man* from Alexander Pope on the title page of an academic essay *On the Figure of the Earth* in 1839/1840.¹

Applying this principle, the French physicist (Nicolas Léonard) Sadi Carnot (1796-1832) established thermodynamics² in 1824 with the aim of increasing the efficiency of steam machines.³ Later on, William Thomson formulated a first definition of thermodynamics and heat⁴ and defined thermodynamics as the relation between heat and forces.⁵ Thus, thermodynamics is a phenomenological theory of microscopic systems in equilibrium, using macroscopic variables like entropy, temperature, or pressure,⁶ but the physics of the microscopic constituents is not described.

In some sense, statistical physics fills the gap between Newton's mechanics and the thermodynamics of Lord Kelvin and S. Carnot and describes the physical behavior of the microscopic constituents, using variables like particle velocities and particle interactions. The main idea of statistical physics⁷ is the calculation of the partition function that takes into account all possible states or configurations of a system. Knowing this function, all thermodynamic quantities can be deduced from it. Consequently, statistical physics has been used to develop thermodynamics on a microscopic understanding. Thus, statistical physics is an ideal and necessary starting point to develop microscopic theories for many body systems, leading to a more fundamental understanding than by using phenomenological theories.

¹S. P. Thompson in Ref. [33] on page 10. The poem is taken from *An Essay on Man*, Epistle II, pages 376f in Ref. [34].

²For example, see K. C. Cheng about the historical development of thermodynamics [35].

³The article from 1824 is about *Reflections on the Motive Power of Fire and on Machines Fitted to Develop that Power* [36] (Orig. title: "Réflexions sur la puissance motrice du feu et sur les machines propres à développer cette puissance").

⁴Similarly, Joseph Fourier (1768-1830) developed a mathematical theory of heat [35].

⁵See *The Life of Lord Kelvin* by S. P. Thompson [33].

⁶A well-structured textbook is written by H. B. Callen [13].

⁷For example, see textbooks of F. Reif or J. E. Mayer and M. G. Mayer [37, 38].

One of these theories based on statistical physics is the *density functional theory* (DFT). It was developed in 1964 by P. Hohenberg and W. Kohn [19] and has been extended by N. D. Mermin [20] to finite temperature one year later. Adapted to classical (colloidal) systems [21, 22], DFT is a theoretical framework to describe the one-particle distribution function (or density profile) of particles as well as the energy and structure of systems in equilibrium. For this reason, a functional is introduced that returns the free energy which corresponds to a particle density distribution function in a system.

In this chapter, thermodynamics and statistical physics are re-called in Sec. 2.1 and Sec. 2.2, including the definitions of averages, thermodynamic potentials, and density distributions. From this foundations, the framework of DFT is derived in Sec. 2.3, for the moment without including particle interactions in an explicit form; this will be the topic of chapter 3. Finally, the static framework of DFT is extended to non-equilibrium situations in a dynamical density functional theory (DDFT) which is presented in Sec. 2.4.

This chapter is mainly based on textbooks of H. B. Callen [13], F. Reif [37], J. E. Mayer and M. G. Mayer [38], and J.-P. Hansen and I. R. McDonald [39], as well as on articles and lecture notes of R. van Roij⁸ and R. Evans⁹ [22].

2.1 Thermodynamics

In this section, the basic principles of thermodynamics are outlined [13, 39]. Referring to the definition by William Thomson (1824–1907), [42]

thermo-dynamics falls naturally into two divisions, of which the subjects are respectively, the relation of heat to the forces acting between contiguous parts of bodies, and the relation of heat to electrical agency.

In equilibrium, a thermodynamic system is fully specified by so called state variables that characterize the thermodynamical properties of the system and are either extensive or intensive. Extensive state variables scale with the size of the system while the physical properties of the system remain unchanged. Typical representatives are the volume V of the system, the mass m of all particles, the total amount N_i of the particles of a certain species i , the internal energy U , and the entropy S . On the other hand, representatives of intensive variables are the temperature T , pressure p , and chemical potential μ_i of a certain species i . These variables are independent of the size of the system.

Depending on the system and its surroundings, different sets of state variables can be used to fully describe the thermodynamical properties, because the state variables are not independent. For example, pressure and volume depend on each other and on the environment of the system, as it is shown in Fig. 2.1. The environment can consist of a heat reservoir to fix the temperature, a flexible wall or piston to fix the pressure, or a source

⁸Lecture notes of R. van Roij [40, 41] at Utrecht University.

⁹Lecture notes and private communication.

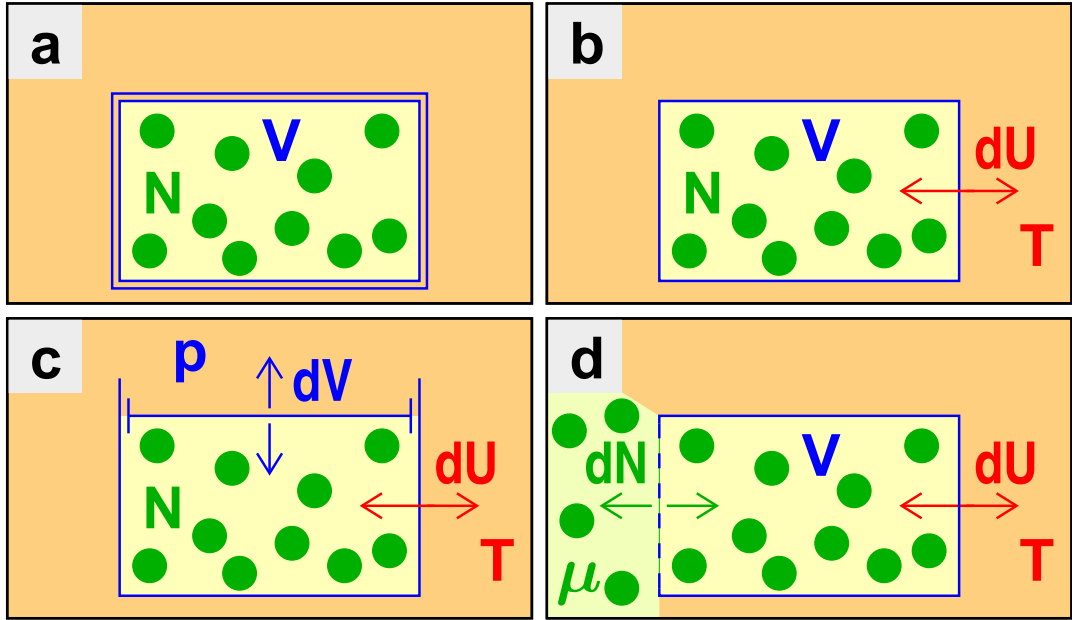


Figure 2.1: (Color) Thermodynamical systems: a) Isolated system (S, V, N), b) system (T, V, N) with heat exchange (canonical system), c) system (T, p, N) with additional change in volume (Gibbs system), d) system (T, V, μ) with particle exchange (grand canonical system).

or sink of particles. Moreover, a thermodynamic system with a special set of related state variables is called a thermodynamical ensemble.

Furthermore, every ensemble is connected to a thermodynamic potential or, in other words, to a kind of energy. Some potentials, as shown in Table 2.1, are the internal energy $U(S, V, \{N_i\})$ of a system with fixed entropy, volume, and particle numbers (see Fig. 2.1a), the (Helmholtz) free energy $F(T, V, \{N_i\})$, differing from the latter in a fixed temperature instead of a fixed entropy (see Fig. 2.1b), and the grand canonical energy $\Omega(T, V, \{\mu_i\})$ with a fluctuating number of particles (see Fig. 2.1d).

Now, all relations between the state variables of an ensemble can be obtained from the corresponding thermodynamic potential. As it becomes apparent from Table 2.1, two potentials differ in the correspondence to their state variables. In other words, one or more state variables are replaced by their, so called, conjugated ones to change between two potentials. This change is performed by a Legendre transformation, where the product of two conjugated variables enters. This product has the dimension of energy, where one factor represents a measure of change in the system (volume, particle number, entropy), while the other factor describes a quantity to perform this change. For example, the transformation between the free energy and the grand canonical energy is applied by

$$\Omega(T, V, \{\mu_i\}) = F(T, V, \{N_i\}) - \sum_i \mu_i N_i, \quad (2.1)$$

Table 2.1: Thermodynamic potentials and their corresponding state variables. In addition, the Legendre transformation between the internal energy and the appropriate potential is given.

Thermodynamic potential	variables	transformation
Internal energy U	$S, V, \{N_i\}$	
(Helmholtz) free energy F	$T, V, \{N_i\}$	$U - TS$
Enthalpy H	$S, p, \{N_i\}$	$U + pV$
Gibbs free energy G	$T, p, \{N_i\}$	$U + pV - TS$
Grand (canonical) energy Ω	$T, V, \{\mu_i\}$	$U - TS - \sum_i \mu_i N_i$

using the product of the chemical potential μ_i and the particle number N_i , where the particle number of species i depends implicitly on the chemical potential, the volume, and temperature.

Consequently, it is of essential importance to know at least one relation that describes one of the thermodynamical potentials. Indeed, the internal energy $U(S, V, N)$ is known to consist of heat TS , work pV , and chemical energy μN , and thus it reads

$$U(S, V, N) = TS - pV + \mu N. \quad (2.2)$$

This fundamental relation is related to the first law of thermodynamics.

Hence, thermodynamics deals with four important postulates or laws, called the laws of thermodynamics. The zeroth law of thermodynamics states that connected systems equilibrate transitively, where the third law states that absolute zero temperature cannot be reached. Additionally, the latter is attributed to W. Nernst.¹⁰

The first law of thermodynamics deals with the conservation of energy and is ascribed to R. Clausius [43,44],¹¹ who stated that in a thermodynamic process, the raise in the internal energy of a system is equal to the difference between the raise of heat accumulated by the system and the raise of work done by it.¹² In other words, a change in internal energy $\Delta U = Q + \Delta W$ causes a conversion into work ΔW and into an amount of heat Q .¹³

The second law of thermodynamics defines the concept of entropy and its increase in closed systems. Its first formulation is attributed to S. Carnot, but R. Clausius and Lord Kelvin also drew equivalent formulations. Moreover, R. Clausius has introduced the concept of entropy [45] and finally Ludwig Eduard Boltzmann (1844-1906) connected it with

¹⁰For further information see K. C. Cheng, *Historical Development of the Theory of Heat and Thermodynamics* [35], page 29.

¹¹The conservation of heat had been stated already before R. Clausius from several scientists.

¹²R. Clausius states in [43] on p. 373: “(...) es soll nur ein (...) Satz als Grundsatz hingestellt werden, nämlich daß in allen Fällen, wo durch Wärme Arbeit entstehe, eine der erzeugten Arbeit proportionale Wärmemenge verbraucht werde, und daß umgekehrt durch Verbrauch einer ebenso großen Arbeit dieselbe Wärmemenge erzeugt werden könne.”

¹³Following Eq. (2.2) it reads $dU = TdS - pdV + \mu dN$.

statistical disorder¹⁴ in his famous law $S = k \log W$, written on his gravestone. The law connects the number of microstates via W with the macroscopic entity of entropy S , where $k = k_{\text{B}}$ is the Boltzmann constant.

Furthermore, thermodynamics deals with the so-called equations of state that connect the (state) variables of a physical system with each other in a certain way, such that the equations describe a real physical state of the system. For example, the laws describing an ideal gas are famous and well-known equations of state and they read¹⁵

$$pV = Nk_{\text{B}}T, \quad E = \frac{3}{2}Nk_{\text{B}}T, \quad (2.3)$$

where E is the energy of the system and k_{B} denotes the Boltzmann constant, relating the individual energy of particles with temperature that is defined on a macroscopic level.

However, the equations do not hold for real gases because interactions between the constituents of the gases are not captured. For this reason, M. Thiesen [49] and H. Kamerlingh Onnes [50] expressed the pressure of a thermodynamic system in equilibrium as a power series in terms of the density $\rho = N/V$ of the system,

$$\frac{p(\rho, T)}{k_{\text{B}}T} = \rho + \sum_{n=2}^{\infty} B_n(T)\rho^n. \quad (2.4)$$

Here, the temperature-dependent prefactors B_n are called n^{th} virial coefficients. It should be noted that the Nobel Prize in physics was awarded in 1913 to Heike Kamerlingh Onnes (1853-1926) *for his investigations on the properties of matter at low temperatures which led, inter alia, to the production of liquid helium* [51].

2.2 Statistical physics

Statistical physics¹⁶ deals with methods and laws of statistics¹⁷ that are applied to microscopic quantities in physical systems, to achieve macroscopic observables that are able to describe properties like energy and the number of particles in many particle systems with particle numbers of about 10^{23} . Hence, statistical methods are needed for their calculation and, for this reason, statistical weights and averages of the physical system are necessary.

In principle, two kinds of averages are common: The time average and the ensemble average.¹⁸ If both averages are equal, the system is called ergodic. The time average \bar{A}

¹⁴From information theory also the Shannon entropy is known.

¹⁵The equation of state for the ideal gas was mentioned first by E. Clapeyron [46], A. Krönig [47], and R. Clausius [48]; for further reading, e.g. see textbooks [13, 39].

¹⁶For further reading see textbooks [37, 38].

¹⁷For example, see textbook of Malcolm Goldman [52].

¹⁸For early discussions, e.g. see work of P. Hertz [53, 54].

of an observable or operator $A(\psi)$ of an physical state ψ of a system measures the mean value of A on a certain time interval $[t_0, t_0 + \Delta t]$ as

$$\bar{A} = \frac{1}{\Delta t} \int_{t_0}^{t_0 + \Delta t} A(\psi(t)) dt. \quad (2.5)$$

Following the spirit of the law of large numbers, this average is, in general, only independent of t_0 if $\Delta t \rightarrow \infty$, and thus, the time average is sometimes directly defined in this limit [39].

On the contrary, the ensemble (or configuration) average $\langle A \rangle$ of any operator A measures the average over all possible configurations $\psi \in \Gamma$ of the system. Here, the configuration space or phase space Γ holds all possible configurations of the system. Likewise, a subset $\Gamma_A \subset \Gamma$ is called an ensemble, if the macroscopic observable A is constant for all $\psi \in \Gamma_A$.

Because some of the configurations $\psi \in \Gamma$ appear more often than others, the configurations of the system are weighted with a statistical weight $f_0(\psi, t)$, reflecting the probability to find a certain state ψ of the set Γ at time t . Similarly, the distribution of phase points ψ in a given ensemble Γ_A is given by a phase space probability density $f_A(\psi \in \Gamma_A, t)$, where f_A is defined on the $\psi \in \Gamma_A$. Correspondingly, the ensemble average is calculated by

$$\langle A \rangle = \text{Tr}_{\text{cl}}(f_0 A) \quad (2.6)$$

as an average over all possible states Γ of the system. Here, the classical trace Tr_{cl} for an operator A is defined by¹⁹

$$\text{Tr}_{\text{cl}} A = \sum_{N=0}^{\infty} \frac{1}{h^{3N} N!} \int_{\Gamma_N} A d\psi, \quad (2.7)$$

where h denotes the Planck constant. Furthermore, the weight f_0 is normalized and therefore holds $\text{Tr}_{\text{cl}} f_0 = 1$.

It should be mentioned that the definition of the classical trace Eq. (2.7) is also possible without the factor $1/(h^{3N} N!)$, even without the sum over the number of particles. Then, the definitions of the partition sums in the next subsection also alter. This change would allow the more general definition of the classical trace by $\int_{\Gamma} A d\psi$, but in literature and with respect to classical N -particle systems the used definition is more common.

The time evolution of a probability density f_A is given by the Liouville equation

$$\frac{\partial f_A(\psi, t)}{\partial t} + \nabla_{\Gamma}(f_A(\psi, t)) \frac{d\psi}{dt} = 0, \quad (2.8)$$

where ∇_{Γ} is the gradient in phase space. In other words, the Liouville equation states the preservation of volumes (or areas) in phase space and, thus, it is similar to the continuity equation. Consequently, the time evolution of a system is given by the time evolution of

¹⁹Compare the definitions of R. Evans [22] and J.-P. Hansen and I. R. McDonald (Appendix B) [39].

its corresponding phase point $\psi(t) \in \Gamma$.

Applying the concept to a classical system of N particles in three dimensions, a phase point contains the $3N$ positions $\vec{r}^N = \{\vec{r}_i\}$ and momenta $\vec{p}^N = \{\vec{p}_i\}$ of all particles. Accordingly, the phase space has a dimension of $\dim(\Gamma) = 6N$. The Hamiltonian of such a system is then given by

$$\mathcal{H}(\psi) = \mathcal{T}(\vec{p}^N) + \mathcal{U}(\vec{r}^N) + \mathcal{V}_{ext}(\vec{r}^N) \quad (2.9)$$

and provides the energy to a given system state $\psi = (\vec{r}^N, \vec{p}^N)$, where $\mathcal{U} = \mathcal{U}(\vec{r}^N)$ is the particle interaction potential depending on all particle positions,

$$\mathcal{V}_{ext}(\vec{r}^N) = \sum_{i=1}^N V_{ext}(\vec{r}_i) \quad (2.10)$$

is the energy due to an external potential V_{ext} that acts on single particles, and

$$\mathcal{T}(\vec{p}^N) = \sum_{i=1}^N \frac{|\vec{p}_i|^2}{2m_i} \quad (2.11)$$

is the kinetic energy of all particles.

2.2.1 Classical ensembles and connection to thermodynamics

Conserved quantities are of particular interest in physics. Since some variables of a thermodynamic system are conjugated, several ensembles exist that differ in their conserved thermodynamic variables as well as their probability density and occupied volume in phase space. In general, three ensembles of particular interest exist, by name the microcanonical, the canonical, and the grand canonical, that will be discussed in the following paragraphs.²⁰

First, the microcanonical ensemble combines all isolated systems that have fixed energy E_0 , volume V , and particle number N . Its energy equals the Hamiltonian of every single system. Consequently, its probability density

$$f_m(\psi) = \frac{\delta(E_0 - \mathcal{H}(\psi))}{\omega(E_0, V, N)} \quad (2.12)$$

$$\omega(E_0, V, N) = \int_{\Gamma_N} \delta(E_0 - \mathcal{H}(\psi)) d\psi \quad (2.13)$$

consists of a Dirac δ -function,²¹ that fixes the internal energy to a value E_0 , and of a normalization factor ω . In principle, the latter is similar to a partition sum that counts all

²⁰Following lecture notes by R. van Roij of Utrecht University [40, 41] and [39].

²¹This is not a function in a mathematical sense (see also Eq. (A.16)).

possible states in an ensemble.

Furthermore, the microcanonical ensemble is linked to thermodynamics by the famous law of J. Stefan and L. Boltzmann,

$$S(U, V, N) = k_B \log (Z_m(U, V, N)), \quad (2.14)$$

and thus, it is characterized by entropy S . Here, $Z_m(U, V, N) = \omega(U, V, N)k_B T/(h^{3N}N!)$ is the microcanonic partition sum.²²

Second, the canonical ensemble describes systems that are connected to an external energy reservoir with fixed temperature. For this reason, such systems have a fixed temperature. It reflects everyday life in a more natural way than the microcanonical ensemble, because closed rooms normally have a fixed temperature T , volume V , and particle number N . In the canonical ensemble, the total energy is distributed according to the Boltzmann distribution and, therefore, its probability density f_c and partition sum Z_c read

$$f_c(\psi) = \frac{\exp(-\beta\mathcal{H}(\psi))}{Z_c(T, V, N)} \quad (2.15)$$

$$Z_c(T, V, N) = \frac{1}{h^{3N}N!} \int_{\Gamma_N} d\psi \exp(-\beta\mathcal{H}(\psi)) \quad (2.16)$$

with $\beta = 1/k_B T$ denoting the inverse temperature.

Similar to Eq. (2.14), the link to thermodynamics is applied by the statistical logarithmic law of Boltzmann. Since the corresponding thermodynamic potential for the canonical ensemble is the (Helmholtz) free energy $F(T, V, N)$, its connection to the partition sum reads

$$F(T, V, N) = -k_B T \log (Z_c(T, V, N)). \quad (2.17)$$

If the free energy is known, all thermodynamical parameters of the canonical ensemble can be obtained by using the relations which are known from thermodynamics.

As an example, the ideal gas consists of non-interacting classical particles. In a canonical ensemble, the partition sum Z_c (Eq. 2.16) reduces to²³

$$Z_c^{\text{id}}(T, V, N) = \frac{V^N}{h^{3N}N!} \int_{\mathbb{R}^{3N}} \exp \left(-\beta \sum_{i=1}^N \frac{|\vec{p}_i|^2}{2m} \right) d\vec{p}^N = \frac{V^N}{N!\Lambda^{3N}} \quad (2.18)$$

with $\Lambda = h/\sqrt{2\pi mk_B T}$ denoting the thermal (De Broglie) wavelength [55]. Then, using

²²In literature sometimes $\omega(U, V, N)$ is already defined as microcanonic partition sum.

²³Remembering the definition of a phase point $\psi = (\vec{r}^N, \vec{p}^N)$, of the kinetic energy (2.11) of an ideal gas, and $\int \exp(-x^2/c)dx = \sqrt{c\pi}$.

Stirling's approximation,²⁴ the free energy (2.17) for an ideal gas reads

$$F^{\text{id}}(T, V, N) = Nk_B T \left[\log \left(\frac{N}{V} \Lambda^3 \right) - 1 \right]. \quad (2.19)$$

Following this result, the equations of state (2.3) are derived directly using the thermodynamic relations $p = -\partial F(T, V, N)/\partial V$ and $E = \partial(\beta F(T, V, N))/\partial\beta$. In addition, the chemical potential $\mu^{\text{id}} = \partial F^{\text{id}}(T, V, N)/\partial N = k_B T \log(\Lambda^3 N/V)$ for an ideal gas is obtained.

As third ensemble, the grand canonical ensemble describes systems that allow energy and particle exchange at a fixed chemical potential and temperature. For example, houses have a fixed volume V and allow particle and energy exchange with their environment that has a fixed chemical potential μ and temperature T . Since the grand canonical ensemble can be seen as a combination of canonical ensembles, in the grand canonical ensemble not only the energy fluctuates but also the number of particles. Hence, the grand canonical probability density f_g and partition sum Ξ reads

$$f_g(\psi, N) = \frac{\exp(-\beta(\mathcal{H}(\psi) - \mu N))}{\Xi(T, V, \mu)}, \quad (2.20)$$

$$\Xi(T, V, \mu) = \sum_{N=0}^{\infty} \frac{\exp(\beta N \mu)}{h^{3N} N!} \int_{\Gamma} \exp(-\beta \mathcal{H}(\psi)) d\psi. \quad (2.21)$$

As for the canonical ensemble, the link to thermodynamics is established by the law of Boltzmann and, since the corresponding potential for the grand canonical ensemble is the grand canonical energy $\Omega(T, V, \mu)$, the connection to the partition sum follows as

$$\Omega(T, V, \mu) = -k_B T \log(\Xi(T, V, \mu)). \quad (2.22)$$

At this point, it is also common to define the fugacity

$$z = \frac{\exp(\beta \mu)}{\Lambda^3} \quad (2.23)$$

to relate the canonical partition function f_c to the grand canonical one, while applying the integration over the momenta for both sums.

²⁴Stirling's approximation (in second order), also called Euler-McLaurin sum rule, reads $\log(N!) = N \log(N) - N + \mathcal{O}(\log(N))$ (for example, see Ref. []).

2.2.2 Particle densities and distributions

The particle density or particle distribution function at position \vec{r} is defined for a system of N particles at positions \vec{r}^N by

$$\hat{\rho}(\vec{r}, \vec{r}^N) = \sum_{i=1}^N \delta(\vec{r} - \vec{r}_i). \quad (2.24)$$

In principle, it counts particles at a certain position \vec{r} and, thus, is a microscopic quantity.

Moreover, the one-particle density $\rho_N^{(1)}$ is defined as a macroscopic quantity as an ensemble average of the particle distribution in an N -particle system and reads

$$\rho_N^{(1)}(\vec{r}) = \langle \hat{\rho}(\vec{r}, \vec{r}^N) \rangle. \quad (2.25)$$

As it is apparent from its definition in Eq. (2.24), an integration over the one-particle density yields $\int_V \rho_N^{(1)}(\vec{r}) d\vec{r} = N$, the number of particles in the system.²⁵ Furthermore, the one-particle density is a continuous and differentiable function, due to its definition in the continuum limit of the classical trace (2.7). Accordingly, it is a bounded function with respect to the supremum norm, if defined on a compact domain $V \subset \mathbb{R}^3$.²⁶

Similar to the definition of the one-particle density, n -particle densities $\rho_N^{(n)}$ can be defined as a trace of products of n independent sums of δ -distributions. At the same time, another route uses the probability density of the corresponding statistical ensemble to define the n -particle densities. Since the probability density $f(\psi)$ holds all states of an ensemble, the n -particle density is obtained by an integration over all momenta and $(N - n)$ spatial coordinates of phase space and reads

$$\rho_N^{(n)}(\vec{r}^n) = \frac{N!}{(N - n)!} \int_{V^{(N-n)}} \int_{\mathbb{R}^{3N}} f(\psi = (\vec{r}^N, \vec{p}^N)) d\vec{p}^N d\vec{r}^{(N-n)}. \quad (2.26)$$

Because the particles and its coordinates are indistinguishable in phase space, a multiplication with a combinatorial factor $N!/(N - n)!$ is necessary.

Nevertheless, the structure of a fluid often is analyzed using the n -particle distribution function

$$g_N^{(n)}(\vec{r}^n) = \frac{\rho_N^{(n)}(\vec{r}^n)}{\prod_{i=1}^n \rho_N^{(1)}(\vec{r}_i)}. \quad (2.27)$$

This function measures the internal structure of a fluid that contains N particles. For example, an ideal gas without any internal structure, due to missing particle interactions, has a constant distribution function $g \equiv 1$. Thus, all particles in the system are distributed randomly.

²⁵Thus, an homogeneous system (like a fluid phase) features the spatial-independent one-particle density $\rho_N^{(1)} = N/V$.

²⁶In general, the definition on \mathbb{R}^n is also possible.

Because the total correlation is zero in this case, a total correlation function $h = g - 1$ can be defined, which gives the non-trivial part of the correlations. Furthermore, a direct pair-correlation function $c^{(2)}$ is often defined by the Ornstein-Zernike relation²⁷

$$h(\vec{r}, \vec{r}') = c^{(2)}(\vec{r}, \vec{r}') + \int_V c^{(2)}(\vec{r}, \vec{r}'')\rho(\vec{r}'')h(\vec{r}'', \vec{r}')d\vec{r}'' \quad (2.28)$$

that can be solved recursively. As an obvious physical interpretation, J.-P. Hansen and I. R. McDonald state:²⁸

the “total” correlation between particles 1 and 2, represented by $h^{(2)}(1, 2)$, is due in part to the “direct” correlation between 1 and 2 but also to the “indirect” correlation propagated via increasingly large numbers of intermediate particles.

2.3 Density functional theory

Density functional theory (DFT) provides a functional of the one-particle density (2.25) to determine the free energy of a classical thermodynamic system. Once having knowledge about this energy functional, all thermodynamic properties of the physical system can be obtained.

In 1964, P. Hohenberg and W. Kohn published an article about the *Inhomogeneous Electron Gas* [19], where they introduced DFT for the ground state ($T = 0$) of the system. One year later, N. D. Mermin expanded DFT to non-zero temperatures [20] in a grand canonical ensemble.²⁹ In the 1970’s, DFT has been applied to classical systems by C. Ebner, W. F. Saam, and D. Stroud, in a work about *Density-functional theory of simple classical fluids (I. Surfaces)* [21], and some years later by R. Evans in a work about *The nature of the liquid-vapour interface and other topics in the statistical mechanics of non-uniform, classical fluids* [22]. In 1998, the nobel prize in chemistry has been awarded³⁰ to Walter Kohn (*1923) for his development of density-functional theory [23, 24].

This section follows the original works of N. D. Mermin [20], R. Evans [22], and the textbook of J.-P. Hansen and I. R. McDonald [39]. For furter reading, see also Refs. [15–18]. In addition, Appendix A.2 gives an outline about the concept of functionals and its derivatives.

²⁷The direct correlation function as a derivative of the intrinsic free energy gives the function greater physical meaning [39]; see also Eq. (2.50) and Ref. [22].

²⁸See p. 59, Sec. 3.5, in Ref. [39].

²⁹N. D. Mermin noted that the theory also works in a canonical ensemble.

³⁰The prize was shared by J. A. Pople.

2.3.1 Existence of the energy functional

For a Hamiltonian \mathcal{H} , an intrinsic chemical potential μ , and a number N of particles of a system, the functional

$$\Omega[f] = \text{Tr}_{\text{cl}} [f (\mathcal{H} - \mu N + k_B T \log(f))] \quad (2.29)$$

can be considered, re-calling the definitions of the classical trace (2.7) and of the probability density f (e.g. Eq. (2.20) for the grand canonical ensemble). Due to the definition of this functional, the grand potential (2.22) is obtained, if the equilibrium probability density (2.20) is inserted in the functional. Thus, remembering $\text{Tr}(f_g) = 1$, it follows

$$\Omega[f_g] = -k_B T \log(\Xi(T, V, \mu)) \equiv \Omega. \quad (2.30)$$

Moreover, the equilibrium probability density minimizes the functional Ω . Accordingly, it satisfies the inequality

$$\Omega[f] > \Omega[f_g] \quad (2.31)$$

for a given probability density $f \neq f_g$. This can be seen easily from the definition of the functional (2.29) in combination with Eq. (2.30),

$$\begin{aligned} \Omega[f] &= \Omega[f_g] + k_B T \log(\Xi(T, V, \mu)) \text{Tr}_{\text{cl}}(f) + \text{Tr}_{\text{cl}}[f(\mathcal{H} - \mu N + k_B T \log(f))] \\ &= \Omega[f_g] + k_B T \text{Tr}_{\text{cl}} \left[-f \log \left(\frac{\exp(-(\mathcal{H}_n - \mu N)/k_B T)}{\Xi(T, V, \mu)} \right) + f \log(f) \right] \\ &= \Omega[f_g] + k_B T \text{Tr}_{\text{cl}} [f \log(f) - f \log(f_g)], \end{aligned} \quad (2.32)$$

and using Gibbs inequality (A.7) from the appendix.

In the following, it is proven that the functional (2.29) is also determined by the one-particle density ρ . Therefore, it is necessary to prove that the probability density f is a functional of the one-particle density ρ . This is done by following the original proof as given in Refs. [20, 22, 39].

Theorem: For a system with given temperature T , volume V , chemical potential μ , interaction potential \mathcal{U} , and an external potential of the form (2.10), the probability density is a functional of the one-particle density. The proof can be structured into three parts:

1. The probability density f is a unique function of the external potential V_{ext} .
2. The one-particle density ρ is a functional of the probability density f .
3. The probability density f is a functional of the one-particle density ρ .

The second part of the proof is trivial, since the one-particle density ρ is defined as a functional of the probability density f in Eq. (2.25). The third part is equivalent to the existence of a surjective map from ρ to f . In other words, if two probability densities are given with $f \neq f'$, then the corresponding one-particle densities must hold $\rho \neq \rho'$.

Moreover, it will be sufficient to proof that V_{ext} is determined by ρ , due to part 1 of this proof.

If f is shown to be a functional of ρ , then it follows that the functional (2.29) also is a functional of the corresponding density ρ and $\Omega[f] = \Omega[\rho]$. Consequently, Eq. (2.29) can be written as

$$\Omega[f] = \text{Tr}_{\text{cl}}[f\mathcal{V}_{\text{ext}}] + \text{Tr}_{\text{cl}}[f(\mathcal{T} + \mathcal{U} + k_{\text{B}}T \log(f))] - \text{Tr}_{\text{cl}}[f\mu N]. \quad (2.33)$$

Using the definition (2.10) of the external potential \mathcal{V}_{ext} and the definition of the one-particle density in Eq. (2.24) and Eq. (2.25), the identity

$$\text{Tr}_{\text{cl}}[f\mathcal{V}_{\text{ext}}] = \text{Tr}_{\text{cl}}\left[f\left(\int_V \sum_{i=1}^N V_{\text{ext}}(\vec{r})\delta(\vec{r} - \vec{r}_i)d\vec{r}\right)\right] = \int_V \rho(\vec{r})V_{\text{ext}}(\vec{r})d\vec{r} \quad (2.34)$$

can be shown. Similarly, the second identity $\text{Tr}_{\text{cl}}[f\mu N] = \mu \int_V \rho(\vec{r})d\vec{r}$ follows.

Proof (part 1): The probability distribution f_g is a function of the external potential V_{ext} , due to its definition in Eq. (2.20). Furthermore, let $\Delta \in C(V)$ be a continuous variation of the external potential $V'_{\text{ext}}(\vec{r}) = V_{\text{ext}}(\vec{r}) + \Delta(\vec{r})$. Thus, the corresponding probability density reads

$$f'_g(\psi_N, N) = \frac{\exp\left(-\beta \sum_{i=1}^N \Delta(\vec{r}_i)\right) \exp(-\beta(\mathcal{H}(\psi_N) - \mu N))}{\text{Tr}_{\text{cl}}\left[\exp\left(-\beta \sum_{i=1}^N \Delta(\vec{r}_i)\right) \exp(-\beta(\mathcal{H}(\psi_N) - \mu N))\right]} \quad (2.35)$$

with $\psi_N \in \Gamma_N$. It is not possible to achieve $f'_g = f_g$ for any variation $\Delta \neq 0$, because $\Delta(\vec{r})$ solely has spatial dependency and in particular is independent of the particle number N . Consequently, an external potential $V_{\text{ext}}(\vec{r})$ uniquely determines a probability density f_g . \square

Proof (part 3): Two external potentials V_{ext} and V'_{ext} with $V_{\text{ext}} \neq V'_{\text{ext}}$ are supposed and give rise to the same equilibrium density ρ_0 . According to part 1 of the proof, the corresponding probability densities hold $f_0 \neq f'_0$ and the corresponding Hamiltonians are denoted with \mathcal{H} and \mathcal{H}' . Thus, inequality (2.31) also holds and the functional (2.29) reads

$$\begin{aligned} \Omega[f'_0] &= \text{Tr}_{\text{cl}}[f'_0(\mathcal{H}' - \mu N + k_{\text{B}}T \log(f'_0))] \\ &< \text{Tr}_{\text{cl}}[f_0(\mathcal{H}' - \mu N + k_{\text{B}}T \log(f_0))] \\ &= \Omega[f_0] + \text{Tr}_{\text{cl}}[f_0(\mathcal{V}'_{\text{ext}} - \mathcal{V}_{\text{ext}})]. \end{aligned} \quad (2.36)$$

Because both probability densities are assumed to lead to the same equilibrium density ρ_0 , the result is also valid if primed and unprimed quantities are interchanged. Accordingly,

the addition of $\Omega[f'_0]$ and $\Omega[f_0]$ with interchanged quantities leads to the contradiction

$$\begin{aligned} \Omega[f'_0] + \Omega[f_0] &< \Omega[f_0] + \int_V \rho_0(\vec{r}) (V'_{\text{ext}}(\vec{r}) - V_{\text{ext}}(\vec{r})) d\vec{r} \\ &+ \Omega[f'_0] + \int_V \rho_0(\vec{r}) (V_{\text{ext}}(\vec{r}) - V'_{\text{ext}}(\vec{r})) d\vec{r}, \end{aligned} \quad (2.37)$$

re-calling (2.34). Considering this result, it follows that the external potential V_{ext} is determined by the equilibrium density ρ_0 . \square

2.3.2 Properties of the energy functional

Now, the functional (2.29) can be rewritten by using Eq. (2.33) with a dependency of the one-particle density ρ instead of the probability density f by

$$\Omega_V[\rho] = \int_V \rho(\vec{r}) V_{\text{ext}}(\vec{r}) d\vec{r} + \mathcal{F}[\rho] - \mu \int_V \rho(\vec{r}) d\vec{r}. \quad (2.38)$$

Incidentally, the term containing the chemical potential μ is often added to the term containing the external potential V_{ext} by introducing the quantity $\Phi(\vec{r}) = \mu - V_{\text{ext}}(\vec{r})$. This quantity also states a unique functional of the equilibrium density. Moreover, in Eq. (2.38) a functional

$$\mathcal{F}[\rho] = \text{Tr}_{\text{cl}} [f (\mathcal{T} + \mathcal{U} + k_B T \log(f))] \quad (2.39)$$

is defined that is also determined by the one-particle density ρ . Due to its definition, the functional (2.38) has the same properties as the original functional (2.29). For an equilibrium density ρ_0 it provides the grand potential $\Omega = \Omega_V[\rho_0]$ and it is minimized by the density ρ_0 , which can be expressed by

$$\left. \frac{\delta \Omega_V[\rho]}{\delta \rho(\vec{r})} \right|_{\rho=\rho_0} = 0. \quad (2.40)$$

The second functional (2.39) describes the intrinsic Helmholtz free energy that is connected with the grand potential via a Legendre transformation (2.1). Thus, the Helmholtz free energy F reads

$$F = \mathcal{F}[\rho_0] + \int_V \rho_0(\vec{r}) V_{\text{ext}}(\vec{r}) d\vec{r}, \quad (2.41)$$

including an external potential V_{ext} .

Finally, the derivative (2.40) of the grand energy functional yields the Euler-Lagrange equation in DFT. This expression for the chemical potential is “the fundamental equation in the theory of non-uniform fluids” [22] and reads

$$\mu = V_{\text{ext}}(\vec{r}) + \mu_{\text{in}}[\rho_0; \vec{r}]. \quad (2.42)$$

By this, an intrinsic chemical potential

$$\mu_{\text{in}}[\rho; \vec{r}] = \frac{\delta \mathcal{F}[\rho]}{\delta \rho(\vec{r})} \quad (2.43)$$

has been defined that corresponds to the intrinsic Helmholtz free energy (2.39).

If the intrinsic free energy functional (2.39) is known, Eq. (2.42) is an implicit equation to determine the equilibrium density ρ_0 . Thus, knowledge of the functional provides entire information of all physical properties of the system. For example, the functional $\mathcal{F}[\rho]$ is known for a system of non-interacting particles (an ideal gas), as shown in Eq. (2.19) for the case $V_{\text{ext}}(\vec{r}) = 0$. For the inhomogeneous case, the ideal gas free-energy functional reads

$$\mathcal{F}_{\text{id}}[\rho] = k_B T \int_V \rho(\vec{r}) [\log(\rho(\vec{r})\Lambda^3) - 1] d\vec{r} \quad (2.44)$$

and the intrinsic chemical potential $\mu_{\text{in}}[\rho; \vec{r}] = k_B T \log(\rho(\vec{r})\Lambda^3)$ results from Eq. (2.43). Now, the equilibrium density directly follows from Eq. (2.42) as

$$\rho_0(\vec{r}) = z \exp(-\beta V_{\text{ext}}(\vec{r})), \quad (2.45)$$

where the fugacity z has been used that is defined in Eq. (2.23). This result is also known as the barometric law. However, if particle interactions are considered, this simple connection between μ and ρ becomes much more complicated.³¹

2.3.3 Particle interactions

In the presence of particle interactions, it is common to split the intrinsic free energy functional

$$\mathcal{F}[\rho] \equiv \mathcal{F}_{\text{id}}[\rho] + \mathcal{F}_{\text{exc}}[\rho] \quad (2.46)$$

into an ideal gas part (2.44) without particle interactions and an over-ideal or excess part \mathcal{F}_{exc} that includes the interactions. Just as for the intrinsic free energy functional, both parts are unique functionals of the density ρ for a given interaction potential U .

Similarly, the intrinsic chemical potential (2.43) can be written as

$$\beta \mu_{\text{in}}[\rho; \vec{r}] = \log(\rho(\vec{r})\Lambda^3) - c[\rho; \vec{r}], \quad (2.47)$$

which is a sum of an ideal part and of an excess part

$$-c[\rho; \vec{r}] \equiv \beta \frac{\delta \mathcal{F}_{\text{exc}}[\rho]}{\delta \rho(\vec{r})} \quad (2.48)$$

that is also called additional, effective one-body potential [22]. Similar to the ideal gas equation of state (2.45), the equilibrium density follows from the Euler-Lagrange

³¹See also the discussion by R. Evans in chapter 2 of Ref. [22].

Eq. (2.42) and reads

$$\rho_0(\vec{r}) = z \exp(-\beta V_{\text{ext}}(\vec{r}) + c[\rho_0; \vec{r}]). \quad (2.49)$$

Thus, Eq. (2.48) determines the equilibrium density in a self-consistent way and provides an iterative solving-method for numerical implementation.³²

Moreover, $c[\rho; \vec{r}]$ only represents the first member in a hierarchy of direct correlation functions $c^{(n)}[\rho; \vec{r}^n]$ that provide full information about the structural properties of a system and are defined by

$$c^{(n)}[\rho; \vec{r}^n] = -\beta \frac{\delta^n \mathcal{F}_{\text{exc}}[\rho]}{\delta \rho(\vec{r}_1) \dots \delta \rho(\vec{r}_n)}. \quad (2.50)$$

In contrast, the direct pair-correlation function $c^{(2)}[\rho; \vec{r}]$ is often defined via the Ornstein-Zernike relation in Eq. (2.28).

To sum up, the density and the physical properties of the system are determined by the grand energy functional $\Omega[\rho]$, or equivalently by the intrinsic (Helmholtz) free energy functional $\mathcal{F}[\rho]$, as seen for the ideal gas in the previous paragraphs. Moreover, the free energy functional consists of an ideal part (2.44) and of an excess part $\mathcal{F}_{\text{exc}}[\rho]$ that is not known in an explicit form in general. Since \mathcal{F}_{exc} contains the whole particle interactions, its determination is an important part of research. For this reason, (mostly approximate) functionals are introduced and discussed for \mathcal{F}_{exc} in chapter 3.

2.3.4 Several species and orientations

The framework of DFT can be extended to systems that contain more than one species of particles or to an orientational dependency of the particles [22]. Then, the (total) density consists of density profiles ρ_ν for every species and orientation. Moreover, μ_ν and V_{ext} are the corresponding chemical and external potentials. If orientational dependency is assumed for one species of particles, the total density $\rho(\vec{r}, \hat{u})$ is resolved into density profiles $\rho_{\hat{u}}(\vec{r})$ for every orientation \hat{u} of one particle. Of course, the chemical potentials are equal for density profiles that solely differ in their corresponding orientation (and not in the species of particles).

Now, the grand canonical energy functional from Eq. (2.38) can be rewritten for several species and/or orientations by

$$\Omega_V[\rho] = \mathcal{F}[\rho] + \sum_\nu \int_V \rho_\nu(\vec{r}) (V_{\text{ext},\nu}(\vec{r}) - \mu_\nu) d\vec{r}. \quad (2.51)$$

The notation is taken from Ref. [56], where ν denotes a specific shape, size, and orientation, for brevity. Accordingly, the sum over ν denotes a sum over all species and, for each anisotropic species, an integral over its orientation.

³²Such methods are presented in Appendix C.1.

2.4 Dynamical Density Functional Theory

Dynamical density functional theory (DDFT) has been presented by U. M. B. Marconi and P. Tarazona in 1999 [30] “to study the relaxational dynamics of an assembly of interacting particles subject to thermal noise. Starting from the Langevin stochastic equations of motion for the velocities of the particles” they were able “to derive a self-consistent deterministic equation for the temporal evolution of the average particle density”.

In 2004, A. J. Archer and R. Evans “presented an alternative derivation (...) that elucidates further some of the physical assumptions inherent in the theory and shows that it is not restricted to fluids composed of particles interacting solely via pair potentials; rather it applies to general, multibody interactions. The starting point for (their) derivation is the Smoluchowski equation and the theory is therefore one for Brownian particles and as such is applicable to colloidal fluids” [31].

Moreover, M. Rex et al. introduced a *dynamical density functional theory for anisotropic colloidal particles* [57], where they “generalize the formalism of (DDFT) for translational Brownian dynamics toward that of anisotropic colloidal particles which perform both translational and rotational Brownian motion.” In a later work, M. Rex and H. Löwen presented “a density functional theory for colloidal dynamics (...) which includes hydrodynamic interactions between the colloidal particles” [32].

The basic approximation in the derivation of DDFT is to use the framework of equilibrium DFT in nonequilibrium situations. Referring to the work of M. Rex et al. [57], this may be called an adiabatic approximation, since the underlying idea is to identify the dynamical one-particle density profile $\rho(\vec{r}, \hat{u}, t)$ with an equilibrium density profile $\rho(\vec{r}, \hat{u})$ and a suitably prescribed external potential at a certain time t . Hence, nonequilibrium correlations are approximated by equilibrium correlations of a suitable equilibrium reference system that possesses the same one-particle density (see also Refs. [30, 57]). Since it is derived from statistical equations that are based on the continuity equation, DDFT preserves the particle number and consequently describes a canonical system.

Now, DDFT is obtained within this adiabatic approximation and without taking hydrodynamics into account by [57]

$$\begin{aligned} \frac{\partial \rho(\vec{r}, \hat{u}, t)}{\partial t} &= \nabla_{\vec{r}} \cdot \overset{\leftrightarrow}{D}(\hat{u}) \left[\rho(\vec{r}, \hat{u}, t) \nabla_{\vec{r}} \frac{\delta \mathcal{F}[\rho]}{\delta \rho(\vec{r}, \hat{u}, t)} \right] \\ &\quad + D_r \hat{\mathcal{R}} \cdot \left[\rho(\vec{r}, \hat{u}, t) \hat{\mathcal{R}} \frac{\delta \mathcal{F}[\rho]}{\delta \rho(\vec{r}, \hat{u}, t)} \right]. \end{aligned} \quad (2.52)$$

Here, $\nabla_{\vec{r}}$ is the gradient w.r.t. $\vec{r} \in \mathbb{R}^3$, $\hat{\mathcal{R}} = \hat{u} \times \nabla_{\hat{u}}$ is the rotational operator acting on the orientation $\hat{u} \in \mathbb{R}^3$, D_r is the rotational short-time diffusion constant, which sets the Brownian time scale $\tau_B = 1/D_r$ and includes rotational friction, and $\overset{\leftrightarrow}{D}(\hat{u})$ is the translational diffusion tensor. For uniaxial (cylindrical) anisotropic particles this tensor

may be expressed as [57]

$$\overleftrightarrow{D}(\hat{u}) = D_{\parallel}\hat{u} \cdot \hat{u}^t + D_{\perp}[\overleftrightarrow{\mathbb{I}} - \hat{u} \cdot \hat{u}^t] \quad (2.53)$$

in terms of the translational diffusion constants D_{\parallel} and D_{\perp} , parallel and perpendicular to the main particle axis \hat{u}_i . Here, \mathbb{I} is the unit matrix and \hat{u}^t is the transpose of \hat{u} .

If the particles are rotationally invariant and the translational diffusion is isotropic, the diffusion tensor simplifies to $\overleftrightarrow{D} = D\overleftrightarrow{\mathbb{I}}$ and the DDFT equation reads

$$\begin{aligned} \frac{k_B T}{D} \frac{\partial \rho(\vec{r}, t)}{\partial t} &= \nabla \cdot \left[\rho(\vec{r}, t) \nabla \left(\frac{\delta \mathcal{F}[\rho]}{\delta \rho(\vec{r}, t)} + V_{\text{ext}}(\vec{r}, t) \right) \right] \\ &= k_B T \nabla^2 \rho(\vec{r}, t) + \nabla \cdot \left[\rho(\vec{r}, t) \nabla \left(\frac{\delta \mathcal{F}_{\text{exc}}[\rho]}{\delta \rho(\vec{r}, t)} + V_{\text{ext}}(\vec{r}, t) \right) \right]. \end{aligned} \quad (2.54)$$

Conversely, if particles are distributed homogeneously in space, the density $\rho(\vec{r}, \hat{u}, t)$ can be split into a spatial bulk part $\bar{\rho}$ and an orientational part $f(\hat{u}, t)$. The latter is normalized on the sphere S^2 by $\int_{S^2} f(\hat{u}, t) d\hat{u} = 1$. Accordingly, the DDFT equation reduces to

$$k_B T \bar{\rho} \frac{\partial f(\hat{u}, t)}{\partial t} = D_r \hat{\mathcal{R}} \cdot \left[f(\hat{u}, t) \hat{\mathcal{R}} \frac{\delta \mathcal{F}[f]}{\delta f(\hat{u}, t)} \right]. \quad (2.55)$$

3

Particle interactions

What is the meaning of interactions
– in an ideal world?

In nature, four fundamental forces are known that describe the way in which elementary particles interact with each other. These forces are electromagnetism, strong interaction, weak interaction, and gravitation, and they generate all physical properties of our surroundings. Knowledge of these interactions allows precise calculations and predictions, but fundamental particle interactions are often not of primary interest. Instead, interactions between more complex composites (like cells, colloids, or planets) are of concern. These interactions result from the constitution of the complex compounds of particles in bodies and can be characterized as an effective interaction. Due to the diversity of possible compounds of particles, effective particle interactions are various.

A rich field of these effective interactions is the one of colloidal soft matter [3, 5]. Also called complex fluids, soft matter systems have significant physical properties on thermal length scales that are comparable with room temperature. Moreover, objects typically have mesoscopic length scales that range from 1nm to $10\mu\text{m}$. Now, Pierre-Gilles de Gennes discovered “that methods developed for studying order phenomena in simple systems can be generalized to more complex forms of matter, in particular to liquid crystals and polymers” [3]. Thus, soft matter systems are ideal model systems to investigate basic physics and to model properties of systems by tuning their effective interactions. For his discovery, the 1991 Nobel prize in physics was awarded to Pierre-Gilles de Gennes.

Classical colloidal soft matter physics deals with objects containing a huge amount of elementary particles. It is quite common to define effective interaction forces for these objects containing all elementary forces. Thus, a colloid is typically described by a radius and a charge, but not by all atomic constituents. Accordingly, individual forces are said to be integrated out or coarse grained. For example, atoms that consist of electrons, positrons, and neutrons are also described by only one mass and one electric charge. Indeed, this description is valid in many situations.

In this context, the hard-core model is an important theoretical model, where particles are not allowed to overlap; thus, they only interact when they are in contact. Accordingly, the phase properties of this model can be described using pure entropic arguments. Moreover, the model has the advantage to be a quite simple one, since interactions are short-ranged and the potential only takes the values 0 and ∞ . Thus, hard-core systems are an ideal starting point to investigate fundamental properties in physics, for example the physics

of freezing. Accordingly, a lot of theoretical approaches have been developed during the last century, like scaled particle theory [58] or the Carnahan-Starling equation of state [59]. The model has also been analyzed in detail using Brownian dynamics and Monte Carlo computer simulations. Even in experiments, the preparation of nearly hard-core like particles is possible, but it is a challenging work.

In this sense, density functional theory is an ideal theoretical framework to describe statistical many-particle systems, as mentioned in the former chapter. Thereby, particle interactions are collected in the excess part (over ideal gas part) of the density functional that is not known exactly in most cases. Accordingly, a collection of approximate functionals has grown over the last decades. During this process, Y. Rosenfeld set up the quite accurate fundamental measure theory (FMT) for spherical hard-core particles [25] which has become an important theoretical tool to study hard-core interactions in the framework of DFT.

In this chapter, first particle interactions are discussed in Sec. 3.1, in particular effective and pairwise interactions. Next, in Sec. 3.2, hard-core interactions and theoretical approaches are introduced, especially in the case of spherical particle shapes. Finally, realizations in DFT are outlined in Sec. 3.3 and FMT is presented, coming along with several functional approaches in Sec. 3.4.

3.1 Soft matter interactions

Soft matter objects, like colloids, live on various length scales [5] that typically range from 1nm to $10\mu\text{m}$ (mesoscopic), where fluid particles in the solvent usually have atomic sizes (microscopic). Consequently, the particles of the solvent are much faster than the mesoscopic particles and the small solvent particles can be coarse grained; their interactions are collected in effective potentials which are acting between the mesoscopic particles. This process of coarse graining reduces the amount of degrees of freedom enormously.

As a consequence, effective particle interactions can be tuned by varying the properties of the solvent and of the colloidal particles, i.e. concentration, materials, or shapes. Accordingly, various types of interaction potentials exist: Some are purely repulsive or purely attractive, such as the Coulomb potential; and some are mixed, repulsive and attractive, such as the Lennard-Jones potential (see Fig. 3.1). Hence, soft matter is of great interest, due to this possibility of manipulating the macroscopic behavior of physical systems.

To give an example, the Asakura-Oosawa model [60, 61] describes a system of big colloidal particles and small polymer spheres. The colloids are neither allowed to overlap each other nor with the polymers, but the polymers do not interact with each other. Consequently, a short-ranged attraction occurs between the colloids, because the colloidal particles like to group together to rise the free volume which is available to the polymers. The resulting effective interaction is purely entropic.

If all particle interactions in a physical system are known, in principle all properties of the

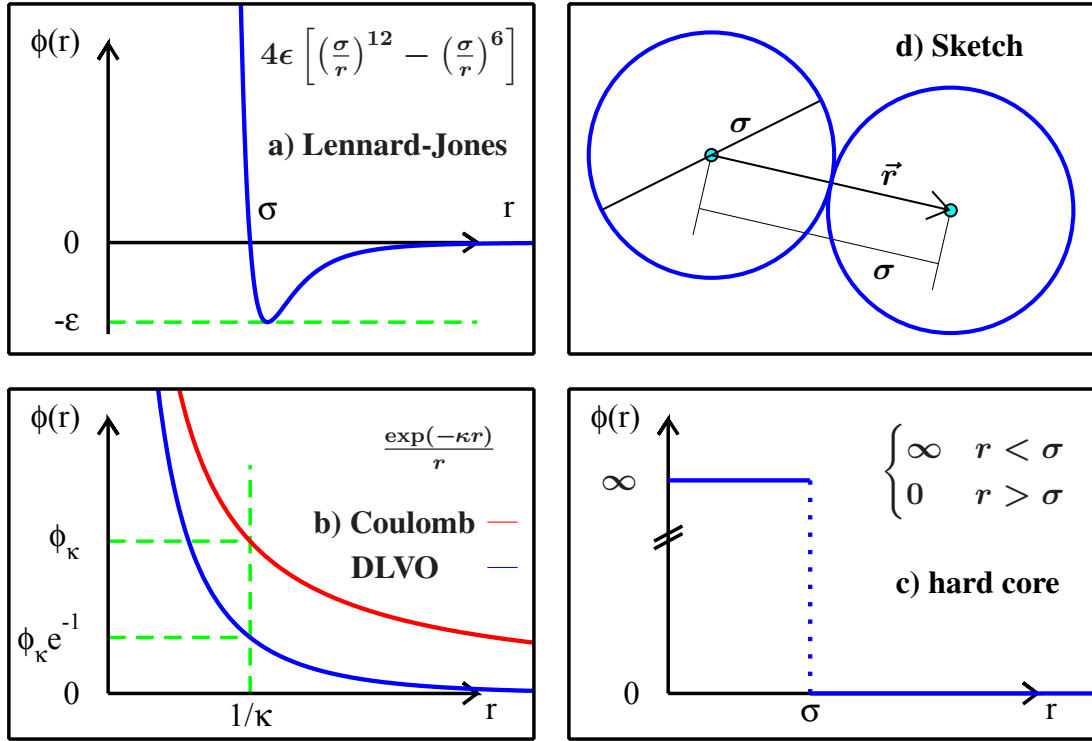


Figure 3.1: (Color) Interaction potentials: a) Lennard-Jones potential, parametrizing a combination of Van der Waals attraction and particle repulsion, b) Coulomb potential $1/r$ (red) and DLVO potential with screening constant κ (blue), c) hard-core potential. The sketch d) visualizes the effective particle diameter and the radial distance of one particle, measured from its center.

system can be obtained. These properties are in general, correlated to the structure of the system in equilibrium. Moreover, for pairwise interactions, the structure is also correlated with the direct pair-correlation function $c^{(2)}$ that is introduced in Sec. 2.2.2 and Sec. 2.3.3. In reciprocal space, this connection reads¹

$$S(\vec{k}) = \left\langle \frac{1}{N} \tilde{\rho}(\vec{k}) \tilde{\rho}(-\vec{k}) \right\rangle = \frac{1}{1 - \rho \tilde{c}^{(2)}(\vec{k})} \quad (3.1)$$

and is known as the structure factor $S(\vec{k})$ of the system. The second identity in Eq. (3.1) follows from the Ornstein-Zernike relation (2.28) by applying a Fourier transformation.

Accordingly, the restriction to pairwise interaction potentials is of strong interest. Since the structure factor can be measured directly from scattering experiments, the properties of the whole system are available from a single measurement via the direct pair-correlation function. Moreover, pairwise interactions simplify theoretical descriptions and are neces-

¹For example, see the textbook of J.-P. Hansen and I. R. McDonald [39].

sary to apply the framework of DFT. For this reason, in the following sections pairwise interactions are discussed.

3.1.1 Pair potentials and the Mayer function

In general, the particle interaction potential $\mathcal{U}(\vec{r}^N)$ depends on all N particles of a system. For example, three conducting spheres that carry the same electric charge must be described by charge distributions instead of point charges. Accordingly, the presence of one sphere affects the charge distribution of the other two spheres and it alters their interaction on each other. Nevertheless, if all charges are assumed to be point charges, localized at the center of each sphere, the interactions become pairwise additive. In fact, this assumption of pairwise interactions is (approximately) valid in most situations. And even more, the advantage of considering only two sets of coordinates over the full dependency of all particle coordinates is a significant simplification of the theoretical description.

For this reason, the interaction potential $\mathcal{U}(\vec{r}^N)$ that enters the Hamiltonian (2.9) is often assumed to be a sum only of pair potentials ϕ_{ij} , acting between particles i and j . Accordingly, the Hamiltonian of such systems reads

$$\mathcal{H}(\psi) = \sum_{i=1}^N \frac{|\vec{p}_i|^2}{2m} + \sum_{1 \leq i < j \leq N} \phi_{ij}(\vec{r}_i, \vec{r}_j) + \sum_{i=1}^N V_{\text{ext}}(\vec{r}_i) \quad (3.2)$$

and the grand partition function from Eq. (2.21) takes the form

$$\Xi(T, V, \mu) = \sum_{N=0}^{\infty} \frac{1}{N!} \int_{V^N} \left(\prod_{1 \leq i < j \leq N} e^{-\beta \phi_{ij}} \right) \left(\prod_{i=1}^N z e^{-\beta V_{\text{ext}}(\vec{r}_i)} \right) d\vec{r}^N. \quad (3.3)$$

Particles of the same species have the same interaction behavior by definition. Consequently, one interaction potential is defined for all particles i and j of one species. Thus, a one-component system has only one interaction potential $\phi \equiv \phi_{ij} \forall i, j$. Furthermore, the pair interaction $\phi(\vec{r}_i - \vec{r}_j)$ of “simple” fluids has a spherical symmetry and it simplifies to $\phi(r_{ij})$, where $r_{ij} = |\vec{r}_i - \vec{r}_j|$ denotes the absolute distance between both particles. In fact, this approximation makes sense for many species of particles, for example for small molecules, as appearing in air.²

For calculations, it is useful to illustrate the sum of products, appearing in Eq. (3.3), by diagrams, similar to Feynman diagrams that are known from Quantum electrodynamics. Such diagrams consist of bonds and circles, where circles are illustrating a factor that solely depends on one single particle position. On the other hand, a bond represents a factor that depends on two particle positions, corresponding to the circles which are connected through the bond. Hence, a product $f(x)f(y)g(x, y)$ can be depicted by two

²This approximation is also known as reference average Mayer (RAM) approximation [62, 63].

f -circles and one g -bond. Moreover, filled (or black) circles represent an additional integration over the coordinate that is represented by the circle. The textbook of J.-P. Hansen and I. R. McDonald [39] is recommended for further reading about diagrammatic methods and about transformation rules of such diagrams.³

It is important to note that the contribution of the N^{th} term in Eq. (3.3) is of the order V^N . Accordingly, the whole sum in Eq. (3.3) diverges if $N \rightarrow \infty$, because the interaction potential ϕ_{ij} vanishes in the limit of far separated particles i and j [38, 39]. Thus, a reformulation of the series in (3.3) is useful, where the $\exp(-\beta\phi_{ij})$ -bonds are replaced by so-called Mayer- f functions⁴

$$f_{ij}(r) \equiv f(|\vec{r}_i - \vec{r}_j|) = \exp[-\beta\phi_{ij}(r)] - 1 \quad (3.4)$$

that tend to vanish fast for an increasing distance $r = |\vec{r}_i - \vec{r}_j|$ between two particles and that vanish in the limit of $r \rightarrow \infty$.

Now, the grand potential (3.3) can be expressed in a series of f -bonds and z^* -circles, where $z^* = z \exp(-\beta V_{\text{ext}})$ is a local activity (compare to the definition of the fugacity z in Eq. 2.23). Furthermore, a change to $\rho^{(1)}$ -circles allows the expression of the direct correlation function $c^{(1)}$ (see definition in Eq. 2.50) in terms of f -bonds and $\rho^{(1)}$ -circles. Accordingly, an expression of the excess free energy \mathcal{F}_{exc} (see Sec. 2.3.3) follows and its expansion in terms of the density $\rho^{(1)}$ reads

$$\begin{aligned} \beta\mathcal{F}_{\text{exc}}[\{\rho_i\}] &= -\frac{1}{2} \sum_{i,j} \int_V \int_V \rho_i(\vec{r}_1) \rho_j(\vec{r}_2) f_{ij}(\vec{r}_{12}) d\vec{r}_1 d\vec{r}_2 \\ &\quad -\frac{1}{6} \sum_{i,j,k} \int_V \int_V \int_V \rho_i(\vec{r}_1) \rho_j(\vec{r}_2) \rho_k(\vec{r}_3) f_{ij}(\vec{r}_{12}) f_{ik}(\vec{r}_{13}) f_{jk}(\vec{r}_{23}) d\vec{r}_1 d\vec{r}_2 d\vec{r}_3 \\ &\quad + \mathcal{O}(\rho^4), \end{aligned} \quad (3.5)$$

where $\vec{r}_{kl} = \vec{r}_k - \vec{r}_l$ denotes the vector between positions \vec{r}_l and \vec{r}_k .

The series expansion of $c^{(1)}$ also yields the virial expansion (2.4) of an homogeneous fluid.⁵ For instance, the first two virial coefficients B_n read

$$B_2(T) = -\frac{1}{2V} \int_V \int_V [\exp(-\beta\phi(r_{12})) - 1] d\vec{r}_1 d\vec{r}_2 \quad (3.6)$$

$$= -\frac{1}{2} \int_V f(\vec{r}) d\vec{r} \quad (3.7)$$

$$B_3(T) = -\frac{1}{3V} \int_V \int_V \int_V f(\vec{r}_{12}) f(\vec{r}_{13}) f(\vec{r}_{23}) d\vec{r}_1 d\vec{r}_2 d\vec{r}_3. \quad (3.8)$$

³An earlier description is also given in chapter 8d of the textbook of J. E. Mayer and M. G. Mayer [38].

⁴The Mayer- f function has already been introduced in 1940 by J. E. Mayer and M. G. Mayer [38, 64] and is defined in [38], Sec. 8d, *Dense Gases. The Cluster Development*.

⁵For further reading see textbook of J.-P. Hansen and I. R. McDonald [39], chapter 3.9, *Virial expansion of the equation of state*.

The third virial coefficient $B_3(T)$ already contains the contribution of three interacting particles. Accordingly, the contribution of $B_3(T)$ vanishes, if all three contributing particles are not located close to each other. In the limit of low densities only the second virial coefficient contributes.

3.2 Hard spheres

An important interaction is given by the hard-core interaction, shown in Fig. 3.1(c,d). In this model, the particles are not allowed to overlap each other and therefore, interactions are purely entropic. Thus, the internal energy U vanishes, and the free energy follows with $F = -TS$ [65]. In the case of spherical shapes, the particles “are treated as though they were minute marbles, exerting no forces except when in contact” [38].

As the most simple kind of interaction, the hard-core potential states an ideal model for fundamental studies. Furthermore, “the structure factor curves $S(q)$ ” (see Eq. (3.1)) “are very similar” for several types of interactions and they “can be simulated by the hard-sphere structure factor” [66] (in the homogeneous fluid). For example, one of these interactions is given by Nickel.⁶

3.2.1 The hard-core interactions

In general, hard particle shapes are various. Starting with shapes of high symmetry like spheres in three dimensions or disks in two dimensions, there exist cubes, spherocubes,⁷ elliptical particles, spherocylinders,⁸ dumbbells,⁹ and many more particle shapes. A huge collection is listed in the article of S. Glotzer and M. J. Solomon [8], where the packing of several species of hard particles is investigated.

The interaction potential ϕ_{ij} of two hard-core particles \mathcal{B}_i and \mathcal{B}_j is defined as

$$\beta\phi_{ij}(\mathcal{B}_i, \mathcal{B}_j) = \begin{cases} \infty & \text{for } \mathcal{B}_i \cap \mathcal{B}_j \neq \emptyset \\ 0 & \text{for } \mathcal{B}_i \cap \mathcal{B}_j = \emptyset \end{cases}. \quad (3.9)$$

Consequently, the Mayer- f function, as defined in Eq. (3.4), takes the simple form

$$f_{ij} = \begin{cases} -1 & \text{for } \mathcal{B}_i \cap \mathcal{B}_j \neq \emptyset \\ 0 & \text{for } \mathcal{B}_i \cap \mathcal{B}_j = \emptyset \end{cases} \quad (3.10)$$

⁶For example, see *Capillary wave analysis of rough solid-liquid interfaces in nickel* by R. E. Rozas and J. Horbach [67].

⁷Spherocubes have a shape somewhere in between that of a sphere and a cube.

⁸Spherocylinders have a cylindrical part with two hemispherical caps.

⁹Dumbbells consist of two overlapping spheres.

for hard-core interactions. For hard spheres the Mayer- f function becomes $-f_{ij}(\vec{r}_{ij}) = \Theta((R_j + R_i) - |\vec{r}_{ij}|)$, where \vec{r}_{ij} denotes the core-to-core distance of both spheres and R_i and R_j denote their radii. Furthermore, the Heavyside step function Θ is defined by¹⁰

$$\Theta(x) = \begin{cases} 1 & \text{for } x > 0 \\ 0 & \text{for } x < 0 \end{cases}. \quad (3.11)$$

Note that temperature does not affect the qualitative behavior of an hard-particle system, because the interaction potential only takes the values 0 and ∞ . Thus, temperature only scales the quantitative behavior of such systems. Since entropic forces do effect hard-sphere systems, it is useful to study the packing behavior of hard particles, which is done for spheres in Sec. 4.1.3.

3.2.2 Experimental realization and simulations

It is difficult to set up hard-core particle interactions in experiments, for example due to electrical charges of the particles. Often, hard spheres are made of polymethylmethacrylate (PMMA) and thus have a little attraction due to Van der Waals interactions. To avoid clustering, the particles are sterically stabilized by thin polymer layers.¹¹

The PMMA particles are typically of slightly different sizes. This polydispersity alters the phase diagram of the system, as schematically shown in Fig. 4.1. Nevertheless, the polydispersity is typically of about 4% or 5%, where the phase transition is not much altered. In addition, polydispersity can be adopted in DFT by using several species of spheres that differ in their radii (see also Sec. 4.2.4).

Early experiments on *A Dynamic Hard Sphere Model* [69] have been developed by D. Turnbull and R. L. Cormia, who state:

MODELS which simulate many atoms interacting together can be useful for giving insight on what assumptions may be satisfactory to treat multiaatomic interactions and for teaching. (...) We have developed a dynamic hard sphere model which is very simple and flexible. In this model many uniform spheres are fenced in on a round horizontal glass plate and agitated by the vibrations of a wooden board, suspended from springs, on which the plate is mounted.

The spheres have diameters of about 4mm and are made of glass, iron, aluminum, or polyethylene. However, the system only has two dimensions, like a billiard table.

In simulations, hard interactions are special. On the one hand, it is tough to implement the discontinuous interaction potential and to avoid overlap, because a small movement of a single sphere instantaneously changes the potential from 0 to ∞ . On the other hand, hard

¹⁰For $x = 0$ the function is sometimes defined as $\frac{1}{2}$, as 0, or as 1. However, the choice for $x = 0$ is irrelevant in most cases, because its measure is zero.

¹¹For example, see K. Sandomirski et al. in Ref. [68].

interactions are short-ranged and the movement of a single sphere only affects its direct neighbors, which significantly improves their implementation.

For example, simulations have been applied by B. J. Alder and T. E. Wainwright [70] to study the *Phase Transition for a Hard Sphere System* or by J. A. Barker and D. Henderson [71] to understand the (liquid) states of matter. Recent simulations have been performed by T. Zykova-Timan et al. [72, 73] and by R. Rozas and co-workers (see Ref. [74]).

3.2.3 Theoretical approaches

The hard-sphere model is motivated from a theoretical background. Various theoretical approaches exist for this model and some of them are discussed in this section.¹² In the following, the radius of a hard sphere of a certain species i is denoted by R_i , where its diameter is $\sigma_i = 2R_i$. The index i is omitted, if a monodisperse system is assumed. Moreover, ρ denotes the mean bulk density and $\eta = \frac{\pi}{6}\sigma^3\rho$ the corresponding volume fraction of the observed hard-sphere system.

The equation of state and *Statistical Mechanics of Rigid Spheres* has already been analyzed in 1959 by H. Reiss, H. L. Frisch, and J. L. Lebowitz [58, 75]. They extracted the pair distribution function $g(r)$ and the surface tension from a fluid phase system by introducing a coupling parameter to add or remove a single sphere. Therefore, this method is also known as *Scaled Particle Theory* (SPT). In more detail, H. Reiss and co-workers analyzed the work that is needed to expand a spherical cavity (a sphere devoid of particles) in a fluid phase [58]. Then, the scaled particle equation follows in the limit of infinite radius $R_i \rightarrow \infty$ of this cavity (or of one sphere) and reads¹³

$$\lim_{R_i \rightarrow \infty} \frac{\beta\mu_{i,\text{exc}}}{V_i} = \beta p, \quad (3.12)$$

where V_i is the omitted volume and $\mu_{i,\text{exc}}$ the excess chemical potential of species i .

However, the virial coefficients $B_n(T)$, appearing in the virial expansion (2.4) and in Eq. (3.8), obviously are constants for the temperature-independent hard-sphere model [13, 39, 76]. Thus, the first terms of the expansion become [39]

$$\begin{aligned} \frac{p(\rho, T)}{k_B T \rho} &= 1 + 4\eta + 10\eta^2 + 18.365\eta^3 + 28.225\eta^4 + 39.74\eta^5 \\ &\quad + 53.5\eta^6 + 70.8\eta^7 + \mathcal{O}(\eta^8). \end{aligned} \quad (3.13)$$

Guided by this expansion, N. F. Carnahan and K. E. Starling constructed a simple but quite accurate *Equation of State for Nonattracting Rigid Spheres* [59]. They replaced the sum in Eq. (2.4) by the term $\sum_{i=1}^{\infty} (i^2 + 3i)\eta^i \rho$, which results in integer coefficients 1, 4, 10,

¹²A wide review about *What is "liquid"? Understanding the states of matter* is given by J. A. Barker and D. Henderson [71].

¹³See also the works of Y. Rosenfeld [25] and R. Roth [29] and Sec. B.2 in this work.

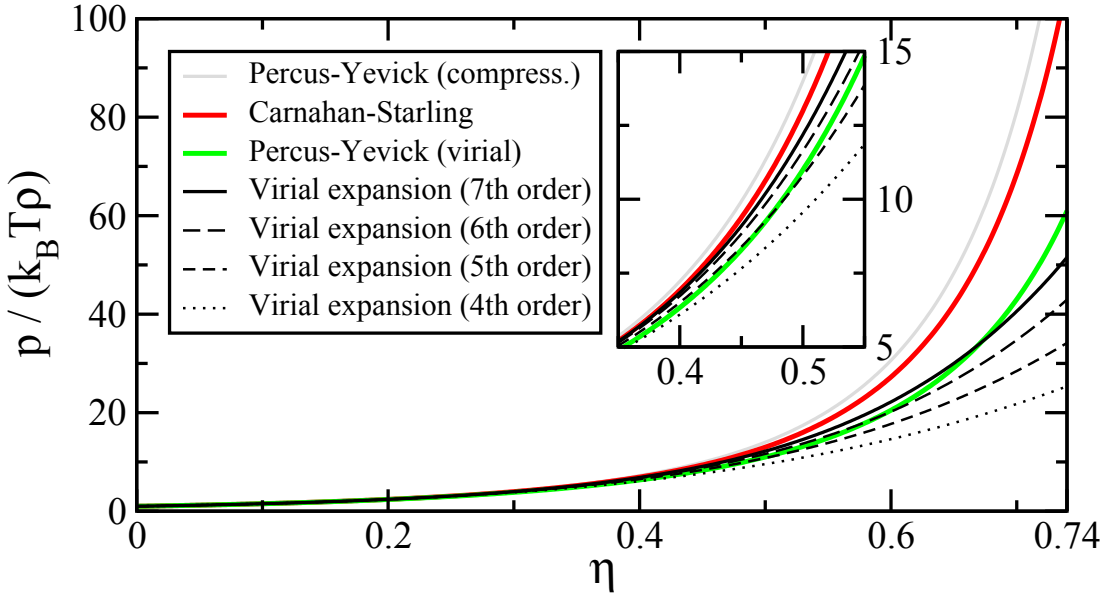


Figure 3.2: Virial pressure $p/(k_B T \rho)$ for given volume fractions $\eta = \rho\pi/6$ for hard spheres of diameter σ . Shown are the virial expansion (3.13) up to 7th order, the Carnahan-Starling equation of state (3.14), and the Percus-Yevick equation of state obtained via the virial route (3.18) and via the compressibility route (see footnote 18). Freezing starts above a volume fraction of $\eta \approx 0.494$ and close packing predicts a maximal packing of $\eta \approx 0.74$.

18, 28, 40 for the expansion (3.13). This expression can be written as a linear combination of the first and second derivative of the geometric series and therefore, can be summed up explicitly to give¹⁴

$$Z = \frac{p}{\rho k_B T} = \frac{1 + \eta + \eta^2 - \eta^3}{(1 - \eta)^3}. \quad (3.14)$$

Indeed, the so-called Carnahan-Starling equation provides an excellent fit to the results of computer simulations over the entire fluid range and therefore, it is widely used, even today.¹⁵ In comparison with computer simulations, its largest discrepancies are of the order of 1%,¹⁶ as shown in Fig. 3.2.

In particular, a closed expression for the excess Helmholtz free energy is obtained by combining Eq. (3.14) with the thermodynamic relation $p = -\partial F/\partial V|_{T,N}$ (also compare with the fundamental equation (3.15) of thermodynamics and Table 2.1) so that the expression reads [39]

$$\frac{F_{\text{exc}}}{k_B TN} = \frac{\eta(4 - 3\eta)}{(1 - \eta)^2}. \quad (3.15)$$

From Sec. 2.2.2 the direct pair-correlation function and the pair-distribution functions are

¹⁴See also Sec. 3.9.17 in the textbook of J.-P. Hansen and I. R. McDonald [39].

¹⁵For example in FMT by H. Hansen-Goos and R. Roth [77] to expand the functional to higher densities.

¹⁶See textbook of J. P. Hansen and I. R. McDonald [39], Fig. 3.3 and Eq. 3.9.17.

known to describe the internal structure of a physical system. They are connected by the Ornstein-Zernike relation (2.28).

J. K. Percus and G. J. Yevick calculated the pair-distribution function $g(\vec{r})$ using approximate integral equations for a fluid with pairwise-additive interaction forces [78, 79]. They interpreted the quantity $\rho g(r)$ as the one-particle density at position \vec{r} in the presence of a single particle that is pinned at the origin $\vec{r} = 0$ by an external pinning field V_{pin} . Accordingly, the one-particle density in presence of the field become $\rho_{(1)}(\vec{r}|V_{\text{pin}}) = \rho^{(2)}(\vec{0}, \vec{r}|V_{\text{pin}} = 0)/\rho$ and the identity $\rho^{(1)}(\vec{r}) = \rho g(r)$ directly follows.

However, the Ornstein-Zernike relation (2.28) is an open relation that can not be solved without knowing $c^{(2)}(\vec{r})$. Using the previous identity, a relation can be deduced to close it by applying the Ornstein-Zernike equation to the DFT equation of state (2.49).¹⁷ This so-called closure follows with

$$g(\vec{r}) = \exp(-\beta V_{\text{ext}}(\vec{r})) \exp(h(\vec{r}) - c^{(2)}(\vec{r})) \quad (3.16)$$

and it is known as the hypernetted-chain (HNC) approximation [80].

Furthermore, the term $\exp(c^{(1)})$ can be expanded in terms of $\Delta\rho = \rho - \rho_{\text{ref}}$ around a reference density ρ_{ref} instead of expanding the direct correlation function $c^{(1)}$ (see Eq. 3.5). This leads to the Percus-Yevick (PY) approximation

$$g(\vec{r}) = \exp(-\beta V_{\text{ext}}(\vec{r})) \exp(1 + h(\vec{r}) - c^{(2)}(\vec{r})). \quad (3.17)$$

Even more, the equations of state for a hard-sphere fluid can be obtained from this closure. For example, the virial equation of state follows with¹⁸ [39]

$$\frac{p}{k_B T \rho} = \frac{1 + 2\eta + 3\eta^2}{(1 - \eta)^2}. \quad (3.18)$$

To learn more about distribution-function theories, see the review of J. A. Barker and D. Henderson [71] and the textbook of J.-P. Hansen and I. R. McDonald [39]. In Sec. 4.3 and Sec. 4.4 of Ref. [39] a comparison between the PY equations of state and the more precise Carnahan-Starling equation of state is given (see also Fig. 3.2). In addition, L. Verlet and J.-J. Weis presented a correction of the Percus-Yevick equation of state, to obtain agreement with the Carnahan-Starling equation of state [83].

3.3 Interactions in density functional theory

Particle interactions are assumed to be solely pairwise interactions in density functional theory (DFT) and they enter the theory via the excess free energy functional \mathcal{F}_{exc} (see

¹⁷The relation can also be deduced from the functional derivative (3.21) by using $\Delta\rho = (g - 1)\rho$.

¹⁸Alternatively, M. S. Wertheim calculated the exact compressibility solution of the Percus-Yevick equation of state [81, 82], $\beta p/\rho = (1 + \eta + \eta^2)/(1 - \eta)^3$.

Sec. 2.3). Thus, the determination of this energy functional is an important problem to apply DFT to over-ideal gas systems that contain particle interactions in addition to the ideal gas terms.

The exact energy functional is only known for the system of one-dimensional hard rods [15, 16, 84–86]. For this reason, a lot of approaches exist to deduce accurate, but always approximate energy functionals, which are only valid for special types of particle interactions sometimes [22, 87].

An important ansatz is given by the low-density expansion of the excess free energy functional in Eq. (3.5) in terms of the density (density circles and Mayer- f bonds). Thus, the exact low-density limit is given by the first term of this expansion in the limit $\rho \rightarrow 0$ of vanishing bulk density. Accordingly, the second functional derivative yields

$$c^{(2)}[\rho; \vec{r}_1, \vec{r}_2] = f(\vec{r}_1 - \vec{r}_2) + \mathcal{O}(\rho) \quad (3.19)$$

and only the Mayer- f function remains in the limit of vanishing density.

Similarly, the excess free energy functional \mathcal{F}_{exc} can be achieved by applying a Taylor expansion around a certain reference density ρ_{ref} , as mentioned in Ref. [88]. In general, the expansion must be defined by integrating along a path between ρ_{ref} and ρ using $\rho(\vec{r}; \lambda) = \rho_{\text{ref}}(\vec{r}) + \lambda \Delta\rho(\vec{r})$.¹⁹ While integrating the direct correlation function $c^{(n)}$ from Eq. (2.50) with respect to this density, the identity

$$c^{(n)}(\vec{r}^n; \lambda) = c_{\text{ref}}^{(n)}(\vec{r}^n) + \int_0^\lambda \int_{V^n} \Delta\rho(\vec{r}') c^{(n+1)}(\vec{r}^n, \vec{r}'; \lambda') d\vec{r}' d\lambda' \quad (3.20)$$

follows, where $c_{\text{ref}}^{(n)}$ denotes the direct correlation function that only depends on the reference density. From this result, the Taylor expansion follows recursively with

$$\begin{aligned} \mathcal{F}_{\text{exc}}[\rho] &= \mathcal{F}_{\text{exc}}[\rho_{\text{ref}}] - \sum_{n=1}^{N-1} \frac{1}{n!} \int_{V^n} c^{(n)}[\vec{r}^n; \rho_{\text{ref}}] \left(\prod_{\nu=1}^n \Delta\rho(\vec{r}_\nu) \right) d\vec{r}^n \\ &\quad - \int_0^1 \int_0^{\lambda_1} \dots \int_0^{\lambda_{N-1}} \int_{V^N} c^{(N)}[\vec{r}^N; \rho] \left(\prod_{\nu=1}^N \Delta\rho(\vec{r}_\nu) \right) d\vec{r}^N d\lambda_N \dots d\lambda_1. \end{aligned} \quad (3.21)$$

Furthermore, it is important to note that the direct correlation function in the remainder term corresponds to the density ρ and not to the reference density ρ_{ref} [22, 39].

A truncation of the series after the third term yields the approach known from T. V. Ramakrishnan and M. Yussouff [66].²⁰ In their work they show that the fluid-solid coexistence of a hard-sphere system can be described by using a liquid bulk density as a reference density.

Indeed, a truncation of the series in Eq. (3.21) after the third term provides the advantage

¹⁹This is shown by J.-P. Hansen and I. R. McDonald in Sec. 3.5, page 61 of Ref. [39].

²⁰See also M. Oettel et al. [88], Eq. (12), or S. van Teffelen et al. [89].

that only the direct pair-correlation function $c^{(2)}$ and the excess free energy of the reference density are needed as an external input. Thereby, the first-order direct correlation function is already given by $-c^{(1)}[\rho_{\text{ref}}] = \beta\mu_{\text{exc}} = \beta\mu - \log(\rho_{\text{ref}})$. Thus, the functional derivative of the excess free energy follows from Eq. (3.21) with

$$\frac{\delta\mathcal{F}_{\text{exc}}[\rho]}{\delta\rho(\vec{r})} = \frac{\delta\mathcal{F}_{\text{exc}}[\rho_{\text{ref}}]}{\delta\rho(\vec{r})} - c^{(1)}[\vec{r}; \rho_{\text{ref}}] - \int_V c^{(2)}[\vec{r}, \vec{r}'; \rho_{\text{ref}}] \Delta\rho(\vec{r}') d\vec{r}', \quad (3.22)$$

where $\delta\mathcal{F}_{\text{exc}}[\rho_{\text{ref}}]/\delta\rho(\vec{r})$ vanishes for a fluid-like reference density.

For an external input, T. V. Ramakrishnan and M. Yussouff used the analytically known direct pair-correlation function $c^{(2)}$ that follows from the Ornstein-Zernicke relation using the Percus-Yevick closure (see Sec. 3.2.3) [66]. Likewise, the direct pair-correlation function and the excess free energy for a hard-sphere fluid are known from the Carnahan-Starling Eq. (3.14) of state. In combination with fundamental measure density functional approaches (see Sec. 3.4 and Ref. [88]), the truncation approach (or Ramakrishnan-Yussouff approach) is a quite powerful tool that allows fast numerical calculations (for example, see Sec. 4.2 and 5.2).

A recent development is also given by the phase-field-crystal (PFC) theory, first introduced as a phenomenological approach in 2002 and 2004 by K. R. Elder et al. in works about *Modeling Elasticity in Crystal Growth* and *Modeling elastic and plastic deformations in nonequilibrium processing using phase field crystals* [90, 91].²¹ In later work, the PFC model has been deduced as an approximation from DFT and DDFT [89, 93, 94]. Moreover, “the crystalline density field is described basically in terms of a single Fourier mode within the PFC model” [93].

Finally, fundamental measure theory (FMT) provides an accurate functional approach for hard-shaped particles [15], e.g. spheres, cubes, or more general particle shapes. The functional depends on so-called weighted densities that are motivated from fundamental (geometric) measures of the particles.²² Then, starting from the low-density expansion in Eq. (3.5), the functional is expanded to higher densities using additional theoretical approaches like the Carnahan-Starling equation of state or others. FMT is presented in detail in the following section.

3.4 Fundamental Measure Theory

The fundamental measure theory (FMT) has been set up by Y. Rosenfeld in 1989 for a hard sphere mixture [25]. It provides a framework to determine an excess free energy functional for hard pair-interaction potentials in density functional theory (DFT).

²¹See also Ref. [92] by H. Emmerich for an overview over the essentials of the conceptual background of the PFC method.

²²Also compare with the *Weighted density approximation* (WDA), introduced by W. A. Curtin and N. W. Ashcroft [95] and applications to it, i.e. in Ref. [96, 97].

To achieve a functional, the low-density limit of the excess free energy functional is taken as a starting point. For vanishing density $\rho_0 \rightarrow 0$, the exact limit directly follows from the diagrammatic expansion (3.19) of the direct pair-correlation function $c^{(2)}$ in terms of the density ρ and reads

$$\beta\mathcal{F}_{\text{exc}}[\rho] = -\frac{1}{2} \sum_{i,j} \int_V \int_V \rho(\vec{r}) \rho(\vec{r}') f_{ij}(|\vec{r} - \vec{r}'|) d\vec{r} d\vec{r}'. \quad (3.23)$$

Recalling Sec. 3.2, the Mayer- f function (3.4) includes the hard particle interaction between two particles i and j . Thus, the Mayer- f function reads $-f_{ij}(|\vec{r}_i - \vec{r}_j|) = \Theta((R_i + R_j) - |\vec{r}_i - \vec{r}_j|)$ in the case of hard spheres with constant particle radii R_i and R_j . The Heavyside step function Θ is defined in Eq. (3.11).

The above mentioned Mayer- f function in principle states a measure for the overlap volume of two contributing particles i and j . As known from Hadwiger's volume theorem [98, 99], a continuous rigid motion invariant valuation can be written as a linear combination of intrinsic volumes, also known as fundamental measures. In principle, the latter depict m -dimensional measures in an n -dimensional space with $m \leq n$. For example, in a three-dimensional space there are the geometrical fundamental measures volume, surface area, curvature, and Euler characteristic.

However, Y. Rosenfeld recognized that the Mayer- f function of hard spheres can be written in terms of these fundamental measures, which gives rise to the naming of FMT [25, 29, 100]. Moreover, he noticed that this sum of fundamental measures can be decomposed into a sum of convolutions of geometrical motivated weight functions, where each weight function $w^{(\alpha)}$ solely corresponds to one single particle, respectively [25]. Furthermore, these weight functions are related to the already mentioned fundamental measures.

In later work, Y. Rosenfeld extended his version of FMT for spheres to general anisotropic particle shapes [56] and he observed [101] that the deconvolution of the Mayer- f function in weighted densities is a special case of the Gauss-Bonnet theorem [102, 103]

$$\int_S K dA + \int_{\partial S} k_g ds = 2\pi\chi(S), \quad (3.24)$$

where S is a compact surface, K is the Gaussian curvature, and k_g the geodesic curvature along the edge ∂S of the surface S . The Euler characteristic $\chi(S)$ describes the topology of the surface S (also see [104]).

This observation gives an interpretation of the prefactors $1/R_i$ and $1/R_i^2$ appearing in the original weight functions for hard spheres, as introduced by Y. Rosenfeld.²³ These factors describe the mean curvature H_i and the Gaussian curvature K_i at a certain position on the surface of the particle [28, 105].

²³Compare the more general weight functions (3.25)-(3.30) with the original ones for hard spheres listed in Sec. B.3.

The deconvolution via the Gauss-Bonnet theorem allows a more general formulation of the weight functions for arbitrary convex hard particles, as noted by Y. Rosenfeld in Refs. [56, 101]. Following this formulation, H. Hansen-Goos and K. Mecke introduced the so-called extended deconvolution FMT (edFMT)²⁴ for convex non-spherical hard-body fluids [28, 105], using the Gauss-Bonnet theorem (3.24) with a constant Euler characteristic $\chi = 2$. As already mentioned by Y. Rosenfeld, this is only valid for convex particles, because the surface of a general intersection volume of two non-convex particles is not always a single, convex body [104, 106]. For example, the intersection between two dumbbells (see Sec. 6.3) can consist of $n = 1, 2, 3, 4$ disjoint convex bodies, which lead to an Euler characteristic $\chi(\partial[\mathcal{B}_i \cap \mathcal{B}_j]) = 2n$, and it can also be a single body with a hole in it, leading to $\chi(\partial[\mathcal{B}_i \cap \mathcal{B}_j]) = 0$.²⁵ So, setting the Mayer function equal to $-\chi(\partial[\mathcal{B}_i \cap \mathcal{B}_j])/2$, as is done in edFMT, is an approximation for non-convex particles. However, this is not a bad approximation as long as the intersection between the particles in most of the possible configurations is a single simply connected body (*i.e.* without any holes) with Euler characteristic two. The difficulties that arise when edFMT is applied to non-convex particles are explicitly discussed in the work of M. Marechal et al. [104]. Moreover, in Sec. 6.3 and in Ref. [104] it is shown that edFMT is still a surprisingly good density functional theory, in spite of these difficulties.

In another sense, convexity is useful while performing a parametrization of a particle \mathcal{B}_i . Convexity assumes that every point of a connected set \mathcal{B} of points can be connected with all points of the surface $\partial\mathcal{B}$ of the set by a straight line such that all points of the line are in \mathcal{B} . Consequently, the surface $\partial\mathcal{B}_i$ can be parametrized by a radial function $\vec{R}_i(\hat{r})$, pointing from a certain reference point C_i to the surface of the particle along the direction \hat{r} , where \hat{r} denotes a vector $\vec{r}/|\vec{r}|$ of unit length [28].

Applying this parametrization, the weighted densities for convex particles read [56, 101, 105]

$$w_i^{(3)}(\vec{r}) = \Theta(|\vec{R}_i(\hat{r})| - |\vec{r}|), \quad (3.25)$$

$$w_i^{(2)}(\vec{r}) = \delta(|\vec{R}_i(\hat{r})| - |\vec{r}|) \frac{1}{\hat{n}_i(\hat{r}) \cdot \hat{r}}, \quad (3.26)$$

$$w_i^{(1)}(\vec{r}) = \frac{H_i(\hat{r})}{4\pi} w_i^{(2)}(\vec{r}), \quad (3.27)$$

$$w_i^{(0)}(\vec{r}) = \frac{K_i(\hat{r})}{4\pi} w_i^{(2)}(\vec{r}), \quad (3.28)$$

$$\vec{w}_i^{(2)}(\vec{r}) = \hat{n}_i(\hat{r}) w_i^{(2)}(\vec{r}), \quad (3.29)$$

$$\vec{w}_i^{(1)}(\vec{r}) = \hat{n}_i(\hat{r}) w_i^{(1)}(\vec{r}), \quad (3.30)$$

where $\hat{n}_i(\hat{r})$ denotes the outward normal vector to the surface $\partial\mathcal{B}_i$ at the position indicated

²⁴For details, see Sec. 3.4.1 about the construction of FMT functionals.

²⁵Discussed by M. Marechal et al. in Ref. [104].

by \hat{r} via the radial function $\vec{R}_i(\hat{r})$.²⁶ The mean and Gaussian curvature in this point are denoted by $H_i(\hat{r})$ and $K_i(\hat{r})$ and they follow from the local principal curvatures κ_i^I and κ_i^{II} by $H_i = \frac{1}{2}(\kappa_i^I + \kappa_i^{II})$ and $K_i = \kappa_i^I \kappa_i^{II}$.

As already mentioned, for hard spheres the principal curvatures are equal to $1/R_i$ and $\hat{n}_i(\hat{r}) \cdot \hat{r} = 1$ (if the reference point C_i is located in the center of a sphere). Thus, the weight functions (3.25)-(3.30) simplify and result in the original hard-sphere weight functions, shown in Sec. B.3. In addition, their Fourier transforms are also listed in the appendix, because they are required for explicit numerical calculations.

To sum up, as a fundamental step Y. Rosenfeld recognized that the Θ function (or Mayer- f function for hard-spheres) can be decomposed into the form²⁷

$$\begin{aligned} \Theta((R_i + R_j) - |\vec{r}_{ij}|) = & (w_i^{(0)} \circledast w_j^{(3)})(\vec{r}_{ij}) + (w_i^{(1)} \circledast w_j^{(2)})(\vec{r}_{ij}) \\ & + (w_i^{(2)} \circledast w_j^{(1)})(\vec{r}_{ij}) + (w_i^{(3)} \circledast w_j^{(0)})(\vec{r}_{ij}) \\ & - (\vec{w}_i^{(1)} \circledast \vec{w}_j^{(2)})(\vec{r}_{ij}) - (\vec{w}_i^{(2)} \circledast \vec{w}_j^{(1)})(\vec{r}_{ij}), \end{aligned} \quad (3.31)$$

where $\vec{r}_{ij} \equiv \vec{r}_i - \vec{r}_j$.²⁸ Furthermore, the convolution product \circledast of two functions w_i and w_j is defined as

$$(w_i \circledast w_j)(\vec{r}_{ij}) = \int_V w_i(\vec{r} - \vec{r}_i) w_j(\vec{r} - \vec{r}_j) d\vec{r} \quad (3.32)$$

and differs from the definition of the standard convolution product $*$, defined in (A.29).

Nevertheless, the choice of weight functions and the resulting decomposition of the Mayer- f function is not unique. In 1990, E. Kierlik and M. L. Rosinberg presented an alternative decomposition [108] using only scalar weight functions. This alternative decomposition is equivalent to that one of Y. Rosenfeld, as shown by S. Phan et al. three years later [109].

Moreover, H. Hansen-Goos and K. Mecke introduced two additional tensorial weight functions that have been achieved from the deconvolution via the Gauss-Bonnet theorem (3.24). These tensorial weight functions read [105]

$$\overset{\leftrightarrow}{w}_i^{(1)} = \frac{\Delta \kappa_i(\hat{r})}{4\pi} ((\hat{v}_i^I) \cdot (\hat{v}_i^I)^t - (\hat{v}_i^{II}) \cdot (\hat{v}_i^{II})^t) w_i^{(2)}(\vec{r}), \quad (3.33)$$

$$\overset{\leftrightarrow}{w}_i^{(2)} = \hat{n}_i(\hat{r}) \cdot \hat{n}_i(\vec{r})^t w_i^{(2)}(\vec{r}), \quad (3.34)$$

where \hat{v}_i^I and \hat{v}_i^{II} are tangential unit vectors to the surface $\partial\mathcal{B}_i$, which point along the directions of principal curvature, and \hat{v}^t denotes the transposed of \hat{v} . In addition, $\Delta \kappa = \frac{1}{2}(\kappa_i^I - \kappa_i^{II})$ denotes the deviatoric curvature. Now, the decomposition (3.31) is extended by the terms $-\zeta \overset{\leftrightarrow}{w}_i^{(1)} \circledast \overset{\leftrightarrow}{w}_j^{(2)}$ and $-\zeta \overset{\leftrightarrow}{w}_i^{(2)} \circledast \overset{\leftrightarrow}{w}_j^{(1)}$. This result goes beyond the

²⁶The Dirac δ -distribution is defined around Eq. (A.16), the Heaviside step function in Eq. (3.11).

²⁷Either the decomposition (Eq. 2) or the definition of the convolution are erroneous in the original work of Y. Rosenfeld [25]. Later this mistake has been corrected (see e.g. Ref. [107]).

²⁸The proof is re-written in Sec. B.4.

previous one in Eq. (3.31), but remains approximative for non-spherical particles, due to the parameter $\zeta = (1 + n_i n_j)^{-1}$ that must be set to a constant mean value to allow the terms to be written as a convolution product of only rank two tensorial weight functions. The deviatoric curvature $\Delta\kappa$ vanishes in the case of hard spheres and thus, the previous result of Y. Rosenfeld is obtained (for any ζ).

The deconvolution (3.31) in combination with the starting point of FMT, the excess free energy (3.23) in the low density limit, gives rise to the definition of so-called weighted densities

$$n_\alpha(\vec{r}) = \sum_{i=1}^{\nu} \left(\rho_i * w_i^{(\alpha)} \right) (\vec{r}) = \sum_{i=1}^{\nu} \int_V \rho_i(\vec{r}') w_i^{(\alpha)}(\vec{r} - \vec{r}') d\vec{r}'. \quad (3.35)$$

On the contrary to previous usage, now the index i refers to the density ρ_i and weight functions $w_i^{(\alpha)}$ of different particle species and orientations in general. Thus, the whole system consists of ν species of particles, for example spheres of different radii.

Accordingly, the combination of Eq. (3.23) and Eq. (3.31) leads to the low density limit

$$\beta\mathcal{F}_{\text{exc}}[\rho] = \int_V (n_0(\vec{r})n_3(\vec{r}) + n_1(\vec{r})n_2(\vec{r}) - \vec{n}_1(\vec{r}) \cdot \vec{n}_2(\vec{r})) d\vec{r}. \quad (3.36)$$

Thus, a strong motivation is given to construct the excess free energy functional as

$$\beta\mathcal{F}_{\text{exc}}[\{\rho_i\}] = \int_V \Phi(\{n_\alpha(\vec{r})\}) d\vec{r}, \quad (3.37)$$

introducing an excess free energy density Φ that is a regular function of the weighted densities n_α . Of course, the construction must respect the low density limit (3.36).

In recent works, S. Korden derived “the Rosenfeld functional from the virial expansion” [110, 111]. Re-summing the cluster integrals of the diagrammatic virial expansion [39, 112], he found the first term yielding the Rosenfeld functional that is given in Eqn. (3.50-3.52). Going beyond the first term, he also obtained the Tarazona replacement, given in Eq. (3.54), as part of higher order terms. However, his results and its discussion are topic of present research and should be applied to simple models, to learn more about its relevance and about the improvement of FMT.

3.4.1 Construction of FMT functionals

In this section, excess free energy functionals are constructed, following the work of Y. Rosenfeld [25], R. Roth et al. [113], H. Hansen-Goos et al. [27, 28, 105], and P. Tarazona et al. [26, 114, 115]. Moreover, a well-written review about *Fundamental Measure Theory for Hard-Sphere Mixtures* by R. Roth has appeared in 2010 [29].

As outlined in the previous section, a strong motivation is given by the result of Eq. (3.36)

to construct the excess free energy density Φ as a function of the weighted densities n_α . Since these densities differ in their dimension, Y. Rosenfeld established the ansatz [25]

$$\begin{aligned}\Phi = f_1(n_3)n_0 &+ f_2(n_3)n_1n_2 + f_3(n_3)\vec{n}_1 \cdot \vec{n}_2 \\ &+ f_4(n_3)n_2^3 + f_5(n_3)n_2\vec{n}_2 \cdot \vec{n}_2,\end{aligned}\quad (3.38)$$

where Φ has the dimension of an energy density. Since n_3 is the only dimensionless weighted density, the coefficient functions f_i can only depend on it.²⁹

Moreover, the general identities $f_3 = -f_2$ and $f_5 = -3f_4$ follow from the equivalence between the weight functions introduced by Y. Rosenfeld and the scalar ones introduced by E. Kierlik and M. L. Rosinberg [108], because a connection between the scalar and vectorial weight functions arises due to this equivalence [109]. To recover the low density limit (3.36) and the direct pair-correlation function up to first order, the functions f_i must have low density expansions [29]

$$f_1(n_3) = n_3 + \frac{n_3^2}{2} + \mathcal{O}(n_3^3), \quad (3.39)$$

$$f_2(n_3) = 1 + n_3 + \mathcal{O}(n_3^2), \quad (3.40)$$

$$f_3(n_3) = -1 - n_3 + \mathcal{O}(n_3^2), \quad (3.41)$$

$$f_4(n_3) = \frac{1}{24\pi} + \mathcal{O}(n_3), \quad (3.42)$$

$$f_5(n_3) = -\frac{3}{24\pi} + \mathcal{O}(n_3). \quad (3.43)$$

Nevertheless, Y. Rosenfeld used the SPT equation (3.12) to achieve an extrapolation of the functional that is also valid for higher densities. The left-hand side of Eq. (3.12) is given by the functional derivative $\delta\Phi/\delta\rho$ and the right-hand side is given by the thermodynamic bulk relation $\Omega = -pV$. It follows [25, 29]

$$\frac{\partial\Phi}{\partial n_3} = -\Phi + \sum_{\alpha} \frac{\partial\Phi}{\partial n_{\alpha}} n_{\alpha} + n_0. \quad (3.44)$$

With respect to the above mentioned restrictions to the functions $f_i(n_3)$, the solution as

²⁹See Sec. B.2 for further information regarding the dimensions of the weighted densities.

obtained by Y. Rosenfeld [25] and therefore denoted with RF reads

$$f_1^{RF}(n_3) = -\log(1 - n_3), \quad (3.45)$$

$$f_2^{RF}(n_3) = \frac{1}{1 - n_3}, \quad (3.46)$$

$$f_3^{RF}(n_3) = -f_2^{RF}(n_3), \quad (3.47)$$

$$f_4^{RF}(n_3) = \frac{1}{24\pi(1 - n_3)^2}, \quad (3.48)$$

$$f_5^{RF}(n_3) = -3f_4^{RF}(n_3), \quad (3.49)$$

Introducing the sum $\Phi = \Phi_1 + \Phi_2 + \Phi_3$, the excess free energy density follows with

$$\Phi_1^{RF} = -n_0 \log(1 - n_3), \quad (3.50)$$

$$\Phi_2^{RF} = \frac{n_1 n_2 - \vec{n}_1 \cdot \vec{n}_2}{1 - n_3}, \quad (3.51)$$

$$\Phi_3^{RF} = \frac{n_2^3 - 3n_2 \vec{n}_2 \cdot \vec{n}_2}{24\pi(1 - n_3)^2}. \quad (3.52)$$

However, this result fails to predict the fluid-solid phase transition of the pure hard-sphere system, as already mentioned by Y. Rosenfeld in 1989. Thus, the functional has been investigated intensively within the following years [100, 107, 108, 116, 117]. During this research, it has also been applied to systems in other dimensions, for example to a two-dimensional space (plane). To allow for this, the powerful concept of dimensional crossover can be applied, where the three-dimensional density $\rho(x, y, z)$ is restricted to less dimensions by external fields. This is done by introducing δ -functions and, for example, the two-dimensional density follows as $\rho^{(2d)}(x, y)\delta(z) = \rho(x, y, z)$. Even more, this system is equivalent to a system of hard disks.³⁰ However, the freezing transition is not well described within this framework, but reasonable functionals for hard-disk systems exist [118].

Due to these investigations, the third term Φ_3^{RF} of the functional was found to diverge in the exact one-dimensional limit. Accordingly, new approaches have been developed that yield the exact zero- and one-dimensional limit [114]. Then, P. Tarazona presented [26]

a new free energy density functional for hard spheres (...), which reproduces the Percus-Yevick equation of state and direct correlation function for the fluid, with a tensor weighted density. The functional, based on the zero-dimension limit, is exact for any one-dimensional density distribution of the spheres. The application to the hard sphere crystals gives excellent results, solving all of the qualitative problems of previous density functional approximations, including the unit cell anisotropy in the fcc lattice and the description of the metastable bcc lattice.

³⁰Compare also chapter 6 and the review of R. Roth [29].

In this work, P. Tarazona introduced the tensorial weight function³¹

$$\vec{w}_i^{(m_2)}(\vec{r}) = \left(\frac{\vec{r} \cdot \vec{r}^t}{|\vec{r}|^2} - \frac{\overleftrightarrow{\mathbb{I}}}{3} \right) \delta(R_i - |\vec{r}|) = \left(\frac{\vec{r} \cdot \vec{r}^t}{|\vec{r}|^2} - \frac{\overleftrightarrow{\mathbb{I}}}{3} \right) w_i^{(2)}(\vec{r}) \quad (3.53)$$

and he replaced the numerator of the third term Φ_3^{RF} of the excess free energy density by³²

$$n_2^3 - 3n_2\vec{n}_2 \cdot \vec{n}_2 \Rightarrow n_2^3 - 3n_2\vec{n}_2 \cdot \vec{n}_2 + \frac{9}{2} (\vec{n}_2^t \cdot \vec{n}_{m_2} \cdot \vec{n}_2 - \text{Tr}(\vec{n}_{m_2}^3)). \quad (3.54)$$

Here, \vec{r}^t is the transposed of \vec{r} , \mathbb{I} is the unit matrix in 3×3 -dimensional space, and Tr denotes the trace of matrices.

In 2002, R. Roth et al. presented the *White Bear version* of a fundamental measure density functional, named after a local institution. The functional “keeps the structure of Rosenfeld’s FMT whilst inputting the Mansoori-Carnahan-Starling-Leland bulk equation of state” [113].³³ The structure of the functional follows from the new functions $f_i^{WB}(n_3) = f_i^{RF}(n_3)$ for $i \in \{1, 2, 3\}$ and $f_5^{WB}(n_3) = -3f_4^{WB}(n_3)$ with

$$f_4^{WB}(n_3) = \frac{n_3 + (1 - n_3)^2 \log(1 - n_3)}{36\pi n_3^2 (1 - n_3)^2}. \quad (3.55)$$

Since the result is similar to that one of the White Bear mark II version that is introduced in the next paragraph, both functionals are presented together, only differing in the functions ϕ_2 and ϕ_3 . For the White Bear version, their values are $\phi_2^{WB} = 0$ and³⁴

$$\phi_3^{WB}(n_3) = \frac{9n_3^2 - 6n_3 - 6(1 - n_3)^2 \log(1 - n_3)}{4n_3^3}. \quad (3.56)$$

The *White Bear version mark II* has been introduced by H. Hansen-Goos and R. Roth “in the spirit of the White Bear version”. It is based on the Carnahan-Starling equation of state (see Eq. 3.14) and “improves upon consistency with an exact scaled-particle theory relation in the case of the pure fluid” [27]. The White Bear II excess free energy density

³¹The tensor has originally been defined without the term $\overleftrightarrow{\mathbb{I}}/3$. The notation that is used in this work is ascribed to a work of M. Schmidt et al. [119].

³²Erroneously, a factor 1/2 is often missing in this replacement in literature.

³³In Eq. (24) of Ref. [113] a bracket is misplaced in the replacement of P. Tarazona.

³⁴Its expansion reads $\phi_3^{WB}(n_3) = \frac{1}{2} + \frac{1}{8}n_3 + \mathcal{O}(n_3^2)$.

follows with

$$\Phi_1^{WBII} = \Phi_1^{RF} = -n_0 \log(1 - n_3), \quad (3.57)$$

$$\Phi_2^{WBII} = \left(1 + \frac{1}{9}n_3^2\phi_2(n_3)\right) \frac{n_1n_2 - \vec{n}_1 \cdot \vec{n}_2}{1 - n_3}, \quad (3.58)$$

$$\Phi_3^{WBII} = \left(1 - \frac{4}{9}n_3\phi_3(n_3)\right) \frac{n_2^3 - 3n_2\vec{n}_2 \cdot \vec{n}_2}{24\pi(1 - n_3)^2}, \quad (3.59)$$

where the functions ϕ_2 and ϕ_3 are defined by

$$\phi_2(n_3) = \frac{6n_3 - 3n_3^2 + 6(1 - n_3)\log(1 - n_3)}{n_3^3}, \quad (3.60)$$

$$\phi_3(n_3) = \frac{6n_3 - 9n_3^2 + 6n_3^3 + 6(1 - n_3)^2\log(1 - n_3)}{4n_3^3}. \quad (3.61)$$

Of course, the replacement (3.54), introduced by P. Tarazona, can be applied. And due to the construction of the functional, its fluid properties follow directly from the Carnahan-Starling results, like its excess free energy (3.15).³⁵ In addition, the functional is given in an explicit form in Sec. B.1, including its low-density expansion and its derivative with respect to the density.

In 2009, H. Hansen-Goos and K. Mecke presented a *Fundamental Measure Theory for Inhomogeneous Fluids of Nonspherical Hard Particles* [28]. They deconvolute the Mayer- f function in not only those weight functions introduced by Y. Rosenfeld, but also a series of ever higher rank tensorial weight functions, using the Gauss-Bonnet theorem (3.24). Thereby, the first terms of this expansion are given in Eq. (3.33) and Eq. (3.34). “The functional captures the isotropic-nematic transition for hard spherocylinders” [28], as also shown in Sec. 6.2, and is still a surprisingly good functional for non-convex dumbbells,³⁶ as discussed by M. Marechal in Ref. [104] and also shown in Sec. 6.3.

Due to the deconvolution in additional tensorial weight functions, the theory is named *extended deconvolution FMT*. Consequently, the excess free energy density Φ contains an additional term $\Phi^{\Delta\kappa} = -\zeta \text{Tr}[\vec{n}_1 \cdot \vec{n}_2]/(1 - n_3)$, which follows from the tensorial weight functions (3.33) and (3.34) [28, 105]. Here, the parameter ζ that enters edFMT is a renormalization factor to correct for errors due to the truncation of the expansion of the Mayer- f function in tensorial weight functions after the term involving rank two tensors. In addition, the term Φ_3 follows with

$$\Phi_3^{\text{edFMT}} = \frac{3}{16\pi} \frac{\vec{n}_2^t \cdot \vec{n}_2 \cdot \vec{n}_2 - n_2 \vec{n}_2 \cdot \vec{n}_2 - \text{Tr}[\vec{n}_2^3] + n_2 \text{Tr}[\vec{n}_2^2]}{(1 - n_3)^2}. \quad (3.62)$$

Comparing this result with that one of the White Bear version mark II (with the replace-

³⁵The equation of state can be obtained for FMT functionals in general, such as shown in Ref. [104].

³⁶For non-convex particles the Euler characteristic of the intersection volume of two particles can differ from 2, which is not considered in edFMT.

ment of P. Tarazona), the tensor $\overleftrightarrow{n}_{m_2}$ has simply been exchanged by the tensor \overleftrightarrow{n}_2 .³⁷ Of course, for hard spheres the result of Y. Rosenfeld and P. Tarazona is obtained, because the deviatoric curvature $\Delta\kappa$ vanishes.

In recent works, S. Korden re-summed the cluster integrals of the diagrammatic virial expansion [39, 112] and obtained the approach (3.50-3.52) of Y. Rosenfeld as a first term of the new series [110]. Higher orders are going beyond this result and, for example, contain the term (3.54), introduced by P. Tarazona [111]. However, higher orders of this FMT expansion have not been applied to any physical model up to now, which is a recommended topic of future work.

3.4.2 Functional derivatives and direct correlation functions

To solve the equation of state (2.49) in DFT, the functional derivative of the excess free energy functional is needed as an input. In another sense, the direct correlation functions $c^{(1)}$ and $c^{(2)}$ of a reference density are needed in the Ramakrishnan-Yussouff approach (3.22). Accordingly, it is necessary to determine direct correlation functions (2.50) in the framework of FMT.

Since the excess free energy functional (3.37) is a function of weighted densities, the direct correlation function in FMT follows from the excess free energy density Φ and its corresponding weighted densities n_α for species i with

$$-c_i^{(1)}[\rho; \vec{r}] = \sum_{\alpha} \int_V \frac{\partial \Phi}{\partial n_\alpha}(\vec{r}') w_i^{(\alpha)}(\vec{r}' - \vec{r}) d\vec{r}', \quad (3.63)$$

$$-c_{ij}^{(2)}[\rho; \vec{r}, \vec{r}'] = \sum_{\alpha, \beta} \int_V \frac{\partial^2 \Phi}{\partial n_\alpha \partial n_\beta}(\vec{r}'') w_i^{(\alpha)}(\vec{r}'' - \vec{r}) w_j^{(\beta)}(\vec{r}'' - \vec{r}') d\vec{r}''. \quad (3.64)$$

In the case of non-scalar weighted densities, the notation is explained in more detail in Sec. B.1. In addition, the functional derivatives are listed there for the White Bear mark II functional in an explicit form.

Furthermore, the excess free energy density Φ becomes constant in space for a homogeneous density ρ_{fl} of a fluid. Accordingly, Eq. (3.64) simplifies to

$$-c_{ij}^{(2)}[\rho_{\text{fl}}; \vec{r}] = \sum_{\alpha, \beta} \frac{\partial^2 \Phi}{\partial n_\alpha \partial n_\beta} w_i^{(\alpha)} \circledast w_j^{(\beta)}(\vec{r}). \quad (3.65)$$

For example, the explicit result for the direct pair-correlation function is given for the White Bear functional in Eq. 41 of Ref. [113]. Like the Percus-Yevick direct pair-correlation function, this result is given by a polynom of third order in r .

³⁷Remember the additional term $\overleftrightarrow{\mathbb{I}}/3$ in Eq. (3.53) in contrast to Eq. (3.34).

Indeed, the polynomial form is of the same order for all functionals with the same choice of weight functions. Thus, M. Oettel et al. also list the direct pair-correlation functions [88]

$$c^{(2)}[\rho_0; r] = \left(a_1 + a_2 \frac{r}{\sigma} + a_3 \frac{r^3}{\sigma^3} \right) \Theta(\sigma - r) \quad (3.66)$$

in the one component case for the White Bear II functional and for the tensor version of the Rosenfeld functional, introduced by P. Tarazona. However, the latter is equal to the Percus-Yevick solution³⁸ by construction.³⁹

Following Ref. [88], the coefficients a_i for the tensor version of the White Bear II functional read⁴⁰

$$a_1 = -\frac{1 + 4\eta + 4\eta^2 - 4\eta^3 + \eta^4}{(1 - \eta)^4}, \quad (3.67)$$

$$a_2 = \frac{-2 + 25\eta + 12\eta^2 - 10\eta^3 + 2\eta^4}{3(1 - \eta)^4} - \frac{2\log(1 - \eta)}{3\eta}, \quad (3.68)$$

$$a_3 = \frac{1 - 4\eta + 2\eta^2 - 3\eta^3 + \eta^4}{(1 - \eta)^4} + \frac{\log(1 - \eta)}{\eta}. \quad (3.69)$$

Its Fourier transform is given in Appendix B.2.

³⁸“Percus-Yevick equation of state” usually means the one obtained via the compressibility route in DFT works, unless mentioned otherwise.

³⁹For example, see Eq. (31) in the work of M. Oettel et al. [88].

⁴⁰In Ref. [88], a wrong sign is noted for the second term in the coefficient a_2 .

4

Bulk phases and the hard-sphere crystal

Stand still you ever moving spheres (...)

(from: *Doctor Faustus* [120], scene 13, l. 64,
Christopher Marlowe 1564 - 1593)

The particles in a physical system generate different states of aggregation, depending on the (thermodynamic) properties of the system and the particles. The states are called phases and the parameters allowing to distinguish between different phases are called order parameters. Typically, one phase is stable in equilibrium, but several phases can also coexist next to each other, when they are energetically equivalent.

As known from water, in principle, three states of matter exist: the gas phase (or vapor phase), the liquid phase, and the solid phase. Moreover, the gas and the liquid phase are sometimes combined to a fluid phase, if both phases are indistinguishable due to the lack of a phase transition, for example in the case of hard spheres. Furthermore, especially the solid phase often splits up into additional and more special phases, for example different types of crystalline structures, multi-crystalline structures, ceramic or amorphous materials, glass phases, or grains.¹ Of course, many more kinds of phases may exist (see Sec. 6 for orientational phases).

Phases (and their properties) are usually displayed in so-called phase diagrams, where every point is characterized by the order parameters of the system. Regions that denote different phases are separated by lines. For example, the phase diagram of polydisperse hard spheres is schematically sketched in Fig. 4.1. In this diagram, the macroscopic variables are given by the amount δ of polydispersity² and by the mean density ρ of the hard-sphere system. The illustrated phases are the fluid and the solid phase. In between these regions of pure, unmixed phases, there are also regions where phases would coexist in equilibrium, for instance solid and fluid or even solid and solid with different crystalline structures or lattice orientations. In the limit $\delta \rightarrow 0$ of vanishing polydispersity, the phase diagram of monodisperse hard spheres is obtained which solely depends on the mean density ρ . Its fluid-solid transition takes place in between densities of $\rho_{\text{fl}}\sigma^3 \approx 0.944$ and $\rho_{\text{s}}\sigma^3 \approx 1.04$.

¹The monodisperse hard-sphere system builds a glassy phase around a mean density of $1.22/\sigma^3$ (volume fraction 0.637), as shown in Refs. [121, 122]. However, the nature of glasses is not completely understood (see e.g. Ref. [123] by Y. Rahmani et al.).

²For further reading about polydispersity, see Sec. 4.2.4.

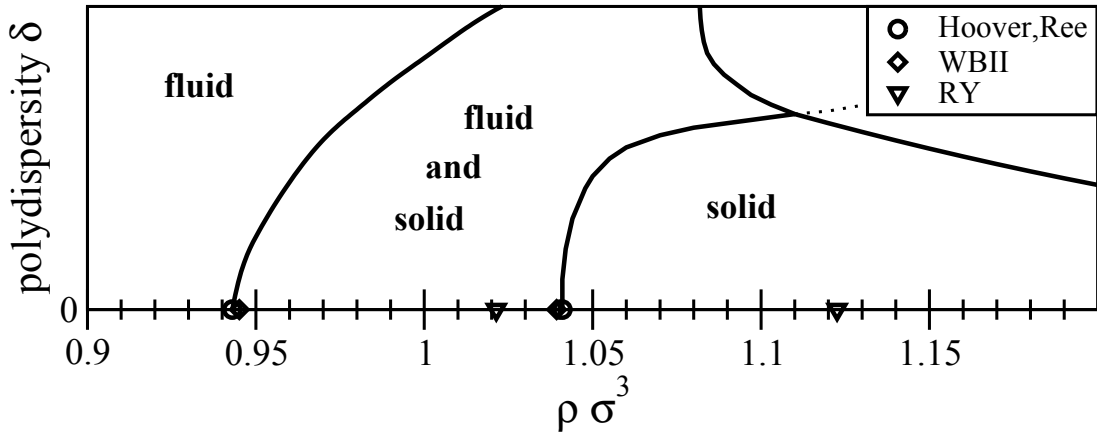


Figure 4.1: Schematic sketch of the phase diagram for polydisperse hard spheres. For monodisperse ($\delta = 0$) spheres, the fluid and solid (fcc crystal) transition points are shown with data from W. G. Hoover and F. H. Ree [124] and results from this work, using the White Bear mark II FMT approach and the Ramakrishnan-Yussouff DFT approach (see Sec. 4.2). The regions with stable phases in equilibrium are marked (fluid, solid), in the other regions phases are coexisting in equilibrium (fluid-solid, fluid-solid-solid, ..., solid-solid, ...). The range of polydispersity, sketched here, is about [0,0.1]. For further information about the Equilibrium Phase Behavior of Polydisperse Hard Spheres, see Ref. [65] by M. Fasolo and P. Sollich.

Different phases can be distinguished and characterized by their internal structure. For example, a fluid hard-sphere phase has less structure than the corresponding crystalline phase. In general, the internal structure can be measured by the structure factor $S(\vec{k})$ that is known from Sec. 3.1. Moreover, it is connected with the direct pair-correlation function $c^{(2)}(r)$ and with the particle distribution function $g(r)$ (also cmp. Sec. 2.2.2). In this context, T. V. Ramakrishnan and M. Yussouff wrote an article about *First-principles order-parameter theory of freezing* [66] (q_m is the position in reciprocal space of the first maximum of the graph of $S(q)$) and state:³

Verlet observed that near freezing, $S(q_m)$ is nearly 2.85 for all classical fluids. Computer results for the Lennard-Jones liquid along the melting curve, for the hard-sphere fluid, the one-component plasma, and experimental results for Ar, Na, Rb, Pb, all show $S(q_m)$ to be between 2.8 and 3.1 near freezing. The $S(q_m)$ values for fluids freezing into fcc and bcc structures cluster around 2.8 and 3.0, respectively. In the solid phase, the analogue of Verlet's rule is perhaps the Lindemann criterion of melting, i.e. the criterion that the mean-square displacement $\langle u^2 \rangle$ scaled by the square of the interatomic separation r_{int}^2 has nearly a constant value (0.01).

For this reason, the hard-sphere system is an ideal model system to learn more about internal structures, phases, and transitions between them. Theoretical approaches to the

³All references have been removed from this quotation

hard-sphere system have been discussed in Sec. 3.2.3.

However, external fields or phase borders change the local properties of a physical system, for example in the vicinity of a wall or next to other coexisting phases.⁴ For this reason, phases are typically analyzed in the bulk, which is a region deep inside the phase of interest, where no effects from the borders affect its properties.⁵

Finally, comprehensive literature about liquids and fluids exists. For example, J. A. Barker and D. Henderson have discussed the question *What is "liquid"?* *Understanding the states of matter* [71] and textbooks are available from H. L. Frisch and J. L. Lebowitz about *the equilibrium theory of classical fluids* [127] and from J.-P. Hansen and I. R. McDonald about the *theory of simple liquids* [39].

In this chapter, first crystalline (periodic) structures are introduced, in particular lattices, unit cells, packing problems, and density distributions. Next, hard spheres are discussed, starting with an outline of the historical progress in research. Then, density distributions, obtained by DFT calculations, are analyzed and compared to simulation results. Finally, the crystal-fluid phase transition is explained, including the effects due to polydispersity, and a conclusion is drawn.

4.1 Crystalline structures

Crystals or materials with a crystalline structure are solids. They are characterized by a repeating pattern of the arrangement of their constituents in all spatial directions. Using mathematics, a crystalline structure is described by a lattice, defined by its translational symmetries and by a basis. However, it is important to distinguish between crystalline structures and quasicrystalline ones [128] that have long-range orientational order but no translational symmetry (only local). “For the discovery of quasicrystals”, the Nobel Prize in Chemistry 2011 was awarded to Dan Shechtman.

In nature, crystalline solids typically consist of grains, several crystalline regions that differ in orientation or structure, and they are not expanded infinitely, as assumed in perfect lattices. Moreover, the constituents in a crystalline region are usually not exactly located on lattice positions, due to temperature and impurities. For example, single constituents can be removed from a perfect structure (vacancies) or they can be added (additional particles), as known from doping semiconductors. In another sense, lattice points can be dislocated, if e.g. one lattice plane is shifted against another. However, this crystallographic defects have an important influence on the physical properties of the material⁶ and their study bares interesting phenomena, for example about the dynamics of dislocations [129].

⁴For example, a hard-sphere fluid next to a planar wall is discussed by R. Roth [29] and spherocylinders and dumbbells between two hard walls are discussed by H. Hansen-Goos and K. Mecke [105] and M. Marechal et al. [104] (see also Sec. 6).

⁵External fields can also be present in the bulk (compare Sec. 6.2 and A. Härtel et al. [125, 126]).

⁶Doping semiconductors allows the construction of diodes and transistors (and consequently of modern computers) due to a total change in the electrical properties of the material.

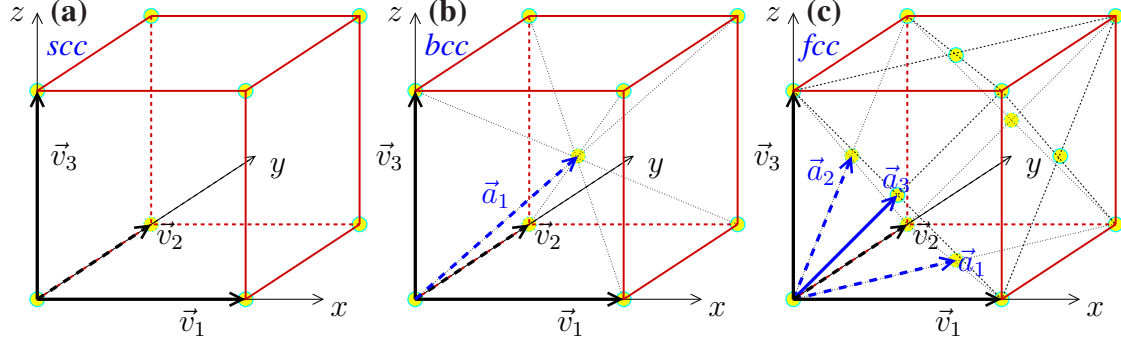


Figure 4.2: (Color) Sketches of the cubic unit cells, spanned by the vectors $\{\vec{v}_i\}$, $i = 1, 2, 3$: a) simple cubic crystal (sc) structure, where the unit cell already is a primitive cell, b) body-centered cubic (bcc) structure, where the primitive vectors \vec{a}_2 and \vec{a}_3 point to the central lattice point of two neighbour cells (not included in this figure), and c) face-centered cubic (fcc) structure, where all primitive lattice vectors $\{\vec{a}_i\}$ of the infinite lattice are shown. The lattice positions are indicated by circles.

If crystalline regions are big enough, their properties correspond well with those of an infinite perfect crystal. Such a mono-crystalline structure is described by a lattice, where the constituents of the crystal (e.g. atoms, molecules, or colloidal particles) are located on (or around) the lattice points. The mathematical concept of lattices is introduced in the following section, to describe crystalline structures. For further reading, the textbooks of N. W. Ashcroft and N. D. Mermin [130] or J. M. Ziman [131] are recommended.

4.1.1 Crystalline lattices

An n -dimensional lattice \mathbb{L} is defined by the symmetry group of a translational symmetry in n directions, corresponding to a set of n translation operators T_i , $i = 1, \dots, n$. Due to their symmetries, these operators preserve the lattice and $\mathbb{L} = T_i \mathbb{L}$ holds $\forall i$. For example, the integer numbers \mathbb{Z} represent a lattice in the Euclidean space \mathbb{R}^n and are generated by the translation operators T_i that add 1 to the i^{th} component $(\vec{x})_i$ of elements \vec{x} in Euclidean space.

A lattice is spanned by so-called *primitive vectors* \vec{a}_i that correspond to the directions of the translational symmetries (for example, see Fig. 4.2). Thus, a lattice consisting of discrete points can be defined by

$$\mathbb{L} = \left\{ \sum_{i=1}^n m_i \vec{a}_i \mid m_i \in \mathbb{Z} \right\}, \quad (4.1)$$

where $m_i \in \mathbb{Z}$ are integer numbers. Such discrete lattices have been studied by Auguste Bravais (1811-1863)⁷ and therefore, are called Bravais lattices.

⁷See *Lexikon der Physik*, Ref. [132].

To describe directions and planes in (Bravais) lattices, William Hallowes Miller (1801–1880)⁸ introduced Millerian indices, commonly called Miller indices. They are defined by using a reciprocal (or dual⁹) lattice $\tilde{\mathbb{L}}$.

The reciprocal lattice $\tilde{\mathbb{L}}$ consists of all those wave vectors \vec{k} that correspond to a wave with the same symmetry as the lattice \mathbb{L} . For elements $\vec{R} \in \mathbb{L}$, such plane waves fulfill the condition

$$e^{i\vec{k}\cdot\vec{r}} = e^{i\vec{k}\cdot(\vec{r}+\vec{R})}. \quad (4.2)$$

Thereby, it is useful to define the vectors \vec{k} of the reciprocal lattice without the factor 2π that enters the wave vectors due to its periodic definition $\exp(i\vec{k} \cdot \vec{R}) = 1$ in Eq. (4.2). Consequently, the primitive vectors \vec{b}_i of the reciprocal lattice are obtained from the matrix product $[\vec{b}_1 \dots \vec{b}_n]^T \cdot [\vec{a}_1 \dots \vec{a}_n] = \vec{I}$, where \vec{I} denotes the $n \times n$ -dimensional unit matrix and $[\vec{a}_1 \dots \vec{a}_n]$ is the matrix with the columns \vec{a}_i . In other words, a multiplication of primitive vectors \vec{a} of the lattice \mathbb{L} and \vec{b} of the reciprocal lattice $\tilde{\mathbb{L}}$ results in integer values. In conclusion, in three dimensions the reciprocal primitive vectors of an infinite lattice \mathbb{L} read

$$\vec{b}_1 = \frac{\vec{a}_2 \times \vec{a}_3}{\vec{a}_1 \cdot (\vec{a}_2 \times \vec{a}_3)}, \quad \vec{b}_2 = \frac{\vec{a}_3 \times \vec{a}_1}{\vec{a}_1 \cdot (\vec{a}_2 \times \vec{a}_3)}, \quad \vec{b}_3 = \frac{\vec{a}_1 \times \vec{a}_2}{\vec{a}_1 \cdot (\vec{a}_2 \times \vec{a}_3)}, \quad (4.3)$$

where \times denotes the cross product in three dimensions.

Now, the Miller indices (ijl) define a plane perpendicular to the reciprocal lattice vector (or wave vector) $\vec{K} = i\vec{b}_1 + j\vec{b}_2 + l\vec{b}_3$ in a reciprocal three-dimensional lattice $\tilde{\mathbb{L}}$. Similarly, $[ijl]$ defines a vector $\vec{R} = i\vec{a}_1 + j\vec{a}_2 + l\vec{a}_3$ in the three-dimensional lattice \mathbb{L} in terms of the primitive lattice vectors \vec{a}_i . In general, $[ijl]$ is not perpendicular to (ijl) . Furthermore, it is common to present negative indices $-i$ by its positive value \bar{i} , marked with a bar.

In cubic structures (as shown in Fig. 4.2), planes like (100) , (010) , (001) , and $(\bar{1}00)$, $(0\bar{1}0)$, $(00\bar{1})$ are equivalent, due to symmetry. Accordingly, all equivalent planes (ijl) are collectively addressed by $\{ijl\}$. Similarly, the directions $[\bar{1}00]$, $[001]$, and $[0\bar{1}0]$ are equivalent in a cubic structure. Thus, equivalent directions $[ijl]$ are denoted by $\langle ij l \rangle$.

In addition to this, in a three-dimensional space, 14 possible Bravais lattices exist and are ordered in 7 lattice systems, called triclinic, monoclinic, orthorhombic, tetragonal, rhombohedral, hexagonal, and cubic. They are named like the shapes of their corresponding repeated pattern in space. These patterns are called unit cells and are discussed in the next section. In Fig. 4.2, the three cubic patterns and their Bravais lattices are shown. The most simple structure is the simple cubic crystal (sc) structure, shown in Fig. 4.2(a). More important, the body-centered cubic (bcc) structure and the face-centered cubic (fcc) structure are shown in Fig. 4.2(b) and Fig. 4.2(c). They often occur in nature, for example in elements like Fe and Na (bcc) or Ar, Cu, and Ni (fcc).

⁸See *Obituary Notices of Fellows Deceased* in the R. Soc. Lond. [133].

⁹The concept of dual lattices is more general than needed in this context.

4.1.2 Unit cells

A unit cell is the volume $V_c \subset \mathbb{R}^n$ in space that fills the whole space by translations along a set \mathbb{L}_c of vectors of the underlying lattice \mathbb{L} . In other words, the whole space is tiled by a unit cell. Accordingly, a crystal is completely defined by the definition of one of its unit cells. However, the choice of a unit cell is not unique, because the cell must not have the smallest amount of volume that is possible (see Fig. 4.3, for example). It can be defined translated in space as well. Thus, the half-open intervals $[-\frac{1}{2}, \frac{1}{2})$ and $[0, 1)$ both define equivalent unit cells for the lattice \mathbb{Z} in \mathbb{R} .

All lattice points inside a unit cell are called the basis of this cell. Accordingly, the lattice \mathbb{L} can be split into a basis \mathbb{B} and a sublattice \mathbb{L}_c that holds all possible translations of the basis (to achieve the original lattice). Thus, the corresponding unit cell fills the whole volume without spacing in between cells or intersections of them, if translated along the sublattice \mathbb{L}_c . The precise definition reads

$$\mathbb{L} = \mathbb{L}_c \otimes \mathbb{B} = \left\{ \vec{l} + \vec{b} \mid \vec{l} \in \mathbb{L}_c, \vec{b} \in \mathbb{B} \right\}. \quad (4.4)$$

However, a unit cell is called a *primitive cell*, if it has the smallest volume that is possible. Because it is a unit cell, a primitive cell also tiles space by translations along all vectors of the lattice. Moreover, a primitive cell only contains one lattice point, but its construction is still not unique. Therefore, the two most common kinds of constructions will be introduced in the following paragraphs.

First, a primitive cell can be spanned by the primitive lattice vectors of the underlying lattice. An example is given in Fig. 4.2(a) for the simple cubic (sc) structure. In comparison to the body-centered cubic (bcc) structure in Fig. 4.2(b) and to the face-centered cubic (fcc) structure in Fig. 4.2(c), the simple cubic structure only has one lattice point in its unit cell (the other seven corners in Fig. 4.2(a) correspond to the neighbouring cells). For the fcc structure, the primitive lattice vectors that span a primitive cell are also shown.¹⁰

Second, a Wigner-Seitz cell¹¹ is a primitive cell. Its construction is based on the mathematical concept of the fundamental domain or the construction of a Voronoi cell¹², where the space is split up into regions around discrete points. The Wigner-Seitz cell is constructed around one lattice point p and contains all space points with a smaller distance to the point p as to any other point of the lattice. Therefore, it can be constructed by placing planes in the center between the point p and all other lattice points, respectively. Then, a Wigner-Seitz cell is formed by the resulting volume that is confined by all planes. In addition, the Wigner-Seitz cell of the reciprocal lattice is called the first Brillouine zone.

¹⁰For non monoatomic systems, where the face-centered particles belong to another species, the cubic unit cell may be primitive in general. In this case only the corners belong to the lattice, so the lattice is a simple cubic one and the unit cell again contains only one lattice point, but two particles.

¹¹Named after Eugen(e) Paul Wigner (1902-1995) and Frederick Seitz (1911-2008) [134, 135].

¹²These concepts decompose space around general subsets in space and are more general than the decomposition with respect to a highly symmetric lattice.

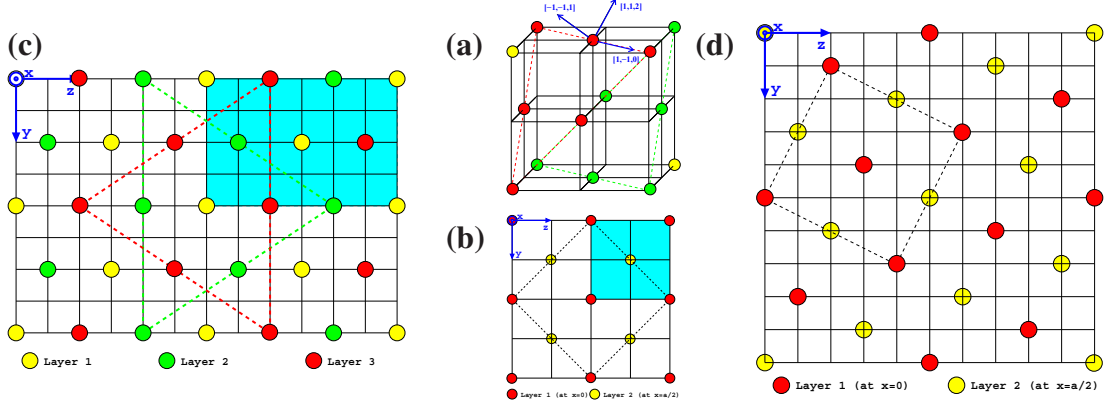


Figure 4.3: (Color) Schematic sketches of the fcc-crystal lattice sites for (minimal) rectangular cuboid cells. The orientations in z -direction are: a) [001] (colors correspond to panel c), b) [011], c) [112] (in x -direction also [$\bar{1}\bar{1}1$]), d) [210].

To run numerical calculations, it is useful to construct a rectangular cuboid box with periodic boundary conditions that recovers the crystalline fcc lattice. Of course, this box should have minimal volume in order to decrease computational time. If interfaces are involved in calculations, the rectangular cuboid box must also reflect the symmetry of the interface. Thus, one face of the unit cell is required to be oriented parallel to the interfacial plane. For this reason, lattice properties are listed in Table 4.1 for the five interfacial orientations (001), (011), (111), (012), and (112) that are of interest in the context of this work (see Chapter 5). The properties are obtained in Sec. A.3, where rotated unit cells are constructed by using a mathematical scheme. In addition, schematic sketches of the lattice sites of these five cells are shown in Fig. 4.3.

4.1.3 Packing of hard spheres

For a given system, the nature of packing [136,137] is an interesting and highly non-trivial problem, especially for hard-core bodies, where no overlap between particles is allowed and a maximal number of particles per volume exists. This close packing limit defines an upper boundary for the mean particle density of the system. For this reason, knowledge about close packing is interesting, e.g. for shipping or storing. For example, cannonballs have been piled in pyramids for centuries, similar to oranges on the market nowadays. The question, if this packing is the best or not, as well as which way of packing is the energetically preferred one in nature, is actual until today.

In 1611, Johannes Kepler (1572-1630) formulated a theorem for hard spheres, known as the Kepler conjecture [137,138]:

No packing of congruent balls in Euclidean three space has density greater than that of the face-centered cubic packing. This density is $\frac{\pi}{\sqrt{18}} \approx 0.74$.

Table 4.1: Properties of an fcc lattice and a rectangular cuboid unit cell for five interfacial orientations of one face, respectively (001), (011), (111), (012), (112). To obtain the listed properties, a mathematical schema is given in Sec. A.3. Using the notation from the example in Sec. A.3.4, \hat{n} is the normal vector on the interface of given orientation and ϕ and θ are angles that are used for its parametrization. The angles α_z and α_x determine the rotation of the lattice around the axis z and x , to obtain the given interface orientation parallel to a Cartesian coordinate plane. The vectors \vec{v}_1 , \vec{v}_2 , and \vec{v}_3 are the edges that span the unit cell, given in terms of the primitive vectors \vec{a}_1 , \vec{a}_2 , and \vec{a}_3 (see Fig. 4.2). Finally, V_c is the volume of the unit cell in terms of the lattice constant a , given as a product of the length of the three edges of the unit-cell.

	(001)	(011)	(111)	(012)	(112)
ϕ	0	$\frac{\pi}{2}$	$\frac{\pi}{4}$	$\frac{\pi}{2}$	$\frac{\pi}{4}$
θ	$\frac{\pi}{2}$	$\frac{\pi}{4}$	$\arctan(\sqrt{2})$	$\arctan(\frac{1}{2})$	$\arctan\left(\frac{\sqrt{2}}{2}\right)$
\hat{n}	$\begin{pmatrix} 0 \\ 0 \\ 1 \end{pmatrix}$	$\frac{1}{\sqrt{2}}\begin{pmatrix} 0 \\ 1 \\ 1 \end{pmatrix}$	$\frac{1}{\sqrt{3}}\begin{pmatrix} 1 \\ 1 \\ 1 \end{pmatrix}$	$\frac{1}{\sqrt{5}}\begin{pmatrix} 0 \\ 1 \\ 2 \end{pmatrix}$	$\frac{1}{\sqrt{6}}\begin{pmatrix} 1 \\ 1 \\ 2 \end{pmatrix}$
α_z	0	0	$\frac{\pi}{4}$	0	$\frac{\pi}{4}$
α_x	0	$\frac{\pi}{2}$	$\arctan(\sqrt{2})$	$\arctan(\frac{1}{2})$	$\arctan\left(\frac{\sqrt{2}}{2}\right)$
\vec{v}_1	$\vec{a}_1 - \vec{a}_2 + \vec{a}_3$	$\vec{a}'_1 - \vec{a}'_2 + \vec{a}'_3$	$\frac{\vec{a}'_3 - \vec{a}'_2}{\sqrt{2}/2}$	$\vec{a}'_1 - \vec{a}'_2 + \vec{a}'_3$	$\frac{-\vec{a}'_2 + \vec{a}'_3}{\sqrt{2}/2}$
\vec{v}_2	$\vec{a}_1 + \vec{a}_2 - \vec{a}_3$	$\frac{\vec{a}'_1 - \vec{a}'_3}{\sqrt{2}/2}$	$\frac{2\vec{a}'_1 - \vec{a}'_2 - \vec{a}'_3}{\sqrt{3}/2}$	$\frac{3\vec{a}'_1 + \vec{a}'_2 - 3\vec{a}'_3}{\sqrt{5}}$	$\frac{3\vec{a}'_1 - \vec{a}'_2 - \vec{a}'_3}{\sqrt{3}}$
\vec{v}_3	$-\vec{a}_1 + \vec{a}_2 + \vec{a}_3$	$\frac{\vec{a}'_2}{\sqrt{2}/2}$	$\frac{\vec{a}'_1 + \vec{a}'_2 + \vec{a}'_3}{\sqrt{3}}$	$\frac{-\vec{a}'_1 + 3\vec{a}'_2 + \vec{a}'_3}{\sqrt{5}}$	$\frac{\vec{a}'_2 + \vec{a}'_3}{\sqrt{3}/2}$
V_c	$a \times a \times a$	$a \times \frac{a}{\sqrt{2}} \times \frac{a}{\sqrt{2}}$	$\frac{\sqrt{2}a}{2} \times \frac{\sqrt{3}a}{\sqrt{2}} \times \sqrt{3}a$	$a \times \sqrt{5}a \times \sqrt{5}a$	$\frac{a}{\sqrt{2}} \times \sqrt{3}a \times \frac{\sqrt{3}a}{\sqrt{2}}$

About 400 years later, T. C. Hales carried out a proof of this conjecture [137–139], but his proof could not yet be fully validated [140].¹³

However, close packing is achieved by a structure formed by hexagonal layers. If the first two layers are labeled by A and B, the third layer can either be placed as the first one (A) or on a third position (C). So, two stacking sequences are possible, where the sequence ABCABC results in a fcc structure. On the contrary, the sequence ABAB is called hexagonal close packed (hcp). The hcp structure is not correlated to a Bravais lattice, but several elements like Mg, Ti, and Zn crystallize in it [130]. Till this day it is discussed which of both structures is the more stable one (with respect to energy) and why, but the fcc structure seems to be more stable [141, 142].

In another sense, a maximal limit of the packing fraction can be achieved by randomly packing particles together. In a recent work about jammed matter, C. Song et al. found the random close packing limit to be about 0.634 [143]. In addition, J. D. Bernal and J. Mason studied the packing of rigid spheres in a given volume in 1960 and found 0.64 for random

¹³The simple cubic lattice has a maximal packing fraction of $\frac{4}{3}\pi R^3/(2R)^3 = \frac{\pi}{6} \approx 0.5236$.

close packing and 0.60 for loose packing [144].¹⁴ Also, J. G. Berryman performed an early work about random close packing of hard spheres and disks [145] and for disks he published a value of $\eta = \pi/\sqrt{12} \approx 0.9069$ for close packing.

4.1.4 Crystalline density profiles and order parameters

This subsection is a re-formulation of parts of Sec. V.C from Ref. [146] by M. Oettel and co-workers; defects in hard-sphere crystals in FMT have been discussed in Sec. II of this reference.

The density profile $\rho(\vec{r})$ of a hard sphere crystal consists of nearly isolated and identical density peaks ρ_{peak} at the lattice points of the lattice \mathbb{L} and reads

$$\rho(\vec{r}) = \sum_{\vec{r}_i \in \mathbb{L}} \rho_{\text{peak}}(\vec{r} - \vec{r}_i). \quad (4.5)$$

Thus, one of these density peaks describes one particle i that is located around¹⁵ the corresponding lattice position \vec{r}_i . Accordingly, an integration of the density peak distribution should result in one particle.

The density peak \vec{r}_{peak} also contains crystalline defects like vacancies, occurring in some of the unit cells of the whole crystal. For this reason, an integration of a crystalline peak follows with

$$\int_V \rho_{\text{peak}}(\vec{r}) d\vec{r} = 1 - n_{\text{vac}}, \quad (4.6)$$

defining the concentration n_{vac} of vacancies in the crystal.¹⁶

To allow analytical and/or fast calculations, an approximate description of the density peaks ρ_{peak} is useful, e.g. in the form of a trial function, where solely a few order parameters enter the approximation.¹⁷ Thus, a single peak ρ_{peak} can be assumed to have the normalized Gaussian form

$$\rho_{\text{peak}}(\vec{r}) \approx \rho_G(|\vec{r}|) = \left(\frac{\alpha}{\pi}\right)^{\frac{3}{2}} \exp(-\alpha|\vec{r}|^2) \quad (4.7)$$

with a width parameter α in first approximation.

¹⁴Loose packing is obtained by randomly packing spheres and random close packing is obtained by shaking a loose packed system.

¹⁵A density peaks is similar to a distribution of particles around the peak position.

¹⁶For further reading, see e.g. the works by C. H. Bennett and B. J. Alder [147] about *Vacancies in Hard Sphere Crystals*, by S. Pronk and D. Frenkel [148] about *Point Defects in Hard-Sphere Crystals*, or by S. K. Kwak et al. [149] about the *Characterization of mono- and divacancy in fcc and hcp hard-sphere crystals*.

¹⁷For example, T. V. Ramakrishnan and M. Yussouff analyzed the solid-liquid phase transition with one single order parameter [66].

In order to analyze the deviations from the Gaussian form, the density distribution can be assembled in terms of an average radial deviation $f_{\Delta G}(r)$ and of a directional anisotropic deviation $f_{\text{aniso}}(\vec{r})$, in addition to the Gaussian form $\rho_G(r)$ itself [26, 146]. Thus, the density distribution of a crystalline peak follows with

$$\rho_{\text{peak}}(\vec{r}) = \rho_G(r)f_{\Delta G}(r)f_{\text{aniso}}(\vec{r}). \quad (4.8)$$

M. Oettel et al. parametrized and expanded both deviations in the form [146]

$$f_{\Delta G}(r) \approx \exp [b_2 \alpha r^2 + b_4 (\alpha r^2)^2 + b_6 (\alpha r^2)^3], \quad (4.9)$$

$$\begin{aligned} f_{\text{aniso}}(\vec{r}) \approx & 1 + K_4 \alpha^2 \left(x^4 + y^4 + z^4 - \frac{3}{5} r^4 \right) \\ & + K_6 \alpha^3 \left(x^6 + y^6 + z^6 - \frac{3}{7} r^6 \right), \end{aligned} \quad (4.10)$$

where $\vec{r} = (x, y, z)^t$ and $b_2, b_4, b_6 \ll 1$ are expected to be small. This result corresponds to the leading two terms in the cubic cell asymmetry (consistent with the point symmetry of the fcc lattice), what is explained in more detail in a footnote on page 10 of Ref. [146].

Furthermore, it is convenient to quantify the spread of the density distribution around a solid peak by the Lindemann parameter [150, 151] that is defined as the dimensionless root mean-square displacement by

$$\mathcal{L} = \frac{1}{r_{nn}} \sqrt{\int_{WSC} rr^2 \rho(\vec{r}) d\vec{r}}. \quad (4.11)$$

Here the spatial integration is over a Wigner-Seitz cell (WSC), centered around a lattice position at the origin, and $r_{nn} = \sigma (\sqrt{2}/\rho_0)^{1/3}$ denotes the distance between two nearest neighbours in the crystal lattice (the length of the shortest primitive lattice vector).

Finally, an analysis of the bond-orientational order can be used to distinguish between crystalline and fluid particles and gives rise to the definition of a rotational-invariant bond-order parameter $q_6 q_6(i)$ of a particle i [152, 153]. For example, a particle i is identified as a crystalline particle in several works (see also Sec. 5.2), if $q_6 q_6(i) > 0.68$ [72–74]. However, other conditions or other order parameters are available and they may be preferred for crystalline structures differing from fcc.

4.2 Hard-sphere phases

The system of rigid (or hard) spheres is one of the systems that have been investigated the most intensely in the field of soft matter and constitutes an important benchmark system for the investigation of more complex particle shapes or interactions. Solely driven by entropic forces, the internal energy U of a hard-sphere system vanishes, which gives

raise to a separation of the free energy in an entropic part and an internal energy part, in general [96]. Moreover, the packing of hard spheres has been a controversial issue and a stringent proof is owing to this day, as known from the previous section. Similarly, the question has been discussed intensely, whether a hard-sphere system has a fluid-solid phase transition or not.

In this section, the historical progress of investigations in hard spheres is outlined first. Next, recent results from DFT and MC simulations are presented and density profiles as well as the crystal-fluid phase transition are discussed. Finally, the polydispersity of hard spheres and outcomes for the properties of hard-sphere systems are outlined.

Parts of this section are rewritten from the work *Free energies, vacancy concentrations, and density distribution anisotropies in hard-sphere crystals: A combined density functional and simulation study* by M. Oettel et al. [146] ©2010, The American physical Society, especially Subsections 4.2.2 and 4.2.3 about density profiles and phase transitions. In addition, a statement about the individual contributions of the authors is given in the preface of this work.

4.2.1 Historical progress

Already in 1914, P. W. Bridgman investigated the melting line in several substances by experiments [154, 155] and he was convinced that molecules of any “shape” would crystallize at sufficiently high pressure.¹⁸ Later, in 1954, *Further Results on Monte Carlo Equations of State* has been presented for hard spheres by M. N. Rosenbluth and A. W. Rosenbluth [156]. They found “a clear evolution with increasing volume from a crystalline structure to a liquid type structure” and outlined “that the Monte Carlo method is a useful tool for solving statistical mechanical problems”.¹⁹ Moreover, in 1957, an order-disorder transition at about 15% below close packing was found in a combined work by Molecular Dynamics and Monte Carlo computer simulations of W. W. Wood and J. D. Jacobsen [157] and B. J. Adler and T. E. Wainwright [70].

Thus, a discussion about the existence of a phase transition can be referred in the *Round Table on Statistical Mechanics* discussion, held in New Jersey in 1957 [158]. An excerpt from pages 497f reads:

G. E. Uhlenbeck: Recently, there has been some indication, numerically, that a gas of hard spheres has a transition point. (...)

J. G. Kirkwood: We are now again speaking of the classical case for hard spheres, and the question comes up as to whether, for sufficiently high densities, the fluid of hard spheres will crystallize. (...)

G. E. Uhlenbeck: Last fall, there was something similar (...) and there I finished the discussion on hard spheres with a vote. The vote was simply on the

¹⁸This is outlined by W. G. Hoover and F. H. Ree in 1968 on page 3609 in Ref. [124].

¹⁹See conclusion of M. N. Rosenbluth and A. W. Rosenbluth on page 884 in Ref. [156].

matter of your belief in what you have heard, whether a gas of hard spheres has a transition point or not; at Seattle, the vote was even. (...) May I ask first of the panel to put up their hands if they believe there is a transition in the classical case.... Now those who believe there is not a transition.... Even again!

Later during the discussion, J. G. Kirkwood noted, “Well, I think we are all aware that we have to take numerical calculations relating to transitions with a grain of salt.”

As requested, W. G. Hoover and F. H. Ree performed Monte Carlo computer measurements in 1968, “in order to confirm the existence of a first-order melting transition for a classical many-body system of hard spheres and to discover the densities of the coexisting phases” [124]. For an equilibrated system with 12 up to 780 particles, they found a coexistence pressure of about $p_{\text{co}} = 11.70(18)k_{\text{B}}T/\sigma^3$, a Lindemann parameter of $\mathcal{L} = 0.126$, and coexistence bulk densities (volume fractions) of $\rho_{\text{fl,co}}\sigma^3 = 0.943(4)$ ($\eta_{\text{fl,co}} = 0.494(2)$) for the fluid and of $\rho_{\text{fcc,co}}\sigma^3 = 1.041(4)$ ($\eta_{\text{fcc,co}} = 0.545(2)$) for the solid (fcc crystal) phase. Even more, these results are valid till this day.

At the same time, early experiments have been performed on hard spheres in two dimensions: D. Turnbull and R. L. Cormia investigated *A Dynamic Hard Sphere Model* using stain balls on a flat plate [69] (see also Sec. 3.2.2). Moreover, the equation of state and *Statistical Mechanics of Rigid Spheres* have been analyzed for fluid phases by H. Reiss, H. L. Frisch, and J. L. Lebowitz in 1959 [58, 75]. From their scaled particle theory, they extracted the pair distribution function $g(r)$ and the surface tension of a fluid. Even more, the *Equation of State for Nonattracting Rigid Spheres* has been developed by N. F. Carnahan and K. E. Starling [59] from an analysis of the reduced virial series.²⁰

In 1979, T. V. Ramakrishnan and M. Yussouff presented a *First-principles order-parameter theory of freezing* [66]. In 1985, G. L. Jones and U. Mohanty performed a *density functional-variational treatment of the hard sphere transition* [159], including a comparison with simulation results from a review about *Computer Simulations of Freezing and Supercooled Liquids* of D. Frenkel and J. P. McTague [160] and additional theoretical approaches by A. D. J. Haymet [161] and P. Tarazona [162]. In 1990, M. Baus compared “the results obtained for the freezing of hard-core systems” from Refs. [95, 124, 163, 164] in a work about *the present status of the density-functional theory of the liquid-solid transition* [165]. All results predict a phase transition from a fluid bulk density of $\rho_{\text{fl}}\sigma^3 = 0.8917..0.993$ to a (fcc) crystal density of $\rho_{\text{cr}}\sigma^3 = 0.9662..1.083$ and a Lindemann parameter in the range of 0.048..0.145. Moreover, vacancy concentrations have been compared in Ref. [159], but they are much higher than in recent works (see Sec. 4.2.2 or Ref. [146]).

Then, in 1986 the theoretical results concerning the phase transition could be confirmed in experiments by P. N. Pusey and W. van Megen [121]. Using polymethylmethacrylate (PMMA) spheres with radii of $305 \pm 10 \text{ nm}$ (a polydispersity of about 0.03), they measured the *Phase behavior of concentrated suspensions of nearly hard colloidal spheres*, result-

²⁰More details about these theoretical approaches are discussed in Sec. 3.2.3.

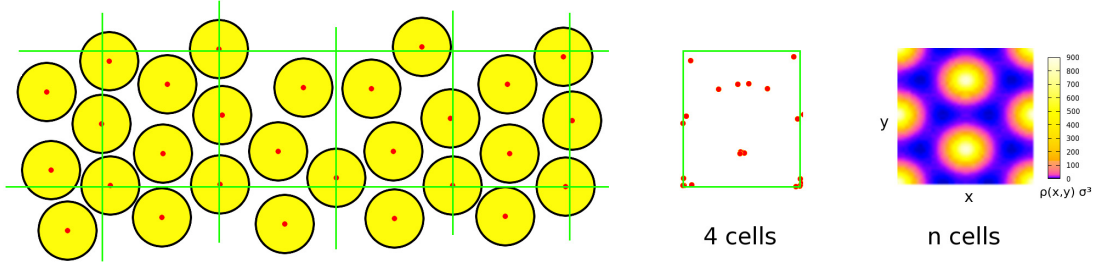


Figure 4.4: Schematic view of a periodic one-particle density (distribution). Left: Single particles in a 2-dimensional system, structured in unit cells that correspond to the periodicity of the whole system. Center: All particle positions of the 4 cells, mapped to one unit cell. Right: The same map as for the 4 cells, but for $n \rightarrow \infty$ cells of an infinitely expanded system, divided by the volume of the total system. Such periodic density distributions are used in DFT.

ing in effective volume fractions²¹ of $\eta_{\text{fl},\text{co}} = 0.494$ for the fluid and of $\eta_{\text{fcc},\text{co}} = 0.536$ for the solid. Moreover, they found glass phases that have fluid-like structure, but mechanical properties of an (amorphous) solid. Showing the colloidal patterns at different volume fractions, the photograph of their experiment is well known and a more accurate version has recently been published in a work about *Hard sphere crystals and glasses* [122].

On the contrary of previous descriptions of the solid hard-sphere phase, R. Ohnesorge et al. performed a free minimization of the density distribution on a cuboid rectangular grid [97,166], similar to that used in this work. However, the (M)WDA approach predicted very small values of the surface tension (see next chapter). In another sense, H. Dong and G. T. Evans analyzed *the freezing transition of a hard sphere fluid subject to the Percus-Yevick approximation*, but they also obtained a Lindemann parameter that in comparison to simulation results is too low.

In 2000, P. Tarazona introduced a *Density Functional for Hard Sphere Crystals: A Fundamental Measure Approach*, improving the original FMT of Y. Rosenfeld [25] that failed to predict the fluid-solid phase transition for hard spheres. Finally, the White Bear version of FMT of R. Roth et al. [113] and the mark II approach from H. Hansen-Goos and R. Roth [27] predict quite accurate values for the fluid-solid phase transition [146] and are discussed in the next section.

4.2.2 Density distributions

As known from Sec. 2.3, particles are described in DFT by one-particle density distributions $\rho(\vec{r})$ that range over the whole volume V of a system. Accordingly, infinitely expanded crystalline lattices and bulk phases are described on volumes, which take the

²¹Done by including a hard-sphere interaction radius of about 20nm, that is roughly the thickness of the stabilizer layer, to achieve the scaling value of $\eta_{\text{fl},\text{co}} = 0.494$.

whole \mathbb{R}^3 . However, periodic density distributions are fully described by their values on one single unit cell (see Sec. 4.1). For this reason, the density profiles ρ are only defined on a subset $V_{\text{uc}} \subset V$ of the total volume, as schematically illustrated in Fig. 4.4.

The fluid phase gives a description of the simplest density distribution, because it has no spatial dependence. Consequently, the system is described by one mean density value ρ_{fl} . On the contrary, a crystalline phase must be described on one or more unit cells, depending on its symmetries. If now density profiles are calculated that minimize the energy of the system, this is done on a given volume V_{uc} that itself again depends on the density. Therefore, either the symmetry must be known during a calculation or the volume V_{uc} must be handled as a free minimization parameter. For example, Fig. 4.10 shows the energies of minimized density profiles for given volumes $V_{\text{uc}} = a^3$, respectively. Apparently, the system results in an equilibrium situation only for a volume V_{uc} that corresponds to the periodicity of the crystalline lattice (for one lattice constant a).

Now, the equation of state in Eq. (2.49) must be solved to achieve a physical density profile of a system in equilibrium. For this purpose, the White Bear version mark II functional from Sec. 3.4.1 is used in the framework of FMT and DFT. Due to the complexity of this functional, analytical solutions can only be obtained for the fluid phase and are given in Sec. B.2. To achieve general solutions, the equation of state must be solved numerically, as outlined in Sec. C.1. At the same time, the chemical potential μ is used as an order parameter of the system. It contains the (irrelevant) thermal wavelength Λ that has no effect on velocity-independent properties of a system in equilibrium, such as those that are investigated in this work. Thus, in this work the chemical potential is used in a shifted form, where the shift $-\log(\Lambda^3/\sigma^3)$ removes the terms that result from the integrals over the translational momenta in the partition sum (see also Sec. 2.2.1).

To apply numerical methods, the density profile $\rho(\vec{r})$ must be parametrized. The most simple parametrization is given by Eq. (4.7), where density peaks are assumed to have a Gaussian form. Moreover, a free minimization (or full minimization) is performed in this work, where the density profile $\rho(\vec{r})$ is parametrized on a cubic rectangular grid consisting of $N_x \times N_y \times N_z$ grid points [74, 97, 146]. This method allows the description of nearly arbitrary density profiles $\rho(\vec{r})$. For example, a typical profile is given in Fig. 4.5, where contour plots of plane cuts through the three-dimensional density are shown. Apparently, a second cut of the contour plots at very low density $\rho\sigma^3 = 0.003$ proves the more explicit structure of the one-particle density $\rho(\vec{r})$: Anisotropies are clearly visible on different scales and for different positions in the unit cell and they depict possible ways of particle movement inside the crystalline structure. So, the most preferred uncertainty in positional ordering seems to be along the nearest neighbour distances inside a face of the unit cell, respectively, or from one face-centered particle to another one (with exception of the opposite face).

Using the Gaussian parametrization in Eq. (4.7), the width α is the only parameter, if the normalization of the density peaks is given. The latter follows from the mean bulk density $\rho\sigma^3$, including vacancies. A minimization of the grand energy of the system results in an equilibrium width parameter α that is shown in Fig. 4.6(a) [146]. Moreover, the results

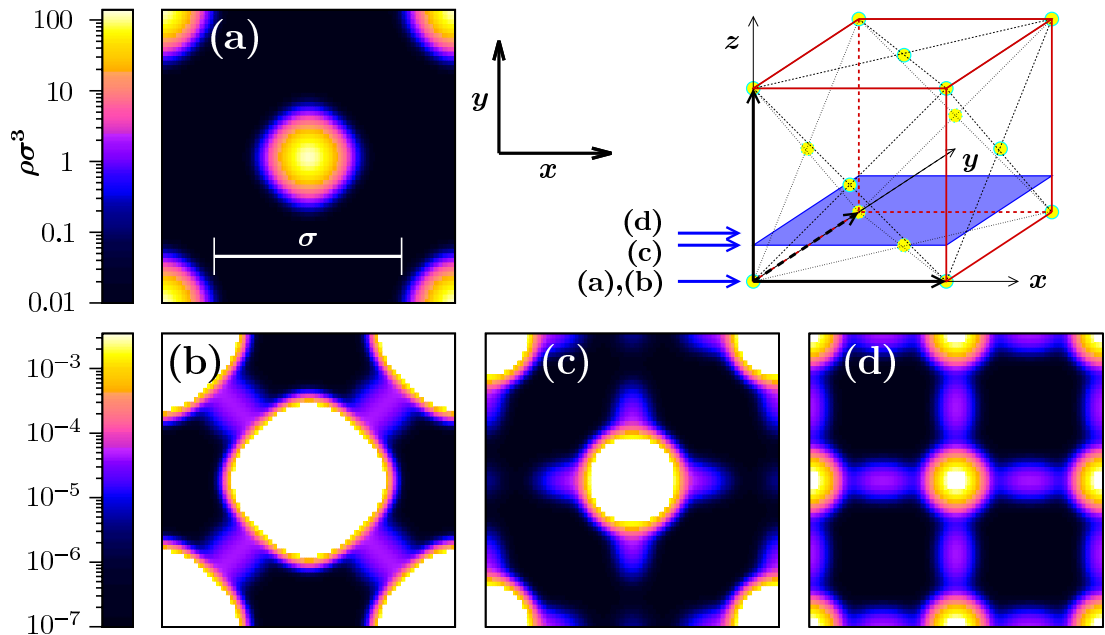


Figure 4.5: (Color) Contour plots of plane cuts through a three-dimensional density distribution of a crystalline hard-sphere fcc phase in equilibrium. The density has been obtained by full minimization on a numerical grid with 64^3 points with a chemical potential of $\mu_{\text{co}} = 16.3787k_{\text{B}}T$. The resulting density distribution has a lattice constant of $a = 1.5671\sigma$, a mean density of $\rho_{\text{fcc,co}}\sigma^3 = 1.0393465(1)$, and a vacancy concentration $n_{\text{vac,co}} = 2.18(1) \times 10^{-5}$. In (a) the full profile at $z/\sigma = 0$ is shown, in (b-d) the profile is cut at a maximal value of $\rho\sigma^3 = 0.003$. The position of the plane cuts is shown schematically in the sketch of a unit cell and positions are (a,b) $z/\sigma = 0$, (c) $z/\sigma = 12/64$, and (d) $z/\sigma = 16/64$.

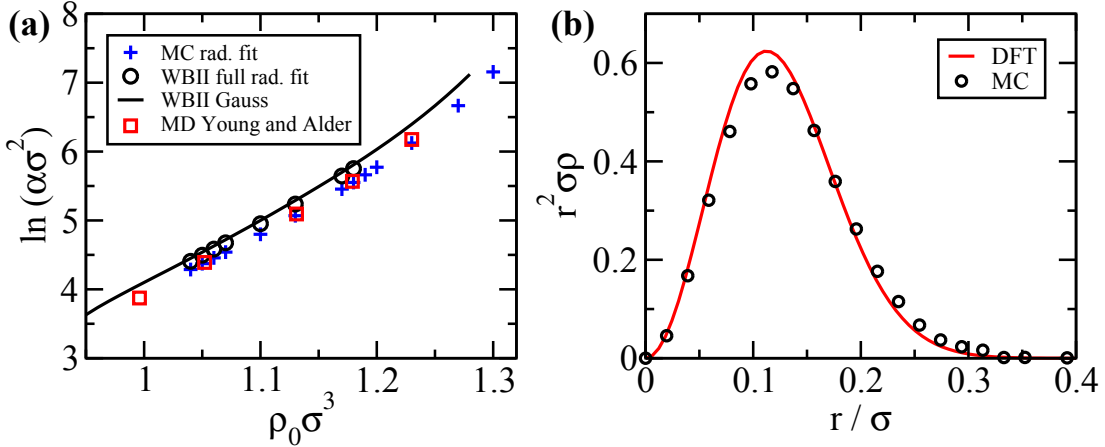


Figure 4.6: (Color) (a): Logarithm of the Gaussian width parameter α vs. bulk density ρ_0 : DFT–WBII in Gaussian approximation (full line), DFT–WBII in full minimization (circles), extrapolation to the thermodynamic limit in MC (+ symbols) and results from Ref. [167] (squares). (b): radial probability $r^2\rho(r)$ in [100] direction for the bulk density $\rho_0\sigma^3 = 1.04$. Comparison between DFT and MC simulations. This figure is reprinted with permission from Ref. [146] by M. Oettel et al. ©2010, The American Physical Society.

from a Gaussian parametrization are compared to data, extracted from a full minimization of the density profile, to Monte Carlo simulation results from S. Görig, M. Radu, and T. Schilling, and to Molecular Dynamics simulation results from D. A. Young and B. J. Alder [167]. In all cases, the Gaussian width parameter is extracted by a global fit with Eq. (4.7). Furthermore, the MC simulation results are given in the thermodynamic limit that is extracted from values at finite box length.²² Figure 4.6(b) shows a comparison of the radial probability $r^2\rho(r)$ along the [100] direction between DFT and MC results.

The Gaussian form Eq. (4.7) only states an approximation to the real form of a crystalline density peak. In principle, there are two effects that cause this deviation. First, a real density profile can be more localized or less localized around one crystalline lattice position. This amount of localization of the distribution around one peak is called *kurtosis* and its deviation from the Gaussian form can be measured by using Eq. (4.9), especially by the leading term b_4 . Second, the radial distribution of a single peak depends on its angular direction and this anisotropy can be measured by using Eq. (4.10). Both deviations are analyzed in Fig. 4.7 for a mean bulk density of $\rho_0\sigma^3 = 1.04$ near fluid-solid phase coexistence, comparing MC results (panels a,b) and DFT free minimization results (panels c,d). In addition, the same figure is also given for a bulk density of $\rho_0\sigma^3 = 1.20$ in Ref. [146].

Following Ref. [146], a comparison between different bulk densities states that the kurtosis (panels a,c in Fig. 4.7) is higher for DFT results than for a corresponding Gaussian peak for all bulk densities, while this behavior depends on density for MC simulations.²³

²²For further information, see works of M. Oettel et al [146] and of D. A. Young and B. J. Alder [167].

²³For $\rho\sigma^3 = 1.20$, the kurtosis is smaller for MC results than for a corresponding Gaussian form [146].

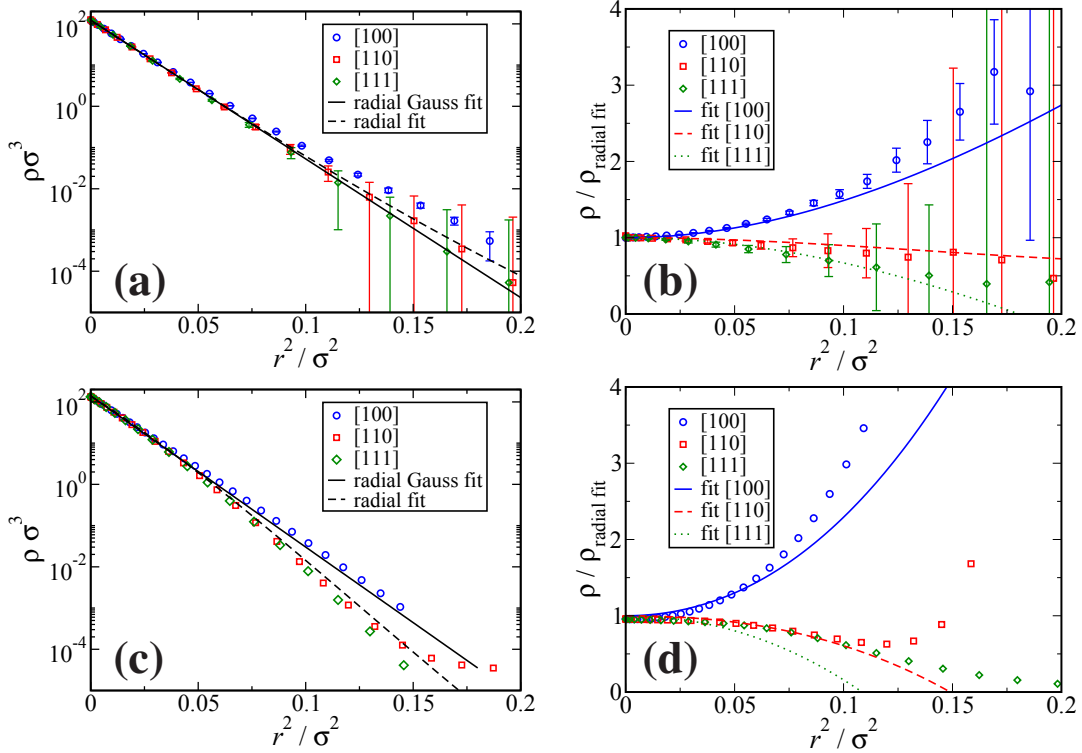


Figure 4.7: (Color) Density distributions at a bulk density $\rho_0 \sigma^3 = 1.04$ around a lattice position along the lattice directions [100], [110], and [111]. Panels (a) and (b) show MC results ($N = 8788$), panels (c) and (d) results from DFT–WBII. In panels (a) and (c) the density ρ is shown vs. r^2 in logarithmic scale, thus illustrating the deviation from a Gaussian form (straight line). Here, the full line is a fit to the Gaussian form ρ_G (Eq. 4.7) with parameter $\alpha = 77.5$ (MC) and $\alpha = 84.4$ (DFT–WBII). The dashed line is a fit to the non-Gaussian form $\rho_G f_{\Delta G}$ (Eq. 4.9) with parameters $b_2 = -0.011$, $b_4 = 0.0021$, $b_6 = -0.0002$ (MC) and $b_2 = 0.090$, $b_4 = -0.029$, $b_6 = 0.0009$ (DFT–WBII). In panels (b) and (d) the density is shown along the three lattice directions relative to the radial fit $\rho_{\text{radial fit}} = \rho_G f_{\Delta G}$. Here, the corresponding anisotropies along the three lattice directions are clarified that result from a fit by f_{aniso} (Eq. 4.10) with parameter $K_4 = 0.022$ (MC) and $K_4 = 0.039$ (DFT–WBII). This figure is reprinted with permission from Ref. [146] ©2010, The American Physical Society.

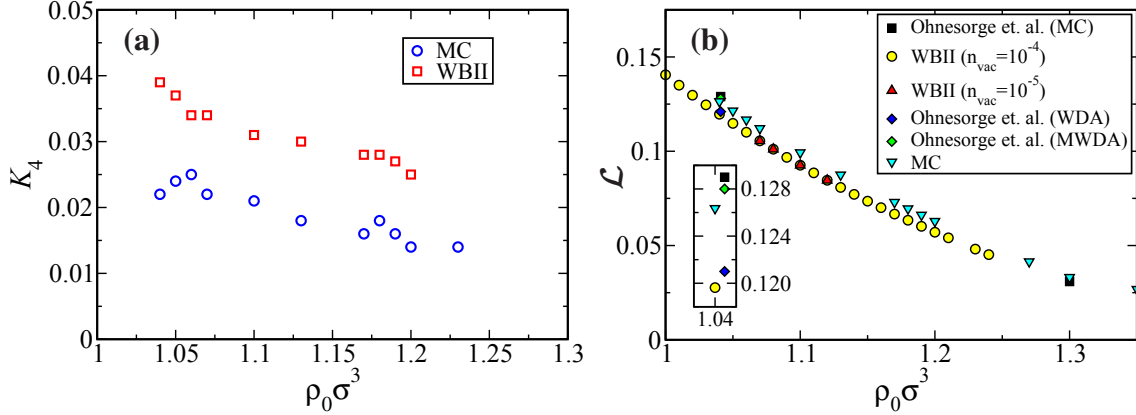


Figure 4.8: (Color) (a): Leading anisotropy coefficient K_4 vs. bulk density ρ_0 as obtained from a fit to the density distributions from MC simulations (circles) and from DFT-WBII (squares). (b): Lindemann parameter \mathcal{L} vs. bulk density ρ_0 for Monte Carlo simulation (MC) and DFT, also in comparison with Ref. [166] (Ohnesorge et al.). Results for (M)WDA from Ref. [166] are achieved by full minimization. This figure is reprinted with permission from Ref. [146] ©2010, The American Physical Society.

Though, the parameter b_4 from Eq. (4.9) changes sign at a density of about $\rho_0 \sigma^3 = 1.10$, as mentioned in Ref. [146]. Concerning the anisotropies, shown in panels (b,d), the trends are similar for MC simulations (panel b) and DFT results (panel d); only the magnitude of the leading anisotropy coefficient K_4 is larger in DFT by a factor of 1.7, as mentioned in Ref. [146].

The leading anisotropy parameter K_4 is shown in Fig. 4.8(a) for given bulk densities. Ignoring the spread in data due to the fitting process, the trend of decreasing parameter K_4 for increasing density is consistent with the observation that density peaks become Gaussian ones ($K_4 = 0$) next to close packing [167].

The Lindemann parameter \mathcal{L} , as defined in Eq. (4.11), is shown in Fig. 4.8(b) for several bulk densities and for fixed vacancy concentrations of $n_{\text{vac}} = 10^{-4}$ and $n_{\text{vac}} = 10^{-5}$, comparing DFT results and MC simulation data from M. Oettel et al. [146] to MC results [166] and to (M)WDA results [166] from R. Ohnesorge and co-workers. Apparently, the Lindemann parameter is about $\mathcal{L} = 0.13$ at the melting density $\rho \sigma^3 = 1.04$ and decreases with increasing bulk density. In other words, the density distribution becomes more localized for higher bulk densities ρ . However, re-calling the quotation on page 46, the Lindemann parameter has a slightly higher value than mentioned in the work of T. V. Ramakrishnan and M. Yussouff [66].

Finally, an analysis of the vacancy concentration n_{vac} , as defined in Eq. (4.6), is given in Fig. 4.9, taken from Ref. [146]. The analysis is performed for DFT results, using three different density functionals, and for simulation results from S. K. Kwak et al. [149] and from C. H. Bennet and B. J. Alder [147]. In comparison to simulation results, vacancy

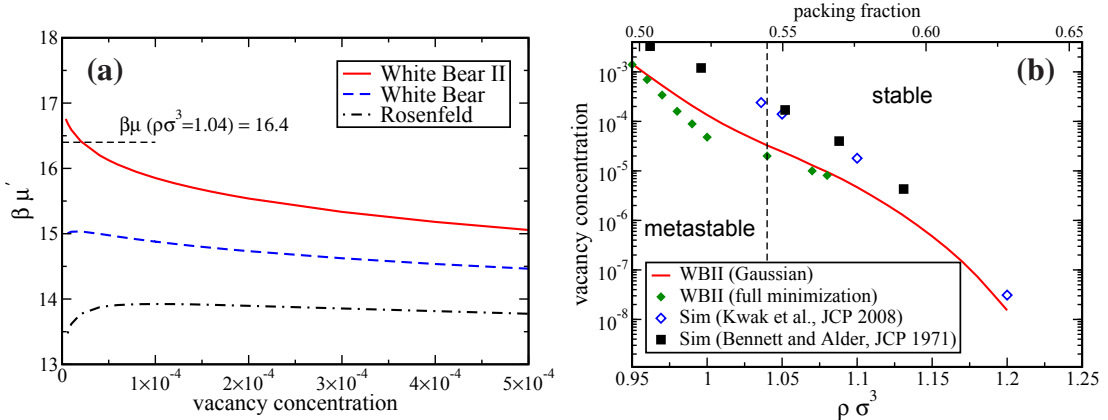


Figure 4.9: (Color) (a): The constrained chemical potential $\mu'(\rho_0, n_{\text{vac}})$ as obtained by full minimization of the three DFT models at the bulk density $\rho_0\sigma^3 = 1.04$. The dashed line shows the value for the chemical potential following from the thermodynamic definition of $\mu = df_{\text{cr}}/d\rho_0$ where f_{cr} is the free energy density. It is equal for the three DFT models to the given accuracy. If and only if $\mu'(\rho_0, n_{\text{vac}}) = \mu$, the free energy per particle is minimal and thus thermodynamic consistency holds. (b): Equilibrium vacancy concentration vs. bulk density as obtained for the White Bear mark II functional (full line—Gaussian approximation, filled diamonds—full minimization) and compared to available simulation results (open diamonds—Ref. [149], filled squares—Ref. [147]). This figure is reprinted with permission from Ref. [146] ©2010, The American Physical Society.

concentrations are smaller for DFT results, which matches more localized density peaks in DFT calculations. As expected, the vacancy densities decrease for increasing bulk density.

4.2.3 The crystal-fluid phase transition

The phase diagram of a monodisperse system of hard spheres is shown in Fig. 4.1 for vanishing polydispersity $\delta = 0$. Though, every point of the phase diagram corresponds to system states in equilibrium, having minimal energy and fulfilling the constraints that are given by the phase diagram. Thus, the phase transition occurs at that point, where the energies Ω_{fl} and Ω_{cr} of the fluid and of the crystalline phase are equal.

Now, calculations are applied by using the White Bear version mark II of FMT. Thus, the energy Ω_{fl} of the fluid phase is given by Eq. (2.38) and by the Carnahan-Starling free energy in Eq. (3.15).²⁴ The grand energy $\Omega_{\text{fl}}(\mu)$ of the fluid phase can be obtained (numerically) as a function of the chemical potential, using the fundamental equation of state (2.42) of DFT.

²⁴Also see Fig. 3.2 in the context of the Carnahan-Starling equation of state.

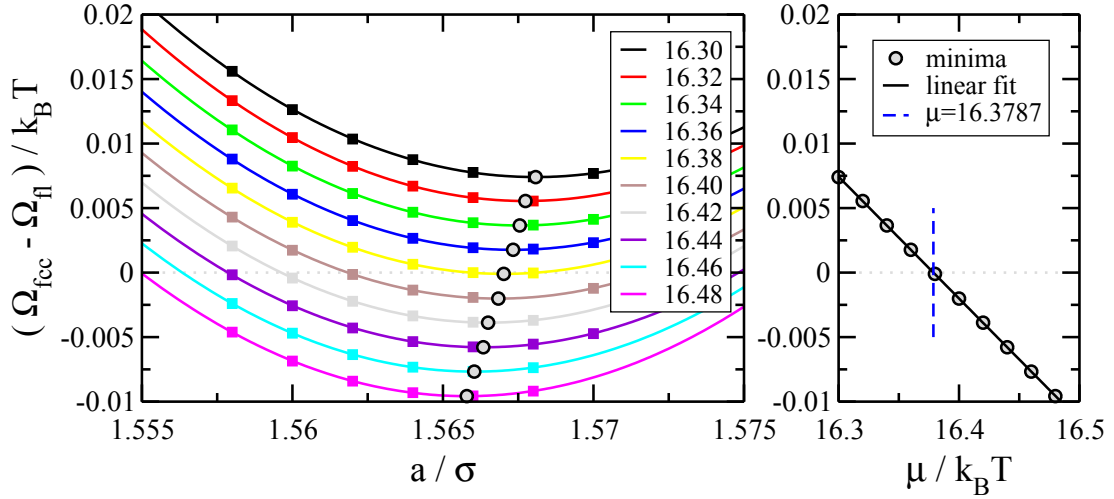


Figure 4.10: (Color) Phase coexistence results for the hard-sphere fcc and fluid phase. In the left plot, squares give the grand energy difference between a fcc phase with a lattice constant a and a corresponding fluid phase at the same chemical potential $\mu/k_B T$ that is shown in the legend of the plot. Moreover, the lines are parabolic fits ($y = a_0(x-a_1)^2+a_2$) and their minima are marked by circles. In the right plot, the minima from the left plot are shown in combination with a linear fit. Accordingly, the zero-crossing value gives the coexistence chemical potential $\mu/k_B T = 16.3787$.

At the same time, crystalline equilibrium density profiles must be generated to obtain similar results for the crystalline phase. The simplest method is the parametrization of the density profile, for example with the Gaussian form in Eq. (4.7). Resulting energies are listed in Table I of Ref. [146], in comparison to results from MC simulations and from free minimization. To obtain the latter, an initial guess is iterated numerically to an equilibrium situation, using numerical methods from Sec. C.1. Since this guess already contains the crystalline structure, knowledge of the crystal is necessary a priori; testing all possible structures does not seem to be a useful option. Hence, the fcc structure is chosen in this work, since it is known as most stable structure from Sec. 4.1.3.

However, the lattice constant is generally unknown for a given chemical potential. Accordingly, a minimization is necessary with respect to the lattice constant or the volume of the unit cell, respectively. Such minimizations are shown in Fig. 4.10 for the White Bear II (WBII) functional and in Fig. 4.11 for the Ramakrishnan-Yussouff (RY) approach from Sec. 3.3. Here, the energy of the corresponding fluid phase is already subtracted, since it is independent from the lattice constant a .

Now, the coexistence chemical potential can be obtained as illustrated in the right panel of Fig. 4.10 and Fig. 4.11. It follows with $\mu_{\text{co}}/k_B T = 16.3787$ (WBII) and $\mu_{\text{co}}/k_B T = 21.5070$ (RY). A calculation with this chemical potential yields a lattice constant $a_{\text{co}} = 1.5671\sigma$ (WBII) and $a_{\text{co}} = 1.47845\sigma$ (RY) and a coexistence pressure of $p_{\text{co}} = 11.86760(3)k_B T/\sigma^3$ (WBII) and $p_{\text{co}} = 16.92013(3)k_B T/\sigma^3$ (RY); the coexistence

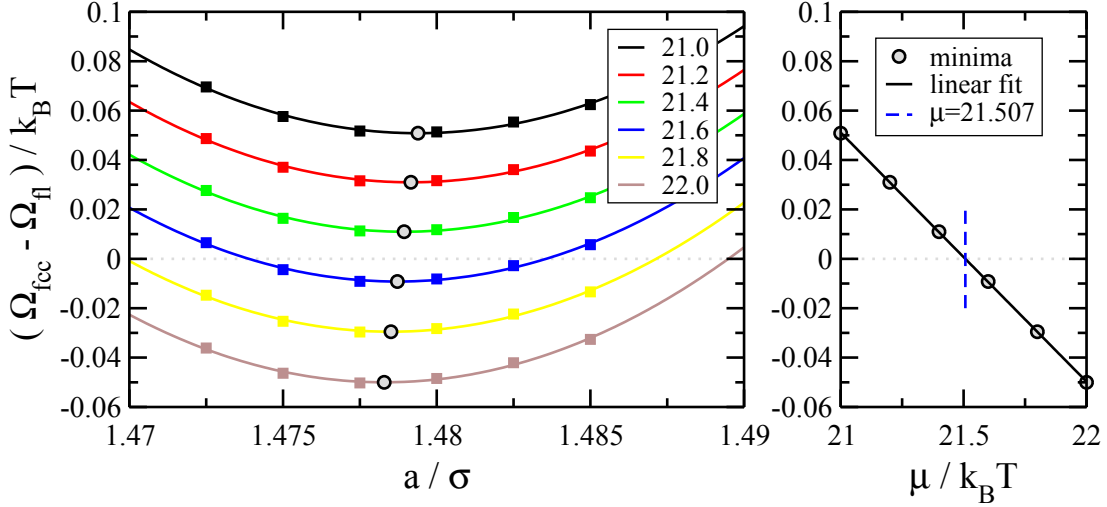


Figure 4.11: (Color) Phase coexistence results for the hard-sphere fcc and fluid phase using the Ramakrishnan-Yussouff functional. In the left plot, squares give the grand energy difference between a fcc phase (lattice constant a) and a corresponding fluid phase at the same chemical potential $\mu/k_B T$ that is shown in the legend of the plot. Moreover, the lines are parabolic fits ($y = a_0(x-a_1)^2 + a_2$) and their minima are marked by circles. In the right plot, the minima from the left plot are shown in combination with a linear fit. Accordingly, the zero-crossing value gives the coexistence chemical potential $\mu/k_B T = 21.507$.

densities (and volume fractions) read $\rho_{\text{fcc},\text{co}}\sigma^3 = 1.0393465(1)$ ($\eta_{\text{fcc},\text{co}} = 0.5442006$) and $\rho_{\text{fl},\text{co}}\sigma^3 = 0.9451061$ ($\eta_{\text{fl},\text{co}} = 0.4948564$) (WBII), and $\rho_{\text{fcc},\text{co}}\sigma^3 = 1.1225767(1)$ ($\eta_{\text{fcc},\text{co}} = 0.5877798$) and $\rho_{\text{fl},\text{co}}\sigma^3 = 1.0213797$ ($\eta_{\text{fl},\text{co}} = 0.5347931$) (RY). Consequently, the vacancy density in the fcc phase follows with $n_{\text{vac},\text{co}} = 2.18(1) \times 10^{-5}$ (WBII) and $n_{\text{vac},\text{co}} = 0.0930(1)$ (RY).²⁵

In addition, the results are collected in Table 4.2 that is partly re-printed from Table I in Ref. [146] by M. Oettel and co-workers. Moreover, a comparison is drawn between several functional approaches and recent MC computer simulations of T. Zykova-Timan et al. [73]. Further coexistence values can be found in Table 2 of Ref. [159] by G. L. Jones and U. Mohanty, in Table I of Ref. [165] by M. Baus, and in Table I of Ref. [29] by R. Roth, where additional results are listed comparatively.

4.2.4 Polydispersity

Following P. N. Pusey and W. van Megen, W. C. K. Poon et al. mention in a work *On measuring colloidal volume fractions* [168] (see also Ref. [169]) that the

determination of (the volume fraction) ϕ is emphatically not unproblematic, because: (1) no real colloid is truly 'hard', since there is always some softness

²⁵For details about calculations see Sec. C.1.6.

Table 4.2: Coexisting fluid (ρ_{fl}) and crystal (ρ_{cr}) densities (the corresponding packing fractions are given in brackets), as well as the chemical potential μ_{co} and the pressure p_{co} at coexistence for the investigated DFT models in Ref. [146] and in this work. Here, RF is the tensor modified Rosenfeld functional, WB is the tensor modified White Bear functional, and WBII is the tensor modified White Bear II functional (the functionals are listed in Sec. 3.4.1 and the tensor modification in Eq. 3.54 has been used). RY is the Ramakrishnan-Yussouff approach with the direct correlation functions of the White Bear II functional, as mentioned in Sec. 3.4.2. The MC results are taken from Ref. [73]. In order to obtain numbers, $\Lambda = \sigma$ has been used for the thermal de Broglie wavelength. This table is partly re-printed from Ref. [146].

	$\rho_{\text{fl}}\sigma^3$ (η_{fl})	$\rho_{\text{cr}}\sigma^3$ (η_{cr})	$\beta\mu_{\text{co}}$	$\beta p_{\text{co}}\sigma^3$
RF	0.892 (0.467)	0.984 (0.515)	14.42	9.92
WB	0.934 (0.489)	1.022 (0.535)	15.75	11.28
WBII	0.945 (0.495)	1.039 (0.544)	16.38	11.867
RY	1.021 (0.535)	1.123 (0.588)	21.51	16.92
MC	0.940 (0.492)	1.041 (0.545)		11.576

in the interparticle potential; and (2) real colloids always have a finite size distribution, i.e. they are polydisperse.

Likewise, R. Kurita and E. R. Weeks discussed this problems carefully in a work about *measuring every particle's size from three-dimensional imaging experiments* [170].

Accordingly, the effect of polydispersity on a hard-sphere model system has been investigated for years. Detailed references are discussed in the works of S.-E. Phan et al. [171] and of M. Fasolo and P. Sollich [65] about the *effects of polydispersity on hard sphere crystals* and about the *equilibrium phase behavior of polydisperse hard spheres*. In this context, P. G. Bolhuis and D. A. Kofke [172] mention:

Pusey [121] performed experiments in which he observed that dispersions with a polydispersity of 7.5% would (partly) freeze, while those with a polydispersity of 12% did not.

Moreover, R. McRae and A. D. J. Haymet analyzed the *Freezing of polydisperse hard spheres* with DFT methods [173]. In general, this analysis is possible when using a set of density distributions ρ_σ that differ in the diameter of the hard spheres. Similarly, the density distribution can be extended with a particle-size distribution function $f(\sigma)$. Applying this concept to FMT, the function f enters the equation of state (2.42) and only additional numerical integrations of the product between weight functions $w^{(\alpha)}$ and $f(\sigma)$ are necessary with respect to the particle size.²⁶

To allow theoretical description, “the width of the diameter distribution can be characterized by a polydispersity parameter δ , defined as the standard deviation of the size distri-

²⁶The particle-size distribution only enters the free energy functional. With respect to Eq. (3.63), the equation of state follows with $\mu_\sigma = \ln(\rho) - k_B T c^{(1)}[\rho; \vec{r}]$.

bution divided by its mean” [65]. Accordingly, it reads

$$\delta = \frac{\sqrt{\langle \sigma^2 \rangle - \langle \sigma \rangle^2}}{\langle \sigma \rangle}. \quad (4.12)$$

A sketch of the corresponding phase diagram of polydisperse hard spheres is shown in Fig. 4.1. Detailed results are given by M. Fasolo and P. Sollich in a work about the *Equilibrium Phase Behavior of Polydisperse Hard Spheres* [65] and the phase diagram is discussed in a recent work about *Polydispersity induced solid-solid transitions in model colloids* by P. Sollich and N. B. Wilding [174].

4.3 Conclusion

In conclusion, free energies and density distributions of the hard-sphere system have been obtained for the (fcc) crystal and fluid phase by applying FMT functionals. The free energies are in good agreement with Monte Carlo (MC) simulation results and demonstrate the applicability of the functionals to the treatment of other problems involving crystallization. Moreover, the agreement between FMT and simulations on the level of the free energies is also reflected in the density distributions around single lattice sites. While the peak widths and anisotropic shapes for different lattice directions agree, it is found that FMT gives slightly narrower peaks with more anisotropy than seen in the simulations. In addition to this, from the studied variants of FMT only the White Bear mark II (WBII) functional shows qualitative correct behavior, whereas the Rosenfeld and the White Bear functional give qualitative incorrect results. This implies that only the WBII functional is a promising candidate for further studies, such as the free minimization of the crystal-fluid interface or nucleation processes.

However, the deviations that have been observed between simulation and FMT results point to possibilities of further improvement in the FMT functionals. Tarazona’s construction of the tensor part of these functionals is an approximate representation of the three-cavity overlap situation which leads to a complicated expression. It would be interesting to study the close-packing limit of this expression in a systematic manner. In this sense, a promising ansatz is given by re-summing the virial expansion to obtain the Rosenfeld functional as the first order term [110, 111].

5

The crystal-fluid interface

Dixit quoque Deus
fiat firmamentum in medio aquarum
et dividat aquas ab aquis.

(*The bible, Genesis 1,6*)

Solidification and melting processes involve crystal-fluid interfaces that separate the disordered from the ordered phase. Understanding the properties of such interfaces on a microscopic scale is pivotal to control and optimize crystal nucleation and the emerging microstructure of the material. Important applications include the fabrication of defect-free metallic alloys [175] and of photonic [176], phononic [177], and protein [178] crystals. In equilibrium, i.e. between a coexisting crystal and fluid phase, creating a crystal-fluid interface results in a free energy penalty per area which is called interfacial tension. Unlike the liquid-gas or fluid-fluid interface, the structure of the solid-fluid interface depends on its orientation [179]. This anisotropy is associated with a difference between the interfacial tension and the interfacial stiffness of a crystalline surface.

Predicting crystal-fluid interfacial tensions by a molecular theory is a very challenging task. Classical density functional theory of freezing provides a unifying framework to describe the solid and liquid on the same footing and in principle, it is a promising tool. In this respect, the simple athermal hard sphere system which exhibits a freezing transition from a fluid into a face-centered-cubic (fcc) crystal, is an important reference and benchmark system [180, 181]. The accuracy of previous density functional calculations of the hard sphere solid-fluid interface [97, 182–184], however, was hampered by the lack of knowledge of a reliable functional and severe restrictions in the parametrization of the trial density profile (see Fig. 5.1). Thus, U. Gasser reviewed the “recent progress in the study of homogeneous and heterogeneous crystal nucleation in colloids and the controlled growth of crystalline colloidal structures” [185] that “is also relevant for a deeper understanding of soft matter materials in general as well as for possible applications based on colloidal suspensions.”

In this chapter, interfacial tensions and stiffnesses of the equilibrium hard-sphere crystal-fluid interface are predicted by using the fundamental measure density functional theory [27] that is introduced in Sec. 3.4, which has been shown to predict accurate bulk freezing data in Sec. 4.2 [146]. The interfacial tension and stiffness for five different orientations are obtained, namely along the (001), (011), (111), (012), and (112) orientations (see Fig. 5.3). Moreover, Monte Carlo simulations have been conducted to extract the stiffness from capillary wave fluctuations for the above mentioned orientations, except (012). Thereby, the accuracy of earlier data [72, 186–191] is improved. The history of the interfacial tension is sketched in Fig. 5.1.

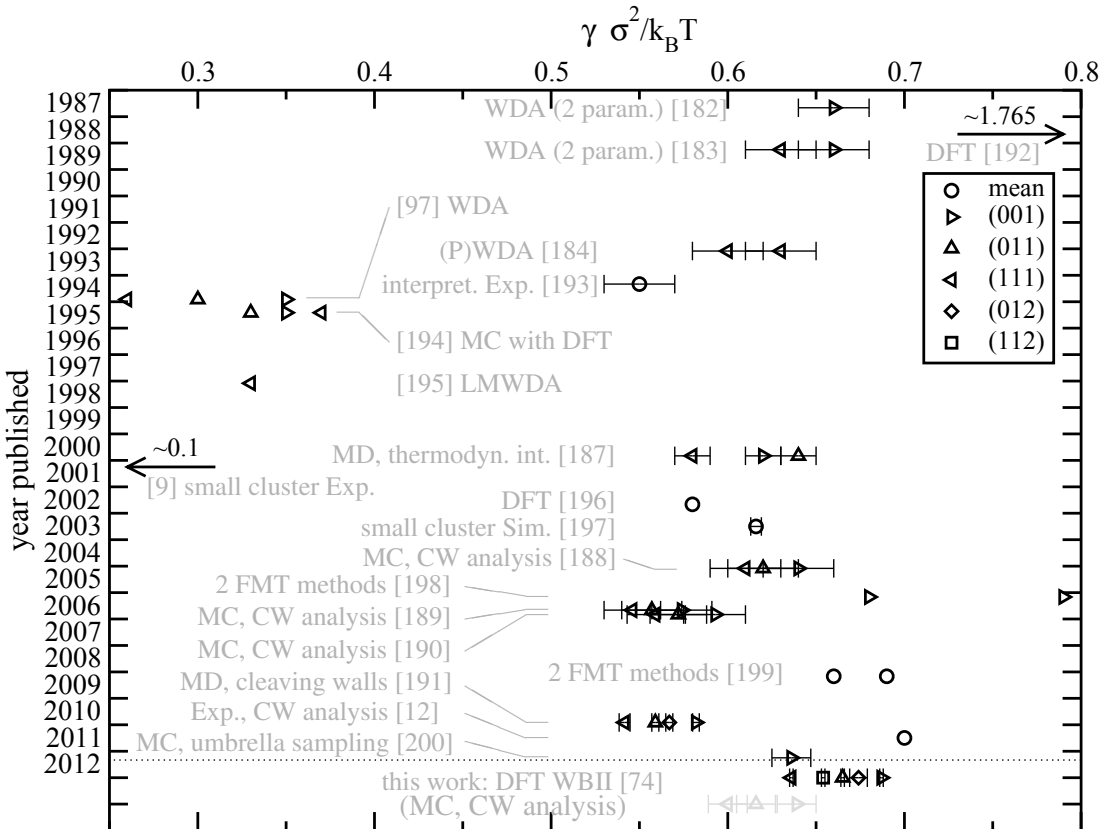


Figure 5.1: Selected interfacial tensions presented against the date (month and year), the containing work has been published. If no error bars are shown, the errors have not been available. The dotted line marks May 2012, when Ref. [74] by A. Härtel et al. has been published. The related Monte Carlo (MC) simulation results have been applied via capillary wave analysis (CW), using the expansion in Eq. (5.3).

This chapter mostly is a revised version of the work *Tension and stiffness of the hard sphere crystal-fluid interface* [74] ©2012, The American physical Society. First, interfaces and their theoretical descriptions are discussed, including definitions for the tension and the stiffness. In Sec. 5.2, calculations in theory and simulation are explained and discussed, as well as the analysis of resulting data. In addition, experimental results are analyzed using classical nucleation theory. Then, interfacial tensions and stiffnesses, as obtained in this work, are discussed in Sec. 5.3 and are compared to existing results, as shown in Fig. 5.1. Finally, conclusions regarding this chapter are outlined in Sec. 5.4.

5.1 Theoretical description of interfaces

Interfaces are very common and can be found everywhere in our live. For example, the interface between water and air occurs in a glass of drinking water as well as in form of

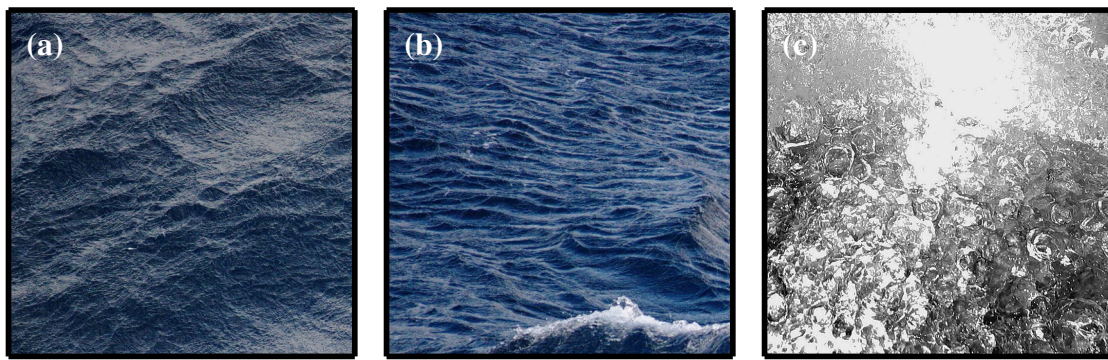


Figure 5.2: (Color) Liquid-air interfaces in nature of (a,b) the Mediterranean Sea and of (c) boiling nitrogen. Both interfaces exist due to the gravitational field of earth. In (a,b), surface waves can be seen on several length scales (partly due to external forces, like wind). In (c), the liquid-air surface is disturbed by gaseous nitrogen bubbles that form because the system is not in equilibrium. However, the structure of the surface depends on the tension of the interface, while considering all external effects.

the rough surface of the sea on a windy day, as shown in Fig. 5.2(a,b). Interfaces are often curved and separate droplets as well as clusters from the surrounding phase, for instance gas bubbles in a liquid phase or nuclei in a melt (i.e. of metals). In this case, both phases that are separated by the interface are of the same material, where the liquid-air interfaces that are shown in Fig. 5.2 are not.

The knowledge about the properties of interfaces is of great relevance to understand the processes of freezing and melting that are necessary for the production of solid workpieces like motors, turbines, screws, or steel beams. In such processes, the solids are made by solidification from melted material (often metallic alloys). To obtain pure and defect-free materials, detailed knowledge about energy barriers and phase transitions of the used materials is important.

Interfaces separate two phases from each other and, in particular, the crystal-fluid interface separates the ordered from the disordered phase. In general, an interface is an area with a certain thickness that stores an amount of energy per area (of the interface), called interfacial tension.¹ Even if the involved bulk phases usually have a lower energy than the coexisting phases that are separated by the interface, the interface can be stable, because breaking it up needs to overcome an energy barrier. Moreover, both involved phases admix in the interface in a certain way. As shown in Fig. 5.2, waves and oscillations are existing inside and along the interface, due to external forces (like wind) and temperature. These waves are called capillary waves (CW) and they are provide a measure for the stiffness of the interface.

In equilibrium, the principle of minimizing the energy of a system also causes the interfacial tension to be minimal. For example, this principle leads to the occurrence of a meniscus, if water is filled in a glass, and is responsible to the round shape of soap bub-

¹For definitions, see for example chapter II of the textbook by A. W. Adamson and A. P. Gast [201].

bles. Unlike the liquid-gas or fluid-fluid interface, the structure of the solid-fluid interface depends on its orientation [179], which i.e. leads to the existence of surface facets of crystals. This anisotropy is associated with a difference between the interfacial tension and the interfacial stiffness of a crystalline surface.

Typically, the surface tension is shown in so-called γ -plots or Wulff plots [179, 202], as given for the hard-sphere crystal(fcc)-fluid interface in Fig. 5.3. Moreover, the resulting surface structure of clusters or interfaces can be obtained by a Wulff construction, where minima in the γ -plot (with respect to the orientation of the surface) are used to construct surface facets [179]. In addition, the surface tension of small droplets is related to the Tolman length [203], “a quantity related to the curvature dependence of the interface free energy” [204].²

As known from previous chapters, the athermal hard sphere model in equilibrium is solely characterized by the volume fraction ϕ and the thermal energy $k_B T$ just sets the energy scale. The fluid-solid(fcc) freezing transition is first-order with coexisting fluid and solid volume fractions of $\phi_f = 0.492$ and $\phi_s = 0.545$, respectively, and a coexistence pressure of $p_c = 11.576 k_B T / \sigma^3$ [73]. For a given volume V that contains coexisting bulk fluid and solid phases, and a planar fluid-solid interface of area A , the excess grand free energy per area is the surface or interface tension, given by

$$\gamma = \frac{\Omega + pV}{A}, \quad (5.1)$$

where Ω is the grand-canonical free energy. For crystal-fluid interfaces, γ depends on the orientation of the interface, characterized by a normal unit vector \hat{n} relative to the crystal lattice. The latter is fixed with the fcc cubic unit cell edges parallel to the Cartesian coordinate axes of the system.³ Additionally, it should be mentioned that the volume V contains two interfaces, due to the periodic boundary conditions.

The central quantity to describe thermal fluctuations, i.e. capillary waves, along the anisotropic crystal-fluid interface, is the interfacial stiffness, defined tensorially [205] as

$$\bar{\gamma}_{\alpha\beta}(\hat{n}) = \gamma(\hat{n}) + \frac{\partial^2 \gamma(\hat{n})}{\partial \hat{n}_\alpha \partial \hat{n}_\beta} \quad (5.2)$$

for two directions \hat{n}_α and \hat{n}_β that are orthogonal to \hat{n} . In some sense, the amount of capillary waves also defines an interfacial width. However, this definition is problematic, because the structure of the interface in general depends on the extent of the system and diverges for infinite extended interfaces.

To compare tensions and stiffnesses, the orientationally resolved interfacial tension can be well-fitted by a cubic harmonic expansion [67, 206]. If the anisotropy in the tension is

²The Tolman length enters, for example, in classical nucleation theory (CNT), where small clusters are of interest.

³See Fig. 5.3, Table 4.1 in Sec. 4.1.2, and Sec. A.3 about the construction of rotated unit cells.

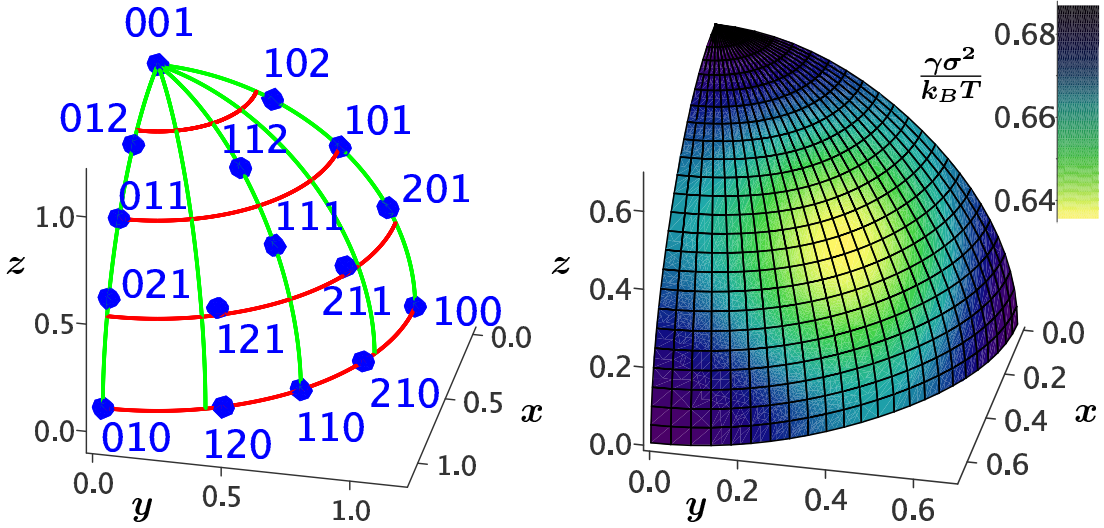


Figure 5.3: (Color) In the left panel, the surface orientations, such as listed in Table 5.1, are indicated on an octant of the unit sphere. The right panel shows a Wulff plot of the corresponding interfacial tension $\gamma(\hat{n})$; here, the colors display the value of the tension for a given orientation. This figure is reprinted with permission from Ref. [74] ©2012, The American Physical Society.

weak, the expansion reads

$$\begin{aligned} \frac{\gamma(\hat{n})}{\gamma_0} = & 1 + \epsilon_1 \left(Q - \frac{3}{5} \right) + \epsilon_2 \left(3Q + 66S - \frac{17}{7} \right) \\ & + \epsilon_3 \left(5Q^2 - 16S - \frac{94}{13}Q + \frac{33}{13} \right) \end{aligned} \quad (5.3)$$

with $\hat{n} = (n_1, n_2, n_3)$, $Q = n_1^4 + n_2^4 + n_3^4$, $S = n_1^2 n_2^2 n_3^2$ and four fit parameters γ_0 , ϵ_1 , ϵ_2 , and ϵ_3 . Now, the expansion (5.3) can be used to obtain the interfacial stiffness (5.2) from the DFT data of the anisotropic interfacial tension [67, 73], as listed in Table 5.1. The resulting anisotropy of the stiffness is considerably larger than the one of the tension (thus, the resulting errors of $\bar{\gamma}_{\alpha\beta}(\hat{n})$ are also larger). For the five considered orientations in this work, the resulting data for the interfacial stiffness and for the fit parameters are also listed in Table 5.1.

Starting from the tensions $\gamma(n_\alpha) \pm \gamma^{\text{err}}(n_\alpha)$ for α being one of the five directions of interest, the four parameters γ_0 , ϵ_1 , ϵ_2 , and ϵ_3 have been determined via a least-squares fit with Eq. (5.3) for all combinations of $\gamma(n_\alpha) - \gamma^{\text{err}}(n_\alpha)$, $\gamma(n_\alpha)$, and $\gamma(n_\alpha) + \gamma^{\text{err}}(n_\alpha)$. From the set of all resulting $(\gamma_0, \epsilon_1, \epsilon_2, \epsilon_3)_i$, $i \in [1, \dots, m]$, the stiffness for a certain tangential

direction β has been determined as $\bar{\gamma}_{\beta\beta}(n_\alpha) \pm \bar{\gamma}_{\beta\beta}^{\text{err}}(n_\alpha)$, respectively, where

$$\bar{\gamma}_{\beta\beta}(n_\alpha) = \frac{1}{m} \sum_{i=1}^m [\bar{\gamma}_{\beta\beta}(n_\alpha)] ((\gamma_0, \epsilon_1, \epsilon_2, \epsilon_3)_i), \quad (5.4)$$

$$\bar{\gamma}_{\beta\beta}(n_\alpha) - \bar{\gamma}_{\beta\beta}^{\text{err}}(n_\alpha) = \min_i [\bar{\gamma}_{\beta\beta}(n_\alpha)] ((\gamma_0, \epsilon_1, \epsilon_2, \epsilon_3)_i), \quad (5.5)$$

$$\bar{\gamma}_{\beta\beta}(n_\alpha) + \bar{\gamma}_{\beta\beta}^{\text{err}}(n_\alpha) = \max_i [\bar{\gamma}_{\beta\beta}(n_\alpha)] ((\gamma_0, \epsilon_1, \epsilon_2, \epsilon_3)_i). \quad (5.6)$$

Similarly, starting from the stiffnesses, the four parameters have been determined via a minimization of

$$\sum_{\alpha, \beta} \left(\bar{\gamma}_{\beta\beta}(n_\alpha) - [\bar{\gamma}_{\beta\beta}(n_\alpha)] ((\gamma_0, \epsilon_1, \epsilon_2, \epsilon_3)_i) \right)^2, \quad (5.7)$$

again for all combinations of $\bar{\gamma}_{\beta\beta}(n_\alpha) - \bar{\gamma}_{\beta\beta}^{\text{err}}(n_\alpha)$, $\bar{\gamma}_{\beta\beta}(n_\alpha)$, and $\bar{\gamma}_{\beta\beta}(n_\alpha) + \bar{\gamma}_{\beta\beta}^{\text{err}}(n_\alpha)$. Then, the resulting tensions follow similarly to the calculations in Eq. (5.4-5.6).

In principle, enough data is available to determine more than four fit parameters, using the expansion in Ref. [206] for up to ten parameters. However, this is only recommended, if the ϵ_i decrease for increasing index i and can be illustrated by analyzing the terms of the expansion that correspond to the ϵ_i (the cubic harmonic functions). Calculations with five parameters show that this principle is not given, so the amount of parameters has been limited to four in this work.

Finally, a theoretical description must, at least, describe both phases that are involved. For this reason, density functional theory (DFT) and simulations provide adequate theoretical description, as observed in the previous chapters of this work. For a hard-sphere system, results from DFT and simulations are shown in the next sections.

5.2 The interface in theory and simulations

In this section, the hard-sphere crystal-fluid interface is investigated by applying density functional theory (DFT) and MC computer simulations. The results are presented in Sec. 5.2.1 for DFT and in Sec. 5.2.2 for simulations. Here, the White Bear mark II functional is used to determine the interfacial tension within DFT, where in simulations the frequently used capillary wave theory that has been applied already to liquid-vapor interfaces [207] or nickel [208], is used to determine the interfacial stiffness. The stiffness has also been extracted from confocal microscope images [209], but, more often, classical nucleation theory is used to obtain the interfacial tension from the distribution of small clusters in experiments, as discussed in Sec. 5.2.3.

5.2.1 Density functional theory

Classical density functional theory (DFT) provides direct access to the grand-canonical free energy Ω (see Sec. 2.3). Thus, the tension of the hard-sphere crystal-fluid interface is directly calculated from an equilibrium density profile that contains the interface. To employ DFT, the geometric fundamental measure approach first established by Rosenfeld [25, 26] and most accurately refined in the so-called White Bear version mark II [27] is used, as explained in Sec. 3.4. A free minimization of this theory in the bulk phases (see Ref. [146] and Sec. 4.2) gives accurate hard sphere bulk coexistence data which is needed as a reliable input for the calculation of the interface and its tensions. To repeat, the crystal-fluid phase transition occurs at a coexistence chemical potential⁴ $\mu_c/k_B T = 16.3787$ and at a coexistence pressure $p_c \sigma^3/k_B T = 11.8676$. The coexistence packing fractions of the fluid and solid are respectively $\phi_f = 0.495$ and $\phi_s = 0.544$, in close agreement with the aforementioned computer simulation data [73].

At the prescribed coexistence chemical potential μ_c , the grand free energy functional is numerically minimized inside a rectangular cuboid box of lengths L_x , L_y , and L_z with periodic boundary conditions in all three directions [97]. The surface normal is pointing along the z -direction and the box length L_z is chosen large enough (about $50 - 60\sigma$) to ensure a large part of bulk crystal and fluid phase at coexistence, which are separated by two interfaces. The lateral dimensions L_x and L_y of the box depend on the surface orientation, relative to the fcc crystal. They are determined by the minimal size of a periodic rectangular cross section which accommodates the prescribed relative orientation.⁵ As described in the previous chapter, the density field is resolved on a fine rectangular grid in real space with a spacing of about 0.02σ . Starting from an initial profile, the density functional is minimized by using a Picard iteration scheme combined with a *direct inversion in the iterative subspace* method [210, 211] and a simulated annealing technique [97].⁶ Finite size effects due to the finite grid size were excluded by also using smaller grid spacings to ensure free minimization of the density functional in practice.

The initial profile contains the two bulk parts of pre-minimized crystal and fluid, as obtained in Sec. 4.2. To constitute an initial crossover between the bulk phases, a variation $f(z)$ is introduced that is one in the crystalline and zero in the fluid phase [182–184, 212, 213]. For instance, W. A. Curtin has applied such variations to parametrize the entire crystal-fluid interface by using only two parameters [182, 183]. Now, common variations $f(z)$ are

$$\frac{1}{2} \left[1 + \tanh \left(-\frac{z - z_0}{\Delta z} \right) \right] \text{ and} \quad (5.8)$$

$$\frac{1}{2} \left[1 + \cos \left(\pi \frac{z - z_0}{\Delta z} \right) \right] \text{ for } z_0 \leq z \leq z_0 + \Delta z. \quad (5.9)$$

⁴In this work, the chemical potential is used in a shifted form, where the shift $-\log(\Lambda^3/\sigma^3)$ removes the terms that result from the integrals over the translational momenta in the partition sum (see also Sec. 2.2.1).

⁵For further information about the properties of this unit cells see Sec. 4.1.2.

⁶See also Sec. C.1 for further information about the numerical methods.

Here, the first variation is centered around the position z_0 and reaches the values one or zero only in the limit of infinite $|z|$. The second equation only varies between z_0 and $z_0 + \Delta z$ and must be set to 1 for $z < z_0$ and to 0 for $z > z_0 + \Delta z$. These distinct borders are of benefit, because two interfaces cannot interact with each other. Now, the mean bulk variation of the density, $\bar{\rho}(z)$, and the spatial resolved version $\rho(\vec{r})$ between the fcc and the fluid bulk phases are defined similarly to the definitions in Refs. [182–184] as

$$\bar{\rho}(z) = \rho_{\text{fl}} + (\rho_{\text{cr}} - \rho_{\text{fl}})f(z), \quad (5.10)$$

$$\rho(\vec{r}) = \bar{\rho}(z) + (\rho_{\text{cr}}(\vec{r}) - \bar{\rho}(z))f(z), \quad (5.11)$$

where ρ_{fl} and ρ_{cr} are the mean bulk densities of the fluid and crystal phase and $\rho_{\text{cr}}(\vec{r})$ is the density profile of the fcc crystal. In contrary to parametrizations with Gaussian peaks [182–184], the broadening of the crystalline layers in the interface is not included in this variation. However, including the broadening of the crystalline layers in the interface could improve the minimization process.⁷

On contrary to the variation in Eq. (5.9), the interfacial width cannot be defined in real systems, because the envelope function of the density profile decays exponentially; only an approximative mean width can be defined, if (very) long capillary waves in the interface are ignored.⁸ Thus, the variation from Eq. (5.8) has been used in this work. For both interfaces, contained in the periodic volume, the used variation reads $f(z) + f(L_z - z)$. Typical values are $z_0 = L_z/4$ and $\Delta z \approx 1.65\sigma$.

Having established an initial density profile for the interface, the profile is brought to an equilibrium situation by minimizing the grand canonical energy of the system for a given chemical potential. The energy is given by the White Bear mark II energy functional that is introduced in Sec. 3.4.1, and the numerical methods are described in Sec. C.1. Nevertheless, obtaining convergence is a demanding task due to the term $1/(1 - n_3)$ that enters the functional. The term diverges already for small numerical errors at the lattice sites of the crystal, which results in a local packing fraction of about $n_3 \approx 1$ (or higher). On the other side, comparatively large changes must be applied in the interface region to obtain convergence. Thus, the amount of variation in the density profile per iteration step has been varied along the z -direction, being quite small in the bulk phases and much higher in the interfaces. The convergence is monitored by order parameters, like the total energy per volume or by a quadratic norm, defined on the space of density profiles (see Sec. C.1.5). In addition, almost no numerical problems occur, if the Ramakrishnan-Yussouff approach is used instead of the White Bear mark II FMT.

Small perturbations have often been observed in the fluid phase and in the valleys of the density profile of the crystalline phase during minimization. These fluctuations amplify

⁷Broadening the crystal in the interface also changes the local packing fraction, which must not exceed one! Since the local packing already is critical during the minimization, the broadening has not been applied in this work.

⁸In general, the interfacial width would diverge for an infinitely extended interface, due to the existence of long capillary waves.

themselves during the calculations and lead to numerical instabilities (or unphysical local packing) finally. Similar fluctuations⁹ can be observed in the presence of hard walls, even if only fluid densities are assumed. Thus, a more detailed analysis of this phenomenon should be part of future work.

Results for the minimized density profiles are displayed in Fig. 5.4 for five orientations. Both, the laterally integrated (z -resolved) density field

$$\bar{\rho}(z) = \frac{1}{L_x L_y} \int_0^{L_x} \int_0^{L_y} \rho(x, y, z) dy dx \quad (5.12)$$

and contour plots $\rho(x = 0, y, z)$, are shown. A direct comparison of the laterally integrated density profile from Fig. 5.4(a) for the (001) orientation to a corresponding density profile that has been obtained by MC simulations [72] shows that the density peaks in DFT are about 15% higher than in simulations, while structure and crystal broadening are fitting very well. However, a direct comparison is problematic, because capillary waves are captured in both approaches in different ways. In addition, the contour plot of the (012) interface in Fig. 5.4(b) shows an ansatz of facets in the interface region, where the crystalline structure crashes along a certain direction¹⁰ first. However, detailed analysis of structural breakdown in the interface would require a much bigger system in the lateral directions to eliminate effects due to periodicity.

Another powerful method, to analyze the structure of density profiles, has been introduced recently by M. Oettel [214]. He applied a *Mode expansion for the density profile of crystal-fluid interfaces* and used *Hard spheres as a test case*. For example, he found “a density depletion zone just in front of the bulk crystal”. In a second work, M. Oettel et al. [88] discussed the *Description of hard-sphere crystals and crystal-fluid interfaces as A comparison between density functional approaches and a phase-field crystal model*.

The DFT results for the interfacial tension are summarized in Table 5.1 for the five orientations analyzed in this work. With a slight orientational dependence, all the values vary around $0.66 k_B T / \sigma^2$. The errors given in Table 5.1 are estimated from several independent minimization runs. Since the anisotropy is weak, the orientational resolved interfacial tension can be well-fitted by the cubic harmonic expansion, as given in Eq. (5.3). The expansion is used to obtain the interfacial stiffness (5.2) from the DFT data for the anisotropic interfacial tension [67, 73]. The resulting anisotropy of the stiffness is considerably larger than the one of the tension (thus, the resulting errors of $\bar{\gamma}_{\alpha\beta}(\hat{n})$ are also larger). For the five orientations considered in this work, the resulting data for the interfacial stiffness and for the fit parameters are also listed in Table 5.1.

⁹Often, the fluctuations have a periodic length of the order of the spacing of the grid.

¹⁰The direction seems to be [001], but this is only a plane cut, ignoring vertical structure.

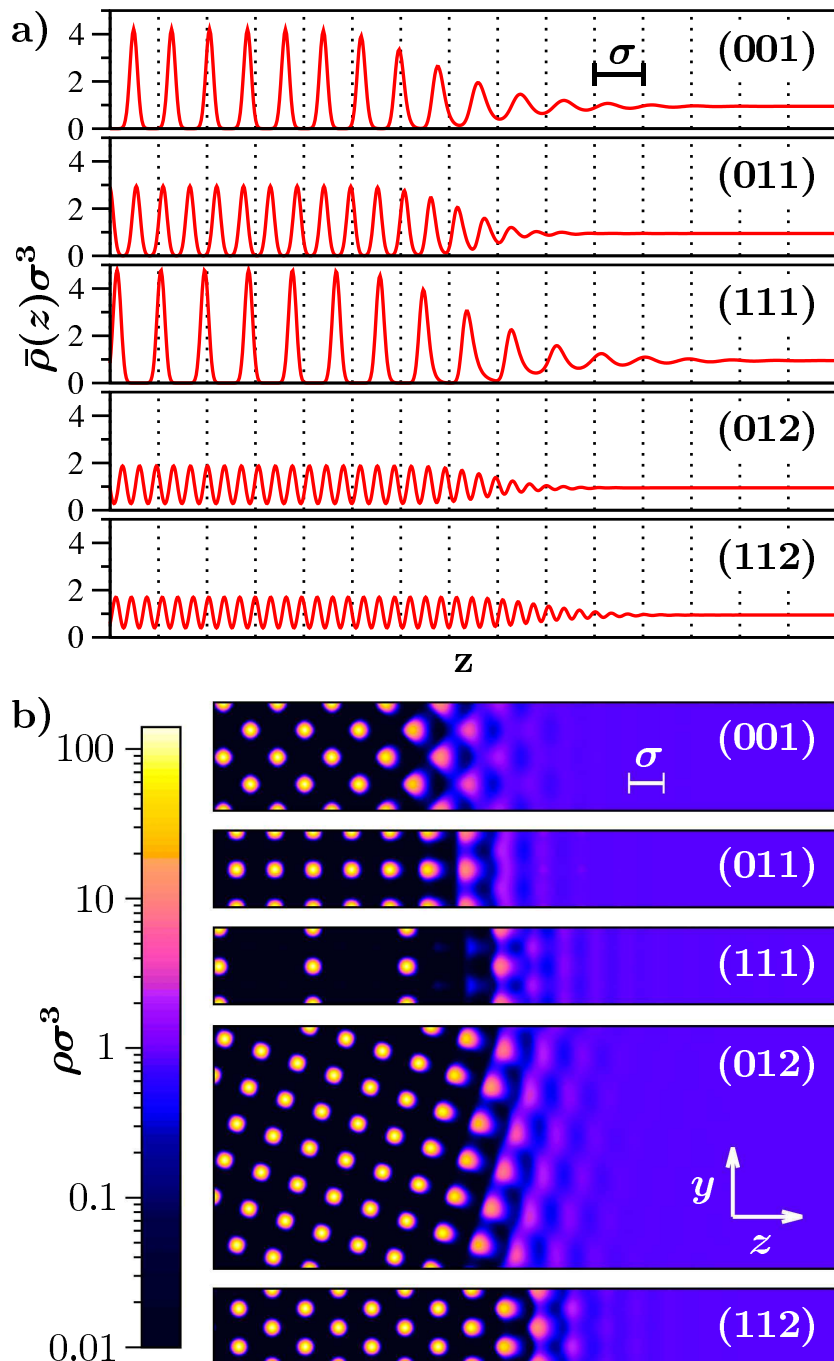


Figure 5.4: (Color) DFT results: a) Laterally integrated density profiles $\bar{\rho}(z)$ for the five surface orientations, as indicated; b) contour plots at $x = 0$. The periodic length of the total profiles in z -direction is 50.15σ (001), 53.19σ (011), 65.15σ (111), 56.07σ (012), and 61.42σ (112). This figure is reprinted with permission from Ref. [74] ©2012, The American Physical Society.

5.2.2 Monte Carlo simulations

In the Monte Carlo (MC) simulations, similar to the procedure in [72, 73], inhomogeneous hard-sphere systems at the coexistence pressure p_c are prepared, followed by production runs in the canonical ensemble. The canonical MC simulation consists of particle displacement moves according to a standard Metropolis criterion, where the trial displacements of the particles are randomly chosen from the interval $[-0.11\sigma, +0.11\sigma]$. The inhomogeneous solid-fluid systems are placed in rectangular cuboid simulation boxes of nominal size $L \times L \times 5L$ ($L \approx 25\sigma$), containing about 10^5 particles. Moreover, periodic boundary conditions are applied in all three dimensions. Here, the fcc crystal with z -extension of about $2L$ resides in the middle of the box and is separated from the fluid by two planar interfaces. Since the system is in equilibrium, the amount of crystal and fluid phase, as well as the interfaces, remain stable during the simulation. The five considered crystal orientations are (001), (011), (111), and (112), see Fig. 5.3. At each orientation, 10 independent runs are performed and in each of these runs, 10,000 independent configurations are generated that are used for the analysis of the interfaces.

The stiffnesses $\bar{\gamma}$ are extracted from the capillary wave spectrum $\langle h^2(\vec{q}) \rangle$ [67, 215], i.e. the correlation function of the interface height fluctuation $h(\vec{q})$. Here, $\vec{q} = (q_x, q_y)$ is the two-dimensional wave-vector along the lateral extension of the interface. In order to determine $h(\vec{q})$, a criterion has to be introduced according to which one can distinguish between fluid and crystal particles. Following the works [72, 73], the rotational-invariant bond-order parameter $q_6 q_6(i)$ was used [152, 153]. To distinguish between crystalline and fluid particles, the same criterion as in Refs. [72, 73] is adopted, where a particle i was identified as one with crystalline order if $q_6 q_6(i) > 0.68$, otherwise it was defined as a liquid-like particle. Moreover, the local position of the interface is defined by the set of crystalline particles at the interface (particles which have less than 11 crystalline neighbors). Some particles in the liquid bulk identified as crystalline were removed by searching the largest cluster among the particles identified as interface-particles. The fluctuation of the local interface position is defined as $h(x_i, y_i) = z_i - \langle z \rangle$, with i the index of a particle on the surface and $\langle z \rangle$ the instantaneous average location of the interface. The irregularly distributed particle coordinates (x_i, y_i) are then mapped onto a regular grid in the xy plane with grid spacing $\Delta x = \Delta y = \sigma$ using Shepard interpolation [67]. Finally, the height fluctuation $h(\vec{q})$ is obtained from a Fourier transformation of the interpolated heights.

Figure 5.5 shows the q -dependent interfacial stiffness,¹¹ as defined by the equation

$$\bar{\gamma}_1(q_x)q_x^2 + \bar{\gamma}_2(q_y)q_y^2 = \frac{k_B T}{L_x L_y \langle h^2(\vec{q}) \rangle}. \quad (5.13)$$

For the (001) and (111) orientation, $\bar{\gamma}(q) = \bar{\gamma}_1(q_x) = \bar{\gamma}_2(q_y)$ holds, whereas for the (011) and (112) orientation there are two different coefficients $\bar{\gamma}_1(q_x)$ and $\bar{\gamma}_2(q_y)$ that can be determined from the latter equation by considering $q_y = 0$ or $q_x = 0$, respectively. The

¹¹See also Ref. [215] by R. L. C. Vink et al. about *Capillary waves in a colloid-polymer interface*.

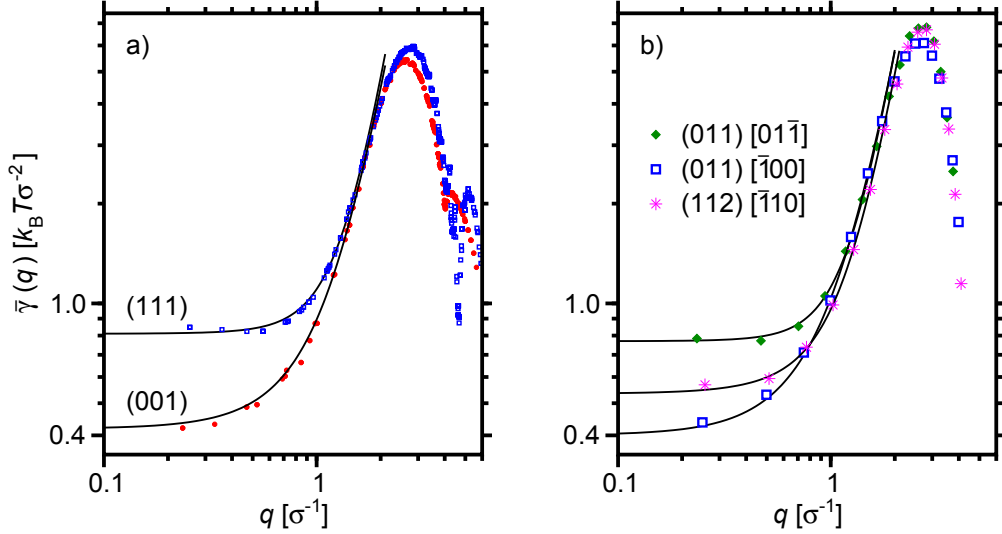


Figure 5.5: (Color) q -dependent interfacial stiffness $\bar{\gamma}(q)$ for (a) the (001) and (111) orientation as well as (b) the (011) and (112) orientation for the indicated directions. Note that for (112) only the $[1\bar{1}0]$ direction is shown because $\bar{\gamma}(q)$ for the $[11\bar{1}]$ direction is very similar to that of the latter direction. This figure is reprinted with permission from Ref. [74] ©2012, The American Physical Society.

solid lines in Fig. 5.5 are fits of the data for $q < 1.5 \text{ } \sigma^{-1}$ with the function $\bar{\gamma}(q) = \bar{\gamma} + aq^2 + bq^4$ yielding the values for the stiffness $\bar{\gamma}$ for $q \rightarrow 0$.

5.2.3 Classical nucleation theory and experiments

In classical nucleation theory (CNT) [9, 179, 185, 201], the size distribution of nuclei is observed in a metastable liquid phase that will (partly) crystallize. The nuclei are clusters of N crystalline particles and their size distribution $P(N)$ that is shown in Fig. 5.6 is related to the free-energy difference

$$\Delta G(N) = -k_B T \log \left(\frac{P(N)}{P_0} \right) = -N \Delta \mu + A(N) \gamma, \quad (5.14)$$

where A is the surface area of a cluster that contains N particles. Here, the difference in the chemical potential between the inside and outside of the clusters is $\Delta \mu = \mu_{\text{fl}} - \mu_{\text{fcc}}$. Assuming a spherical cluster with radius R_{cl} and with the volume of the N contained particles, the surface area

$$A(N) = 4\pi R_{\text{cl}} = \pi \sigma^2 \eta_{\text{fcc}}^{3/2} N^{2/3} \gamma \quad (5.15)$$

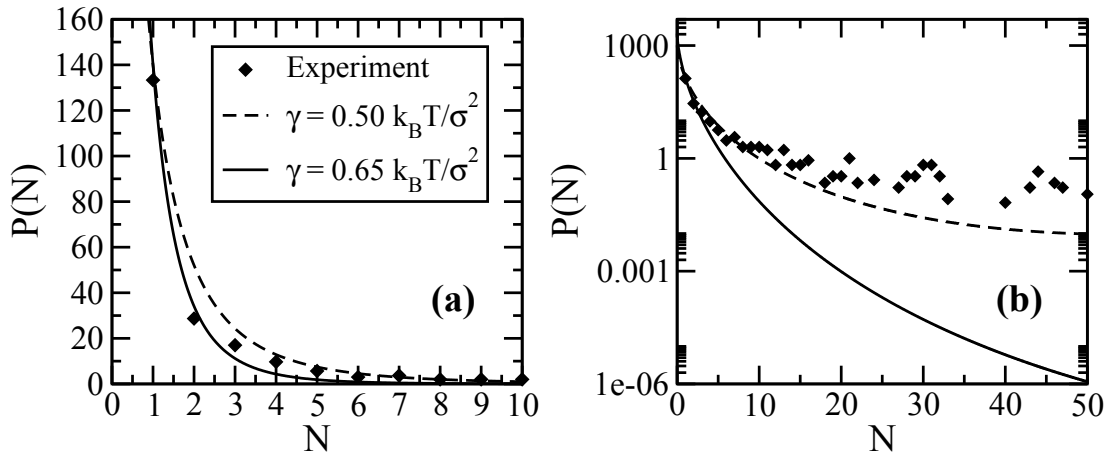


Figure 5.6: Distribution $P(N)$ of nuclei sizes as a function of the number of particles N in the nuclei for a sample with volume fraction $\phi = 0.53$ and a time after homogenization $t = 240$ min. (diamonds). The solid and dashed lines are fits to $P(N)$ following Eq. (5.14) for small nuclei for interfacial tensions $\gamma\sigma^2/k_B T = 0.5$ and 0.65 . Data are shown linear (a) and in a logarithmic plot (b).

follows from $\eta_{\text{fcc}} = N \frac{\pi}{6} \sigma^3 / (\frac{4}{3} \pi R_{\text{cl}}^3)$. This is a quite rough assumption, because small clusters are observed to not have a spherical [9], but an elliptical shape.¹² Now, following U. Gasser et al. [9], the surface tension γ can be obtained from investigating the occurrence of small nuclei, which is demonstrated in Fig. 5.6. However, next to the approximations that enter the classical nucleation theory, small nuclei have a strongly curved surface and the correct surface tension should only be obtained in the limit of big clusters.

To analyze the experimental data¹³ shown in Fig. 5.6, the chemical potential difference $\Delta\mu$ must be obtained. For instance, V. D. Nguyen et al. [12] found a value of $\Delta\mu = 0.41k_B T$ for a hard-sphere system. However, the White Bear mark II functional states a chemical potential of $\mu_{\text{fl}} = 20.80k_B T$ at a pressure $p = 20.206k_B T/\sigma^3$ for a fluid phase with a volume fraction $\eta_{\text{eta}} = 0.53$. For the same pressure, calculations yield $\mu_{\text{rmfcc}} = 20.38k_B T$ for a crystalline fcc phase. Thus, the difference in chemical potential during nucleation is $\Delta\mu = 0.42k_B T$ for the experimental system, described in the next paragraph.

The following paragraph and the resulting data are taken from K. Sandomirski and S. U. Egelhaaf [private communication]. For further details of the samples, imaging, and analysis procedures see Ref. [68]. Experimental measurements have been applied (by K. Sandomirski) for systems with $\eta = 0.53$ of hard-sphere like colloids made of polymethylmethacrylate (PMMA) with a diameter $\sigma = 1.83 \mu\text{m}$ and a polydispersity of less than 4 %, which are sterically stabilized and fluorescently labelled. They are suspended in a mixture of cis-decalin and cycloheptylbromide to match their density and approximate their refractive index. To reduce and screen the particles' charges, the solvents are distilled

¹²Possibly, a function for a mean surface could be obtained by weighing all possible shapes of clusters with a probability of their occurrence.

¹³Experiments are applied by K. Sandomirski, see next paragraph.

and salt (tetrabutylammonium chloride) added, respectively. Samples are prepared by diluting a stock solution, which is obtained by centrifugation and assumed to be a random close-packed sediment with $\phi = 0.64$ [216]. About 0.3 ml of the samples are kept and imaged in glass vials with a diameter of about 1 cm whose bottoms are replaced by cover slips, which are covered by an inhomogeneous film of polydisperse PMMA particles with a different size to avoid heterogeneous nucleation [217]. The samples are imaged by using an Olympus Fluoview FV1000 confocal microscope equipped with an Ar ion laser operated at a wavelength of 488 nm and connected to an Olympus IX81 inverted microscope with an 1.35 NA 60 \times oil-immersion objective. A volume of $96 \times 96 \times 60 \mu\text{m}^3$ is imaged at a distance of $10 - 70 \mu\text{m}$ from the cover slip. Particle positions are determined [218] and the local orientational-order parameter $\vec{q}_6(i)$ calculated for each particle i [152, 153]. Two neighboring particles i and j , where particles are declared neighbors if their centers are within 1.17σ , are considered connected in a crystalline cluster, if $\vec{q}_6(i) \cdot \vec{q}_6(j) \geq 0.5$. If a particle has at least 8 connected neighbours, it is regarded a crystalline particle.

For a volume fraction of $\eta = 0.53$, three independent sets of data have been obtained from the experiments (by K. Sandomirski), each set listing numbers of clusters that have been found in the system for a given cluster-size N . Combining all three sets, a distribution $P(N)$ of clusters can be determined, which is shown in Fig. 5.6. In addition, the distribution $P(N)$, obtained by CNT, from Eq. (5.14) is shown for two surface tensions $\gamma = 0.50k_{\text{B}}T/\sigma^2$ and $\gamma = 0.65k_{\text{B}}T/\sigma^2$, using $\Delta\mu = 0.42k_{\text{B}}T$ and the condition $P(1) = 140$; the latter results in $P_0 = 1012.4$ and $P_0 = 2079.0$, respectively. Regarding Fig. 5.6, the solid line adapts the first two data points for $N = 1$ and $N = 2$, where the dashed line adapts better to the tail of the data. Thus, it is a challenge to fit the curve $P(N)$ from Eq. (5.14) to the data without making arbitrary assumptions. Finally, the system is not in equilibrium when the clusters are counted. So, the result will also depend on the time, when the measurement is applied. However, values, obtained from literature, predict very low tensions of about $\gamma \approx 0.1k_{\text{B}}T$ [9].

5.3 Interfacial tensions and stiffnesses

Searching in literature, over the last decades various results can be found regarding the crystal-fluid surface tension of hard-sphere systems.^{14,15} A selection is listed in Fig. 5.1, where the tensions, presented by several works, are represented against the date (month and year), when the containing work has been published.

Apparently, early results by W. A. Curtin [182, 183] and D. W. Marr and A. P. Gast [184] are in good agreement with the results obtained in this work. The results are obtained using the weighted density approximation (WDA) in the framework of DFT and are quite

¹⁴Of course, the interfacial tension and stiffness has also been investigated for other systems, like Lennard-Jones [219, 220] or nickel (Ni) [67, 208, 221]. The methods are often similar.

¹⁵The structure of the hard-sphere interface has also been investigated without determining the interfacial tensions and stiffnesses in previous studies, for example in Refs. [186, 222, 223].

Table 5.1: Interfacial tensions γ and stiffnesses $\bar{\gamma} \equiv \bar{\gamma}_{\alpha\alpha}$ in units of $k_{\text{B}}T/\sigma^2$ for different surface normal vectors (round brackets) and tangential directions n_α (square brackets). In DFT the tensions are measured directly, in the simulation the stiffnesses. The other data are listed italicized and are calculated using the fit function (5.3). The fit parameters are obtained from a least square fit to the measured data. For DFT they are $\gamma_0 = 0.664(2)k_{\text{B}}T/\sigma^2$, $\epsilon_1 = 0.1076(120)$, $\epsilon_2 = -0.01364(292)$, $\epsilon_3 = -0.0023(209)$ and for simulation $\gamma_0 = 0.618(11)k_{\text{B}}T/\sigma^2$, $\epsilon_1 = 0.0905(32)$, $\epsilon_2 = -0.00547(44)$, $\epsilon_3 = 0.0054(25)$. As a reference, previous simulation results for tensions [191] and stiffnesses [189] are shown in the last column. The numbers in parentheses indicate the uncertainty in the last digit(s).

orientation	theory	simulation	Ref. [189, 191]
γ (001)	0.687(1)	<i>0.639(11)</i>	0.5820(19)
$\bar{\gamma}$ (001)	<i>0.53(14)</i>	0.419(5)	0.44(3)
γ (011)	0.665(1)	<i>0.616(11)</i>	0.5590(20)
$\bar{\gamma}$ (011)[$\bar{1}00$]	<i>0.283(35)</i>	0.401(5)	0.42(3)
$\bar{\gamma}$ (011)[$01\bar{1}$]	<i>0.86(14)</i>	0.769(5)	0.70(3)
γ (111)	0.636(1)	<i>0.600(11)</i>	0.5416(31)
$\bar{\gamma}$ (111)	<i>1.025(79)</i>	0.810(5)	0.67(4) ¹⁷
γ (012)	0.674(5)	<i>0.623(11)</i>	0.5669(20)
$\bar{\gamma}$ (012)[$\bar{1}00$]	<i>0.454(57)</i>	0.575(5)	0.59(3)
$\bar{\gamma}$ (012)[$02\bar{1}$]	<i>0.71(12)</i>	0.420(5)	0.43(3)
γ (112)	0.654(1)	<i>0.611(11)</i>	
$\bar{\gamma}$ (112)[$\bar{1}\bar{1}0$]	<i>0.973(41)</i>	0.606(5)	
$\bar{\gamma}$ (112)[$11\bar{1}$]	<i>0.704(50)</i>	0.550(5)	

interesting, because a parametrization of the interface density profile is used that only contains two parameters.¹⁶ Moreover, the WDA predicts much smaller values, if the density profile is minimized freely (on a grid) [97]. In Monte Carlo (MC) and Molecular Dynamics (MD) simulations, either the interfacial stiffness is measured through a capillary wave (CW) analysis of the interface [74, 188–190], or the interfacial tension is measured directly via integration methods (cleaving walls [187, 191], umbrella sampling [200, 224]). If the stiffness is obtained, an additional transfer to tensions is necessary that is described in the following section. In experiments, the tension is often extracted by classical nucleation theory (CNT) [9, 193], as shown in Sec. 5.2.3, but also using the capillary wave analysis [12].

Now, this work [74] presents interfacial tensions and stiffnesses that have been obtained

¹⁶See also Ref. [214] by M. Oettel, for a discussion of density modes and simple parametrizations.

¹⁷This value is for the rhcp-crystal-liquid interface, rather than for the fcc-crystal-liquid interface. See Ref. [189] for details.

from density functional theory (White Bear mark II) and MC computer simulations. Quantitative agreement has been found between both methods. In Table 5.1, the values of $\bar{\gamma}$, as obtained from simulations, are given in comparison to previous simulation results and to DFT. A direct comparison is not possible, since in DFT the *tensions* are calculated whereas in MC simulations the *stiffnesses* are measured. A comparison is only possible when using a tension-stiffness conversion through a least-square fit to the tension anisotropy expansion (5.3) and the corresponding expression for the stiffnesses (through a combination of (5.3) and (5.2)), giving the average tension γ_0 and the parameters ϵ_i ($i=1,2,3$).¹⁸ Here, an element of uncertainty is added by the truncation of the expansion since the single terms, especially in the stiffness expansion are not small (note also the associated error bars in the converted quantities).

As expected for a fcc crystal-fluid interface, DFT shows the largest interfacial tension for the (001) interface orientation and the lowest one for the (111) orientation, giving the tension anisotropy $(\gamma(001) - \gamma(111))/2 = 0.025k_B T/\sigma^2$. The average tension $\gamma_0 = 0.664 k_B T/\sigma^2$ is 7.4% higher than that one from the simulation.¹⁹ Most likely, this deviation stems from the fact that in DFT (long-ranged) fluctuations in the interface are averaged out. For the stiffnesses the data is spread in a much wider range between $0.28 k_B T/\sigma^2$ for the (011) orientation with lateral direction $[\bar{1}00]$ and $1.03 k_B T/\sigma^2$ for the (111) orientation. A comparison between the stiffnesses obtained from theory and simulations shows deviations from up to $0.36 k_B T/\sigma^2$ for the (112)[$\bar{1}10$] direction to less than one percent for the (012)[$02\bar{1}$] direction.

Previous simulations obtained the values $0.559(17) k_B T/\sigma^2$ [189] and $0.5610(12) k_B T/\sigma^2$ [191] for γ_0 (see also Fig. 5.1). These values are 10% smaller than the simulation results presented in this work. An obvious discrepancy appears for the (111) interface orientation, where deviations from a fcc packing have not been observed in contrast to [189]. Further differences to previous simulations are the use of a different geometry and of a rotational-invariant order parameter for the identification of crystalline particles.

Now, the resulting data is compared to real-space experiments on dispersions of hard-sphere-like colloids (see also Fig. 5.1). They often carry residual charges and are polydisperse. This renders a comparison with theoretical results on hard spheres difficult. Hitherto, the interfacial tension was indirectly measured by interpreting the probability to find small (non-spherical) clusters in terms of classical nucleation theory (CNT) [9], yielding data for a mean tension of about $\gamma_0 = 0.1 k_B T/\sigma^2$.²⁰ Clearly, given the limitations of the hard-sphere model due to particle charging and the inherent assumption of small spherical crystalline nuclei, this is just a rough estimate of γ_0 . An alternative experimental route is

¹⁸Because the fit function (5.3) can not reproduce the inner anisotropy for the (012) orientation (shown in the theory column of Table 5.1), the simulation data for the stiffnesses at the orientations (012) and (112) have not been taken into account for the least-square fit. The different inner anisotropy therefore is not a shortcoming of DFT.

¹⁹Using the Ramakrishnan-Yussouff approach, a tension of $\gamma(001) = 1.31 k_B T/\sigma^2$ was found.

²⁰Compare also to Sec. 5.2.3 about CNT in experiments.

via the analysis of the capillary-wave spectrum, similar to what is done in the MC simulations of this work [10–12] and providing direct access to the interfacial stiffnesses. In Ref. [10], the reported stiffness of $1.2k_{\text{B}}T/\sigma^2$ for an interface between a randomly stacked hexagonal close packed (hcp) crystal and its melt is significantly higher, compared to the results of this work, which might reflect the slight charge, the limited ensemble averaging, and an ad-hoc value for the viscosity required for the analysis in this experiment. In Ref. [11], the reported stiffnesses are in the range of about $(0.7 - 1.3)k_{\text{B}}T/\sigma^2$. Interestingly, the stiffness for the (011) interface is found to be isotropic and the highest value for the stiffness is found for the (001) orientation, oppositely to what the authors have expected and what has been found for hard spheres in this work. This might be due to a limited number of crystalline layers and the small gravitational length of $\sigma/7$, which limits the thickness of the liquid. Finally, V. D. Nguyen et al. [12] grew crystals of PNIPAM particles in a temperature gradient and analyzed the capillary waves along crystal-fluid interfaces after the removal of the temperature gradient. They measured averaged stiffnesses for several interface orientations in the range of $(0.19 - 1.13)k_{\text{B}}T/\sigma^2$ that show the best agreement with the results of this work. Nevertheless, the latter experiment is not accurate enough to validate theory and simulation on a quantitative level but shows that more experimental explorations are required.

5.4 Conclusion

Accurate values for the anisotropic crystal-fluid surface tensions and stiffnesses of a hard sphere system have been predicted by using both, fundamental measure density functional theory and Monte Carlo simulations. A small anisotropy in the tensions of about 10% is found which is, however, crucial for the transformation to stiffnesses which differ up to a factor of 4. These predictions can help to clarify apparent discrepancies found in real-space experiments of sterically-stabilized colloidal suspensions [9–12]. Since the anisotropic tensions control changes of the interfacial shape, their precise quantitative determination help to understand crystal nucleation [185, 225] and the transport of larger carriers through the interface. They may also serve as further input to phase-field-crystal calculations, which explore solidification processes on larger length and time scales [90, 226, 227].

Future work should address soft interactions and attractions (as relevant, e.g. for colloid-polymer mixtures), in order to scan the full range from a fluid-crystal to a vapor-crystal interface. Further extensions can be done along similar ideas as used and proposed here for binary mixtures. Finally, the recent extension of DFT towards dynamics for Brownian systems can be used to explore the time-dependent growth kinetics and relaxation towards equilibrium for the hard-sphere interface [228]. In this context, an analysis of the numerical perturbations is also of interest, to ensure the usage of relatively big time steps.

6

Anisotropic colloidal particles

Liquid crystals are beautiful and mysterious;

(from preface of Ref. [229], Pierre-Gilles de Gennes 1932-2007)

Anisotropic colloidal particles have additional orientational degrees of freedom, if compared to spherical particles. Thus, spherocylinders, discs or platelets, needles, cubes, or dumbbells generate isotropic (no orientational order) and nematic (orientations aligned along a certain direction, called nematic director) phases, when the spatial order remains fluid-like. Combinations of spatial and orientational ordering are possible and lead to so-called smectic phases. Additionally, orientations are of import for plastic crystals or rotator phases. However, orientational ordering is in some sense similar to translational freezing and thus, liquids with orientational ordering are called liquid crystals [229]. Liquid crystals can be composed either of anisotropic molecular or colloidal particles with orientational degrees of freedom. The latter have the advantage that they can be studied directly in real-space [230–232].

The key mechanisms in optical displays and switching devices are governed by the dynamical response of liquid crystals to external aligning fields [233, 234].¹ In particular, it is essential to understand and control the switching dynamics of the nematic director upon a change of the externally imposed alignment field [236]. However, due to their orientational degrees of freedom, the rheological behavior and nonequilibrium dynamics of rod-like particles are much more complex than that of spherical particles [237]. For imposed shear flow, for instance, the nematic director exhibits an intricate dynamical behavior which can be classified as tumbling, wagging, kayaking, log-rolling, and flow-aligning [238–244].

Moreover, wall effects and effects of gravity are typically very important in colloidal suspensions, which can be exploited to steer crystallization, for instance by sedimentation onto a substrate [245–247]. Therefore, it is paramount to investigate the effects of gravity and of the confining walls on colloidal suspensions. Simulation studies on crystallization of spheres [248, 249], spherocylinders [250], and dumbbells [251] have shown that the phase behavior of the system under gravity can be understood by a mapping onto the bulk phase diagram. Comparisons between the density profiles for fluids in the presence

¹For example, already in 1927 V. Fréedericksz and A. Repiewa investigated the transition of a isotropic phase within a external (magnetic) field (called Fréedericksz-Transition) [235].

of external fields obtained from DFT calculations and those measured in simulations are often used to validate the theoretical approach. For instance, the FMT for hard spheres has been very successful in describing the density profile near a hard wall [113] and edFMT is equally successful for (convex) spherocylinders [28, 105]. The density profile obtained from an older semi-empirical weighted density approach, specifically tailored to dumbbells, has also shown quite good agreement with simulation results [252]. However, the deviation between the simulations and the semi-empirical DFT for dumbbells [252] is larger than the deviation between results from simulations and edFMT for spherocylinders [105].

Simultaneously, the interest in liquid crystals has been a motivation to apply DFT to anisotropic particles, for instance to hard spherocylinders as idealized rod-like molecules. The isotropic–smectic and nematic–smectic phase transitions of these rods were determined using a weighted density version of DFT for anisotropic particles [253, 254] and showed reasonable agreement with the essentially exact simulations results of Ref. [255]. However, the construction of the free energy functional of this theory is ad hoc and not solely based on the geometry of the particles, such as FMT is (see Sec. 3.4).² Now, edFMT provides excellent agreement with simulations for the isotropic–nematic transition [105, 125]. The theory has also been applied to fluids of spherocylinders under the influence of an external field that couples to the orientations of the particles and a dynamic version of edFMT has been derived for time dependent external fields [125, 126], such as shown in Sec. 6.2. In addition, FMT approaches also exist for parallel cubes [258–260], parallel spherocubes [261],³ or disks [107, 118].⁴ In two dimensions, the latter can be obtained by dimensional crossover [29, 107], where spheres are trapped in one dimension, for example in between two glass plates [107]. Similarly, cubes can be reduced to squares [260].

Historically, hard-core interaction potentials have been very useful as the basis for theories that apply to more general atomic and molecular systems. More recently, the realization of hard-particle systems in the form of colloidal suspensions has given the study of anisotropic hard particles a new incentive. Colloids have been synthesized in an impressive number of shapes [8], many of which have no atomic or molecular analogue. Many of these colloidal shapes are non-convex and a theory predicting the phase behavior of non-convex particles would be of great value. Although convexity of the particle-shape is assumed in their derivations and so far only convex shapes have been studied, the recent edFMT [105] and the older version of FMT [56] for anisotropic particles are expected to approximately hold for non-convex particles as well. This expectation is tested in Ref. [104] and Sec. 6.3 by investigating the accuracy of edFMT for non-convex particles.

In this chapter, first, additional theoretical foundations are discussed in Sec. 6.1, con-

²Such density functional theories have also been constructed for specific shapes with zero volume, namely infinitely thin rods [256] and disks [257].

³Cubes with rounded edges that are spheres in one limit and cubes in the other.

⁴Distinguish between hard spheres in two and three dimensions and platelets.

cerning the orientational degrees of freedom and the edFMT approach. Next, a system of colloidal spherocylinders is exposed to an external rotating field that solely couples to the particle orientations. And finally, edFMT is applied to non-convex dumbbells in Sec. 6.3, where density profiles of dumbbell fluids in between two walls or under gravity obtained from edFMT are compared to those measured in simulations.

6.1 Additional theoretical foundations

The extended deconvolution fundamental measure theory (edFMT) has been developed by H. Hansen-Goos and K. Mecke to describe inhomogeneous fluids of anisotropic hard particles [28, 105].⁵ The factor ζ that enters edFMT is a free parameter and stems from the truncation of the expansion of the Mayer- f function in tensorial weight functions (see also Sec. 6.3 and Refs. [28, 104, 105]). It should be independently determined for every particle shape by minimizing the mean squared difference between the exact excluded volume $v_{\nu,o}^{\text{excl}}$ and the edFMT approximation $v_{\nu,o}^{\text{edFMT}}$ of two particles ν and o . Here, the excluded volume is given by

$$v_{\nu,o}^{\text{excl}} = -\frac{1}{V} \int_V \int_V f_{\nu o}(\vec{r}_\nu - \vec{r}_o) d\vec{r}_\nu d\vec{r}_o \quad (6.1)$$

and the edFMT approximation $v_{\nu,o}^{\text{edFMT}}$ is obtained in the same way with $f_{\nu o}$ replaced by the approximated Mayer- f function $f_{\nu o}^{\text{edFMT}}$, which depends on ζ . Results for this approximate excluded volume can be found for spherocylinders in the work by H. Hansen-Goos et al. [105] and in the work of A. Härtel and H. Löwen [125], and for dumbbells in the work by M. Marechal et al. [104]. On the other side, the exact excluded volume has been calculated by L. Onsager for spherocylinders [262] and by M. Marechal for dumbbells [104].⁶

The structure of very elongated particles is affected largely by the excluded volume, which justifies its use for determining ζ for spherocylinders with a total length-over-diameter ratio larger than 3.5, to which edFMT was applied in Refs. [28, 105, 125, 126]. For less elongated particles, the excluded volume is not the only important quantity as the structure is determined by both translational and positional ordering. For instance, this can be seen in the phase diagram of spherocylinders in Refs. [255, 264].

For this reason, it is somewhat arbitrary to fit ζ by minimizing the difference between the exact and the edFMT excluded volumes for dumbbells. However, for spherocylinders an optimal parameter ζ is determined in Refs. [105, 125] depending on the orientational state of the system. For an isotropic system, $\zeta = 5/4$ is found to be optimal and for a total

⁵For further information about the construction of the extended deconvolution FMT functional, see the passage around Eq. (3.62).

⁶For dumbbells, A. Isihara calculated the second virial coefficient, including the integration over the angle between the dumbbells [263].

nematic state (all particles oriented parallel), $\zeta = 2$. Therefore, in Refs. [125, 126] a value of $\zeta = 1.6$ is chosen for the investigation of the isotropic-nematic phase transition.

Nevertheless, for any non-convex shape, ζ_{CE} can be defined as the value for ζ that minimizes the difference between the exact and the edFMT excluded volumes for its convex envelope (CE).⁷ For dumbbells, this value $\zeta = 5/4$ turns out to be the value that gives the smallest deviation, where the convex envelope of a dumbbell is a spherocylinder. However, the result for $\zeta = 1$ is nearly indistinguishable from the result for $\zeta = 5/4$. So, it would be interesting to consider other non-convex shapes to investigate the conjecture that ζ_{CE} is the optimal value for ζ for any non-convex particle.

Furthermore, other approximations are made than the truncation of the tensor-expansion at first order when edFMT is applied to non-convex particles [104]. In Ref. [104] it is shown that the most pronounced effects of these additional approximations can not be decreased by choosing an appropriate value for ζ . Moreover, the tensor $\vec{\hat{n}}_1$ does not have to be calculated if ζ is set to zero. Considering the limited improvement achieved by a non-zero ζ , choosing a non-zero ζ seems not to be worth the extra effort of calculating the tensor $\vec{\hat{n}}_1$. Therefore, $\zeta = 0$ has been used in Ref. [104] and in Sec. 6.3. However, edFMT still yields reasonable results for inhomogeneous fluids of dumbbells even with $\zeta = 0$.

6.2 Driven colloidal liquid crystals [126]

This section is mostly rewritten from the work *Towing, breathing, splitting and overtaking in driven colloidal liquid crystals* by A. Härtel et al. [126] ©2010, The American physical society. A statement about the individual contributions of the authors is given in the preface of this work.

Motivated by the importance of changing alignment fields, the dynamics of a colloidal nematic phase is investigated in the presence of an orientation-aligning field which rotates in a plane with a frequency ω_0 . A wealth of different dynamical states is found as a function of the system density and the external drive frequency. For very small frequencies, the field tows the nematic director such that the latter is rotating with the same external frequency ω_0 as the field and in the same plane. During this *towing* process, the orientational distribution function keeps a time-independent internal shape. Then, above a threshold frequency the width of the orientational distribution exhibits an internal oscillation with another frequency ω_b , which is called orientational *breathing* and linked to particles in oscillating traps [32, 265]. Further, above a higher threshold frequency, the peak of the orientational distribution splits into two peaks, which is referred to as *splitting*. For an even higher external rotation frequency ω_0 , the driven nematics cannot follow the drive any longer and is decelerated; rotating with another angular velocity ω_p it is *overtaken* by the external field. Finally, for even higher ω_0 , the monopeak is reentrant before the orientational distribution becomes static in the limit $\omega_0 \rightarrow \infty$.

⁷See M. Marechal et al. in Ref. [104].

This work is based on the microscopic DDFT for Brownian rod-like particles [266] with the recently-developed edFMT equilibrium density functional [28, 105], which accounts for nontrivial correlations in the inhomogeneous system.⁸ The functional is employed for hard spherocylinders in an external time-dependent driving field and has been tested carefully in previous work [125]. Thereby, a microscopic approach for nonequilibrium dynamics in dense liquid crystals has been established.

The dynamical states of towing, breathing, splitting, and overtaking, which are predicted by DDFT, can be confirmed in various systems using different experimental set-ups. Apart from molecular liquid crystals in rotating aligning fields [267–270], rod-like colloidal particles form nematic phases and can be exposed to rotating electric [271] or magnetic [232, 272] aligning fields. A similar effect occurs in ferrofluids in rotating magnetic fields [273], or in complex plasmas of rod-like particles in rotating electric fields [274]. As an equivalent set-up, one can rotate the sample and keep the aligning field static which was proposed recently in Ref. [273]. The different dynamical states in the switching response of the colloidal liquid crystal can be exploited to fabricate new smart devices which generate polarization amplification and mixing.

6.2.1 The model of hard spherocylinders

In this model, hard spherocylinders are employed for lyotropic colloidal liquid crystals in the absence of system boundaries. The spherocylinders have a fixed aspect ratio $L/\sigma = 5$,⁹ where L is the length of the cylindrical part and σ the diameter. The averaged number density of the spherocylinders $\bar{\rho}$ is typically chosen in the region where the bulk phases are isotropic or nematic [255].

In the following, the density $\bar{\rho}$ is expressed in a reduced form via $\rho^* = \bar{\rho}/\rho_{cp}$ with the close packing density $\rho_{cp}\sigma^3 = \frac{2}{\sqrt{2+L/\sigma}\sqrt{3}}$. The spherocylinders perform completely overdamped Brownian motion in a solvent which keeps them at finite temperature T . Then, a time-dependent external driving field is applied which brings the suspension into nonequilibrium. The nonequilibrium dynamics are characterized in terms of a time-dependent one-particle density field $\rho(\hat{u}, t) = \bar{\rho}f(\hat{u}, t)$ (the one-body density is a statistical average over different directors in domains) which is homogeneous in the translational but heterogeneous in the orientational variable given by an orientational vector \hat{u} on the unit sphere S_2 . It should be mentioned that although the density field is translational homogeneous, the density functional still contains nontrivial positional correlations. In polar coordinates, the unit vector \hat{u} can be expressed by the polar and azimuthal angles, $\hat{u}(\varphi, \vartheta) = (\cos \varphi \sin \vartheta, \sin \varphi \sin \vartheta, \cos \vartheta)$. The dimensionless and normalized quantity $f(\hat{u}, t)$ measures the distribution of orientations of the spherocylinders at a given time t on the unit sphere. Clearly, as particles are apolar, $f(-\hat{u}, t) = f(\hat{u}, t)$.

⁸In detail, the theoretical foundations are presented in the previous chapters of this work.

⁹Larger aspect ratios do not change the qualitative dynamical scenario of the dynamical state diagram.

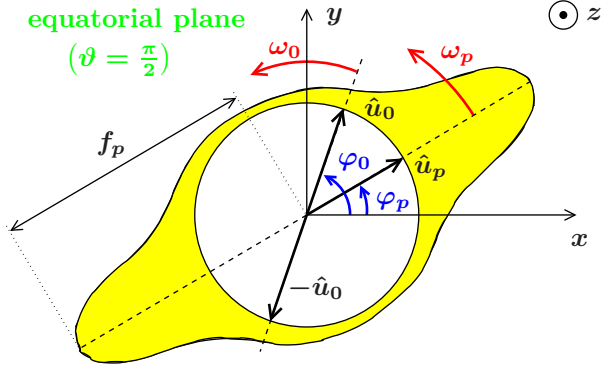


Figure 6.1: (Color) Schematic view of an orientational profile $f(\varphi, \theta)$ in the equatorial plane. The surface of the shaded area is given by $f(\varphi, \theta)\hat{u}$ with \hat{u} , i.e. it is a polar plot of $f(\hat{u})$; f_p is the peak value in the direction \hat{u}_p of the maximum of f . The amplitude of the driving field is maximal along the unit vector \hat{u}_0 . The external frequency ω_0 and the peak angular velocity ω_p are also indicated. This figure is reprinted with permission from Ref. [126] ©2010, The American Physical Society.

As for a microscopic theory for nonequilibrium dynamics, dynamical density functional theory is applied which provides a deterministic equation for $f(\hat{u}, t)$ in a time-dependent external potential. For orientational degrees of freedom, the evolution equation of DDFT in the absence of hydrodynamic interactions is given in Eq. (2.55). Note that hydrodynamic interactions can be neglected if the physical volume fraction is smaller than the effective volume fraction of the interactions, as realized e.g. for charged rods. Backflow effects [275] are also not considered. However, it is clear that hydrodynamic interactions between the spherocylinders are important for large physical volume fractions and would lead to more complex dynamical response. Finally, all microscopic information is contained in the equilibrium free energy density functional $\mathcal{F}[f(\hat{u})]$. As shown in Sec. 2.3, the latter is conveniently decomposed into three terms $\mathcal{F}[f] = \mathcal{F}_{id}[f] + \mathcal{F}_{ext}[f] + \mathcal{F}_{exc}[f]$, where $\mathcal{F}_{id}[f] = k_B T \int_{S^2} f(\hat{u}) [\ln(f(\hat{u})) - 1] d\hat{u}$ is the entropy of ideal rotators, $\mathcal{F}_{ext}[f] = \int_{S^2} f(\hat{u}) V_{ext}(\hat{u}, t) d\hat{u}$ describes the coupling to an external time-dependent potential $V_{ext}(\hat{u}, t)$, and $\mathcal{F}_{exc}[f]$ involves the particle correlations. For the latter, the recently proposed edFMT is used that is presented in Sec. 3.4. The technical parameter ζ is fixed to 1.6 in this work. Moreover, the external aligning potential is chosen as

$$V_{ext}(\hat{u}, t) = -V_0 \cdot \cos^2(\omega_0 t - \varphi) \sin^2(\vartheta) \quad (6.2)$$

and describes a rotation of an optimal alignment direction $\hat{u}_0(t) = \pm(\cos \omega_0 t, \sin \omega_0 t, 0)$ in the equatorial plane of the unit sphere with an external frequency ω_0 and an amplitude $V_0 = 5k_B T$. The \pm sign reflects the symmetry of apolar particles, which is schematically shown in Fig. 6.1.

6.2.2 Towing, breathing, splitting, and overtaking

The DDFT Eq. (2.55) has been solved numerically¹⁰ for $f(\hat{u}, t)$ by using a finite difference scheme with a time-step of $\Delta t = 5 \times 10^{-5} \tau_B$. Various combinations of reduced densities ρ^* and external frequencies ω_0 were explored by starting with a homogeneous orientational distribution. After typically 500 cycles, the system reaches a dynamical steady state, which is characterized by several order parameters. In fact, five qualitative different dynamical orientational distributions are found for increasing frequency. They are first described step-by-step before the full nonequilibrium state diagram is represented in the $\rho^* - \omega_0$ parameter space.

For vanishing ω_0 , the external potential is static and leads, at any density ρ^* , to a nematic state with a director along the x -axis. For $\omega_0 \rightarrow \infty$, on the other hand, the system effectively feels a static time-averaged external potential $-V_0 \sin^2(\vartheta)/2$. Here the system undergoes a paranematic-nematic transition at about $\rho^* = 0.3717$ [266]. Apart from these two bracketing equilibrium limits, the system shows a complex nonequilibrium response at finite frequencies ω_0 . For small ω_0 , the external field drags the orientational field $f(\hat{u}, t)$ slowly such that its peak position $\hat{u}_p(t)$ follows the optimal orientation $\hat{u}_0(t)$ with the same angular velocity ω_0 and keeps a constant internal shape. This dynamical state is called “*towing*”. The characteristic dynamics in the towing state is summarized in Fig. 6.2(a). In the left panels, the unit sphere is mapped onto a rectangular stripe showing the height of $f(\hat{u}, t)$ for a fixed time. The latter is indicated by an arrow on the time axis of the right panels. The white cross in the left panels indicates the position of $\hat{u}_0(t)$ at this time and reveals the towing behavior.¹¹ Full time-dependent movies for $f(\hat{u}, t)$ are also available.¹² During the towing process, the peak amplitude $f_p(t) = \max_{\varphi, \vartheta} f(\varphi, \vartheta, t)$ is constant and its polar angle $\varphi_p(t)$ is lagging behind the polar angle $\varphi_0(t)$ of $\hat{u}_0(t)$ as given by the solid and dotted lines in the right panel of Fig. 6.2(a). Obviously, the polar angles are only unique up to a multiple of π , therefore multiple lines are shown in the left panel of Fig. 6.2(a).

Above a threshold frequency, the peak amplitude $f_p(t)$ starts to oscillate with another internal “*breathing*” frequency ω_b different from ω_0 , see the dashed line in the right panel of Fig. 6.2(b). The position of the maximum $\varphi_p(t)$ follows the drive position $\varphi_0(t)$ with the same speed on average but has an internal breathing oscillation on top of that, see the solid line in the right panel of Fig. 6.2(b). The intuitive explanation of the breathing process is that the peak is dragged and pushed periodically by the two bracketing minima of the rotating potential.

If ω_0 is increased further, the peak of $f(\varphi, \vartheta, t)$ splits into two peaks in solid angle (φ, ϑ) -space. For this “*splitting*” a convenient order parameter is the maximal peak number

¹⁰See also chapter C for further information.

¹¹The towing behavior is qualitatively similar to the propagating soliton state found in a confined liquid crystal by C. Zheng and R. B. Meyer in Ref. [276].

¹²See supplementary material at <http://link.aps.org/supplemental/10.1103/PhysRevE.81.051703> for movies of the five phases over some cycles of the internal frequency in a dynamical state.

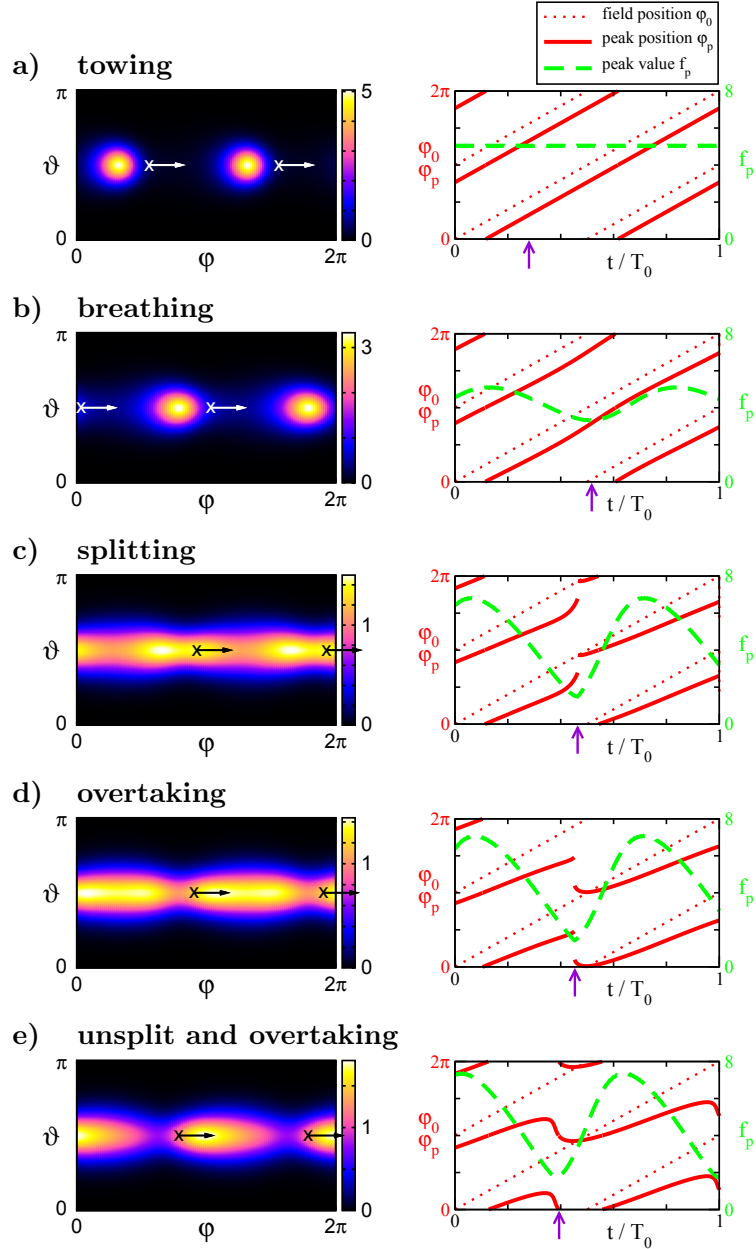


Figure 6.2: (Color) Left figures: orientational distribution function $f(\varphi, \vartheta, t)$ for fixed time given by the arrow on the time axis in the right figure. The cross shows the position of $\hat{u}_0(t)$. Right figures: polar angles of the peak maximum (solid line) and of $\hat{u}_0(t)$ (dotted line) and the peak amplitude f_p (dashed line) versus reduced time t/T_0 along one cycle of the driving potential. The parameters are $\rho^* = 0.5$ and $\omega_0\tau_B/2\pi = 0.8$ (a), 0.9 (b), 1.02 (c), 1.07 (d), 1.16 (e). This figure is reprinted with permission from Ref. [126] ©2010, The American Physical Society.

Table 6.1: Characterization of the different dynamical states via the breathing frequency ω_b , the splitting parameter \mathcal{N} and the averaged angular velocity ω_p of the peak.

	ω_b	\mathcal{N}	ω_p
towing	$= 0$	$= 1$	$= \omega_0$
breathing	> 0	$= 1$	$= \omega_0$
splitting	> 0	$= 2$	$= \omega_0$
overtaking	> 0	$= 2$	$< \omega_0$
unsplit and overtaking	> 0	$= 1$	$< \omega_0$

$\mathcal{N} = \max_t N_{\max}[f(\varphi, \vartheta, t)]$, where $N_{\max}[f(\varphi, \vartheta, t)]$ counts any maxima on a hemisphere (such that $N_{\max} = 1$ describes a monopeak and $N_{\max} = 2$ a split peak). A splitting state is shown in Fig. 6.2(c). The function $N_{\max}[f(\varphi, \vartheta, t)]$ is periodic in time with the internal breathing frequency ω_b . Since the angle $\varphi_p(t)$ corresponds to the peak of $f(\varphi, \vartheta, t)$ with maximal amplitude, it jumps during the splitting process (see right panel of Fig. 6.2(c)) which is associated with a cusp in $f_p(t)$. At higher ω_0 , this jump exceeds $\pi/2$. A unique function $\varphi_p(t)$ is composed by coupling branches of $\varphi_p(t)$ together such that their jump is always smaller than $\pi/2$. Using this function, a mean angular velocity of the peak maximum is defined by $\omega_p = \frac{1}{T_b} \int_0^{T_b} \dot{\varphi}_p(t) dt$, where $T_b = 2\pi/\omega_b$ is the breathing period. Therefore, when the jump exceeded $\pi/2$, the averaged angular velocity of the peak becomes $\omega_p < \omega_0$. This state is called “overtaking”, since the external field is faster than the orientational peak. A characteristic situation is plotted in Fig. 6.2(d). Finally, for even higher ω_0 , there is a monopeak again, a situation referred to as “unsplit and overtaking”. Here, there is no ambiguity in $\varphi_p(t)$ and again $\omega_p < \omega_0$. In this dynamical state, there is a simple relation between ω_0 , ω_b and ω_p which comes from the fact that during one cycle of breathing (cf. Fig. 6.2(e)) the peak position moves from one minimum of the potential backwards to the next one. This means a backward angular velocity of $\pi/T_b = \omega_b/2$. Hence, the difference between the angular velocity of the driving potential and the backward velocity of $\omega_b/2$ is then equal to the angular velocity ω_p of the peak, resulting in

$$\omega_0 = \frac{1}{2}\omega_b + \omega_p. \quad (6.3)$$

The relation (6.3) holds also in the towing state as a special case, where $\omega_b = 0$.

The different dynamical states are summarized in Table 6.1 together with their characterizing order parameters ω_b , \mathcal{N} and ω_p .

A nonequilibrium state diagram is shown in Fig. 6.3 as a function of external frequency ω_0 and reduced density ρ^* . There is a small density-dependent frequency band in which the cascade of different dynamical states occurs. In fact, the splitting phase is only found stable above a critical value of $\rho^* \approx 0.38$. For large ω_0 , the transitions tends to the equilibrium paranematic-nematic transition as shown by the arrow in Fig. 6.3.

In Fig. 6.4 the three order parameters are shown for a fixed density $\rho^* = 0.5$ (along the

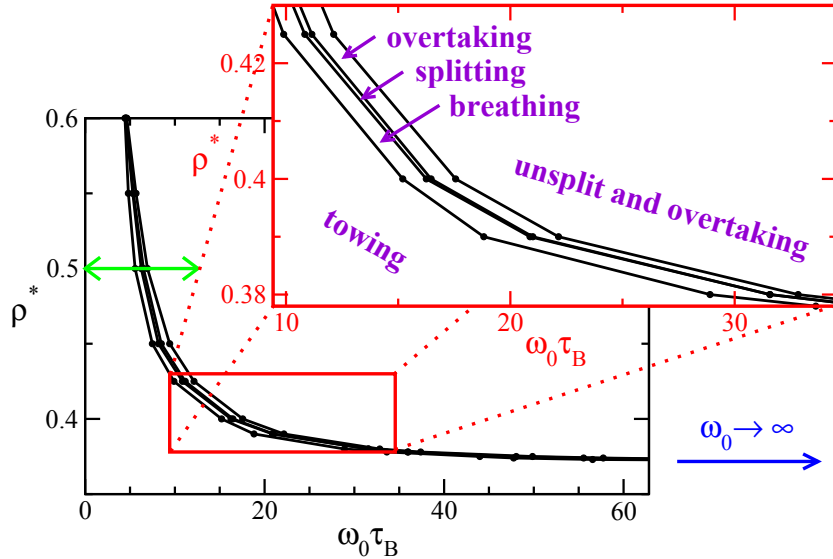


Figure 6.3: (Color) Nonequilibrium state diagram in the plane of driving frequency ω_0 and reduced density ρ^* . The double headed arrow at $\rho^* = 0.5$ is marking the range of (ω_0, ρ^*) for that snapshots were taken in Fig. 6.2. The arrow at the right side gives the position ($\rho^* \approx 0.3717$) of the static paranematic-nematic transition in the limit $\omega_0 \rightarrow \infty$. This figure is reprinted with permission from Ref. [126] ©2010, The American Physical Society.

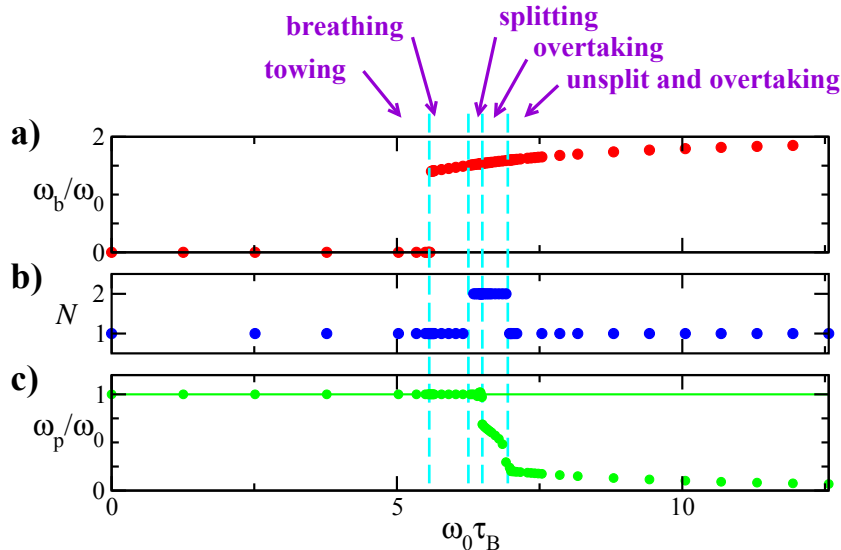


Figure 6.4: (Color) Behaviour of a) the breathing frequency ω_b , b) the splitting parameter N and c) the averaged angular velocity ω_p of the peak, shown against the external driving frequency ω_0 . The transitions are marked by the vertical slashed lines and the arrows are pointing at those frequencies ω_0 shown in Fig. 6.2. The density is $\rho^* = 0.5$ (double headed line in Fig. 6.3). This figure is reprinted with permission from Ref. [126] ©2010, The American Physical Society.

double headed line in Fig. 6.3). While the breathing frequency ω_b jumps discontinuously from the towing to the breathing state, it behaves continuously across the following transitions. Conversely, the angular velocity ω_p of the peak jumps twice discontinuously across the splitting→overtaking and the overtaking→unsplit transition.

6.2.3 Conclusion

In conclusion, an in-plane aligning field, which rotates with an external frequency ω_0 , gives rise to a complex dynamical orientational response of a colloidal liquid crystal with five different states characterized by towing, breathing, splitting, overtaking, and unsplit overtaking, as ω_0 increases. Finally, two applications of the dynamical response can be mentioned: First, in microfluidic devices, filled with a nematic liquid crystal [277], localized rotating driving fields can be used as micromixers, whose mixing efficiency can be conveniently steered by the external driving frequency, in particular in the regime of the *unsplit and overtaking* state. Second, if an electromagnetic wave is passing through a rotating nematic liquid crystal [278], its polarization can be amplified and nonlinearly changed by tuning the external drive frequency. The internal breathing state will mix another frequency to the wave coming out and the splitting state will induce further nonlinearities. Therefore, the dynamical states can in principle be exploited for the construction of smart switching and mixing devices. Moreover, dynamical states are expected for spherical colloids in traveling colloidal wave fields [279], where the equations of motion are formally similar [280]. It also would be interesting to resolve the spatial dependence of the density field. This is particularly important if system boundaries are included. Finally, a comparison to Brownian dynamics computer simulations of hard spherocylinders [281, 282] would provide a test for the dynamical theory proposed in this work.

6.3 Inhomogeneous fluids of colloidal hard dumbbells [104]

This section is mostly rewritten from the work *Inhomogeneous fluids of colloidal hard dumbbells: Fundamental measure theory and Monte Carlo simulations* by M. Marechal et al. [104], ©2011, American Institute of Physics. A statement about the individual contributions of the authors is given in the preface of this work.

Dumbbells, that consist of two fused hard spheres, are arguably the simplest non-convex colloids. A reason for investigating this model, apart from its simplicity, is that colloids with the exact shape of the dumbbell can be fairly easily synthesized. In fact, quite a few different synthesis methods have been successfully applied [283–285]. Colloidal dumbbells have been used to experimentally investigate bulk crystallization [286], quasi-two-dimensional degenerate crystals [285, 287, 288] and the effects of charge and an external electric field on a bulk crystal [289]. Furthermore, the phase behavior of bulk systems of

the dumbbells is well-known from simulations [290–294], which is convenient for further studies.

This section quotes the work of M. Marechal et al. [104] and is organized as follows: First, dumbbells are defined and the model of a system of dumbbells is described. Then, the additional approximations are shortly pointed out, which are made when considering non-convex particles instead of convex ones. Next, the Monte Carlo simulations are briefly described, including a definition of the density and orientational order profiles which are employed. Turning to the results, the reasonable agreement between edFMT results and simulation data for a dumbbell fluid near a wall is presented, when the adjustable parameter ζ in edFMT is set to zero. Finally, the effects of applying a gravitational field are briefly discussed.

6.3.1 Model and system parameters

In Ref. [104], a system of hard dumbbells is investigated, where the dumbbells are consisting of spheres of diameter σ , whose centers are separated by a distance $L \leq \sigma$. Accordingly, $L^* \equiv L/\sigma = 0$ corresponds to a single sphere, while the dumbbell consists of two touching spheres for $L^* = 1$. Moreover, the volume of a dumbbell is given by

$$v_{\text{db}} = \frac{\pi}{6} \left(\sigma^3 + \frac{3}{2}L\sigma^2 - \frac{1}{2}L^3 \right). \quad (6.4)$$

The systems of interest are considered to be inhomogeneous due to the presence of an external potential, resulting either from a gravitational field and a hard bottom wall or from two hard walls. Here, the direction of gravity and the normals to the walls are oriented along the z -direction. Moreover, only densities or chemical potentials below the crystallization transition are investigated [251, 294], such that the system is always fluid-like.

Now, the averaged packing fraction is fixed at $\eta = v_{\text{db}}N/(HA)$, if the external potential solely represents two hard walls. Here, N is the number of particles, H is the distance between the walls, and A is the area of the system perpendicular to the z direction. On the other hand, the averaged packing fraction η is zero, if the system is subjected to a gravitational field, because the system extends up to infinity in the positive z -direction. In this case, the chemical potential μ is held fixed.

The dimensionless chemical potential μ^* is defined as $\mu^* = \beta[\mu - \log(\mathcal{V}/4\pi\sigma^3)]$, where \mathcal{V} is the (irrelevant) thermal volume¹³ and $\beta = 1/k_B T$ an inverse temperature. The shift $-\log(\mathcal{V}/\sigma^3)$ removes the terms in the chemical potential that result from the integrals over the translational and angular momenta in the partition sum.¹⁴ The thermal wavelength has no effect on velocity-independent properties of the system in equilibrium, such as those that are investigated here. Moreover, the dimensionless strength of the gravitational

¹³For hard spheres, the thermal volume is $\mathcal{V} = \Lambda^3$ with Λ denoting the thermal de Broglie wavelength.

¹⁴See also Sec. 2.2.1.

field is defined as $g^* = mg\sigma/k_B T$, where m is the (buoyant) mass of the dumbbell and g is the gravitational acceleration. The definitions of μ^* and g^* are such that the density $\rho(z)$ at large z is given by $\lim_{z \rightarrow \infty} \rho(z)\sigma^3 = \exp(\mu^* - g^*z/\sigma)$, a dimensionless form of the barometric formula (also compare with Eq. (2.45)).

The systems are investigated using the edFMT approach from Sec. 3.4, extended to dumbbells as shown in the next section. In addition, standard Monte Carlo (MC) simulations in the *NVT* ensemble are applied for dumbbells between two walls [295]. In both methods, periodic boundary conditions are employed in the lateral directions.¹⁵

In principle, three values for L^* have been analyzed in Ref. [104]: 0.3, 0.6, and 0.9. The shape of the corresponding dumbbells varies from basically convex and similar to a spherocylinder for $L^* = 0.3$, to highly non-convex for $L^* = 0.9$. Additionally, a few other values of L^* have briefly been investigated, but no qualitative differences have been found. However, in this work only results for $L^* = 0.6$ are presented.

As shown in the next section, the density profile $\rho(z, \theta)$ is obtained from edFMT as a function of z and θ (see also Sec. C.1), due to the dependency of the orientations of the dumbbells. In principle, this profile can also be measured in Monte Carlo simulations, but as this is a function of two variables, plotting the results from Monte Carlo and edFMT in the same figure is difficult. Instead, the center-of-mass (com) density profile is shown, that is only a function of z . It reads

$$\eta_{\text{com}}(z) = \left\langle \frac{v_{\text{db}}}{A} \sum_i \delta(z - z_i) \right\rangle = \int \sin(\theta) \eta(z, \theta) d\theta, \quad (6.5)$$

where the first term denotes the method by which η_{com} is measured in the simulations and the second term the way of obtaining it from the local packing fraction $\eta(z, \theta) \equiv v_{\text{db}}\rho(z, \theta)$ which is obtained from edFMT.

6.3.2 Application of FMT to dumbbells

If edFMT (see Sec. 3.4) is applied to non-convex particles like dumbbells, some difficulties arise that are explicitly written down in Ref. [104]. Now, the distance $R_\nu(\hat{r})$ is defined as a vector which points from a reference point $C_i = \vec{r}_\nu^{(0)}$ in the center of a particle along a ray \hat{r} to the surface of the particle. It should be noted that the definition of the surface in terms of this vector $R_\nu(\hat{r})$ is ambiguous for some non-convex particles, as some rays may cross the surface of the particle in more than one point. In this case, the weighted densities can no longer be written as a convolution such as in Eq. (3.35), and they should be defined as

$$n_\alpha(\vec{r}) = \sum_\nu \begin{cases} \int_{\mathcal{B}_\nu} \rho_\nu(\vec{r} - \vec{r}') d\vec{r}' & \text{for } \alpha = 3 \\ \int_{\partial\mathcal{B}_\nu} \rho_\nu(\vec{r} - \vec{R}_\nu(\hat{s})) \bar{w}_\nu^{(\alpha)}(\hat{s}) d\vec{s} & \text{otherwise,} \end{cases} \quad (6.6)$$

¹⁵For further information about the methods, see Ref. [104].

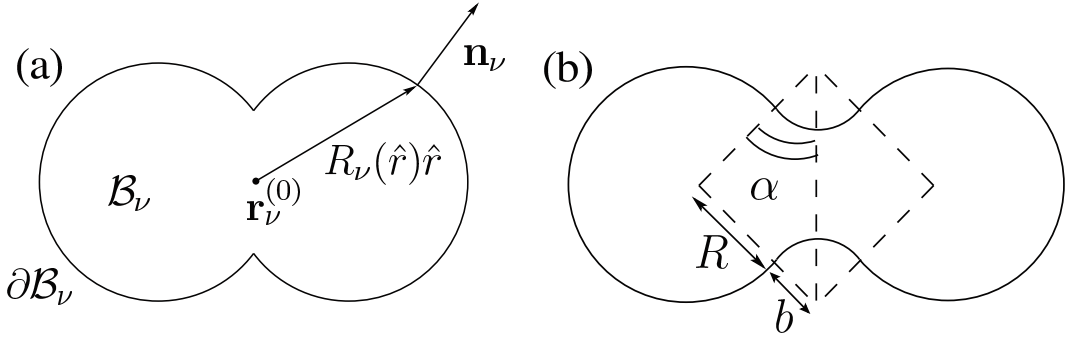


Figure 6.5: (a) The surface $\partial\mathcal{B}_\nu$ of a body \mathcal{B}_ν is parametrized by a unit vector \hat{r} , such that the corresponding point on the surface is $\vec{R}_\nu(\hat{r}) = R_\nu(\hat{r})\hat{r}$. The normal at this point is denoted by $\hat{n}_\nu(\hat{r})$. (b) The kink in the surface of a dumbbell is regularized by replacing it by a section of a torus, as indicated by the small arcs. The torus has a tube radius of b and the dumbbell is recovered in the limit $b \rightarrow 0$. This figure is reprinted with permission from Ref. [104] by M. Marechal et al. ©2011, American Institute of Physics.

where \mathcal{B}_ν is a particle of species/orientation ν and $\hat{s} \equiv \vec{s}/|\vec{s}|$. Here, $\partial\mathcal{B}_\nu$ is its surface, parametrized by \hat{s} , and $d\vec{s}$ is a surface element. Furthermore, the functions $\bar{w}_\nu^{(\alpha)}$ denote the weight functions $w_\nu^{(\alpha)}$ for $\alpha \neq 3$, where the factor $w_\nu^{(2)}$ has been removed ($\bar{w}_\nu^{(2)}(\vec{s}) = 1$).¹⁶

Now, one-component systems of dumbbells is considered, where $\hat{u} \in S^2$ is the orientation of a dumbbell on the unit sphere S^2 . Accordingly, the sum over ν is replaced by an integration $\int d\hat{u}$ and the density profile becomes $\rho(\vec{r}, \hat{u})$. A difficulty arises for dumbbells in evaluating the weight functions at the “neck” of the particle, i.e., the intersection circle between the partial spherical shells that the surface of the dumbbell consists of, since the curvature on this circle is ill-defined. To circumvent this problem, the dumbbell is redefined as the limit of a particle with a smooth surface for which the “neck” is replaced by some inner section of a torus, as shown in Fig. 6.5(b). After performing this limit, the scalar, the vector, and the tensor weighted densities n_α for $\alpha = 0, 1, 2$ can be expressed as

$$\begin{aligned} n_\alpha(\vec{r}) &= \int_{S^2} \left\{ \sum_{m=+,-} \int_{S_m^2(\hat{u})} R^2 \bar{w}_h^{(\alpha)}(\hat{s}, \hat{u}) \rho \left(\vec{r} - m \frac{L}{2} \hat{u} - \hat{s} \frac{\sigma}{2}, \hat{u} \right) d\hat{s} \right. \\ &\quad \left. + \int_{C(\hat{u})} \bar{w}_c^{(\alpha)}(l, \hat{u}) \rho(\vec{r} - R_c \hat{n}_c(l, \hat{u}), \hat{u}) dl \right\} d\hat{u}, \end{aligned} \quad (6.7)$$

where $S_m^2(\hat{u})$ consist of all \hat{s} on the unit sphere, such that $m\vec{s} \cdot \hat{u} > -L/\sigma$ (this is one half of the surface of a dumbbell). Here, $C(\hat{u})$ is the circle where the curvature has a singularity, l parametrizes $C(\hat{u})$, $R_c \equiv \sqrt{R^2 - L^2/4}$ is the radius of the circle $C(\hat{u})$, and $\hat{n}_c(l)$ is the outward normal to this circle in the plane perpendicular to \hat{u} . The functions

¹⁶In detail, the functions are listed in Ref. [104] for dumbbells.

$\bar{w}_h^{(\alpha)}$ are integrated over one half of the surface of a dumbbell in Eq. (6.7) and they read

$$\bar{w}_h^{(0)}(\hat{s}, \hat{u}) = 1/(4\pi R^2), \quad (6.8)$$

$$\bar{w}_h^{(1)}(\hat{s}, \hat{u}) = 1/(4\pi R), \quad \bar{w}_h^{(2)}(\hat{s}, \hat{u}) = 1, \quad (6.9)$$

$$\vec{w}_h^{(1)}(\hat{s}, \hat{u}) = \hat{s}/(4\pi R), \quad \vec{w}_h^{(2)}(\hat{s}, \hat{u}) = \hat{s}, \quad (6.10)$$

$$\overleftrightarrow{w}_h^{(1)}(\hat{s}, \hat{u}) = \vec{0}, \quad \overleftrightarrow{w}_h^{(2)}(\hat{s}, \hat{u}) = \hat{s} \cdot \hat{s}^t, \quad (6.11)$$

which are just the weight functions of a sphere (compare with Eq. B.1-B.7). The functions $\bar{w}_c^{(\alpha)}$ are integrated over the “neck” of the dumbbell and are given by

$$\bar{w}_c^{(0)}(l, \hat{u}) = -L^*/(2\pi R_c), \quad (6.12)$$

$$\bar{w}_c^{(1)}(l, \hat{u}) = -\alpha_0/(4\pi), \quad (6.13)$$

$$\bar{w}_c^{(2)}(l, \hat{u}) = 0, \quad (6.14)$$

$$\vec{w}_c^{(1)}(l, \hat{u}) = -\mathbf{n}_c(l)L^*/(4\pi), \quad (6.15)$$

$$\vec{w}_c^{(2)}(l, \hat{u}) = \vec{0}, \quad (6.16)$$

$$\begin{aligned} \overleftrightarrow{w}_c^{(1)}(l, \hat{u}) &= \frac{1}{4\pi} \left[\alpha_0 \mathbb{I} - \left(\frac{3}{2}\alpha_0 + \frac{1}{4}\sin(2\alpha_0) \right) \hat{u} \cdot \hat{u}^t \right. \\ &\quad \left. - \left(\frac{3}{2}\alpha_0 - \frac{1}{4}\sin(2\alpha_0) \right) \hat{n}_c(l) \cdot \hat{n}_c(l)^t \right], \end{aligned} \quad (6.17)$$

$$\overleftrightarrow{w}_c^{(2)}(l, \hat{u}) = \vec{0}. \quad (6.18)$$

Here, $L^* = L/\sigma$, $\alpha_0 = \lim_{b \rightarrow 0} \alpha(b) = \arcsin(L/\sigma)$, and \mathbb{I} is the 3×3 unit matrix.

Moreover, the systems of inhomogeneous fluids are subjected to a one-dimensional external potential $V_{\text{ext}}(z)$, where \hat{z} is the direction in which the external potential varies. For this reason, the density profile only depends on z and on the angle θ between \hat{z} and the orientational vector \hat{u} of a particle. Accordingly, the integral over \hat{s} in Eq. (6.7) reduces to an integral over z' and θ and follows as

$$n_\alpha(z) = \iint v^{(\alpha)}(z', \theta) \rho(z - z', \theta) dz' d\theta, \quad (6.19)$$

where the modified weight functions $v^{(\alpha)}$ are obtained analytically by splitting the integrals in Eq. (6.7) into slices perpendicular to the z -axis, over which the weight functions can be integrated as the density only depends on z . Finally, the density profile is normalized such that $A \iint \rho(z, \theta) dz d\theta = N$, where θ runs from 0 to $\pi/2$ due to the up-down symmetry of the dumbbells.

The difficulties that arise due to the intersections of non-convex particles are discussed in detail in Ref. [104]. As already mentioned in Sec. 6.1, the free parameter ζ that enters the theory is set to zero for the calculations concerning dumbbells [104]. However, in the Results section of Ref. [104] and in the next section, it is shown that edFMT is still a

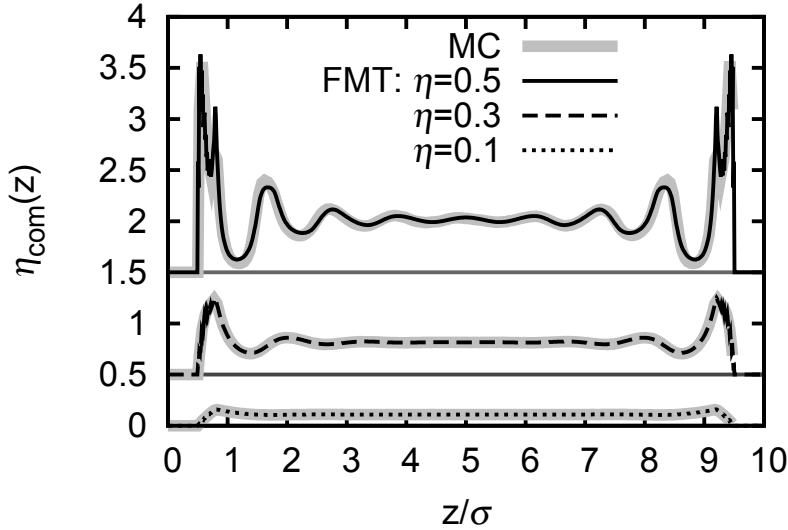


Figure 6.6: The center-of-mass density profile of dumbbells with an aspect ratio $L^* = 0.6$ for three different packing fractions: $\eta = 0.1, 0.3$, and 0.5 . The black lines denote the edFMT results, while the circles denote the MC results. The results for $\eta = 0.3$ and 0.5 are shifted upwards by 0.5 and 1.5 , respectively, for clarity of display. This figure is reprinted with permission from Ref. [104] by M. Marechal et al. ©2011, American Institute of Physics.

surprisingly good density functional theory, in spite of these difficulties.

6.3.3 Results for hard walls and gravity

The results shown in this section are rewritten from the work *Inhomogeneous fluids of colloidal hard dumbbells: Fundamental measure theory and Monte Carlo simulations* by M. Marechal et al. [104]. The fluid equation of state for hard dumbbells has been analyzed in Ref. [104] to learn more about the extended edFMT functional approach for non-convex particles. The edFMT features a free parameter ζ , which has to be nonzero, to obtain a stable nematic phase even for very elongated particles. Adjusting it has been shown to lead to unrealistically large values for ζ , presumably because the full theory is not valid for non-convex particles like dumbbells.¹⁷ However, the theory with $\zeta = 0$ gives excellent results when compared to MC simulations for not too large packing fractions. The agreement is somewhat worse than that obtained for spherocylinders in Ref. [105], but it is better than the results obtained for dumbbells in a slit compared to a previous DFT study of hard dumbbells near a hard wall [252]. For this reason, the free parameter ζ is used with $\zeta = 0$ in this section. Moreover, the minimization of the grand potential Ω (2.38) is performed iteratively, as described in Sec. C.1.

¹⁷See also Sec. 6.1 and Ref. [104].

The structure of a fluid confined between two hard walls has been investigated by means of simulations and edFMT. The resulting center-of-mass density profile for $L^* = 0.6$ is shown in Fig. 6.6 for three packing fractions η (results for additional aspect ratios L/σ are shown in Ref. [104]). At the lowest packing fraction, the main effect of the elongation of the particles is an entropy reduction when particles are close to the wall, due to a decrease in the available orientations. This effect pushes the particles away from the wall, while the presence of the other particles pushes them towards the wall. This competition causes the first peak to be located slightly away from $z = \sigma/2$, which is the position of the first peak for hard spheres near a hard wall. As the density increases, more peaks in the density profile appear, indicative of layering. For the larger aspect ratios $L/\sigma = 0.6$ and 0.9 and at the highest packing fraction $\eta = 0.5$, the density profile shows an intricate structure as the layering of the spheres of which the dumbbells consist competes with the layering of the center of mass [251]. This causes a splitting of the first peak near the wall, where the two resulting peaks can be ascribed to the primarily horizontal ($z \simeq \sigma/2$) and vertical ($z \simeq (\sigma + L)/2$) orientations.

All observed peaks in the profiles obtained from the simulations are reproduced in the FMT results and the agreement between the two profiles is excellent for all but the highest density near the wall. This highest density $\eta = 0.5$ is considerably higher than the densities investigated by H. Hansen-Goos and K. Mecke for hard spherocylinders, which is 0.346 at most [28, 105]. For this reason, the deviations from the MC results can not certainly be said to be caused by the non-convex nature of the dumbbells, as the theory has not been tested for inhomogeneous systems of convex particles at such high densities.

Moreover, the results for the center-of-mass profile have been compared with the results obtained by D. Henderson et al. [252] (not shown) and both DFT approaches show a reasonable qualitative agreement for all aspect ratios and densities considered. Although, the characteristic splitting of the first peak seems to be absent in the theory of Ref. [252] for the larger aspect ratios. Quantitatively, edFMT also seems to perform a bit better than the older DFT approach [252].

In addition, results from MC simulations are compared with results from edFMT for dumbbells under gravity in Fig. 6.7. As presented in Ref. [104], only the results for $g^* = 2$, $\mu^* = 20$, and $L^* = 0.6$ are shown, because the density profiles for different gravitational force, chemical potential, and L are similar (except for the behavior at the wall). However, the behavior at the wall is similar to the results obtained in the absence of gravity, which becomes apparent by comparing Fig. 6.6 for $\eta = 0.5$ with Fig. 6.7. The bulk density that corresponds to $\mu^* = 20$ is $\eta = 0.491$ for FMT and the MC bulk packing fraction is 0.500, which differs from the FMT packing fraction due to the differences between the bulk equations of state [104]. The difference of about 0.01 between these volume fractions causes an additional small error in the edFMT density profile under gravity if compared to the results with two hard walls, where the average packing fraction was used as an input parameter. This effect seems to be small, which can be seen by comparing the deviation between the MC data and the theory in the absence of gravity with that for dumbbells under gravity, shown in Fig. 6.6 for $\eta = 0.5$ and in Fig. 6.7.

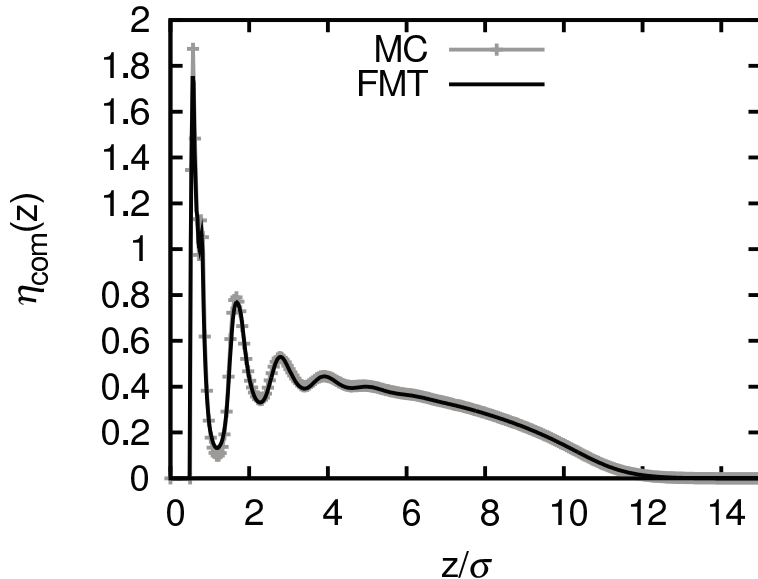


Figure 6.7: The center-of-mass density profile for dumbbells ($L^* = 0.6$, $\mu^* = 20$) under gravity ($g^* = 2$) in units of the volume of a dumbbell and as a function of the height z . Simulation results are denoted by the gray crosses and the edFMT results (with $\zeta = 0$) by the black line. This figure is reprinted with permission from Ref. [104] by M. Marechal et al. ©2011, American Institute of Physics.

6.3.4 Conclusion

Inhomogeneous fluids of hard dumbbells have been analyzed in a slit and under gravity [104] by using the extended deconvolution FMT [28]. The edFMT features a free parameter ζ , which has to be nonzero, to obtain a stable nematic phase even for very elongated particles. Adjusting it has been shown to lead to unrealistically large values for ζ , presumably because the theory is not valid for non-convex particles like dumbbells. However, the theory with $\zeta = 0$ gives excellent results when compared to MC simulations for not too large packing fractions. The agreement is somewhat worse than that obtained for spherocylinders in Ref. [105], but it is better than the results obtained for dumbbells in a slit compared to a previous DFT study of hard dumbbells near a hard wall [252]. At very large packing fraction ($\eta = 0.5$), the theory still predicts the positions of the various density peaks well, but does not always predict the correct height for the peaks. Additionally, the possibility of choosing a nonzero value for ζ is investigated, but it leads to additional effort in evaluating the free energy functional, which does not seem justified considering the limited effect for inhomogeneous fluids of dumbbells that are not very elongated.

The FMT-density functional for hard dumbbells, which was constructed and explored in Ref. [104], can serve as a starting point for further studies. These future topics should include the full bulk freezing diagram including plastic and full crystalline phases of hard dumbbells. The functional itself might be improved by adjusting it such that it yields the excellent Carnahan-Starling equation (see Sec. 3.2.3) for the homogeneous fluid in the

hard-sphere limit [27, 113].

Moreover, the functional can be used as a reference system for an additional attractive interaction, which possibly leads to gas-liquid phase separation. For instance, the attractions are treatable within a mean-field perturbation theory [96, 296–298]. Furthermore, a dipolar interaction force [299] can be added on top of the dumbbell and can again be treated in DFT by a mean-field theory [300]. Moreover, Brownian dynamics (both translational and orientational) [301] can be explored by dynamical density functional theory, where a good static functional is needed as an input [57, 125, 126]. Finally, other particle shapes can be described using FMT-like functionals, like platelets [302], cubes [303], tetrahedra [304], or helical particles [305]. This finally leads to a full microscopic theory of the phase behavior of anisometric particles.



Have fun on sea and land
Unhappy it is to become famous
Riches, honors, false glitters of this world
All is but soap bubbles

(from: *Nobel Lectures, Pierre-Gilles de Gennes 1932 - 2007*)

Conclusion

In this work about *density functional theory of hard colloidal particles*, spheres, spherocylinders, and dumbbells have been investigated in the bulk and at interfaces. Therefore, the theoretical framework of density functional theory (DFT) and fundamental measure theory (FMT) has been applied to hard-sphere systems, where free energies and density distributions were obtained for the (fcc) crystal and the fluid phase by using FMT functionals. The free energies are in good agreement with Monte Carlo (MC) simulation results and demonstrate the applicability of the functionals to the treatment of other problems involving crystallization. Moreover, the agreement between FMT and simulations on the level of free energies is also reflected in the density distributions around single lattice sites. While the peak widths and anisotropy shapes for different lattice directions agree, it is found that FMT gives slightly narrower peaks with more anisotropy than seen in the simulations. In addition, from the studied variants of FMT only the White Bear mark II (WBII) functional shows qualitatively correct behavior, whereas the Rosenfeld and the White Bear functional give qualitative incorrect results. This implies that only the WBII functional is a promising candidate for further studies, such as the free minimization of the crystal-fluid interface or nucleation processes.

Accordingly, accurate values for the anisotropic hard-sphere crystal-fluid surface tensions and stiffnesses have been predicted by using the accurate WBII approach in combination with MC computer simulations. The full equilibrium density profiles have been obtained within FMT from a free minimization. Thus, the complete structure of the crystal-fluid phase transition is available. Regarding the interfacial tensions and stiffnesses, quantitative agreement between FMT and simulations is found and FMT predicts a tension of $0.66 k_B T / \sigma^2$ with a small anisotropy of about $0.025 k_B T$. The corresponding stiffnesses are determined with e.g. $0.53 k_B T / \sigma^2$ for the (001) orientation and $1.03 k_B T / \sigma^2$ for the (111) orientation of the interface, where $k_B T$ is the thermal energy and σ is the diameter of the hard spheres. However, the anisotropy in the tension of about 10% is crucial for the transformation to stiffnesses, which differ up to a factor of 4. Moreover, the results from theory and simulation are compared with existing experimental findings and classical nucleation theory is discussed in the context of analyzing experimental results.

In another sense, FMT has also been applied to non-spherical particles. For this purpose, the recently developed extended deconvolution FMT (edFMT) has been applied

to systems of orientationally resolved spherocylinders and dumbbells. The spherocylinders are assumed to constitute a fluid phase with the possibility of orientational ordering and are subjected to an in-plane aligning field which rotates with an external frequency ω_0 . Consequently, the system is investigated by using dynamical DFT, an extension of DFT to non-equilibrium, time-dependent situations. The setup causes a complex orientational response of the colloidal liquid crystal with five different dynamical states which are characterized by towing, breathing, splitting, overtaking, and unsplit overtaking, as ω_0 increases.

Applied to hard dumbbells, inhomogeneous fluids are analyzed in a slit and under gravity [104]. The edFMT features a free parameter ζ , which has to be nonzero, to obtain a stable nematic phase even for very elongated particles. Adjusting it has been shown to lead to unrealistically large values for ζ , presumably because the theory is not valid for non-convex particles like dumbbells. However, the theory with $\zeta = 0$ gives excellent results when compared to MC simulations for not too large packing fractions. The agreement is somewhat worse than the one obtained for spherocylinders in Ref. [105], but it is better than the results obtained for dumbbells in a slit compared to a previous DFT study of hard dumbbells near a hard wall [252]. At very large packing fraction ($\eta = 0.5$), the theory still predicts the positions of the various density peaks well, but does not always predict the correct height for the peaks. Additionally, the possibility of choosing a nonzero value for ζ is investigated, but it leads to additional effort in evaluating the free energy functional, which does not seem justified considering the limited effect for inhomogeneous fluids of dumbbells that are not very elongated.

Finally, numerical methods to solve the equation of state in DFT are discussed in the appendix of this work. Due to the structure of FMT functionals, the highly localized density peaks in a crystal cause critical numerical behavior where local packing fractions exceed physical values. Unfortunately, this behavior leads to a divergence of the FMT functional. For this reason, methods are outlined to avoid problems within this critical limit and to ensure convergence of solutions.

This numerical knowledge can help to set up adequate software packages, such as *Tramonto*. The software project provides DFT based “computational tools for predicting the structure and properties of fluids at the nanoscale near surfaces and macromolecules”.¹ In this context, a detailed analysis of the numerical perturbations that were observed within FMT may help to perform further numerical studies, for example in the presence of walls, where similar instabilities occur as observed in calculations regarding the crystalline phase. The observed deviations between simulations and FMT also point to possibilities of further improvement in the FMT functionals. In this sense, a promising ansatz is given by re-summing the virial expansion to obtain the Rosenfeld functional as the first order term of an expansion [110, 111]. As the knowledge of accurate functionals is important, the FMT functional for hard dumbbells can serve as a starting point for future studies, which should contain the full bulk freezing diagram including plastic

¹See Sandia National Laboratories web page, <https://software.sandia.gov/DFTfluids/>

and full crystalline phases. Moreover, other particle shapes should be described by using FMT-like functionals, for example platelets [302], cubes [261, 303], tetrahedra [304], and helical particles [305]. This finally will lead to a full microscopic theory of the phase behavior of anisometric particles.

In another sense, regarding the observation of the five dynamical phases in the system of hard spherocylinders, two applications of the dynamical response could be mentioned: First, in microfluidic devices filled with a nematic liquid crystal [277] localized rotating driving fields may be used as micromixers. Their mixing efficiency can be conveniently controlled by the driving frequency of the external fields, in particular in the regime of the *unsplit and overtaking* state. Second, if an electromagnetic wave is passing through a rotating nematic liquid crystal [278], its polarization can be amplified and nonlinearly changed by tuning the frequency of the external driving field. Then, the internal breathing state will add a second frequency to the original wave and the splitting state will induce further nonlinearities. Therefore, the dynamical states can in principle be exploited for the construction of smart switching and mixing devices. Moreover, dynamical states are expected for spherical colloids in traveling colloidal wave fields [279], where the equations of motion are formally similar [280]. It would also be interesting to resolve the spatial dependence of the spherocylinders' density field, which is particularly important if system boundaries are included. Furthermore, a comparison to Brownian dynamics computer simulations of hard spherocylinders [281, 282] would provide a test for the dynamical theory proposed in this work.

However, changes of the shape of the crystal-fluid interface are controlled by the anisotropic tensions of the hard-sphere system. Thus, the precise quantitative determination of the tensions helps to understand crystal nucleation [185, 225] and the transport of larger carriers through the interface. Furthermore, the obtained results can help to clarify apparent discrepancies found in real-space experiments of sterically-stabilized colloidal suspensions [9–12]. At the same time, results can serve as input to phase-field-crystal calculations which explore dynamics such as solidification processes on very large length and time scales [90, 226, 227]. For this reason, it is necessary to improve the methods that are used in experiments to determine the interfacial tensions and stiffnesses precisely, since further studies are needed to confirm the results obtained for the hard-sphere crystal-fluid interface in this work.

Future work should also address soft interactions and attractions (as relevant, e.g. for colloid-polymer mixtures), in order to scan the full range from a fluid-crystal to a vapor-crystal interface. Further extensions may be done along similar ideas as used and proposed here for binary mixtures as well as for crystalline structures different from fcc, such as bcc and hcp. Furthermore, the recent extension of DFT towards translational and orientational Brownian dynamics was used to describe the growth of tumors [306], which may be of great significance for medical science. Accordingly, accurate static functionals are needed as an input. And finally, DDFT can be used to explore the time-dependent growth kinetics and relaxation towards equilibrium for the hard-sphere crystal-fluid interface.

Il libro della natura è scritto in lingua matematica.

(from *Il Saggiatore*, Galileo Galilei 1564-1642)

APPENDIX



Mathematics

In this chapter, mathematical topics are introduced and discussed, supporting the content of this work. Almost all topics can be found in mathematical textbooks, as for example Ref. [307] by E. H. Lieb and M. Loss. However, two important definitions are given right now before the begin of the first section, because they are of import for all following contents.

First, function spaces are used in this work to define functional derivatives and the density profiles that are used in DFT. In this context, the L^p -space of measurable functions is an important function space. It is defined as [307]

$$L^p(\mathbb{R}^n) = \left\{ f : \mathbb{R}^n \rightarrow \mathbb{C} \mid f \text{ measurable (thus } > 0), \int |\mathbf{f}|^p < \infty \right\} \quad (\text{A.1})$$

along with the L^p -norm

$$\|f\|_p = \left(\int_{\mathbb{R}^n} |f(x)|^p dx \right)^{1/p}. \quad (\text{A.2})$$

Second, a spherical parametrization is used to apply explicit calculations as performed in Chapter B. In this work, it is defined as

$$\vec{r} = \begin{pmatrix} r_x \\ r_y \\ r_z \end{pmatrix} = |\vec{r}| \begin{pmatrix} \cos(\varphi) \sin(\vartheta) \\ \sin(\varphi) \sin(\vartheta) \\ \cos(\vartheta) \end{pmatrix}, \quad (\text{A.3})$$

parametrizing the three-dimensional vector $\vec{r} \in \mathbb{R}^3$ with the spherical coordinates $(|\vec{r}|, \varphi, \vartheta)$. The locally defined and normalized unit vectors in Euclidean space, pointing along the variations of the spherical coordinates, are

$$\hat{e}_\vartheta = \begin{pmatrix} \cos(\vartheta) \cos(\varphi) \\ \cos(\vartheta) \sin(\varphi) \\ -\sin(\vartheta) \end{pmatrix}, \quad \hat{e}_\varphi = \begin{pmatrix} -\sin(\varphi) \\ \cos(\varphi) \\ 0 \end{pmatrix}, \text{ and } \hat{e}_r = \frac{\vec{r}}{|\vec{r}|}, \quad (\text{A.4})$$

where $|\vec{r}| = r$. In addition, the metric tensor follows with

$$g = \begin{pmatrix} 1 & 0 & 0 \\ 0 & r^2 \sin^2(\vartheta) & 0 \\ 0 & 0 & r^2 \end{pmatrix} \quad (\text{A.5})$$

and the corresponding gradient operator reads

$$\nabla = \hat{e}_r \frac{\partial}{\partial r} + \hat{e}_\vartheta \frac{1}{r} \frac{\partial}{\partial \vartheta} + \hat{e}_\varphi \frac{1}{r \sin(\vartheta)} \frac{\partial}{\partial \varphi}. \quad (\text{A.6})$$

In the following sections, first *Gibbs inequality* is explained in Sec. A.1, which is needed while presenting DFT. Functionals and its derivatives are defined and discussed in Sec. A.2. Then, rotated unit cells are constructed in Sec. A.3 in close connection to the definition of unit cells and crystalline structures in Sec. 4.1. In addition, the properties of an fcc lattice and a rectangular cuboid unit cell are summarized in Table 4.1. Finally, Fourier transformations and convolutions are defined in Sec. A.4.

A.1 Gibbs inequality

Let Tr be a trace on a measurable space Γ and let p and q be probability distributions on Γ with $p \neq q$ that are locally nonzero.¹ Accordingly, they hold $\text{Tr } p = \text{Tr } q = 1$. Then the inequality

$$\text{Tr}(p \log(q)) < \text{Tr}(p \log(p)) \quad (\text{A.7})$$

is called a *Gibbs inequality* (or Gibbs-Bogoliubov inequality)² and is a consequence of the convexity of the negative logarithm function. This becomes obvious by deducing Gibbs inequality from *Jensen's inequality* that reads [307]

$$\langle J \circ f \rangle \geq J(\langle f \rangle) \quad (\text{A.8})$$

for $J : \mathbb{R} \rightarrow \mathbb{R}$ being a convex function, f being a real-valued and integrable function on some set Ω that is measurable and has finite measure, and an average $\langle \dots \rangle$. Moreover, equality only holds for a constant function f .

To perform the deduction,³ the convex function is set to $J = -\log$ and the real-valued function to $f = q/p$ that is not constant due to the assumption $q \neq p$. Thus, Jensen's

¹The assumption of a local non-vanishing probability distributions is needed for the deduction. For ergodic systems, the phase space distribution function is locally nonzero.

²See Appendix B in the textbook of J.-P. Hansen and I. R. McDonald [39].

³An outline of the deduction is given in Wikipedia, Jensen's inequality, accessed on August 25th 2012.

inequality (A.8) reads

$$\int_{\Gamma} p(\psi) \log \left(\frac{p(\psi)}{q(\psi)} \right) d\psi > -\log \left(\int_{\Gamma} p(\psi) \frac{q(\psi)}{p(\psi)} d\psi \right). \quad (\text{A.9})$$

Due to $\text{Tr } q = 1$, the right-hand side of Eq. (A.9) is zero and consequently, it follows

$$\Rightarrow \int_{\Gamma} p(\psi) \log \left(\frac{p(\psi)}{q(\psi)} \right) d\psi > 0 \quad (\text{A.10})$$

$$\Rightarrow - \int_{\Gamma} p(\psi) \log (q(\psi)) d\psi > - \int_{\Gamma} p(\psi) \log (p(\psi)) d\psi. \quad (\text{A.11})$$

Finally, using $\text{Tr}[A] \equiv \int_{\Gamma} A d\psi$ (for an integrand A) Gibbs inequality (A.7) follows.

A.2 Functionals and its derivatives

A functional is a scalar valued mapping F defined on a subset $D(F)$ of a vector space. Thus, functionals are a limited form of operators, since operators are mappings between general vector spaces, where functionals only have a scalar valued range, usually real or complex valued. Nevertheless, the domain $D(F)$ typically is a function space.

Examples for functionals are various. Thus, a simple functional is given by the function $\delta_x : f \mapsto f(x)$ that maps a function f to its value at position x . A second example is given by the L^p -norm $f \mapsto (\int |f|^p dx)^{1/p}$ on a normed function space.⁴ And last, functionals are often given by integration operations, as used for the determination of the area below a graph of a positive function f on a certain interval I , given by $f \mapsto \int_I f(x) dx$.

Functionals are often found in the field of optimization. For example, the principle of minimal action is well-known from physics, where a Lagrangian function is searched that minimizes the action functional. In the context of this work, the minimization of the energy functional w.r.t. a density distribution function is of interest, because the minimizing function represents a stable solution of the corresponding physical system in equilibrium. Accordingly, the variation of functions becomes important and gives rise to the definition of a functional derivative, to find extremal curves that minimize (or maximize) the functional.⁵

This section is structured as follows: First, variations are defined, following the textbook of D. R. Smith [309] that gives a well-written introduction to functionals and to the whole concept of variations and functional derivatives. Second, functional derivatives are defined based on distributions,⁶ following Chapter 6 of the textbook of E. H. Lieb and M. Loss

⁴See E. H. Lieb and H. Loss [307], page 42.

⁵A well-written outline about the calculus of variations is given in a German textbook by H. Fischer and H. Kaul [308].

⁶Distributions are continuous linear functionals and are useful for a rigid mathematical definitions of functional derivatives.

[307]. Finally, examples are given that are of impact in the context of this work.

In addition, the particle density or particle distribution function (2.25) of a system with volume V is an element of the space $C(V)$ of continuous functions on V . It is defined as a real-valued function on a compact Hausdorff space. Since it is a complete⁷ normed vector space, $C(V)$ also is a Banach space.⁸ Thus, it satisfies the assumptions required in the following definitions.

A.2.1 Variations and generalized derivative

For functions between Banach spaces, the Fréchet derivative can be defined.⁹ Hence, a functional $F : \Pi \rightarrow \mathbb{R}$ is called Fréchet differentiable at a point $f \in \Pi$ on an open subset $\Pi \subset C(V)$, if a bounded linear operator $A_f : C(V) \rightarrow \mathbb{R}$ exists with

$$\lim_{n \rightarrow \infty} \frac{|F[f + h_n] - F[f] - A_f(h_n)|}{\|h_n\|_{C(V)}} = 0 \quad (\text{A.12})$$

for all sequences $\{h_n\}_{n=0}^{\infty}$ with $\lim_{n \rightarrow \infty} h_n = 0$ and $h_n \in \Pi$. If the limit exists, the operator $\delta F[f] := A_f$ is called the (Fréchet) derivative of the functional F and is unique. Even more, the chain rule is valid for the Fréchet derivative, due to its linearity.

The Gâteaux variation or Gâteaux differential provides a generalization of the directional derivative of functions, more general than the Fréchet derivative.¹⁰ Thus, a functional F on an open subset U of a normed real vector space X has a Gâteaux variation (or differential) $\delta F[f]$ at f , if the limit

$$\lim_{\epsilon \rightarrow 0} \frac{F[f + \epsilon h] - F[f]}{\epsilon} = \delta F[f; h] \quad (\text{A.13})$$

exists for all vectors $h \in X$ and $\epsilon \in \mathbb{R}$. Its values $\delta F[f; h]$ are defined for all vectors $h \in X$ and the functional is said to be Gâteaux differentiable at f .

If the Fréchet derivative $\delta F[f]$ exists at a point $f \in \Pi$, then the Gâteaux differential also exists at f and they are equal (identifying $C(V)$ with X). Thus, the same notation is used for the Gâteaux variation and for the Fréchet derivative. Consequently, if Fréchet differentiability is given, the derivative can also be calculated by a Gâteaux variation for one certain vector $h \in C(V)$.

The Gâteaux differential can be written in a more simple form for a real-valued functional F with existing Gâteaux differential. Then, the Gâteaux differential of F is a functional

⁷A space X is complete, if every Cauchy sequence has a limit in X .

⁸See D. G. Luenberger in Ref. [310], Example 3 in Sec. 2.11.

⁹See *Optimization by vector space methods* by D. G. Luenberger [310], Chapter 7.

¹⁰See D. R. Smith in Ref. [309], p. 35, Sec. 2.2, and D. G. Luenberger in [310], Chapter 7.

with respect to $h \in X$ for each fixed $f \in U$ and reads¹¹

$$\delta F[f; h] = \left. \frac{d}{d\epsilon} F[f + \epsilon h] \right|_{\epsilon=0}. \quad (\text{A.14})$$

A.2.2 Functional derivatives

The term $\delta F/\delta f$ denotes the functional derivative of the functional F with respect to a function f . In general, it is already given by the derivative $\delta F[f]$. Per definition, it is a distribution, if the Fréchet derivative is continuous.¹² Thus, it can be written for all continuous functions $f \in C(V)$ as

$$\frac{\delta F[f]}{\delta f}[h] = \lim_{\epsilon \rightarrow 0} \frac{F[f + \epsilon h] - F[f]}{\epsilon}. \quad (\text{A.15})$$

In addition, the functions h represent a class of variational vectors¹³ that can be restricted to a subset of the whole function space $C(V)$ to apply boundary conditions.

However, the common functional derivative denotes a variation solely around a single point y in the domain of the functions in $C(V)$, where the general derivative is defined for variations ϵh on the total domain. Accordingly, the variations must be restricted to local variations around a single point. For comparison, a similar concept is given by the definition of partial derivatives that only represent one single point of the whole gradient.

Such local variations can be obtained by special (test) functions or distributions h , for example by the Dirac δ -distribution. The Dirac δ -distribution around a fixed point y is defined as $\delta_y(f) = f(y)$ [307] and can formally be written as [311]

$$\int f(x)\delta(x - y)dx = f(y), \quad (\text{A.16})$$

using the δ -function with $\int \delta(x - a) = 1$. It is important that the Dirac δ -function $\delta(x)$ is not a function in mathematical sense, but it can be achieved as the limit of a sequence $\{h_n\}_{n=0}^{\infty}$ of functions $h_n \in C(V)$.

For example, in a one-dimensional form this sequence reads $h_n(x - y) = \frac{n}{\sqrt{\pi}} \exp(-(x - y)^2 n^2)$.¹⁴ Similarly, the sequence can be achieved in a multi-dimensional form by applying a Fourier transformation to the constant unit function.

Applying this concept to Eq. (A.15), the common local form of the functional derivative

¹¹This form is also given in the German textbook [308] by H. Fischer and H. Kaul.

¹²See E. H. Lieb and M. Loss [307], Sec. 6.3 on page 138.

¹³Compare Section 1.2 in Chapter §2 of the German textbook [308] by H. Fischer and H. Kaul.

¹⁴If the functions h_n are defined on a compact set V , its normalization factor differs for different n . But, in the limit $n \rightarrow \infty$ this does not matter.

can be defined by

$$\begin{aligned}\frac{\delta F[f]}{\delta f(y)}(x) &= \lim_{n \rightarrow \infty} \frac{\delta F[f]}{\delta f}[h_n(\circ - y)](x) \\ &= \lim_{n \rightarrow \infty} \lim_{\epsilon \rightarrow 0} \frac{F[f(x) + \epsilon h_n(x - y)] - F[f(x)]}{\epsilon},\end{aligned}\quad (\text{A.17})$$

where \circ denotes a placeholder with the meaning of $f(\circ, y)(x) = f(x, y)$.

Because the functional derivative $\delta F[f]$ is assumed to be continuous, the derivative and the limits in Eq. (A.17) exist for all h_n . Consequently, the limits can be interchanged and the common functional derivative follows with

$$\frac{\delta F[f]}{\delta f(y)}(x) = \lim_{\epsilon \rightarrow 0} \frac{F[f(x) + \epsilon \delta(x - y)] - F[f(x)]}{\epsilon} \quad (\text{A.18})$$

$$= \left. \frac{d}{d\epsilon} F[f(x) + \epsilon \delta(x - y)] \right|_{\epsilon=0}. \quad (\text{A.19})$$

A.2.3 Examples for functional derivatives

In the following, two examples of explicit calculations are given for typical functionals and its derivatives. The first corresponds to the definition of the weighted densities in Eq. (3.35), used in FMT. The second states a part of the derivative of the ideal free energy functional, given in Eq. (2.44).

First, assume $F[f] = \int_V F[f](z) dz = \int_V f(z) w(x - z) dz$. Then, the functional derivative follows from (A.18) and reads

$$\begin{aligned}\frac{\delta F[f]}{\delta f(y)}(z) &= \lim_{\epsilon \rightarrow 0} \int_V \frac{f(z) w(x - z) + \epsilon \delta(z - y) w(x - z) - f(z) w(x - z)}{\epsilon} dz \\ &= \int_V \delta(z - y) w(x - z) dz \\ &= w(x - y).\end{aligned}\quad (\text{A.20})$$

Second, assume $F[f] = \int_V f(x) \log[f(x)] dx$. Then, applying the law of l'Hospital, the functional derivative reads

$$\begin{aligned}\frac{\delta F[f]}{\delta f(y)}(x) &= \lim_{\epsilon \rightarrow 0} \int_V \frac{(f(x) + \epsilon \delta(x - y)) \log[f(x) + \epsilon \delta(x - y)] - f(x) \log[f(x)]}{\epsilon} dx \\ &= \int_V \delta(x - y) (\log[f(x)] + 1) dx \\ &= \log[f(y)] + 1.\end{aligned}\quad (\text{A.21})$$

A.3 Construction of rotated unit cells

To run numerical calculations, it is useful to construct a rectangular cuboid box with periodic boundary conditions that recovers the crystalline fcc lattice. Of course, this box should have minimal volume with respect to computational time. If interfaces are involved in calculations, the rectangular cuboid box must also reflect the symmetry of the interface. Thus, one face of the unit cell is required to be oriented parallel to the interfacial plane.

Accordingly, the following proof draws out a scheme to find such periodic rectangular cuboid boxes for a given orientation of an fcc lattice, where notations and definitions are taken from Sec. 4.1.2. In fact, the restriction to an fcc lattice does not change the fundamental principle of the theorem, but it provides clarity. In addition, resulting lattice properties are listed in Table 4.1 for the five interfacial orientations (001), (011), (111), (012), and (112) which are of interest in the context of this work.

A.3.1 Definition: fcc-lattice

Let \mathbb{L} be a (fcc) lattice as defined in Eq. (4.1). Its basis $A := \{\vec{a}_1, \vec{a}_2, \vec{a}_3\}$ consists of the primitive lattice vectors \vec{a}_i and generates the infinite fcc-lattice, as sketched in Fig. 4.2(c). Accordingly, the lattice positions $\vec{l} \in \mathbb{L}$ can be represented by the coordinate vector $m = \{m_i\}, i = 1, 2, 3$ in terms of the basis A .

Moreover, let $\{\vec{v}_1, \vec{v}_2, \vec{v}_3\}$ be an orthogonal basis that spans the periodic cuboid (001) unit cell volume V_c of this lattice. In terms of this basis, the primitive vectors are $\vec{a}_1 = \frac{1}{2}\vec{v}_1 + \frac{1}{2}\vec{v}_2$, $\vec{a}_2 = \frac{1}{2}\vec{v}_2 + \frac{1}{2}\vec{v}_3$, and $\vec{a}_3 = \frac{1}{2}\vec{v}_1 + \frac{1}{2}\vec{v}_3$.

A.3.2 Definition: rotation of the lattice

Furthermore, let R be a rotational matrix around a certain axis and a certain angle. Then, the rotated lattice \mathbb{L}' has the basis $A' = \{R \cdot \vec{a}_1, R \cdot \vec{a}_2, R \cdot \vec{a}_3\}$. Nevertheless, a new periodic volume V'_c must be found that is spanned by vectors $\vec{v}'_i := \lambda'_i \vec{v}_i$ for $i = 1, 2, 3$. Therefore, sets M_i are defined by

$$M_i := \left\{ (m_1, m_2, m_3) \left| \sum_{j=1}^3 m_j R \cdot \vec{a}_j = \lambda \vec{v}_i, m_j \in \mathbb{Z}, j \in \{1, 2, 3\}, \lambda \in \mathbb{R} \right. \right\}, \quad (\text{A.22})$$

such that every $m \in M_i$ in terms of the basis A' spans a vector parallel to \vec{v}_i , respectively for all $i = 1, 2, 3$. Since $(0, 0, 0) \in M \neq \emptyset$, the M_i are well-defined.

A.3.3 Theorem: irreducible coordinate vectors

Theorem: If an $m = (m_1, m_2, m_3) \in M_i$ exists with $m \neq (0, 0, 0)$, respectively, then an $m' = (m'_j) \in M_i$ exists such that there is no number $k \in \mathbb{N}$ with $k > 1$ that fulfills $\{m'_j/k\} \subset \mathbb{N}$ (the set $\{m'_j\}$ is irreducible).

Moreover, if this holds for all $i = 1, 2, 3$, the corresponding λ'_i are minimal, positive, and not zero and the set $\{\vec{v}'_i := \lambda'_i \vec{v}_i\}$ spans the minimal periodic unit cell volume V'_c that recovers the rotated lattice with its basis A' .

Proof: Without loss of generality the proof is done for $i = 1$. Accepting the existence of a $(0, 0, 0) \neq m \in M_1$, the existence of a λ follows with $m_1 \vec{d}'_1 + m_2 \vec{d}'_2 + m_3 \vec{d}'_3 = \lambda \vec{v}_1$ and $\lambda \neq 0$. If $\lambda < 0$, the element $m = (m_1, m_2, m_3)$ is replaced by its negative one $(-m_1, -m_2, -m_3) \in M_1$. Now, let C be the greatest common divisor of the m_i , so $C \geq 1$ is an integer. Thus, the irreducible m' is $\{m'_j = m_j/C\}$ and the corresponding $\lambda' = \lambda/C$. \square

A.3.4 Example

Let R be a rotational matrix around axis x and z of a Cartesian coordinate system by angles α_x and α_z . Its matrix follows with

$$R = \begin{pmatrix} 1 & 0 & 0 \\ 0 & \cos(\alpha_x) & -\sin(\alpha_x) \\ 0 & \sin(\alpha_x) & \cos(\alpha_x) \end{pmatrix} \cdot \begin{pmatrix} \cos(\alpha_z) & -\sin(\alpha_z) & 0 \\ \sin(\alpha_z) & \cos(\alpha_z) & 0 \\ 0 & 0 & 1 \end{pmatrix}. \quad (\text{A.23})$$

Furthermore, the normal vector of the interface is defined by $\hat{n} = (\cos(\phi) \sin(\theta), \sin(\phi) \sin(\theta), \cos(\theta))^T$, using the spherical parametrization Eq. (A.3).

A rotation around the axis \vec{v}_3 with an angle $\pi/4$ results in a set of equations,

$$\vec{d}'_1 - \vec{d}'_2 + \vec{d}'_3 = \vec{v}_1, \quad (\text{A.24})$$

$$(\vec{d}'_1 - \vec{d}'_3)/(\sqrt{2}/2) = \vec{v}_2, \quad (\text{A.25})$$

$$\vec{d}'_2/(\sqrt{2}/2) = \vec{v}_3. \quad (\text{A.26})$$

From this equations the new minimal unit cell with xy -face parallel to the (011) lattice plane follows. Its volume is $V_c = a \times (a/\sqrt{2}) \times (a/\sqrt{2})$, where $a = |\vec{v}_i|$ for $i = 1, 2, 3$. For all five orientations of interest, the results are listed in Table 4.1.

A.4 Fourier transformation and convolution

Mainly, this section follows chapter 5 of the textbook by E. H. Lieb and M. Loss [307].

Let f be a function in $L^1(\mathbb{R}^n)$. The Fourier transform of f is denoted by \tilde{f} and it is a L^∞ function on \mathbb{R}^n given by

$$\tilde{f}(\vec{k}) = \frac{1}{\sqrt{2\pi^n}} \int_{\mathbb{R}^n} e^{-i\vec{k}\cdot\vec{x}} f(\vec{x}) d\vec{x}. \quad (\text{A.27})$$

The map $f \mapsto \tilde{f}$ is linear in f and a translation is applied by a translation operator $\tau_{\vec{h}}$ with $(\tau_{\vec{h}}f)(\vec{x}) = f(\vec{x} - \vec{h})$, which results in a rotation in the complex phase of \tilde{f} and reads

$$(\tilde{\tau}_{\vec{h}}f)(\vec{k}) = e^{-i\vec{k}\cdot\vec{h}} \tilde{f}(\vec{k}), \quad \vec{h} \in \mathbb{R}^n. \quad (\text{A.28})$$

The convolution of two functions f and g in $L^1(\mathbb{R}^n)$ is denoted by $f * g$ and defined by

$$(f * g)(\vec{x}) = \int_{\mathbb{R}^n} f(\vec{y}) g(\vec{x} - \vec{y}) d\vec{y}. \quad (\text{A.29})$$

Using definition (A.27) and Fubini's theorem, the convolution theorem follows with [307]

$$\begin{aligned} \widetilde{(f * g)}(\vec{k}) &= \frac{1}{\sqrt{2\pi^n}} \int_{\mathbb{R}^n} e^{-i\vec{k}\cdot\vec{x}} \int_{\mathbb{R}^n} f(\vec{y}) g(\vec{x} - \vec{y}) d\vec{y} d\vec{x} \\ &= \frac{1}{\sqrt{2\pi^n}} \int_{\mathbb{R}^n} e^{-i\vec{k}\cdot\vec{y}} f(\vec{y}) \int_{\mathbb{R}^n} e^{-i\vec{k}\cdot(\vec{x}-\vec{y})} g(\vec{x} - \vec{y}) d\vec{x} d\vec{y} \\ &= \sqrt{2\pi^n} \tilde{f}(\vec{k}) \tilde{g}(\vec{k}). \end{aligned} \quad (\text{A.30})$$

The Fourier transformation can also be extended to functions in $L^p(\mathbb{R}^n)$, as shown, for example, in Chapter 5 of Ref. [307]. Similarly, the convolution theorem (A.30) also holds for functions $f \in L^p(\mathbb{R}^n)$ and $g \in L^q(\mathbb{R}^n)$ with $1 + 1/r = 1/p + 1/q$ for $1 \leq p, q, r \leq 2$.

In general, the L^1 Fourier transformation is not an invertible mapping, i.e. not every function in $L^\infty(\mathbb{R}^n)$ is the Fourier transform of some function in $L^1(\mathbb{R})$. But, for $f \in L^2(\mathbb{R}^n)$ it is possible to define an inverse to the Fourier transformation by

$$f_\sim(\vec{x}) := \tilde{f}(-\vec{x}) = \frac{1}{\sqrt{2\pi^n}} \int_{\mathbb{R}^n} e^{i\vec{x}\cdot\vec{k}} f(\vec{k}) d\vec{k} \quad (\text{A.31})$$

and it follows $f = (\tilde{f})_\sim$. This result offers the effort that a convolution can be calculated by a simple product in Fourier space instead of performing the full integration for every point in space.

In addition, a real-valued function f has the complex conjugate symmetry $\tilde{f}(-\vec{k}) = \tilde{f}(\vec{k})^*$ due to the properties of $e^{iz} = \cos(z) + i\sin(z)$, where f^* is the complex conjugate of f .



An equation is worth a thousand words.

(in similar form maybe by P. J. Reuter 1816-1899)

Explicit terms in FMT

In this Chapter, explicit terms of the White Bear mark II functional are written down, including all necessary calculations. The corresponding weight functions for a hard-sphere system are defined by Y. Rosenfeld [25] and the tensorial weight function $\overleftrightarrow{w}^{(m_2)}$ has been introduced later by P. Tarazona [26] to recover the correct bulk limit. These weight functions are given by

$$w_i^{(3)}(\vec{r}) = \Theta(R_i - |\vec{r}|), \quad (\text{B.1})$$

$$w_i^{(2)}(\vec{r}) = \delta(R_i - |\vec{r}|), \quad (\text{B.2})$$

$$w_i^{(1)}(\vec{r}) = \frac{1}{4\pi R_i} \delta(R_i - |\vec{r}|) = \frac{1}{4\pi R_i} w_i^{(2)}(\vec{r}), \quad (\text{B.3})$$

$$w_i^{(0)}(\vec{r}) = \frac{1}{4\pi R_i^2} \delta(R_i - |\vec{r}|) = \frac{1}{4\pi R_i^2} w_i^{(2)}(\vec{r}), \quad (\text{B.4})$$

$$\vec{w}_i^{(2)}(\vec{r}) = \frac{\vec{r}}{|\vec{r}|} \delta(R_i - |\vec{r}|) = \frac{\vec{r}}{|\vec{r}|} w_i^{(2)}(\vec{r}), \quad (\text{B.5})$$

$$\vec{w}_i^{(1)}(\vec{r}) = \frac{\vec{r}}{4\pi R_i |\vec{r}|} \delta(R_i - |\vec{r}|) = \frac{\vec{r}}{|\vec{r}|} w_i^{(1)}(\vec{r}), \quad (\text{B.6})$$

$$\overleftrightarrow{w}_i^{(m_2)}(\vec{r}) = \left(\frac{\vec{r} \cdot \vec{r}^t}{|\vec{r}|^2} - \frac{\overleftrightarrow{\mathbb{I}}}{3} \right) \delta(R_i - |\vec{r}|) = \left(\frac{\vec{r} \cdot \vec{r}^t}{|\vec{r}|^2} - \frac{\overleftrightarrow{\mathbb{I}}}{3} \right) w_i^{(2)}(\vec{r}), \quad (\text{B.7})$$

where \vec{r}^t denotes the transposed of a vector \vec{r} and $\overleftrightarrow{\mathbb{I}}$ denotes the unit matrix in $\mathbb{R}^{3 \times 3}$.

First, the derivative of the White Bear II functional is given in Sec. B.1. In Sec. B.2, limits of the functional are listed in the bulk limit of a fluid phase. Then, necessary Fourier transforms of the weight functions for hard spheres are calculated in Sec. B.3. And finally, the decomposition into weight functions is re-called in Sec. B.4, to ensure completeness.

B.1 Derivative of the White Bear II functional

In this section, an explicit form of the functional derivative of the White Bear II excess free energy functional is given, as it is defined in Sec. 3.4.1. Of course, the tensor extension is

used that has been introduced by P. Tarazona. For this reason, it is necessary to define the derivative with respect to non-scalar quantities, like vectors or tensors.

Non-scalar quantities A can be written in the form $\sum_i a_i \hat{e}_i$, where a_i are the components of A in a parametrization with the basis $\{\hat{e}_i\}$. Now, a derivative $\partial\Phi(A)/\partial A$ is defined as

$$\frac{\partial\Phi(A)}{\partial A} = \sum_i \frac{\partial\Phi(A)}{\partial a_i} \hat{e}_i. \quad (\text{B.8})$$

To give some examples, let \vec{A} , \vec{B} , and \vec{C} be $n \times n$ -matrices, \vec{v} a n -dimensional vector, and \vec{A}^t the transpose of the matrix \vec{A} . Moreover, a symmetric matrix \vec{A} has the quality $\vec{A}^t = \vec{A}$ and the trace Tr is invariant for cyclic changes, $\text{Tr}(\vec{A} \cdot \vec{B} \cdot \vec{C}) = \text{Tr}(\vec{B} \cdot \vec{C} \cdot \vec{A})$. Then, the following equalities hold:¹

$$\frac{\partial}{\partial(\vec{v})_i} \left(\vec{v}^t \cdot \vec{A} \cdot \vec{v} \right) = \hat{e}_i^t \cdot \vec{A} \cdot \vec{v} + \vec{v}^t \cdot \vec{A} \cdot \hat{e}_i \stackrel{\vec{A} \text{ symm.}}{=} 2\hat{e}_i^t \cdot \vec{A} \cdot \vec{v}, \quad (\text{B.9})$$

$$\frac{\partial}{\partial \vec{A}} \text{Tr}(\vec{A} \cdot \vec{B}) = \vec{B}^t, \quad (\text{B.10})$$

$$\frac{\partial}{\partial \vec{A}} \text{Tr}(\vec{A} \cdot \vec{A} \cdot \vec{A}) = 3\vec{A}^t \cdot \vec{A}^t \stackrel{\vec{A} \text{ symm.}}{=} 3\vec{A} \cdot \vec{A}, \quad (\text{B.11})$$

$$\vec{v}^t \cdot \vec{A} \cdot \vec{v} = \text{Tr}(\vec{v}^t \cdot \vec{A} \cdot \vec{v}) = \text{Tr}(\vec{A} \cdot \vec{v} \cdot \vec{v}^t), \quad (\text{B.12})$$

$$\frac{\partial}{\partial(\vec{A})_{ij}} (\vec{v}^t \cdot \vec{A} \cdot \vec{v}) = (\vec{v})_i (\vec{v})_j. \quad (\text{B.13})$$

Some of the underlying weight functions, as listed in Eq. (3.25)-(3.30) and (3.53), differ from each other only by a simple factor. Since numerical calculations take a lot of calculation time, it is useful to reduce the set of weighted densities by considering these dependencies. Accordingly, the set of independent weighted densities only holds n_3 , n_2 , \vec{n}_2 , and \vec{n}_{m_2} , where the remaining weighted densities are achieved using the relations

$$n_1 = \frac{n_2}{4\pi R}, \quad n_0 = \frac{n_2}{4\pi R^2}, \quad \text{and} \quad \vec{n}_1 = \frac{\vec{n}_2}{4\pi R}. \quad (\text{B.14})$$

Applying these replacements, the tensor version of the White Bear II excess free energy density can be re-written in the form

$$\Phi_1^{WBII} = -\frac{n_2}{4\pi R^2} \log(1 - n_3), \quad (\text{B.15})$$

$$\Phi_2^{WBII} = \left(1 + \frac{1}{9}n_3^2\phi_2(n_3)\right) \frac{n_2^2 - \vec{n}_2 \cdot \vec{n}_2}{4\pi R(1 - n_3)}, \quad (\text{B.16})$$

$$\Phi_3^{WBII} = \left(1 - \frac{4}{9}n_3\phi_3(n_3)\right) \frac{n_2^3 - 3n_2\vec{n}_2 \cdot \vec{n}_2 + \frac{9}{2}(\vec{n}_2^t \cdot \vec{n}_{m_2} \cdot \vec{n}_2 - \text{Tr}(\vec{n}_{m_2}^3))}{24\pi(1 - n_3)^2}. \quad (\text{B.17})$$

¹Explicit formulations are also given in the appendix of Ref. [312].

For implementation of the White Bear II functional, it is reasonable to use the functions

$$\phi_2^{\text{num}}(n_3) = 1 + \frac{1}{9}n_3^2\phi_2(n_3) = \frac{5}{3} + \frac{2}{3}\frac{1-n_3}{n_3}\log(1-n_3) - \frac{n_3}{3} \quad (\text{B.18})$$

$$= 1 + \frac{1}{9}n_3^2 + \frac{1}{18}n_3^3 + \frac{1}{30}n_3^4 + \frac{1}{45}n_3^5 + \mathcal{O}(n_3^6), \quad (\text{B.19})$$

$$\phi_3^{\text{num}}(n_3) = 1 - \frac{4}{9}n_3\phi_3(n_3) = 2 - \frac{2}{3}\left(\frac{1}{n_3} + n_3 + \frac{(1-n_3)^2}{n_3^2}\log(1-n_3)\right) \quad (\text{B.20})$$

$$= 1 - \frac{4}{9}n_3 + \frac{1}{18}n_3^2 + \frac{1}{45}n_3^3 + \frac{1}{90}n_3^4 + \mathcal{O}(n_3) \quad (\text{B.21})$$

instead of the original ones that are given in Eqn. (3.60) and (3.61). For completeness, their expansions can also be calculated using the expansion of the natural logarithm² and they follow with

$$\phi_2(n_3) = \frac{6n_3 - 3n_3^2 + 6(1-n_3)\log(1-n_3)}{n_3^3} \quad (\text{B.22})$$

$$= 1 + \frac{1}{2}n_3 + \frac{3}{10}n_3^2 + \frac{1}{5}n_3^3 + \mathcal{O}(n_3^4), \quad (\text{B.23})$$

$$\phi_3(n_3) = \frac{6n_3 - 9n_3^2 + 6n_3^3 + 6(1-n_3)^2\log(1-n_3)}{4n_3^3} \quad (\text{B.24})$$

$$= 1 - \frac{1}{8}n_3 - \frac{1}{20}n_3^2 - \frac{1}{40}n_3^3 - \mathcal{O}(n_3^4). \quad (\text{B.25})$$

Moreover, the partial derivatives of these functions with respect to the weighted density n_3 simply reads

$$\frac{\partial\phi_2(n_3)}{\partial n_3} = -6\frac{n_3 + \log(1-n_3)}{n_3^3} - \frac{3}{n_3}\phi_2(n_3) \quad (\text{B.26})$$

$$= \frac{1}{2} + \frac{3}{5}n_3 + \frac{3}{5}n_3^2 + \mathcal{O}(n_3^3), \quad (\text{B.27})$$

$$\frac{\partial\phi_3(n_3)}{\partial n_3} = \frac{3}{2}\frac{3n_3^2 - 2n_3 - 2(1-n_3)\log(1-n_3)}{n_3^3} - \frac{3}{n_3}\phi_3(n_3) \quad (\text{B.28})$$

$$= -\frac{1}{8} - \frac{1}{10}n_3 - \frac{3}{40}n_3^2 + \mathcal{O}(n_3^3), \quad (\text{B.29})$$

²The natural logarithm can be expanded like $\log(1+x) = \sum_{k=0}^{\infty} (-1)^k \frac{x^{k+1}}{k+1}$, but convergence is bad.

$$\frac{\partial \phi_2^{\text{num}}(n_3)}{\partial n_3} = -\frac{2}{3} \left(\frac{1}{n_3^2} \log(1 - n_3) + \frac{1}{n_3} + \frac{1}{2} \right) \quad (\text{B.30})$$

$$= \frac{2}{9} n_3 + \frac{1}{6} n_3^2 + \frac{2}{15} n_3^3 + \frac{1}{9} n_3^4 + \mathcal{O}(n_3^5), \quad (\text{B.31})$$

$$\frac{\partial \phi_3^{\text{num}}(n_3)}{\partial n_3} = \frac{2}{3n_3^2} \left(2 - n_3 - n_3^2 + 2 \frac{1 - n_3}{n_3} \log(1 - n_3) \right) \quad (\text{B.32})$$

$$= -\frac{4}{9} + \frac{1}{9} n_3 + \frac{1}{15} n_3^2 + \frac{2}{45} n_3^3 + \mathcal{O}(n_3^4). \quad (\text{B.33})$$

However, to calculate the functional derivative given in Eq. (3.63), it is reasonable to replace the integration over the complete space V by a convolution, as defined in Eq. (A.29). For this reason, the convolution product (or cross-correlation product) \circledast , defined in Eq. (3.32) and used in the definition of Eq. (3.63), must be replaced by the standard convolution product $*$ that differs from \circledast in the sign of the argument of the second convolution factor. Thus, the sign of the argument of the weight function must be switched, what gives rise to the definition of a sign function

$$\text{sign}(w_i^{(\alpha)}) = \begin{cases} 1 & \text{for symmetric functions } w_i^{(\alpha)}(-\vec{r}) = w_i^{(\alpha)}(\vec{r}) \\ -1 & \text{for asymmetric functions } w_i^{(\alpha)}(-\vec{r}) = -w_i^{(\alpha)}(\vec{r}) \end{cases}. \quad (\text{B.34})$$

Accordingly, the functional derivative of the excess free energy functional, given in Eq. (3.63), now reads

$$-c_i^{(1)}[\rho; \vec{r}] = \sum_{\alpha} \text{sign} \left(w_i^{(\alpha)} \right) \frac{\partial \Phi}{\partial n_{\alpha}} * w_i^{(\alpha)}(\vec{r}). \quad (\text{B.35})$$

Here, the convolution product is defined for every coordinate, respectively, especially if n_{α} is a non-scalar quantity. Then, Eq. (B.35) also contains a contraction over the vectorial or tensorial functions. Moreover, for a homogeneous density profile ρ_{fl} that corresponds to a fluid phase, the direct pair-correlation function, as given in Eq. (3.65), follows with

$$-c_{ij}^{(2)}[\rho_{\text{fl}}; \vec{r} - \vec{r}'] = \sum_{\alpha, \beta} \text{sign} \left(w_j^{(\beta)} \right) \frac{\partial^2 \Phi}{\partial n_{\alpha} \partial n_{\beta}} w_i^{(\alpha)} * w_j^{(\beta)}(\vec{r} - \vec{r'}). \quad (\text{B.36})$$

Finally, the functional derivative (B.35) follows with the partial derivatives³

$$\frac{\partial \Phi_1^{\text{WBII}}}{\partial n_2} = -\frac{1}{4\pi R^2} \log(1 - n_3), \quad (\text{B.37})$$

$$\frac{\partial \Phi_1^{\text{WBII}}}{\partial n_3} = \frac{n_2}{4\pi R^2(1 - n_3)}, \quad (\text{B.38})$$

³Keep in mind that the tensor \vec{n}_{m_2} is symmetric.

$$\frac{\partial \Phi_2^{\text{WBII}}}{\partial n_2} = \phi_2^{\text{num}}(n_3) \frac{2n_2}{4\pi R(1-n_3)}, \quad (\text{B.39})$$

$$\frac{\partial \Phi_2^{\text{WBII}}}{\partial n_3} = \left(\frac{\phi_2^{\text{num}}(n_3)}{1-n_3} + \frac{\partial \phi_2^{\text{num}}(n_3)}{\partial n_3} \right) \frac{n_2 n_2 - \vec{n}_2 \cdot \vec{n}_2}{4\pi R(1-n_3)}, \quad (\text{B.40})$$

$$\frac{\partial \Phi_2^{\text{WBII}}}{\partial \vec{n}_2} = -2\phi_2^{\text{num}}(n_3) \frac{\vec{n}_2}{4\pi R(1-n_3)}, \quad (\text{B.41})$$

$$\frac{\partial \Phi_3^{\text{WBII}}}{\partial n_2} = \phi_3^{\text{num}}(n_3) \frac{3n_2^2 - 3\vec{n}_2 \cdot \vec{n}_2}{24\pi(1-n_3)^2}, \quad (\text{B.42})$$

$$\frac{\partial \Phi_3^{\text{WBII}}}{\partial n_3} = \left(\frac{2\phi_3^{\text{num}}(n_3)}{1-n_3} + \frac{\partial \phi_3^{\text{num}}(n_3)}{\partial n_3} \right) \times \frac{n_2^3 - 3n_2\vec{n}_2 \cdot \vec{n}_2 + \frac{9}{2}(\vec{n}_2^t \cdot \vec{n}_{m2} \cdot \vec{n}_2 - \text{Tr}(\vec{n}_{m2}^3))}{24\pi(1-n_3)^2}, \quad (\text{B.43})$$

$$\frac{\partial \Phi_3^{\text{WBII}}}{\partial \vec{n}_2} = \phi_3^{\text{num}}(n_3) \frac{9\vec{n}_{m2} \cdot \vec{n}_2 - 6n_2\vec{n}_2}{24\pi(1-n_3)^2}, \quad (\text{B.45})$$

$$\frac{\partial \Phi_3^{\text{WBII}}}{\partial \vec{n}_{m2}} = \frac{9}{2}\phi_3^{\text{num}}(n_3) \frac{\vec{n}_2 \cdot \vec{n}_2^t - 3(\vec{n}_{m2})^2}{24\pi(1-n_3)^2}. \quad (\text{B.46})$$

B.2 Fluid bulk limit of the White Bear II functional

In the fluid bulk limit, the density profiles $\rho_i(\vec{r})$ become homogeneous in space. Accordingly, the weighted densities, as defined in Eq. (3.35), directly follow from the weight functions (B.1)-(B.7) by integration. Apparently, the tensorial and vectorial weighted densities vanish, where the scalar weighted densities reduce to the so-called SPT variables⁴

$$n_3 = \sum_{i=1}^{\nu} \frac{1}{6} \pi \sigma^3 \rho_i = \eta, \quad (\text{B.47})$$

$$n_2 = \sum_{i=1}^{\nu} \pi \sigma^2 \rho_i, \quad (\text{B.48})$$

$$n_1 = \frac{n_2}{2\pi\sigma} = \sum_{i=1}^{\nu} \frac{\sigma}{2} \rho_i, \quad (\text{B.49})$$

$$n_0 = \frac{n_2}{\pi\sigma^2} = \sum_{i=1}^{\nu} \rho_i \quad (\text{B.50})$$

⁴See Review by R. Roth [29], bottom of page 12065. For further reading about *Scaled Particle Theory* see Sec. 3.2.3 and the original work of H. Reiss et al. [58].

in a ν component hard-sphere system. In principle, these are the fundamental measures of one single sphere multiplied with the mean bulk density of the fluid: the volume V , the surface $4\pi R^2$, the radius R , and the Euler characteristic $\chi = 1$.

Since the weighted densities n_α become constant in space, the excess free energy also becomes constant and reads

$$\beta \mathcal{F}_{\text{exc}}[\rho_i] = \beta \Phi^{\text{WBII}} = -3\pi\sigma^3\rho_i^2 \frac{\pi\sigma^3\rho_i - 8}{(\pi\sigma^3\rho_i - 6)^2}. \quad (\text{B.51})$$

Due to the construction of the White Bear functional, this result is equal to the Carnahan-Starling excess free energy, given in Eq. (3.15). Consequently, the grand canonic energy Ω follows directly from the Carnahan-Starling equation of state (3.14). Moreover, the convolution $(\partial\Phi/\partial n_\alpha) * w_i^{(\alpha)}$ in the functional derivative Eq. (B.35) simplifies to $(\partial\Phi/\partial n_\alpha)n_\alpha/\rho_i$. Thus, the functional derivative in a fluid bulk phase follows with

$$\beta \frac{\partial \mathcal{F}_{\text{exc}}}{\partial \rho_i} = \beta \frac{\partial \Phi^{\text{WBII}}}{\partial \rho_i} = -3\pi\sigma^3\rho_i \frac{96 - 18\pi\sigma^3\rho_i + \pi^2\sigma^6\rho_i^2}{(\pi\sigma^3\rho_i - 6)^3}. \quad (\text{B.52})$$

The chemical potential can be obtained from the derivative $\mu = d\mathcal{F}/d\rho_0$ [146], where ρ_0 denotes the bulk density (see also Sec. C.1). Accordingly, the chemical potential can be obtained by

$$\beta \frac{\delta \mathcal{F}_{\text{exc}}}{\delta \rho_0} = \frac{4}{3}\pi R^3 \frac{\beta}{V} \int_V \frac{\delta \mathcal{F}_{\text{exc}}}{\delta n_3(\vec{r})} d\vec{r} + 4\pi R^2 \frac{\beta}{V} \int_V \frac{\delta \mathcal{F}_{\text{exc}}}{\delta n_2(\vec{r})} d\vec{r}. \quad (\text{B.53})$$

Finally, the direct pair-correlation function is listed by M. Oettel et al. [88] and is re-written in Eq. (3.66) in Sec. 3.4.2. The Fourier transforms of the coefficients from Eq. (3.66) read

$$a_1 = \frac{2}{\sqrt{2\pi}} \left[\sin(|\vec{k}| \sigma) - |\vec{k}| \sigma \cos(|\vec{k}| \sigma) \right] \frac{1}{|\vec{k}|^3}, \quad (\text{B.54})$$

$$a_2 = \frac{2}{\sqrt{2\pi}} \left[2|\vec{k}| \sigma \sin(|\vec{k}| \sigma) + (2 - |\vec{k}|^2 \sigma^2) \cos(|\vec{k}| \sigma) - 2 \right] \frac{1}{|\vec{k}|^4 \sigma}, \quad (\text{B.55})$$

$$a_3 = \frac{2}{\sqrt{2\pi}} \left[4 \left(6 + |\vec{k}| \sigma (|\vec{k}|^2 \sigma^2 - 6) \sin(|\vec{k}| \sigma) \right) - (24 - 12|\vec{k}|^2 \sigma^2 + |\vec{k}|^4 \sigma^4) \cos(|\vec{k}| \sigma) \right] \frac{1}{|\vec{k}|^6 \sigma^3}. \quad (\text{B.56})$$

For numerical implementation, the limits of these coefficients are needed and follow with

$$a_1 \xrightarrow{k \rightarrow 0} \frac{2}{\sqrt{2\pi}} \frac{\sigma^3}{3}, \quad (\text{B.57})$$

$$a_2 \xrightarrow{k \rightarrow 0} \frac{2}{\sqrt{2\pi}} \frac{\sigma^3}{4}, \quad (\text{B.58})$$

$$a_3 \xrightarrow{k \rightarrow 0} \frac{2}{\sqrt{2\pi}} \frac{\sigma^3}{6}. \quad (\text{B.59})$$

B.3 Fourier transforms of the weight functions for hard spheres

For explicit numerical calculations, the Fourier transforms of the weight functions (B.1)-(B.7) are needed,⁵ as shown in Sec. B.1. Their explicit calculations are given in Sec. B.3.1 for the Fourier transform of the weight function $w_i^{(3)}$, in Sec. B.3.2 for $w_i^{(2)}$, in Sec. B.3.3 for $\tilde{w}_i^{(2)}$, and in Sec. B.3.4 for the tensor $\tilde{w}_i^{(m_2)}$. To sum up, the results are

$$\tilde{w}_i^{(3)}(\vec{k}) = \frac{4\pi}{|\vec{k}|^3 \sqrt{2\pi}^3} \left(\sin(|\vec{k}|R_i) - |\vec{k}|R_i \cos(|\vec{k}|R_i) \right), \quad (\text{B.60})$$

$$\tilde{w}_i^{(2)}(\vec{k}) = \frac{4\pi R_i}{|\vec{k}| \sqrt{2\pi}^3} \sin(|\vec{k}|R_i), \quad (\text{B.61})$$

$$\tilde{w}_i^{(2)}(\vec{k}) = -i\vec{k}\tilde{w}_3(\vec{k}), \quad (\text{B.62})$$

$$\tilde{w}_i^{(m_2)}(\vec{k}) = \left(\tilde{w}_i^{(2)}(\vec{k}) - \frac{3}{R_i} \tilde{w}_i^{(3)}(\vec{k}) \right) \left(\frac{\vec{k} \cdot \vec{k}^t}{|\vec{k}|^2} - \frac{\overleftrightarrow{\mathbb{I}}}{3} \right), \quad (\text{B.63})$$

where the Fourier transformation from Eq. (A.27) has been applied with a reciprocal vector $\vec{k} = (k_x, k_y, k_z)$. Here, \vec{k}^t is the transpose of \vec{k} and the product in Eq. (B.63) reads $(\vec{k} \cdot \vec{k}^t)_{ij} \equiv k_i k_j$ for $i, j \in \{x, y, z\}$.

Moreover, the limits of the Fourier transformed weight functions (B.60) - (B.63) exist for vanishing $\vec{k} \rightarrow \vec{0}$ and they read

$$\tilde{w}_i^{(3)}(\vec{0}) = \frac{4\pi R_i}{\sqrt{2\pi}^3} \frac{R_i^2}{3}, \quad (\text{B.64})$$

$$\tilde{w}_i^{(2)}(\vec{0}) = \frac{4\pi R_i^2}{\sqrt{2\pi}^3}, \quad (\text{B.65})$$

$$\tilde{w}_i^{(2)}(\vec{0}) = \vec{0}, \quad (\text{B.66})$$

$$\tilde{w}_i^{(m_2)}(\vec{0}) = 0 \overleftrightarrow{\mathbb{I}}. \quad (\text{B.67})$$

⁵For example, they are listed by M. Schmidt et al. [313] in Appendix A of their work.

B.3.1 Fourier transform of the spherical Heaviside step function

In this section, the spherical Heaviside step function $w^{(3)}(\vec{r}) = \Theta(R - |\vec{r}|)$ is Fourier transformed analytically. Applying the Fourier transformation (A.27) yields

$$\tilde{w}^{(3)}(\vec{k}) = \frac{1}{\sqrt{2\pi}^3} \int_{\mathbb{R}^3} \Theta(R - |\vec{r}|) e^{-i\vec{k}\cdot\vec{r}} d\vec{r}. \quad (\text{B.68})$$

Therefore, the real-space vector \vec{r} is parametrized such that its z -component is aligned parallel to \vec{k} , thus $\vec{k} \parallel \hat{e}_z$, using the spherical parametrization (A.3) with $r = |\vec{r}|$. Then, Eq. (B.68) becomes

$$\begin{aligned} \tilde{w}^{(3)}(\vec{k}) &= \frac{2\pi}{\sqrt{2\pi}^3} \int_0^R \int_0^\pi r^2 \sin(\vartheta) e^{-i|\vec{k}|r \cos(\vartheta)} d\vartheta dr \\ &= \frac{2\pi}{\sqrt{2\pi}^3} \int_0^R \left[\frac{r}{i|\vec{k}|} e^{-i|\vec{k}|r \cos(\vartheta)} \right]_{\vartheta=0}^\pi dr \\ &= \frac{2\pi}{\sqrt{2\pi}^3} \int_0^R \frac{r}{i|\vec{k}|} \left(e^{i|\vec{k}|r} - e^{-i|\vec{k}|r} \right) dr \\ &= \frac{2\pi}{\sqrt{2\pi}^3} \int_0^R \frac{2}{|\vec{k}|^3} |\vec{k}|^2 r \sin(|\vec{k}|r) dr. \end{aligned} \quad (\text{B.69})$$

Using the identity $\partial/\partial x[\sin(kx) - kx \cos(kx)] = k^2 x \sin(kx)$, the final result is obtained as

$$\tilde{w}^{(3)}(\vec{k}) = \frac{4\pi}{|\vec{k}|^3 \sqrt{2\pi}^3} \left(\sin(|\vec{k}|R) - |\vec{k}|R \cos(|\vec{k}|R) \right). \quad (\text{B.70})$$

B.3.2 Fourier transform of the spherical Dirac function

Similar to the transformation of the Heaviside step function in Sec. B.3.1, in this section the spherical Dirac δ -function $w^{(2)}(\vec{r}) = \delta(R - |\vec{r}|)$ is Fourier transformed. The transform reads

$$\begin{aligned} \tilde{w}^{(2)}(\vec{k}) &= \frac{1}{\sqrt{2\pi}^3} \int_{\mathbb{R}^3} \delta(R - |\vec{r}|) e^{-i\vec{k}\cdot\vec{r}} d\vec{r} \\ &= \frac{2\pi}{\sqrt{2\pi}^3} \int_0^\pi R^2 \sin(\vartheta) e^{-i|\vec{k}|R \cos(\vartheta)} d\vartheta, \end{aligned} \quad (\text{B.71})$$

where the same parametrization has been used as in the previous section. The final result directly follows from Eq. (B.69) with

$$\tilde{w}^{(2)}(\vec{k}) = \frac{4\pi R}{|\vec{k}| \sqrt{2\pi^3}} \sin(|\vec{k}|R). \quad (\text{B.72})$$

B.3.3 Fourier transform of the vectorial weight function

In this section, the vectorial weight function $\vec{w}^{(2)}(\vec{r}) = \frac{\vec{r}}{|\vec{r}|} \delta(R - |\vec{r}|)$ is Fourier transformed. The transform reads

$$\begin{aligned} \tilde{w}^{(2)}(\vec{k}) &= \frac{1}{\sqrt{2\pi^3}} \int_{\mathbb{R}^3} \frac{\vec{r}}{|\vec{r}|} \delta(R - |\vec{r}|) e^{-i\vec{k}\cdot\vec{r}} d\vec{r} \\ &= \frac{1}{\sqrt{2\pi^3}} \int_{\mathbb{R}^3} \frac{\vec{r}}{|\vec{r}|} \delta(R - |\vec{r}|) e^{-i(\vec{\mathcal{R}}^{(-)}\vec{k})\cdot(\vec{\mathcal{R}}^{(-)}\vec{r})} d\vec{r}. \end{aligned} \quad (\text{B.73})$$

Apparently, the rotation $\vec{\mathcal{R}}^{(-)}$, that has been applied in the second step of Eq. (B.73), does not change the result of the product $\vec{k} \cdot \vec{r}$. Here, the rotation is defined such that $\vec{\mathcal{R}}^{(-)}\vec{k} = \hat{e}_z$ and $\vec{\mathcal{R}}^{(-)}\vec{\mathcal{R}}^{(+)} = \vec{\mathbb{I}}$. Moreover, the transposed of a rotational matrix is equal to its inverse.⁶

In contrast to the previous sections, now the quantity $\vec{\mathcal{R}}^{(-)}\vec{r}/|\vec{r}|$ is parametrized, as described in Eq. (A.3). Inserting a unit $\vec{\mathbb{I}}$, the transform reads

$$\begin{aligned} \tilde{w}^{(2)}(\vec{k}) &= \frac{\vec{\mathcal{R}}^{(+)}}{\sqrt{2\pi^3}} \int_0^{2\pi} \int_0^\pi R^2 \sin(\vartheta) \begin{pmatrix} \cos(\varphi) \sin(\vartheta) \\ \sin(\varphi) \sin(\vartheta) \\ \cos(\vartheta) \end{pmatrix} e^{-i|\vec{k}|R \cos(\vartheta)} d\vartheta d\varphi \\ &= \frac{2\pi R^2}{\sqrt{2\pi^3}} \vec{\mathcal{R}}^{(+)} \hat{e}_z \int_0^\pi \sin(\vartheta) \cos(\vartheta) e^{-i|\vec{k}|R \cos(\vartheta)} d\vartheta, \end{aligned} \quad (\text{B.74})$$

where the components of \hat{e}_x and \hat{e}_y vanish, due to $\int_0^{2\pi} \sin(\alpha) d\alpha = 0$ (and consequently also for $\cos(\alpha)$). Moreover, the rotation $\vec{\mathcal{R}}^{(+)}\hat{e}_z$ is aligned parallel to \vec{k} and the identity

$$\int_0^\pi \sin(\beta) \cos(\beta) e^{-iy \cos(\beta)} d\beta = (y \cos(y) - \sin(y)) \frac{2i}{y^2} \quad (\text{B.75})$$

is known from mathematics software *Mathematica*. Thus, the calculation results in

$$\tilde{w}^{(2)}(\vec{k}) = \frac{\vec{k}}{|\vec{k}|^3} \frac{4\pi i}{\sqrt{2\pi^3}} \left[|\vec{k}|R \cos(|\vec{k}|R) - \sin(|\vec{k}|R) \right]. \quad (\text{B.76})$$

⁶An explicit example for a rotational matrix is given in Eq. (A.23).

B.3.4 Fourier transform of the tensorial weight function

In this section, the tensorial function $\vec{w}^{(m_2)}(\vec{r}) = \left(\frac{\vec{r} \cdot \vec{r}^t}{|\vec{r}|^2} - \frac{\vec{\mathbb{I}}}{3} \right) \delta(R - |\vec{r}|)$ is Fourier transformed. Because the transform of $\frac{\vec{\mathbb{I}}}{3} \delta(R - |\vec{r}|)$ is already known from Sec. B.3.2, solely the remaining summand $\vec{w}^{(m_2,I)}(\vec{r}) = \frac{\vec{r} \cdot \vec{r}^t}{|\vec{r}|^2} \delta(R - |\vec{r}|)$ must be transformed. Thus, the transform of the tensorial part reads

$$\begin{aligned} \tilde{\vec{w}}^{(m_2,I)}(\vec{k}) &= \frac{1}{\sqrt{2\pi}^3} \int_{\mathbb{R}^3} \frac{\vec{r} \cdot \vec{r}^t}{|\vec{r}|^2} \delta(R - |\vec{r}|) e^{-i\vec{k} \cdot \vec{r}} d\vec{r} \\ &= \frac{1}{\sqrt{2\pi}^3} \int_{\mathbb{R}^3} \frac{\vec{r} \cdot \vec{r}^t}{|\vec{r}|^2} \delta(R - |\vec{r}|) e^{-i(\vec{\mathcal{R}}^{(-)} \vec{k}) \cdot (\vec{\mathcal{R}}^{(-)} \vec{r})} d\vec{r} \\ &= \frac{\vec{\mathcal{R}}^{(+)}}{\sqrt{2\pi}^3} \int_0^{2\pi} \int_0^\pi R^2 \sin(\vartheta) \frac{(\vec{\mathcal{R}}^{(-)} \vec{r}) \cdot (\vec{\mathcal{R}}^{(-)} \vec{r})^t}{|\vec{r}|^2} e^{-i|\vec{k}|R \cos(\vartheta)} d\vartheta d\varphi \left(\vec{\mathcal{R}}^{(+)} \right)^t. \end{aligned} \quad (\text{B.77})$$

Similar to Sec. B.3.3, the rotation $\vec{\mathcal{R}}$ has been applied and a unit $\vec{\mathbb{I}}$ has been inserted. Moreover, $\vec{\mathcal{R}}^{(-)} \vec{r}$ is again parametrized using Eq. (A.3). Thus, re-calling the comment after Eq. (B.74), the tensorial kernel can be integrated and follows with

$$\begin{aligned} &\int_0^{2\pi} \sin(\vartheta) \begin{pmatrix} \cos(\varphi) \sin(\vartheta) \\ \sin(\varphi) \sin(\vartheta) \\ \cos(\vartheta) \end{pmatrix} \cdot \begin{pmatrix} \cos(\varphi) \sin(\vartheta) \\ \sin(\varphi) \sin(\vartheta) \\ \cos(\vartheta) \end{pmatrix}^t d\varphi \\ &= \begin{pmatrix} \pi \sin^3(\vartheta) & 0 & 0 \\ 0 & \pi \sin^3(\vartheta) & 0 \\ 0 & 0 & 2\pi \sin(\vartheta) \cos^2(\vartheta) \end{pmatrix} \\ &= 2\pi \sin(\vartheta) \hat{e}_z \cdot \hat{e}_z^t + \pi \sin^3(\vartheta) \left(\vec{\mathbb{I}} - 3\hat{e}_z \cdot \hat{e}_z^t \right). \end{aligned} \quad (\text{B.78})$$

However, $\vec{\mathcal{R}}^{(+)} \cdot \vec{\mathbb{I}} \cdot (\vec{\mathcal{R}}^{(+)})^t = \vec{\mathbb{I}}$ follows from the definition of the rotation in the previous section and $\vec{\mathcal{R}}^{(+)} \cdot \hat{e}_z \cdot \hat{e}_z^t \cdot (\vec{\mathcal{R}}^{(+)})^t = \vec{k} \cdot \vec{k}^t / |\vec{k}|^2$ holds. Moreover, the first summand of the right-hand side in Eq. (B.78) corresponds to Eq. (B.71) and consequently results in $\tilde{w}^{(2)}(\vec{k}) \vec{k} \cdot \vec{k}^t / |\vec{k}|^2$, if re-placed in Eq. (B.77). Finally, the identity $\int_0^\pi \sin^3(\beta) e^{-iy \cos(\beta)} d\beta = 4[\sin(y) - y \cos(y)]/y^3$ is known from mathematics software *Mathematica* and a comparison with Eq. (B.70) shows that the scalar part of the second summand of the right-hand side in Eq. (B.78) corresponds to $\tilde{w}^{(3)}(\vec{k})/R$. Thus, the complete Fourier transformed tensorial weight function follows with

$$\begin{aligned} \tilde{\vec{w}}^{(m_2)}(\vec{k}) &= \tilde{w}^{(2)}(\vec{k}) \frac{\vec{k} \cdot \vec{k}^t}{|\vec{k}|^2} + \frac{\tilde{w}^{(3)}(\vec{k})}{R} \left(\vec{\mathbb{I}} - 3 \frac{\vec{k} \cdot \vec{k}^t}{|\vec{k}|^2} \right) - \frac{\tilde{w}^{(2)}(\vec{k})}{3} \vec{\mathbb{I}} \\ &= \left(\tilde{w}^{(2)}(\vec{k}) - \frac{3}{R} \tilde{w}^{(3)}(\vec{k}) \right) \left(\frac{\vec{k} \cdot \vec{k}^t}{|\vec{k}|^2} - \frac{\vec{\mathbb{I}}}{3} \right). \end{aligned} \quad (\text{B.79})$$

B.4 Decomposition into weight functions

The decomposition into weight functions, given in Eq. (3.31), can simply be proven in Fourier space. For example, the explicit calculation is given in this section. To show equality, both sides of the equation are Fourier transformed in the following. However, it should be recognized that in the original article from Y. Rosenfeld [25] the definition of the convolution \circledast , as defined in Eq. (3.32), differs from that of the standard convolution product $*$, defined in Eq. (A.29), for non-symmetric functions $f(x) \neq f(-x)$. Accordingly, the signs of the vectorial convolution terms (that are non-symmetric) are erroneous in equation (2) of Ref. [25].

Left-hand side: The Fourier transform of the Θ function is given in Sec. B.3.1 and the replacement $R = R_i + R_j$ can be applied by the theorems of summation for Sine and Cosine.⁷ Applying the abbreviations $S_i = \sin(|\vec{k}|R_i)$ and $C_i = \cos(|\vec{k}|R_i)$, the left-hand side reads

$$\begin{aligned}\tilde{\Theta}(\vec{k}) &= \frac{4\pi}{|\vec{k}|^3 \sqrt{2\pi}^3} \left(\sin(|\vec{k}|(R_i + R_j)) - |\vec{k}|(R_i + R_j) \cos(|\vec{k}|(R_i + R_j)) \right) \\ &= \frac{4\pi}{|\vec{k}|^3 \sqrt{2\pi}^3} \left(S_i C_j + C_i S_j - |\vec{k}|(R_i + R_j)(C_i C_j - S_i S_j) \right) \\ &= \frac{4\pi}{|\vec{k}|^3 \sqrt{2\pi}^3} \left((S_i - |\vec{k}|R_i C_i)C_j + (S_j - |\vec{k}|R_j C_j)C_i + |\vec{k}|(R_i + R_j)S_i S_j \right).\end{aligned}$$

Right-hand side: The relation between the Fourier transform and the convolution is given by the convolution theorem in Eq. (A.30). Using the Fourier transforms of the weight functions, given in Sec. B.3, the right-hand side reads

$$\begin{aligned}&\tilde{w}_i^{(0)}(\vec{k})\tilde{w}_j^{(3)}(\vec{k}) + \tilde{w}_i^{(1)}(\vec{k})\tilde{w}_j^{(2)}(\vec{k}) + \tilde{w}_i^{(1)}(\vec{k}) \cdot \tilde{w}_j^{(2)}(\vec{k}) + (i \leftrightarrow j) \\ &= \frac{4\pi}{|\vec{k}|^4 \sqrt{2\pi}^6} \frac{S_i}{R_i} (S_j - |\vec{k}|R_j C_j) + \frac{4\pi}{|\vec{k}|^2 \sqrt{2\pi}^6} R_j S_i C_j \\ &\quad - \frac{4\pi}{|\vec{k}|^4 \sqrt{2\pi}^6} \frac{1}{R_i} \left(|\vec{k}|^2 R_i R_j C_i C_j - |\vec{k}| R_i C_i S_j - |\vec{k}| R_j C_j S_i + S_i S_j \right) + (i \leftrightarrow j) \\ &= \frac{4\pi}{|\vec{k}|^2 \sqrt{2\pi}^6} (R_i + R_j)(S_i S_j - C_i C_j) + \frac{4\pi}{|\vec{k}|^3 \sqrt{2\pi}^6} (C_i S_j + C_j S_i) \\ &= \frac{4\pi}{|\vec{k}|^3 \sqrt{2\pi}^6} \left((S_i - |\vec{k}|R_i C_i)C_j + (S_j - |\vec{k}|R_j C_j)C_i + |\vec{k}|(R_i + R_j)S_i S_j \right),\end{aligned}$$

where $(i \leftrightarrow j)$ denotes a repetition of the previous terms, where the indices i and j are interchanged.

Apparently, both sides are equal. \square

⁷Is is $\sin(a + b) = \sin(a)\cos(b) + \cos(a)\sin(b)$ and $\cos(a + b) = \cos(a)\cos(b) - \sin(a)\sin(b)$.



Numerics

$\pi\alpha\nu\tau\alpha \dot{\rho}\varepsilon\tilde{\iota}$ (panta rhei) "everything flows"

(Heraclitus around 520 B.C. - 460 B.C.)

Numerics is an important part of thesis, because the free energy functional that is used must be calculated numerically and the calculations of the equilibrium density profiles are time-consuming. To achieve free minimization of the density profiles, the profiles $\rho(\vec{r})$ are discretized (or parametrized) on a rectangular cuboid grid of dimensions $N_x \times N_y \times N_z$. In general, several spacings of the numerical grid have been implemented to avoid results due to numerical errors, but especially for the interfaces, most calculations have been restricted to the typical spacings as listed in Table C.1. Moreover, it would be possible to apply intelligent mesh coarsening, to achieve optimal resolutions for the strongly peaked crystalline density profiles, but the effort in programming would be enormous. In addition to this, well optimized fast Fourier transform methods exist for equidistant grids. An exception is done for the calculation of the Lindemann parameter in Sec. 4.2.2, where an integration over a Wigner-Seitz cell must be applied. In this situation, the numerical grid is refined at the borders of the cell.

A well-written collection about numerics is given by the *Numerical Recipes in C* [314]. Moreover, D. Frenkel and J. P. McTague wrote a review about *Computer Simulations of Freezing and Supercooled Liquids* [160] and L. J. D. Frinka and A. G. Salinger discussed numerical approaches regarding mesh coarsening, iteration methods, and parallelization in Refs. [315, 316]. In these works about *Two- and Three-Dimensional Nonlocal Density Functional Theory for Inhomogeneous Fluids* they state:

Table C.1: Typical dimensions $N_x \times N_y \times N_z$ and grid spacings dx , dy , dz of numerical grids that correspond to unit cells and interfaces of given cell orientation. In contrast to unit cells, for an interface cell only its length in z direction changes. The grid spacings are rounded to the last digits that are displayed.

	N_x	N_y	$N_z^{\text{unit cell}}$	$N_z^{\text{interface}}$	dx	dy	dz
(001)	64	64	64	$32 \times 64 = 2048$	0.0245σ	0.0245σ	0.0245σ
(011)	64	64	64	$48 \times 64 = 3072$	0.0245σ	0.0173σ	0.0173σ
(111)	64	128	128	$24 \times 128 = 3072$	0.0169σ	0.0150σ	0.0212σ
(012)	64	192	192	$16 \times 192 = 3072$	0.0245σ	0.0183σ	0.0183σ
(112)	64	128	128	$32 \times 128 = 4096$	0.0173σ	0.0212σ	0.0150σ

One of the key methods for studying the properties of inhomogeneous fluids in simple geometries has been density functional theory (DFT). (...) The computational difficulty arises from the need to perform nested integrals that are due to nonlocal terms in the free energy functional. These integral equations are expensive both in evaluation time and in memory requirements; however, the expense can be mitigated by intelligent algorithms and the use of parallel computers.

Thus, simple parallelization via OpenMP (Open Multiprocessing) has been used in this thesis and results in a speedup of about 3.0 while using 5 parallel cores, for example (speedup of about 4 to 5 if 12 cores are used). In principle, the convolutions can be run on different cores and the calculation of the functional can be carried out independently for each grid point. Of course, further improvements are possible, but it seems not to be worth the effort in programming. In another sense, data storage could perhaps be performed with more efficiency, to allow the usage of bigger volumes. As several weighted densities are needed simultaneously, an amount of about 4 GB of memory is required to minimize a (001) unit cell and 17.5 GB for an interface with (012) orientation (for grid-sizes as listed in Table C.1). One density profile takes about 70 MB memory for the (001) orientation and about 300 MB for (012).

The convolutions, that enter the calculations of the weighted densities in Eq. (3.35) and the functional derivative in Eq. (3.63), are applied in Fourier space. As an advantage, the weight functions δ and Θ have less singular forms than in real space. In addition, R. Roth discusses numerical corrections of the weight functions in Ref. [29]. However, numerical corrections can, in general, cause other problems that have unknown meaning. Thus, they have been avoided in this work, if possible.

In his review, R. Roth also gives examples how to check FMT implementations. Here, it is important to check all implementations twice. For example, small changes in one of the non-scalar weight functions can lead to small differences in the crystal energies, but do not alter liquid properties. Nevertheless, the variation can cause huge errors in quantities like the surface tension. At this position it also should be mentioned that the components of the vectorial and the off-diagonal components of the tensorial weight functions must be set to zero, if $k_\alpha = \pm \frac{2\pi}{L_\alpha} \frac{N_\alpha}{2}$ for $\alpha \in \{x, y, z\}$. Thus, the symmetry of the vectorial weight functions is kept.

In this chapter, first various methods are discussed to solve the equation of state. Then, the discrete Fourier transformation is presented. In addition, an explicit library is introduced and also used to implement numerical convolutions.

C.1 Solving the equation of state

In Sec. 2.3, the fundamental equation of state (2.42) is introduced and leads to the implicit Eq. (2.49),

$$\log(\rho_{\text{eq}}(\vec{r})\Lambda^3) = \beta\mu - \beta V_{\text{ext}}(\vec{r}) + c[\rho_{\text{eq}}; \vec{r}], \quad (\text{C.1})$$

where $-c[\rho; \vec{r}]$ is the functional derivative of the excess free energy functional $\mathcal{F}_{\text{exc}}[\rho]$ with respect to the density profile $\rho(\vec{r})$ and Λ the (irrelevant) thermal wavelength. In principle, iterative methods are used to solve Eq. (C.1). Thus, first an initial guess for the density profile must be obtained.

In general, it is not possible to obtain an inhomogeneous density profile, if the initial profile is a homogeneous one and no external fields are applied, because the necessary fluctuations are not included explicitly in DFT to achieve inhomogeneities. Moreover, it is important to choose a physical density profile that has no local packing fractions $n_3(\vec{r})$ higher than 1. On the one hand, a unit cell can be filled up with Gaussian peaks as described in Sec. 4.1.4, to obtain a crystalline unit cell. On the other hand, it is much more difficult to achieve an initial interface profile. First, the volume can be filled with, i.e. 32, copies of a minimized density profile of a unit cell. Then, the variation between the crystalline phase and a constant, homogeneous fluid phase density can be applied by a variational function, as described in Sec. 5.2.1. However, it is important not to exceed the local limit of $n_3(\vec{r}) \leq 1$ due to the terms $\log(1 - n_3)$ and $(1 - n_3)^{-1}$ that enter the excess free energy functional.

Now, a self-consistent solution of Eq. (C.1) can be achieved by applying the numerical methods, explained in this section. In every step, the given density profile $\rho^{(i)}$ is used to calculate the weighted densities $n_\alpha^{(i)}$ via a convolution with the weight functions w_α , the energy functional $\Phi^{(i)}$, its functional derivative $\delta\mathcal{F}/\delta\rho^{(i)}$, again via a convolution, and finally a new density profile $\rho^{(i+1)}$. While the latter is obtained using one of the numerical methods, it is important to prevent the local packing fraction $n_3(\vec{r})$ from exceeding 1, for example by controlling the mixing parameter of the Picard iteration scheme (see Sec. C.1.1). However, the best method to avoid unphysical situations is the reduction of the speed of convergence (depending on the numerical method), because manipulations of the density profile certainly cause other problems and have no physical meaning. Thus, interventions like smoothing the density profile¹ should be avoided, even if numerical fluctuations appear. In such situations, changing the numerical method can establish stability again. Besides, a discussion of instabilities is given by J. R. Henderson and Z. A. Sabeur in Ref. [317].

In another sense, solving Eq. (C.1) leads to an equilibrium density profile $\rho_{\text{eq}}(\vec{r})$ with a μ -dependent bulk density $\rho_0(\mu) = \int_V \rho_{\text{eq}}(\vec{r}) d\vec{r} / V$ in a unit cell of volume $V = a^3$. The lattice constant a (side length of the unit cell) and the vacancy concentration n_{vac} , defined in Eq. (4.6), should in principle adjust itself to comply with Eq. (C.1), as outlined in Ref. [146]. However, in practice, such a procedure is not feasible. Rather, for a given chemical potential μ or bulk density ρ_0 , also the vacancy concentration (or unit-cell volume) is prescribed and only a constrained solution of Eq. (C.1) is obtained, where $\rho_0(\mu, n_{\text{vac}})$ or $\mu \equiv \mu(\rho_0, n_{\text{vac}})$ play the role of a Lagrangian multiplier to ensure the definition of the vacancy concentration in Eq. (4.6).²

¹A lot of methods have been tried, for example cutting frequencies in Fourier space or convolving with kernels.

²Formulation in parts by M. Oettel; also compare with Sec. III.A of Ref. [146].

In Sec.C.1.1, *Picard iterations* are explained. This iteration scheme can be sped up by applying the *Direct inversion in iterative subspace* (DIIS) method, introduced in Sec. C.1.2. Then, in Sec. C.1.3 a gradient descent method is explained that applies a kind of pseudo-dynamics. Dynamical DFT is discussed for solving the equation of motion in Sec. C.1.4, and the convergence of solutions is discussed in Sec. C.1.5, where also a measure for convergence is defined. Finally, an example for a calculation procedure is given in Sec. C.1.6.

C.1.1 Picard iterations

The Picard iteration schema is named after Charles Émile Picard (1856-1941). It provides a solution method for implicit equations that, in principle, are solvable by iterations. Here, the Picard-Lindelöf theorem and other mathematical existence theorems predict the existence of solutions to such equations as the limit of a convergent sequence, obtained by iterations.

In this sense, the conditional Eq. (C.1) states an iterative equation of the form

$$Af = f, \quad (\text{C.2})$$

where A is a (non-linear) operator on a function space and f a real valued function. Now, the Picard iteration schema follows with

$$f_{n+1} = Af_n, \quad n \in \mathbb{N} \quad (\text{C.3})$$

and an initial guess for f_0 . If the sequence converges, the limiting element will be a solution of (C.2).³

In a numerical sense, the sequence f_n often diverges or oscillates. This problem can be avoided by decreasing the amount of change of f_n per iteration step. Thus, the results obtained from f_n by Eq. (C.2) are not directly set as new elements f_{n+1} of the iterative sequence, but they are intermixed with the previous solutions f_n . For this purpose, a mixing parameter $\alpha \in [0, 1]$ is defined and the scheme reads

$$f_{n+1} = \alpha Af_n + (1 - \alpha)f_n. \quad (\text{C.4})$$

The optimal choice of the mixing parameter α must be determined empirically. In addition, the convergence can be speed up by Broyles' extrapolation in the final stages of the iteration, when the sequence converges very slowly [319].

However, a lot of effort can be raised to optimize the iteration process and speed it up. For example, the mixing parameter α can dynamically be adapted with respect to the speed of convergence. In this sense, R. Roth suggests to determine a maximal mixing parameter α_{\max} to prevent the local packing fraction n_3 in FMT from exceeding a value of 1 [29].

³For example, see the appendix of Ref. [318] by K.-C. Ng.

Because the weighted density n_3 is linear in ρ , a local α_{\max} follows with

$$\begin{aligned} n_3[\rho_{i+1}] &= (1 - \alpha_{\max})n_3[\rho_i] + \alpha_{\max}n_3[A\rho_i] \stackrel{!}{=} 1 \\ \Rightarrow \alpha_{\max} &= \frac{1 - n_3[\rho_i]}{n_3[A\rho_i] - n_3[\rho_i]} \end{aligned} \quad (\text{C.5})$$

and its minimum is chosen as a global one. Accordingly, an optimal α is obtained by minimizing the grand energy $\Omega[\rho_{i+1}(\alpha)]$ with respect to α .

To sum up, the optimal choice of the mixing parameter depends on the problem and on the operator A . By experience with crystalline density profiles and with the White Bear mark II functional, α ranges from about 1% down to 10^{-5} and should be chosen constant (without dynamical adaption). However, an enormous speed up can be obtained by using the *Direct inversion in the iterative subspace* method, introduced in the following.

C.1.2 Direct inversion in iterative subspace (DIIS)

The *Direct inversion in the iterative subspace* (DIIS) method is a combination of a direct and of an iterative method, “developed in the context of ab initio molecular orbital calculations” [211] by P. Pulay [210, 320]. Following Eq. (C.2) and the notation in Ref. [318] by K.-C. Ng, the DIIS output functions are defined for $n \in \mathbb{N}$ by

$$g_n = Af_n. \quad (\text{C.6})$$

Now, DIIS requires a set of N input functions f_n and output functions g_n , for example obtained by simple Picard iterations via $f_{n+1} = g_n$, respectively. Then, the residuum vectors are defined by⁴

$$d_n = g_n - f_n, \quad n \in [1, N], \quad (\text{C.7})$$

$$d = \sum_{n=1}^N c_n d_n \quad (\text{C.8})$$

and d is assumed to approximate the zero vector in a mean-square sense, while $\sum c_i = 1$ holds. Accordingly, a set of $N + 1$ equations is given by

$$\begin{pmatrix} \langle d_1 | d_1 \rangle & \langle d_1 | d_2 \rangle & \dots & \langle d_1 | d_N \rangle & -1 \\ \langle d_2 | d_1 \rangle & \langle d_2 | d_2 \rangle & \dots & \langle d_2 | d_N \rangle & -1 \\ \vdots & \vdots & \ddots & \vdots & \vdots \\ \langle d_N | d_1 \rangle & \langle d_N | d_2 \rangle & \dots & \langle d_N | d_N \rangle & -1 \\ -1 & -1 & \dots & -1 & 0 \end{pmatrix} \cdot \begin{pmatrix} c_1 \\ c_2 \\ \vdots \\ c_N \\ \lambda \end{pmatrix} = \begin{pmatrix} 0 \\ 0 \\ \vdots \\ 0 \\ -1 \end{pmatrix}, \quad (\text{C.9})$$

⁴The method has been adapted to this special problem by M. Oettel.

where $\langle f|g \rangle$ defines a scalar product in the parameter space and λ is a Lagrangian multiplier. Then, the DIIS result f_{N+1} reads

$$f_{N+1} = \sum_{n=1}^N c_n g_n. \quad (\text{C.10})$$

C.1.3 Gradient descent dynamics or simulated quenching

Instead of solving Eq. (C.1) by using iterations, the equilibrium condition $\delta\Omega[\rho]/\delta\rho|_{\rho=\rho_{\text{eq}}}=0$ can be solved directly by minimizing the energy functional $\Omega[\rho]$ with respect to the density profile ρ . For this purpose, a variety of numerical minimizing methods is available, for example the simulated annealing method, the gradient descent method, the Newton algorithm, or the Levenberg-Marquardt algorithm (as a combination of the previous two algorithms). Thereby, all methods have their pros and cons.

R. Ohnesorge et al. introduced a variation of the gradient descent method that might be called *simulated quenching* and is inspired by simulated annealing [97]. For a parametrization of ρ on a numerical grid with $N = N_x \times N_y \times N_z$ points, the method assumes a virtual particle with a certain mass m on this N -dimensional space that follows Newton's second law of motion. Thereby, the functional derivative $\delta\Omega[\rho]/\delta\rho$ acts as a driving force.

Starting from an initial density profile ρ_0 , the particle moves through the N -dimensional space and is stopped, if its kinetic energy reaches a maximum (the “quenching” [97]). Then, the particle is released again, until it reaches the minimum within a given numerical uncertainty.

The dynamics of the virtual particle are discretized using finite timesteps Δt . Here, the position at $t = 0$ is ρ_0 and the acceleration a_0 is determined by

$$a_n = \frac{F_n}{m} = -\frac{1}{m} \frac{\delta\Omega[\rho]}{\delta\rho_n}. \quad (\text{C.11})$$

If the acceleration a_n is assumed to be constant on the time interval $[t_n - \frac{1}{2}\Delta t_n, t_n + \frac{1}{2}\Delta t_n]$, then the velocity in between to positions ρ_n and ρ_{n+1} can be determined by

$$v_{n+\frac{1}{2}} = v_{n-\frac{1}{2}} + \Delta t_n a_n. \quad (\text{C.12})$$

Of course, $v_{-\frac{1}{2}}$ is assumed to be 0. To avoid the implicit form

$$\rho_{n+1} = \rho_n + \frac{1}{2} \left(\frac{\Delta t_n}{2} \right)^2 a_n + \frac{1}{2} \left(\frac{\Delta t_{n+1}}{2} \right)^2 a_{n+1}, \quad (\text{C.13})$$

the velocity $v_{n+\frac{1}{2}}$ is assumed to be constant on the time interval $[t_n, t_{n+1}]$, what is only

correct in the limit of $\Delta t \rightarrow 0$. Hence, an approximative rule follows with

$$\begin{aligned}\rho_{n+1} &= \rho_n + \frac{1}{2} (\Delta t_n + \Delta t_{n+1}) v_{n+\frac{1}{2}} \\ &= \rho_n + (\rho_n - \rho_{n-1}) \frac{\Delta t_n + \Delta t_{n+1}}{\Delta t_{n-1} + \Delta t_n} + \frac{1}{2} (\Delta t_n + \Delta t_{n+1}) \Delta t_n a_n.\end{aligned}\quad (\text{C.14})$$

Apparently, negative density values can occur during such a numerical time step (C.14). To avoid them, a negative value $(\rho_{n+1})_i$ at time t_{n+1} is replaced by $\frac{1}{2}(\rho_n)_i$. Thus, the tendency of decreasing the value is kept. Moreover, typical masses range from $0.01k_B T \sigma^3$ up to $10k_B T \sigma^3$ for a dimensionless time unit.

When the energy profile is too flat around the minimum, the determination of the maximum of the kinetic energy becomes difficult. In such situations, the calculation of a scalar product between the velocity $v_{n-\frac{1}{2}}$ and the acceleration a_n might be helpful, because it can indicate large directional changes of the driving force. Furthermore, a cubic fit can be used to determine the position of the maximum in the kinetic energy.

C.1.4 Dynamical DFT algorithm

In general, an equilibrium density profile can also be obtained by applying dynamical density functional theory (DDFT), as described in Sec. 2.4. For this purpose, the partial derivatives with respect to time and all spatial coordinates must be discretized to allow numerical calculations.

The most simple discretization scheme is the centered-time or centered-space discretization of a differential operator $\partial_x \equiv \frac{\partial}{\partial x}$,⁵ acting on a function $f : \mathbb{R}^3 \rightarrow \mathbb{R}$. On a numerical grid with positions x_i , the scheme reads

$$\frac{\partial}{\partial x} f(x_i, y, z, t) = \frac{f(x_{i+1}, y, z, t) - f(x_{i-1}, y, z, t)}{x_{i+1} - x_{i-1}} = g(x_i, y, z, t).\quad (\text{C.15})$$

However, the centered-time discretization is not stable for the diffusive part of the DDFT Eq. (2.54) when combined with the centered-space discretization, as also observed for the physical model of orientational resolved spherocylinders, which has been introduced in Sec. 6.2. So, negative densities appear already after a few hundred time steps. Thus, for the calculations regarding Sec. 6.2, a forward-time centered-space discretization has been used that remains stable for sufficiently long times and adequate time steps.

Conversely, this simple discretization of the gradient is not stable, if applied to the spatial resolved hard-sphere system, investigated in Sec. 4.2 and Chapter 5 of this work. First investigations show that it could be necessary to decouple the different parts of the DDFT Eq. (2.54) and to solve them by implicit and explicit discretization schemes, respectively.

⁵The parameter x can either denote a spatial coordinate or time.

Especially the Laplacian of the density profile⁶ seems to be unstable for explicit methods, while the remaining terms, involving the excess free energy functional, seem to be stable for explicit methods. For further reading, the Numerical Recipes [314] also intensely discuss the discretization and stabilization of the diffusion equation and similar equations. In this context, interesting topics are for example the Lax-Wendroff scheme and operator splitting.

C.1.5 Convergence of solutions

While solving Eq. (C.2), the existence of a convergence parameter is useful to monitor the order of convergence of the solution. For example, the grand energy of the system states a simple but poor parameter, because its value in the limit of convergence is not known. A more reasonable convergence parameter is defined by

$$\epsilon = \|Af - f\|^2, \quad (\text{C.16})$$

using the L^p -norm $\|f\|_p$ that is defined in Eq. (A.2). For example, a Gaussian fcc density profile (on a unit cell) starts with convergence values of around $\epsilon \approx 10^5$ and ends after a few hundred iteration cycles at a value of around $\epsilon \approx 10^{-7}$. However, the mixing parameter α must be chosen appropriately: Too small mixing parameters cause slow convergence and too large values cause the solution to diverge. In this sense, an automatically chosen mixing parameter easily tends to cause problems.

In another sense, the convergence parameter ϵ is extremely sensitive with respect to the minimization method discussed in Sec. C.1.3. Here, other parameters might be more appropriate that are not (like ϵ) defined via Eq. (C.2).

Sometimes, the process of convergence ($\epsilon \rightarrow 0$) is very slow or the limit of $\epsilon = 0$ can not be reached, typically due to the numerical implementation. If now properties of the exact solution are of interest, an extrapolation is possible, where parameters like the energy of the system are plotted against the convergence ϵ . From this plot, the value for vanishing ϵ can be extracted easily.

In addition, the constrained chemical potential (following from Eq. (C.1)) can be obtained by [146]

$$\mu(\rho_0, n_{\text{vac}}) = \frac{1}{V} \int_V \left(\log(\rho_{\text{eq}}(\vec{r}) \Lambda^3) - c[\rho_{\text{eq}}; \vec{r}] \right) d\vec{r} \quad (\text{C.17})$$

and provides an additional (mean) quantity to monitor convergence.⁷ In principle, an analysis of this quantity also allows a statement about the local convergence of the density profile.⁸

⁶Appearing in the ideal free energy part of the DDFT equation.

⁷An explicit form obtained from reciprocal space (see Ref. [146]) is given in Sec. B.2 for the White Bear mark II functional.

⁸Observations show that regions of low density in the profile ρ converge much slower than other regions.

However, if the bulk density is fixed during calculations, the chemical potential swings from a low value up to a value above its final one and than slowly decreases. Because high chemical potentials correspond to high bulk densities, the local packing fraction could exceed one. In general, this phenomenon marks a problem in FMT, because the functional diverges for local packings that exceed one. To avoid such situations, the best method is to reduce the speed of convergence. In principle, manipulations of the density profile also seem to be a solution, but every manipulation causes other problems. And because manipulations are usually not physical, it is better to avoid them.

C.1.6 Example for a calculation

To give an example, the calculations are described now that have been applied to an initial density profile to achieve the results that are explained in Sec. 4.2.3.

Initial density profiles are achieved by setting up a crystalline fcc structure of a unit cell by using the Gaussian density peak approximation in Eq. (4.7). Then, the equilibrium density profiles are obtained by a combination of ordinary Picard iterations and DIIS steps.

Using the White Bear mark II functional, 300 ordinary Picard iteration steps are applied to the density profiles to achieve a stable starting point for the usage of the DIIS method. Then, 500 steps of Picard iterations and DIIS steps are applied, where at least 20 Picard steps are run before starting a DIIS step. During these 20 waiting steps, the convergence ϵ (see Sec. C.1.5) is not allowed to raise. Moreover, additional 8 Picard steps are needed to obtain the residual vectors, needed to run the DIIS interpolation. Finally, 200 ordinary Picard steps are applied to the density profile to avoid numerical effects due to the DIIS method.

In principle, the same results could be achieved with much less effort, but this procedure ensures convergence even if the procedure is applied to many different parameter settings of a system. Furthermore, only 300 ordinary Picard iteration steps are sufficient to obtain similar results when using the Ramakrishnan-Yussouff functional approach.

The calculations are run on 18 computational cores, using a grid in (001) orientation as described in Table C.1. The Picard iterations were applied with a maximal mixing factor $\alpha = 0.001$.

If calculations are applied to an interface, much more computational effort is needed. Then, the gradient descent dynamics method also is needed to obtain results in reasonable computational time.

C.2 Discrete Fourier transformation and convolution

In this section, the discrete Fourier transformation is introduced, as it is used for numerical calculations. It is especially used to apply convolutions with weight functions from FMT in the context of this work. For further information see also Chapters 12 and 13 of the textbook *Numerical Recipes in C* by W. H. Press et al. [314] about the *Fast Fourier Transform and Fourier and Spectral Applications*.

Let $f : \mathbb{R}^n \rightarrow \mathbb{R}$ be a continuous periodic function with vectors \vec{L}_ν ($1 \leq \nu \leq n$) that span the periodicity of the function and point along the basis vectors \hat{e}_ν of \mathbb{R}^n . Accordingly, f holds

$$f(\vec{x}) = f \left(\vec{x} + \sum_{\nu=1}^n i_\nu \vec{L}_\nu \right). \quad (\text{C.18})$$

Then, the periodic function f can be expanded in a Fourier series that only contains reciprocal vectors which are compatible with the periodicity of the function f . Accordingly, the remaining reciprocal vectors \vec{k} are

$$(\vec{k})_\nu = k_\nu \in \left\{ \pm \frac{2\pi}{|\vec{L}_\nu|} i_\nu \middle| i_\nu = 0, 1, 2, \dots \right\}, \quad \nu = 1, \dots, n. \quad (\text{C.19})$$

Moreover, let V be the volume spanned by the periodicity vectors $\{\vec{L}_\nu\}$. Then, the previous result can also be deduced by rewriting the Fourier transform from Eq. (A.27) in the form

$$\begin{aligned} \tilde{f}(\vec{k}) &= \sum_{\nu=1}^n \sum_{i_\nu} \int_V f \left(\vec{x} + \sum_{\alpha=1}^n i_\alpha \vec{L}_\alpha \right) e^{-i\vec{k} \cdot (\vec{x} + \sum_{\alpha=1}^n i_\alpha \vec{L}_\alpha)} d\vec{x} \\ &= 2 \sum_{\nu=1}^n \sum_{i_\nu} \cos \left(\vec{k} \cdot \left(\sum_{\alpha=1}^n i_\alpha \vec{L}_\alpha \right) \right) \int_V f(\vec{x}) e^{-i\vec{k} \cdot \vec{x}} d\vec{x}. \end{aligned} \quad (\text{C.20})$$

Using arguments from representation theory, only the above mentioned elements (C.19) yield terms that do not vanish. Thus, the transformation of a periodic function is a transformation between the Euclidean space and a trigonometric function space.

Now, the n -dimensional volume V is discretized in real space on a numerical equidistant grid \mathbb{G} of dimensions $N_1 \times \dots \times N_n$. Recalling the formalism of unit cells from Sec. 4.1.2, V is the volume of the unit cell and the vectors that denote periodicity are the basis of the corresponding lattice \mathbb{L} . Combining the grid \mathbb{G} and the lattice \mathbb{L} , the complete space is discretized by the numerical grid resulting from the tensor product $\mathbb{L} \otimes \mathbb{G}$. For numerical reasons, the N_ν should be even integers with small prime factors, best a power of 2. Consequently, the finite step sizes Δx_ν of the grid follow with $\Delta x_\nu = |\vec{L}_\nu|/N_\nu$.

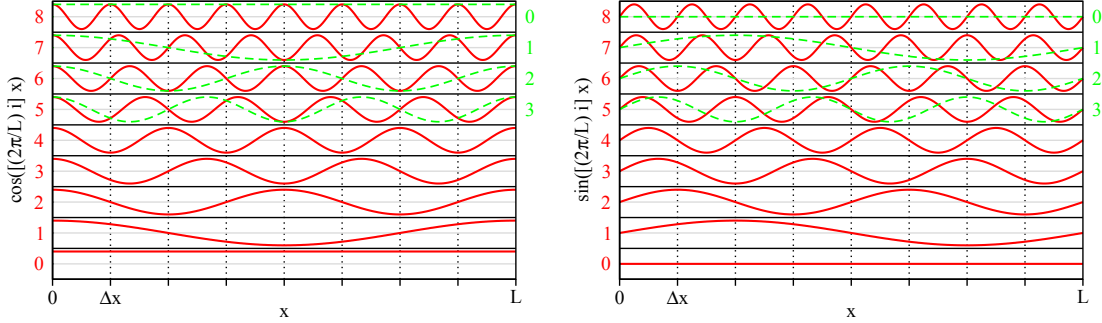


Figure C.1: (Color) Possible wave vectors on a periodic length L shown for a grid of $N = 8$ points and a grid length of $\Delta x = L/8$. The waves are of the form (a) $\cos((2\pi/L)ix)$ and (b) $\sin((2\pi/L)ix)$. The green stroked lines (index i on the right axis) are copies of the first 4 waves (from bottom to top). Apparently, on this grid the waves with $i \in \{0, 1, 2, 3, 4\}$ lead to the same values as the waves with $i \in \{8, 7, 6, 5, 4\}$. Moreover, the upper 4 waves are corresponding to negative frequencies, because (a) $\cos(-(2\pi/N)i) = \cos((2\pi/N)[N-i])$ and (b) $\sin(-(2\pi/N)i) = \sin((2\pi/N)[N-i])$. For (b), the wave vectors with $i \in \{0, 4, 8\}$ are vanishing.

The maximal resolution of such a numerical grid is given by the grid spacings $\Delta x_1, \dots, \Delta x_n$. For this reason, the reciprocal wave vectors \vec{k} from Eq. (C.19) are limited by maximum components $\pi/\Delta x_\nu$, for $1 \leq \nu \leq n$. Accordingly, the reciprocal Fourier space can be discretized by $N_\nu + 1$ grid points in every coordinate or dimension. This restriction becomes apparent in Fig. C.1, where wave functions are shown for one dimension $n = 1$. Though, the functions corresponding to $k = (2\pi/L)N/2$ and to $k = (2\pi/L)(N/2 - N)$ already contain identical information on the grid \mathbb{G} . Of course, the statement also holds for all higher frequencies.

To sum up, the discretizations read $\vec{x}_{i^n} = \sum_\nu i_\nu \Delta x_\nu \vec{e}_\nu$ and $\vec{k}_{a^n} = \sum_\nu a_\nu 2\pi/|\vec{L}_\nu| \vec{e}_\nu$, where $i^n = (i_1, \dots, i_n)$ and $a^n = (a_1, \dots, a_n)$ denote multi-indices. Here, negative frequencies in Fourier space are moved to positive ones, what does not change any results due to the periodicity of the trigonometric functions sin and cos. Using these discretizations, the discrete Fourier transform⁹ of a periodic function f and its inverse follow from Eq. (A.27) with¹⁰

$$\tilde{f}(\vec{k}_{a^n}) = \frac{1}{\sqrt{2\pi}^3} \sum_{i_1=0}^{N_1-1} \dots \sum_{i_n=0}^{N_n-1} \left(\prod_{\nu=1}^n \Delta x_\nu e^{-2\pi i_\nu a_\nu / N_\nu} \right) f(\vec{x}_{i^n}), \quad (\text{C.21})$$

$$f \sim (\vec{x}_{i^n}) = \frac{1}{\sqrt{2\pi}^3} \sum_{a_1=0}^{N_1} \dots \sum_{a_n=0}^{N_n} \left(\prod_{\nu=1}^n \frac{2\pi}{|\vec{L}_\nu|} e^{2\pi i_\nu a_\nu / N_\nu} \right) f(\vec{k}_{a^n}). \quad (\text{C.22})$$

⁹The abbreviation DFT is avoided in this work due to the equal shortcut for *density functional theory*.

¹⁰The sums over the indices i^n in real space must run until N_ν instead of $N_\nu - 1$ for a finite non-periodic volume, because the borders of a non-periodic volume differs, similar to the discretization in Fourier space.

These transformations are changes between two vector spaces, namely the discrete Euclidean space and the discrete Fourier space, spanned by the basis functions \sin and \cos . The latter enter via the identity $\exp(ix) = \cos(x) + i\sin(x)$. Accordingly, the transform of a real-valued function $f : \mathbb{R} \rightarrow \mathbb{R}$ has the complex conjugate symmetry $\tilde{f}(-\vec{k}) = \tilde{f}(\vec{k})^*$, where f^* denotes the complex conjugate of f .

The discrete Fourier transformation can be calculated using efficient fast Fourier transformation (FFT) methods. In this work, the FFT package “Fastest Fourier Transform in the West” (FFTW) is used (version 3.2.2) that was developed at MIT by M. Frigo and S. G. Johnson.¹¹

Now, the FFTW routines $\text{FFTW}_f(f)$ and $\text{FFTW}_b(g)$ denote the forward and backward fast Fourier transforms of the functions f and g . In three dimensions, the routines read

$$\begin{aligned} \text{FFTW}_f(f)(\vec{k}_{a_1 a_2 a_3}) &= \sum_{i_1=0}^{N_1-1} \sum_{i_2=0}^{N_2-1} \sum_{i_3=0}^{N_3-1} f(\vec{x}_{i_1 i_2 i_3}) e^{-2\pi i(i_1 a_1/N_1 + i_2 a_2/N_2 + i_3 a_3/N_3)} \\ &= \frac{\sqrt{2\pi}^3}{\Delta x_1 \Delta x_2 \Delta x_3} \tilde{f}(\vec{k}_{a_1 a_2 a_3}), \end{aligned} \quad (\text{C.23})$$

$$\begin{aligned} \text{FFTW}_b(g)(\vec{x}_{i_1 i_2 i_3}) &= \sum_{a_1=0}^{N_1} \sum_{a_2=0}^{N_2} \sum_{a_3=0}^{N_3} g(\vec{k}_{a_1 a_2 a_3}) e^{2\pi i(i_1 a_1/N_1 + i_2 a_2/N_2 + i_3 a_3/N_3)} \\ &= \frac{|\vec{L}_1||\vec{L}_2||\vec{L}_3|}{\sqrt{2\pi}^3} g_\sim(\vec{x}_{i_1 i_2 i_3}). \end{aligned} \quad (\text{C.24})$$

Apparently, for the FFTW routines the identity $\text{FFTW}_b(\text{FFTW}_f(f)) = N_x N_y N_z f$ holds.

If the function f is a real-valued function, the transform of f has the Hermitian symmetry $\tilde{f}(\vec{k}_{a_1, a_2, a_3}) = \tilde{f}^*(\vec{k}_{a_1, a_2, N_3 - a_3})$, where $(u + iv)^* = (u - iv)$ defines the complex conjugate operation. Moreover, the transform \tilde{f} is periodic with $\tilde{f}(\vec{k}_{a_1, a_2, 0}) = \tilde{f}(\vec{k}_{a_1, a_2, N_3})$. For this reason, the FFTW routines only store values for $a_3 \in \{0, \dots, N_3/2\}$.

Finally, the convolution from Eq. (A.30) can be rewritten in terms of the FFTW routines.

¹¹Visit the webpage <http://www.fftw.org/> for further information about FFTW.

If the Fourier transform \tilde{w} is known, the convolution $f * w$ follows with

$$\begin{aligned}
 (f * w)(\vec{x}) &= \int_{\mathbb{R}^3} f(\vec{y}) w(\vec{x} - \vec{y}) d\vec{y} \\
 &= \left(\sqrt{2\pi}^3 \tilde{f}(\vec{k}) \tilde{w}(\vec{k}) \right) \sim \\
 &= \frac{\sqrt{2\pi}^6}{L_1 L_2 L_3} \text{FFTW}_b \left(\tilde{f}(\vec{k}) \tilde{w}(\vec{k}) \right) (\vec{x}) \\
 &= \frac{\sqrt{2\pi}^6}{L_1 L_2 L_3} \text{FFTW}_b \left(\frac{\Delta x_1 \Delta x_2 \Delta x_3}{\sqrt{2\pi}^3} \text{FFTW}_f(f)(\vec{k}) \tilde{w}(\vec{k}) \right) (\vec{x}) \\
 &= \frac{\sqrt{2\pi}^3}{N_1 N_2 N_3} \text{FFTW}_b \left(\text{FFTW}_f(f)(\vec{k}) \tilde{w}(\vec{k}) \right) (\vec{x}). \tag{C.25}
 \end{aligned}$$

Bibliography

- [1] J. Fauvel, R. Flood, M. Shortland, and R. Wilson, editors, *Let Newton be!*, Oxford University Press, Oxford New York Tokyo (1988).
- [2] V. F. Buchwald, *Iron and steel in ancient times*, *Historisk-filosofiske Skrifter*, volume 29, Special-Trykkeriet Viborg a-s (2005).
- [3] P.-G. de Gennes, *Soft Matter*, pages 8–14, World Scientific Publishing Co., Singapore (1997).
- [4] A. Ajdari, *Pierre-Gilles de Gennes (1932-2007)*, Science **317**, 466 (2007).
- [5] H. Löwen, *Colloidal dispersions in external fields: recent developments*, J. Phys.: Condens. Matter **20**, 404201 (2008).
- [6] A. Ivlev, H. Löwen, G. Morfill, and C. P. Royall, *Complex Plasmas and Colloidal Dispersions: Particle-resolved Studies of Classical Liquids and Solids, Series in Soft Condensed Matter*, volume 5, World Scientific (2012).
- [7] M. Schmiedeberg, T. K. Haxton, S. R. Nagel, and A. J. Liu, *Mapping the glassy dynamics of soft spheres onto hard-sphere behavior*, Eur. Phys. Lett. **96**, 36010 (2011).
- [8] S. C. Glotzer and M. J. Solomon, *Anisotropy of building blocks and their assembly into complex structures*, Nature Mat. **6**, 557 (2007).
- [9] U. Gasser, E. R. Weeks, A. Schofield, P. N. Pusey, and D. A. Weitz, *Real-space Imaging of Nucleation and Growth in Colloidal Crystallization*, Science **292**, 258 (2001).
- [10] J. Hernández-Guzmán and E. R. Weeks, *The equilibrium intrinsic crystal-liquid interface of colloids*, Proc. Natl. Acad. Sci. **106**, 15198 (2009).
- [11] I. B. Ramsteiner, D. A. Weitz, and F. Spaepen, *Stiffness of the crystal-liquid interface in a hard-sphere colloidal system measured from capillary fluctuations*, Phys. Rev. E **82**, 041603 (2010).
- [12] V. D. Nguyen, Z. Hu, and P. Schall, *Single crystal growth and anisotropic crystal-fluid interfacial free energy in soft colloidal systems*, Phys. Rev. E **84**, 011607 (2011).
- [13] H. B. Callen, *Thermodynamics*, John Wiley and Sons, New York, London (1960).
- [14] H. Ayrton, *The Origin and Growth of Ripple-Mark*, Proc. R. Soc. Lond. A **84**, 285 (1910).

- [15] P. Tarazona, J. A. Cuesta, and Y. Martínez-Ratón, *Density Functional Theories of Hard Particle Systems, Lecture Notes in Physics*, volume 753, chapter 7, pages 247–341, Springer-Verlag, Berlin Heidelberg (2008).
- [16] R. Evans, *Density Functional Theory for Inhomogeneous Fluids I: Simple Fluids in Equilibrium*, in B. Cichocki, M. Napiórkowski, and J. Piasecki, editors, *3rd Warsaw School of Statistical Physics*, pages 43–85, Warsaw University Press, Warsaw (2010).
- [17] H. Löwen, *Density Functional Theory for Inhomogeneous Fluids II: Statics, Dynamics, and Applications*, in B. Cichocki, M. Napiórkowski, and J. Piasecki, editors, *3rd Warsaw School of Statistical Physics*, pages 87–121, Warsaw University Press, Warsaw (2010).
- [18] J. F. Lutsko, *Recent Developments in Classical Density Functional Theory*, volume 144, chapter 1, pages 1–92, John Wiley & Sons, Inc. (2010).
- [19] P. Hohenberg and W. Kohn, *Inhomogeneous Electron Gas*, Phys. Rev. **136**, B864 (1964).
- [20] N. D. Mermin, *Thermal Properties of the Inhomogeneous Electron Gas*, Phys. Rev. **137**, A1441 (1965).
- [21] C. Ebner, W. F. Saam, and D. Stroud, *Density-functional theory of simple classical fluids. I. Surfaces*, Phys. Rev. A **14**, 2264 (1976).
- [22] R. Evans, *The nature of the liquid-vapour interface and other topics in the statistical mechanics of non-uniform, classical fluids*, Adv. Phys. **28**, 143 (1979).
- [23] W. Kohn, *Nobel Lecture: Electronic structure of matter – wave functions and density functionals*, Rev. Mod. Phys. **71**, 1253 (1999).
- [24] W. Kohn, *Electronic Structure of Matter – Wave Functions and Density Functionals*, pages 213–237, World Scientific Publishing Co., Singapore (2003), nobel Lecture, January 28, 1999 (one year later).
- [25] Y. Rosenfeld, *Free-Energy Model for the Inhomogeneous Hard-Sphere Fluid Mixture and Density-Functional Theory of Freezing*, Phys. Rev. Lett. **63**, 980 (1989).
- [26] P. Tarazona, *Density Functional for Hard Sphere Crystals: A Fundamental Measure Approach*, Phys. Rev. Lett. **84**, 694 (2000).
- [27] H. Hansen-Goos and R. Roth, *Density functional theory for hard-sphere mixtures: the White Bear version mark II*, J. Phys.: Condens. Matter **18**, 8413 (2006).
- [28] H. Hansen-Goos and K. Mecke, *Fundamental Measure Theory for Inhomogeneous Fluids of Nonspherical Hard Particles*, Phys. Rev. Lett. **102**, 018302 (2009).
- [29] R. Roth, *Fundamental measure theory for hard-sphere mixtures: a review*, J. Phys.: Condens. Matter **22**, 063102 (2010).
- [30] U. M. B. Marconi and P. Tarazona, *Dynamic density functional theory of fluids*, J. Chem. Phys. **110**, 8032 (1999).

- [31] A. J. Archer and R. Evans, *Dynamical density functional theory and its application to spinodal decomposition*, J. Chem. Phys. **121**, 4246 (2004).
- [32] M. Rex and H. Löwen, *Dynamical Density Functional Theory with Hydrodynamic Interactions and Colloids in Unstable Traps*, Phys. Rev. Lett. **101**, 148302 (2008).
- [33] S. P. Thompson, *The Life of Lord Kelvin*, volume I, Chelsea Publishing Company, New York, N.Y., 2nd edition (1976).
- [34] J. W. Croker and W. Elwin, editors, *The Works of Alexander Pope*, volume II, Gordanian Press, New York, new edition (1967).
- [35] K. C. Cheng, *Historical Development of the Theory of Heat and Thermodynamics: Review and Some Observations*, Heat Transfer Eng. **13**, 19 (1992).
- [36] S. Carnot, *Reflections on the Motive Power of Fire*, Dover Publications, Inc., Mineola, New York, new edition (1988).
- [37] F. Reif, *Fundamentals of Statistical and Thermal Physics*, McGraw-Hill, Inc. (1965).
- [38] J. E. Mayer and M. G. Mayer, *Statistical Mechanics*, John Wiley & Sons, Inc., New York, London, Sydney, Totonto, 2nd edition (1966).
- [39] J.-P. Hansen and I. R. McDonald, *Theory of simple liquids*, Elsevier, 3rd edition (2006).
- [40] R. van Roij, *Classical ensemble theory*, in *Soft Condensed Matter & Advanced Colloid Science*, pages 25–44, Utrecht University (2005).
- [41] R. van Roij, *Simple Fluids*, in *Soft Condensed Matter & Advanced Colloid Science*, pages 45–74, Utrecht University (2005).
- [42] W. Thomson, *Mathematical and Physical Papers, Cambridge Library Collection - Physical Sciences*, volume 1, Cambridge University Press, Cambridge (2011), first published in 1882.
- [43] R. Clausius, *Ueber die bewegende Kraft der Wärme und die Gesetze, welche sich daraus für die Wärmelehre selbst ableiten lassen*, Ann. Phys. (Berlin) **155**, 368 (1850).
- [44] R. Clausius, *Ueber die bewegende Kraft der Wärme und die Gesetze, welche sich daraus für die Wärmelehre selbst ableiten lassen*, Ann. Phys. (Berlin) **155**, 500 (1850).
- [45] R. Clausius, *Ueber verschiedene für die Anwendung bequeme Formen der Hauptgleichungen der mechanischen Wärmetheorie*, Ann. Phys. (Berlin) **201**, 353 (1865).
- [46] E. Clapeyron, *Mémoire sur la puissance motrice de la chaleur*, Journal de l’École Polytechnique **XIV**, 153 (1834).
- [47] A. Krönig, *Grundzüge einer Theorie der Gase*, Ann. Phys. (Berlin) **175**, 315 (1856).

- [48] R. Clausius, *Ueber die Art der Bewegung, welche wir Wärme nennen*, Ann. Phys. (Berlin) **176**, 353 (1857).
- [49] M. Thiesen, *Untersuchungen über die Zustandsgleichung*, Ann. Phys. (Berlin) **260**, 467 (1885).
- [50] H. Kamerlingh-Onnes, *Expression of the equation of state of gases and liquids by means of series*, in Royal Netherlands Academy of Arts and Sciences (KNAW), *Proceedings*, volume 4, pages 125–147, Royal Netherlands Academy of Arts and Sciences, Amsterdam (1901–1902).
- [51] N. Foundation, editor, *Nobel Lectures In Physics (1901–1921)*, World Scientific Publishing Co. Pte. Ltd., Singapore (1998).
- [52] M. Goldman, *Introduction to Probability and Statistics*, Harcourt, Bruce & World, Inc., New York, Chicago, San Francisco, Atlanta (1970).
- [53] P. Hertz, *Über die mechanischen Grundlagen der Thermodynamik*, Ann. Phys. (Berlin) **338**, 225 (1910).
- [54] P. Hertz, *Über die mechanischen Grundlagen der Thermodynamik*, Ann. Phys. (Berlin) **338**, 537 (1910).
- [55] J. W. Gibbs, *Elementary Principles in Statistical Physics*, Cambridge University Press, New York (2010).
- [56] Y. Rosenfeld, *Density functional theory of molecular fluids: Free-energy model for the inhomogeneous hard-body fluid*, Phys. Rev. E **50**, R3318 (1994).
- [57] M. Rex, H. H. Wensink, and H. Löwen, *Dynamical density functional theory for anisotropic colloidal particles*, Phys. Rev. E **76**, 021403 (2007).
- [58] H. Reiss, H. L. Frisch, E. Helfand, and J. L. Lebowitz, *Aspects of the Statistical Thermodynamics of Real Fluids*, J. Chem. Phys. **32**, 119 (1960).
- [59] N. F. Carnahan and K. E. Starling, *Equation of State for Nonattracting Rigid Spheres*, J. Chem. Phys. **51**, 635 (1969).
- [60] S. Asakura and F. Oosawa, *On Interaction between Two Bodies Immersed in a Solution of Macromolecules*, J. Chem. Phys. **22**, 1255 (1954).
- [61] A. Vrij, *Polymers at Interfaces and the Interactions in Colloidal Dispersions*, Pure Appl. Chem. **48**, 471 (1976).
- [62] W. R. Smith, *Some Old and New Expansions in the Perturbation Theory of Fluids*, Can. J. Phys. **52**, 2022 (1974).
- [63] W. R. Smith, I. Nezbeda, T. W. Melnyk, and D. D. Fitts, *Reference system selection and average Mayer function perturbation theory for molecular fluids*, Faraday Discuss. Chem. Soc. **66**, 130 (1978).
- [64] J. E. Mayer, *Contribution to Statistical Mechanics*, J. Chem. Phys. **10**, 629 (1942).
- [65] M. Fasolo and P. Sollich, *Equilibrium Phase Behavior of Polydisperse Hard Spheres*, Phys. Rev. Lett. **91**, 068301 (2003).

- [66] T. V. Ramakrishnan and M. Yussouff, *First-principles order-parameter theory of freezing*, Phys. Rev. B **19**, 2775 (1979).
- [67] R. E. Rozas and J. Horbach, *Capillary wave analysis of rough solid-liquid interfaces in nickel*, Eur. Phys. Lett. **93**, 26006 (2011).
- [68] K. Sandomirski, E. Allahyarov, H. Löwen, and S. U. Egelhaaf, *Heterogeneous crystallization of hard-sphere colloids near a wall*, Soft Matter **7**, 8050 (2011).
- [69] D. Turnbull and R. L. Cormia, *A Dynamic Hard Sphere Model*, J. Appl. Phys. **31**, 674 (1960).
- [70] B. J. Alder and T. E. Wainwright, *Phase Transition for a Hard Sphere System*, J. Chem. Phys. **27**, 1208 (1957).
- [71] J. A. Barker and D. Henderson, *What is "liquid"? Understanding the states of matter*, Rev. Mod. Phys. **48**, 587 (1976).
- [72] T. Zykova-Timan, R. E. Rozas, J. Horbach, and K. Binder, *Computer simulation studies of finite-size broadening of solid-liquid interfaces: from hard spheres to nickel*, J. Phys.: Condens. Matter **21**, 464102 (2009).
- [73] T. Zykova-Timan, J. Horbach, and K. Binder, *Monte Carlo simulations of the solid-liquid transition in hard spheres and colloid-polymer mixtures*, J. Chem. Phys. **133**, 014705 (2010).
- [74] A. Härtel, M. Oettel, R. E. Rozas, S. U. Egelhaaf, J. Horbach, and H. Löwen, *Tension and Stiffness of the Hard Sphere Crystal-Fluid Interface*, Phys. Rev. Lett. **108**, 226101 (2012).
- [75] H. Reiss, H. L. Frisch, and J. L. Lebowitz, *Statistical Mechanics of Rigid Spheres*, J. Chem. Phys. **31**, 369 (1959).
- [76] E. J. J. van Rensburg, *Virial coefficients for hard discs and hard spheres*, J. Phys. A: Math. Gen. **26**, 4805 (1993).
- [77] H. Hansen-Goos and R. Roth, *A new generalization of the Carnahan-Starling equation of state to additive mixtures of hard spheres*, J. Chem. Phys. **124**, 154506 (2006).
- [78] J. K. Percus and G. J. Yevick, *Analysis of Classical Statistical Mechanics by Means of Collective Coordinates*, Phys. Rev. **110**, 1 (1958).
- [79] J. K. Percus, *Approximation Methods in Classical Statistical Mechanics*, Phys. Rev. Lett. **8**, 462 (1962).
- [80] J. M. J. van Leeuwen, J. Groeneveld, and J. de Boer, *New method for the calculation of the pair correlation function. I*, Physica **25**, 792 (1959).
- [81] M. S. Wertheim, *Exact Solution of the Percus-Yevick Integral Equation for Hard Spheres*, Phys. Rev. Lett. **10**, 321 (1963).
- [82] M. S. Wertheim, *Analytic Solution of the Percus-Yevick Equation*, J. Math. Phys. **5**, 643 (1964).

- [83] L. Verlet and J.-J. Weis, *Equilibrium Theory of Simple Liquids*, Phys. Rev. A **5**, 939 (1972).
- [84] C. K. Percus, *Equilibrium State of a Classical Fluid of Hard Rods in an External Field*, J. Stat. Phys. **15**, 505 (1976).
- [85] J. K. Percus, *One-dimensional classical fluid with nearest-neighbor interaction in arbitrary external field*, J. Stat. Phys. **28**, 67 (1982).
- [86] T. K. Vanderlick, H. T. Davis, and J. K. Percus, *The statistical mechanics of inhomogeneous hard rod mixtures*, J. Chem. Phys. **91**, 7136 (1989).
- [87] Y. Singh, *Density-functional theory of freezing and properties of the ordered phase*, Phys. Rep. **207**, 351 (1991).
- [88] M. Oettel, S. Dorosz, M. Berghoff, B. Nestler, and T. Schilling, *Description of hard-sphere crystals and crystal-fluid interfaces: A comparison between density functional approaches and a phase-field crystal model*, Phys. Rev. E **86**, 021404 (2012).
- [89] S. van Teeffelen, R. Backofen, A. Voigt, and H. Löwen, *Derivation of the phase-field-crystal model for colloidal solidification*, Phys. Rev. E **79**, 051404 (2009).
- [90] K. R. Elder, M. Katakowski, M. Haataja, and M. Grant, *Modeling Elasticity in Crystal Growth*, Phys. Rev. Lett. **88**, 245701 (2002).
- [91] K. R. Elder and M. Grant, *Modeling elastic and plastic deformations in nonequilibrium processing using phase field crystals*, Phys. Rev. E **70**, 051605 (2004).
- [92] H. Emmerich, *Phase-field modelling for metals and colloids and nucleation therein – an overview*, J. Phys.: Condens. Matter **21**, 464103 (2009).
- [93] H. Löwen, *A phase-field-crystal model for liquid crystals*, J. Phys.: Condens. Matter **22**, 364105 (2010).
- [94] R. Wittkowski, H. Löwen, and H. R. Brand, *Derivation of a three-dimensional phase-field-crystal model for liquid crystals from density functional theory*, Phys. Rev. E **82**, 031708 (2010).
- [95] W. A. Curtin and N. W. Ashcroft, *Weighted-density-functional theory of inhomogeneous liquids and the freezing transition*, Phys. Rev. A **32**, 2909 (1985).
- [96] W. A. Curtin and N. W. Ashcroft, *Density-functional theory and freezing of simple liquids*, Phys. Rev. Lett. **56**, 2775 (1986), see also W. A. Curtin and N. W. Ashcroft, Phys. Rev. Lett. **57**, 1192 (1986).
- [97] R. Ohnesorge, H. Löwen, and H. Wagner, *Density functional theory of crystal-fluid interfaces and surface melting*, Phys. Rev. E **50**, 4801 (1994).
- [98] H. Hadwiger, *Vorlesungen über Inhalt, Oberfläche und Isoperimetrie, Die Grundlehren der mathematischen Wissenschaften in Einzeldarstellungen*, volume XCIII, Springer, 1st edition (1957).

- [99] B. Chen, *A Simplified Elementary Proof of Hadwiger's Volume Theorem*, *Geometriae Dedicata* **105**, 107 (2004).
- [100] Y. Rosenfeld, D. Levesque, and J.-J. Weis, *Free-energy model for the inhomogeneous hard-sphere fluid mixture: Triplet and higher-order direct correlation functions in dense fluids*, *J. Chem. Phys.* **92**, 6818 (1990).
- [101] Y. Rosenfeld, *Free energy model for the inhomogeneous hard-body fluid: application of the Gauss-Bonnet theorem*, *Mol. Phys.* **86**, 637 (1995).
- [102] I. Chavel, *Riemannian geometry – A modern introduction*, *Cambridge Tracts in Mathematics*, volume 108, Cambridge University Press, Cambridge (1993).
- [103] A. N. Pressley, *Elementary Differential Geometry*, Springer Undergraduate Mathematics Series, Springer, 2nd edition (2010).
- [104] M. Marechal, H. H. Goetzke, A. Härtel, and H. Löwen, *Inhomogeneous fluids of colloidal hard dumbbells: Fundamental measure theory and Monte Carlo simulations*, *J. Chem. Phys.* **135**, 234510 (2011).
- [105] H. Hansen-Goos and K. Mecke, *Tensorial density functional theory for non-spherical hard-body fluids*, *J. Phys.: Condens. Matter* **22**, 364107 (2010).
- [106] M. Schmidt and C. von Ferber, *Amphiphilic hard body mixtures*, *Phys. Rev. E* **64**, 051115 (2001).
- [107] Y. Rosenfeld, M. Schmidt, H. Löwen, and P. Tarazona, *Fundamental-measure free-energy density functional for hard spheres: Dimensional crossover and freezing*, *Phys. Rev. E* **55**, 4245 (1997).
- [108] E. Kierlik and M. L. Rosinberg, *Free-energy density functional for the inhomogeneous hard-sphere fluid: Application to interfacial adsorption*, *Phys. Rev. A* **42**, 3382 (1990).
- [109] S. Phan, E. Kierlik, M. L. Rosinberg, B. Bildstein, and G. Kahl, *Equivalence of two free-energy models for the inhomogeneous hard-sphere fluid*, *Phys. Rev. E* **48**, 618 (1993).
- [110] S. Korden, *Deriving the Rosenfeld functional from the virial expansion*, *Phys. Rev. E* **85**, 041150 (2012).
- [111] S. Korden, *Beyond the Rosenfeld Functional: Loop Contributions in Fundamental Measure Theory*, arXiv:1208.3932v1 [cond-mat.stat-mech] (2012).
- [112] S. Korden, *A Short Proof of the Reducibility of Hard-Particle Cluster Integrals*, arXiv:1105.3717v1 [math-ph] (2011).
- [113] R. Roth, R. Evans, A. Lang, and G. Kahl, *Fundamental measure theory for hard-sphere mixtures revisited: the White Bear version*, *J. Phys.: Condens. Matter* **14**, 12063 (2002).
- [114] P. Tarazona and Y. Rosenfeld, *From zero-dimension cavities to free-energy functionals for hard disks and hard spheres*, *Phys. Rev. E* **55**, R4873 (1997).

- [115] P. Tarazona, *Fundamental measure theory and dimensional interpolation for the hard spheres fluid*, Physica A **306**, 243 (2002).
- [116] Y. Rosenfeld, *Free-energy model for the inhomogeneous hard-sphere fluid: “Closure” relation between generating functionals for “direct” and “cavity” distribution functions*, J. Chem. Phys. **93**, 4305 (1990).
- [117] Y. Rosenfeld, M. Schmidt, H. Löwen, and P. Tarazona, *Dimensional crossover and the freezing transition in density functional theory*, J. Phys.: Condens. Matter **8**, L577 (1996).
- [118] R. Roth, K. Mecke, and M. Oettel, *Communication: Fundamental measure theory for hard disks: Fluid and solid*, J. Chem. Phys. **136**, 081101 (2012).
- [119] M. Schmidt, H. Löwen, J. M. Brader, and R. Evans, *Density Functional for a Model Colloid-Polymer Mixture*, Phys. Rev. Lett. **85**, 1934 (2000).
- [120] R. Gill, editor, *Dr. Faustus, The complete works of Christopher Marlowe*, volume II, Clarendon Press, Oxford (1990).
- [121] P. N. Pusey and W. van Megen, *Phase behaviour of concentrated suspensions of nearly hard colloidal spheres*, Nature **320**, 340 (1986).
- [122] P. N. Pusey, E. Zaccarelli, C. Valeriani, E. Sanz, W. C. K. Poon, and M. E. Cates, *Hard spheres: crystallization and glass formation*, Phil. Trans. R. Soc. A **367**, 4993 (2009).
- [123] Y. Rahmani, K. van der Vaart, B. van Dam, Z. Hu, V. Chikkadi, and P. Schall, *Dynamic heterogeneity in hard and soft sphere colloidal glasses*, Soft Matter **8**, 4264 (2012).
- [124] W. G. Hoover and F. H. Ree, *Melting Transition and Communal Entropy for Hard Spheres*, J. Chem. Phys. **49**, 3609 (1968).
- [125] A. Härtel and H. Löwen, *Fundamental measure density functional theory for hard spherocylinders in static and time-dependent aligning fields*, J. Phys.: Condens. Matter **22**, 104112 (2010).
- [126] A. Härtel, R. Blaak, and H. Löwen, *Towing, breathing, splitting, and overtaking in driven colloidal liquid crystals*, Phys. Rev. E **81**, 051703 (2010).
- [127] H. L. Frisch and J. L. Lebowitz, *The equilibrium theory of classical fluids*, W. A. Benjamin, Inc., New York Amsterdam (1964).
- [128] D. Shechtman, I. Blech, D. Gratias, and J. W. Cahn, *Metallic Phase with Long-Range Orientational Order and No Translational Symmetry*, Phys. Rev. Lett. **53**, 1951 (1984).
- [129] M.-C. Miguel, A. Vespignani, S. Zapperi, J. Weiss, and J.-R. Grasso, *Intermittent dislocation flow in viscoplastic deformation*, Nature **410**, 667 (2001).
- [130] N. W. Ashcroft and N. D. Mermin, *Solid State Physics*, Holt, Rinehart and Winston, New York, Chicago, San Francisco, Atlanta, Dallas, Montreal, Toronto, Sydney (1976).

- [131] J. M. Ziman, *Principles of the theory of solids*, Cambridge University Press, Cambridge, 2nd edition (1972).
- [132] W. Greulich, editor, *Lexikon der Physik, Lexikon der Physik*, volume 1, Spektrum Akademischer Verlag, Heidelberg, Berlin (1998), aa bis De.
- [133] J. H. J., *Obituary Notices of Fellows Deceased*, Proc. R. Soc. Lond. **31**, i (1880).
- [134] U. Kilian and C. Weber, editors, *Lexikon der Physik, Lexikon der Physik*, volume 5, Spektrum Akademischer Verlag, Heidelberg, Berlin (2000), sc bis Zz.
- [135] E. L. Goldwasser, A. V. Granato, and R. O. Simmons, *Frederick Seitz*, Phys. Today **61**, 66 (2008).
- [136] T. Ras, R. Schilling, and M. Weigel, *Regular Packings on Periodic Lattices*, Phys. Rev. Lett. **107**, 215503 (2011).
- [137] T. Hales, *Dense Sphere Packings. A Blueprint for Formal Proofs*, London Mathematical Society Lecture Note Series, volume 400, Cambridge University Press, Cambridge (2012).
- [138] T. C. Hales, *A proof of the Kepler conjecture*, Ann. Math. **162**, 1065 (2005).
- [139] T. C. Hales, *An overview of the Kepler conjecture* (2002), arXiv:math/9811071v2 [math.MG].
- [140] G. Szpiro, *Mathematics: Does the proof stack up?*, Nature **424**, 12 (2003).
- [141] A. D. Bruce, N. B. Wilding, and G. J. Ackland, *Free Energy of Crystalline Solids: A Lattice-Switch Monte Carlo Method*, Phys. Rev. Lett. **79**, 3002 (1997).
- [142] H. Koch, C. Radin, and L. Sadun, *Most stable structure for hard spheres*, Phys. Rev. E **72**, 016708 (2005).
- [143] C. Song, P. Wang, and H. A. Makse, *A phase diagram for jammed matter*, Nature **453**, 629 (2008).
- [144] J. D. Bernal and J. Mason, *Packing of Spheres: Co-ordination of Randomly Packed Spheres*, Nature **188**, 910 (1960).
- [145] J. G. Berryman, *Random close packing of hard spheres and disks*, Phys. Rev. A **27**, 1053 (1983).
- [146] M. Oettel, S. Görig, A. Härtel, H. Löwen, M. Radu, and T. Schilling, *Free energies, vacancy concentrations, and density distribution anisotropies in hard-sphere crystals: A combined density functional and simulation study*, Phys. Rev. E **82**, 051404 (2010).
- [147] C. H. Bennett and B. J. Alder, *Studies in Molecular Dynamics. IX. Vacancies in Hard Sphere Crystals*, J. Chem. Phys. **54**, 4796 (1971).
- [148] S. Pronk and D. Frenkel, *Point Defects in Hard-Sphere Crystals*, J. Phys. Chem. B **105**, 6722 (2001).

- [149] S. K. Kwak, Y. Cahyana, and J. K. Singh, *Characterization of mono- and divacancy in fcc and hcp hard-sphere crystals*, J. Chem. Phys. **128**, 134514 (2008).
- [150] F. A. Lindemann, *The calculation of molecular vibration frequencies*, Phys. Z. **11**, 609 (1910).
- [151] A. R. Ubbelohde, *The molten state of matter*, John Wiley, Chichester (1978).
- [152] P. J. Steinhardt, D. R. Nelson, and M. Ronchetti, *Bond-orientational order in liquids and glasses*, Phys. Rev. B **28**, 784 (1983).
- [153] P. R. ten Wolde, M. J. Ruiz-Montero, and D. Frenkel, *Numerical Evidence for bcc Ordering at the Surface of a Critical fcc Nucleus*, Phys. Rev. Lett. **75**, 2714 (1995).
- [154] P. W. Bridgman, *Change of Phase under Pressure. I. The Phase Diagram of Eleven Substances with Especial Reference to the Melting Curve*, Phys. Rev. **3**, 126 (1914).
- [155] P. W. Bridgman, *Change of Phase under Pressure. I. The Phase Diagram of Eleven Substances with Especial Reference to The Melting Curve*, Phys. Rev. **3**, 153 (1914).
- [156] M. N. Rosenbluth and A. W. Rosenbluth, *Further Results on Monte Carlo Equations of State*, J. Chem. Phys. **22**, 881 (1954).
- [157] W. W. Wood and J. D. Jacobson, *Preliminary Results from a Recalculation of the Monte Carlo Equation of State of Hard Spheres*, J. Chem. Phys. **27**, 1207 (1957).
- [158] J. K. Percus, editor, *Round Table on Statistical Mechanics*, chapter XXVIII, pages 493–509, Interscience Publishers, New York, London (1963).
- [159] G. L. Jones and U. Mohanty, *A density functional-variational treatment of the hard sphere transition*, Mol. Phys. **54**, 1241 (1985).
- [160] D. Frenkel and J. P. McTague, *Computer Simulations of Freezing and Supercooled Liquids*, Annu. Rev. Phys. Chem. **31**, 491 (1980).
- [161] A. D. J. Haymet, *A molecular theory for the freezing of hard spheres*, J. Chem. Phys. **78**, 4641 (1983).
- [162] P. Tarazona, *A density functional theory of melting*, Mol. Phys. **52**, 81 (1984).
- [163] A. R. Denton and N. W. Ashcroft, *Modified weighted-density-functional theory of nonuniform classical liquids*, Phys. Rev. A **39**, 4701 (1989).
- [164] J. F. Lutsko and M. Baus, *Nonperturbative density-functional theories of classical nonuniform systems*, Phys. Rev. A **41**, 6647 (1990).
- [165] M. Baus, *The present status of the density-functional theory of the liquid-solid transition*, J. Phys.: Condens. Matter **2**, 2111 (1990).
- [166] R. Ohnesorge, H. Löwen, and H. Wagner, *Density distribution in a hard-sphere crystal*, Eur. Phys. Lett. **22**, 245 (1993).
- [167] D. A. Young and B. J. Alder, *Studies in molecular dynamics. XIII. Singlet and pair distribution functions for hard-disk and hard-sphere solids*, J. Chem. Phys. **60**, 1254 (1974).

- [168] W. C. K. Poon, E. R. Weeks, and C. P. Royall, *On measuring colloidal volume fractions*, Soft Matter **8**, 21 (2012).
- [169] C. P. Royall, W. C. K. Poon, and E. R. Weeks, *In Search of Colloidal Hard Spheres* (2012), arXiv:1205.6665v1 [cond-mat.soft].
- [170] R. Kurita and E. R. Weeks, *Measuring every particle's size from three-dimensional imaging experiments* (2012), arXiv:1112.1460v2 [cond-mat.soft].
- [171] S.-E. Phan, W. B. Russel, J. Zhu, and P. M. Chaikin, *Effects of polydispersity on hard sphere crystals*, J. Chem. Phys. **108**, 9789 (1998).
- [172] P. G. Bolhuis and D. A. Kofke, *Monte Carlo study of freezing of polydisperse hard spheres*, Phys. Rev. E **54**, 634 (1996).
- [173] R. McRae and A. D. J. Haymet, *Freezing of polydisperse hard spheres*, J. Chem. Phys. **88**, 1114 (1988).
- [174] P. Sollich and N. B. Wilding, *Polydispersity induced solid-solid transitions in model colloids*, Soft Matter **7**, 4472 (2011).
- [175] J. Antonowicz, E. Jezierska, M. Kedzierski, A. R. Yavari, L. Greer, P. Panine, and M. Sztucki, *Early stages of phase separation and nanocrystallization in Al-rare earth metallic glasses studied using SAXS/WAXS and HRTEM methods*, Rev. Adv. Mater. Sci. **18**, 454 (2008).
- [176] N. V. Dzhomkina and G. J. Vancso, *Colloidal crystal assembly on topologically patterned templates*, Soft Matter **1**, 265 (2005).
- [177] T. Gorishnyy, C. K. Ullal, M. Maldovan, G. Fytas, and E. L. Thomas, *Hypersonic Phononic Crystals*, Phys. Rev. Lett. **94**, 115501 (2005).
- [178] R. P. Sear, *Nucleation: theory and applications to protein solutions and colloidal suspensions*, J. Phys.: Condens. Matter **19**, 033101 (2007).
- [179] D. P. Woodruff, *The Solid-Liquid Interface*, Cambridge University Press (1973).
- [180] D. Turnbull, *Formation of Crystal Nuclei in Liquid Metals*, J. Appl. Phys. **21**, 1022 (1950).
- [181] B. B. Laird, *The solid-liquid interfacial free energy of close-packed metals: Hard-spheres and the Turnbull coefficient*, J. Chem. Phys. **115**, 2887 (2001).
- [182] W. A. Curtin, *Density-functional theory of the solid-liquid interface*, Phys. Rev. Lett. **59**, 1228 (1987).
- [183] W. A. Curtin, *Density-functional theory of crystal-melt interfaces*, Phys. Rev. B **39**, 6775 (1989).
- [184] D. W. Marr and A. P. Gast, *Planar density-functional approach to the solid-fluid interface of simple liquids*, Phys. Rev. E **47**, 1212 (1993).
- [185] U. Gasser, *Crystallization in three- and two-dimensional colloidal suspensions*, J. Phys.: Condens. Matter **21**, 203101 (2009).

- [186] R. L. Davidchack and B. B. Laird, *Simulation of the hard-sphere crystal-melt interface*, J. Chem. Phys. **108**, 9452 (1998).
- [187] R. L. Davidchack and B. B. Laird, *Direct Calculation of the Hard-Sphere Crystal /Melt Interfacial Free Energy*, Phys. Rev. Lett. **85**, 4751 (2000).
- [188] Y. Mu, A. Houk, and X. Song, *Anisotropic Interfacial Free Energies of the Hard-Sphere Crystal–Melt Interfaces*, J. Phys. Chem. B **109**, 6500 (2005).
- [189] R. L. Davidchack, J. R. Morris, and B. B. Laird, *The anisotropic hard-sphere crystal-melt interfacial free energy from fluctuations*, J. Chem. Phys. **125**, 094710 (2006).
- [190] M. Amini and B. B. Laird, *Kinetic Coefficient for Hard-Sphere Crystal Growth from the Melt*, Phys. Rev. Lett. **97**, 216102 (2006).
- [191] R. L. Davidchack, *Hard spheres revisited: Accurate calculation of the solid?liquid interfacial free energy*, J. Chem. Phys. **133**, 234701 (2010).
- [192] W. E. McMullen and D. W. Oxtoby, *A theoretical study of the hard sphere fluid-solid interface*, J. Chem. Phys. **88**, 1967 (1988).
- [193] D. W. Marr and A. P. Gast, *Interfacial Free Energy between Hard-Sphere Solids and Fluids*, Langmuir **10**, 1348 (1994).
- [194] A. Kyrlidis and R. A. Brown, *Density-functional theory and atomistic simulation of the hard-sphere melt-solid interface*, Phys. Rev. E **51**, 5832 (1995).
- [195] N. Choudhury and S. K. Ghosh, *Modified weighted density-functional approach to the crystal-melt interface*, Phys. Rev. E **57**, 1939 (1998).
- [196] L. Gránásy and T. Pusztai, *Diffuse interface analysis of crystal nucleation in hard-sphere liquid*, J. Chem. Phys. **117**, 10121 (2002).
- [197] A. Cacciuto, S. Auer, and D. Frenkel, *Solid-liquid interfacial free energy of small colloidal hard-sphere crystals*, J. Chem. Phys. **119**, 7467 (2003).
- [198] V. B. Warshavsky and X. Song, *Fundamental-measure density functional theory study of the crystal-melt interface of the hard sphere system*, Phys. Rev. E **73**, 031110 (2006).
- [199] G. I. Tóth and L. Gránásy, *Crystal Nucleation in the Hard-Sphere System Revisited: A Critical Test of Theoretical Approaches*, J. Phys. Chem. B **113**, 5141 (2009).
- [200] L. A. Fernández, V. Martín-Mayor, B. Seoane, and P. Verrocchio, *Equilibrium Fluid-Solid Coexistence of Hard Spheres*, Phys. Rev. Lett. **108**, 165701 (2012).
- [201] A. W. Adamson and A. P. Gast, *Physical Chemistry of Surfaces*, Wiley-Interscience, New York, Chichester, Weinheim, Brisbane, Singapore, Toronto, 6th edition (1997).
- [202] J. M. Howe, *Interfaces in Materials*, Wiley-Interscience, New York, Chichester, Weinheim, Brisbane, Singapore, Toronto (1997).

- [203] R. C. Tolman, *The Effect of Droplet Size on Surface Tension*, J. Chem. Phys. **17**, 333 (1949).
- [204] L. Gránásy, T. Pusztai, G. Tóth, Z. Jurek, M. Conti, and B. Kvamme, *Phase field theory of crystal nucleation in hard sphere liquid*, J. Chem. Phys. **119**, 10376 (2003).
- [205] D. S. Fisher and J. D. Weeks, *Shape of Crystals at Low Temperatures: Absence of Quantum Roughening*, Phys. Rev. Lett. **50**, 1077 (1983).
- [206] W. R. Fehlner and S. H. Vosko, *A product representation for cubic harmonics and special directions for the determination of the Fermi surface and related properties*, Can. J. Phys. **54**, 2159 (1976).
- [207] K. R. Mecke and S. Dietrich, *Effective Hamiltonian for liquid-vapor interfaces*, Phys. Rev. E **59**, 6766 (1999).
- [208] J. J. Hoyt, M. Asta, and A. Karma, *Method for Computing the Anisotropy of the Solid-Liquid Interfacial Free Energy*, Phys. Rev. Lett. **86**, 5530 (2001).
- [209] D. G. A. L. Aarts, M. Schmidt, and H. N. W. Lekkerkerker, *Direct Visual Observation of Thermal Capillary Waves*, Science **304**, 847 (2004).
- [210] P. Pulay, *Convergence acceleration of iterative sequences. The case of scf iteration*, Chem. Phys. Lett. **73**, 393 (1980).
- [211] A. Kovalenko, S. Ten-no, and F. Hirata, *Solution of three-dimensional reference interaction site model and hypernetted chain equations for simple point charge water by modified method of direct inversion in iterative subspace*, J. Comput. Chem. **20**, 928 (1999).
- [212] A. D. J. Haymet and D. W. Oxtoby, *A molecular theory for the solid-liquid interface*, J. Chem. Phys. **74**, 2559 (1981).
- [213] D. W. Oxtoby and A. D. J. Haymet, *A molecular theory of the solid-liquid interface. II. Study of bcc crystal-melt interfaces*, J. Chem. Phys. **76**, 6262 (1982).
- [214] M. Oettel, *Mode expansion for the density profile of crystal-fluid interfaces: Hard spheres as a test case*, arXiv:1203.3756v1 [cond-mat.soft] (2012).
- [215] R. L. C. Vink, J. Horbach, and K. Binder, *Capillary waves in a colloid-polymer interface*, J. Chem. Phys. **122**, 134905 (2005).
- [216] W. Schaertl and H. Sillescu, *Brownian dynamics of polydisperse colloidal hard spheres: Equilibrium structures and random close packings*, J. Stat. Phys. **77**, 1007 (1994).
- [217] M. C. Jenkins and S. U. Egelhaaf, *Confocal microscopy of colloidal particles: Towards reliable, optimum coordinates*, Adv. Colloid Interf. Sci. **136**, 65 (2008).
- [218] J. C. Crocker and D. G. Grier, *Methods of Digital Video Microscopy for Colloidal Studies*, J. Colloid Interf. Sci. **179**, 298 (1996).

- [219] J. Q. Broughton and G. H. Gilmer, *Molecular dynamics investigation of the crystal-fluid interface. VI. Excess surface free energies of crystal-liquid systems*, J. Chem. Phys. **84**, 5759 (1986).
- [220] Y. Mu and X. Song, *Calculations of crystal-melt interfacial free energies by nonequilibrium work measurements*, J. Chem. Phys. **124**, 034712 (2006).
- [221] M. Asta, J. J. Hoyt, and A. Karma, *Calculation of alloy solid-liquid interfacial free energies from atomic-scale simulations*, Phys. Rev. B **66**, 100101 (2002).
- [222] B. B. Laird and A. D. J. Haymet, *The crystal/liquid interface: structure and properties from computer simulation*, Chem. Rev. **92**, 1819 (1992).
- [223] A. Mori, R. Manabe, and K. Nishioka, *Construction and investigation of a hard-sphere crystal-melt interface by a molecular dynamics simulation*, Phys. Rev. E **51**, R3831 (1995).
- [224] L. A. Fernandez, V. Martin-Mayor, B. Seoane, and P. Verrocchio, *Equilibrium fluid-solid coexistence of hard spheres*, arXiv:1103.2599v2 [cond-mat.stat-mech] (2011).
- [225] S. Auer and D. Frenkel, *Numerical Simulation of Crystal Nucleation*, Adv. Polym. Sci. **173**, 149 (2005).
- [226] H. Emmerich, *Advances of and by phase-field modelling in condensed-matter physics*, Adv. Phys. **57**, 1 (2008).
- [227] G. Tegze, L. Gránásy, G. I. Tóth, F. Podmaniczky, A. Jaatinen, T. Ala-Nissila, and T. Pusztai, *Diffusion-Controlled Anisotropic Growth of Stable and Metastable Crystal Polymorphs in the Phase-Field Crystal Model*, Phys. Rev. Lett. **103**, 035702 (2009).
- [228] S. van Teeffelen, C. N. Likos, and H. Löwen, *Colloidal Crystal Growth at Externally Imposed Nucleation Clusters*, Phys. Rev. Lett. **100**, 108302 (2008).
- [229] P.-G. de Gennes, *The physics of liquid crystals*, The international series of monographs on physics, Clarendon Press, Oxford (1974).
- [230] M. P. Lettinga, Z. Dogic, H. Wang, and J. Vermant, *Flow Behavior of Colloidal Rodlike Viruses in the Nematic Phase*, Langmuir **21**, 8048 (2005).
- [231] M. P. Lettinga, K. Kang, P. Holmqvist, A. Imhof, D. Derk, and J. K. G. Dhont, *Nematic-isotropic spinodal decomposition kinetics of rodlike viruses*, Phys. Rev. E **73**, 011412 (2006).
- [232] D. van der Beek, P. Davidson, H. H. Wensink, G. J. Vroege, and H. N. W. Lekkerkerker, *Influence of a magnetic field on the nematic phase of hard colloidal platelets*, Phys. Rev. E **77**, 031708 (2008).
- [233] J.-H. Kim, M. Yoneya, and H. Yokoyama, *Fine Bistable Device of Nematic Liquid Crystal Realized on Orientational Surface Patterns*, Mol. Cryst. Liq. Cryst. **433**, 41 (2005).

- [234] J. Hoogboom, T. Rasing, A. E. Rowan, and R. J. M. Nolte, *LCD alignment layers. Controlling nematic domain properties*, *J. Mater. Chem.* **16**, 1305 (2006).
- [235] V. Fréedericksz and A. Repiewa, *Theoretisches und Experimentelles zur Frage nach der Natur der anisotropen Flüssigkeiten*, *Z. Physik* **42**, 532 (1927).
- [236] R. Berardi, L. Muccioli, and C. Zannoni, *Field response and switching times in biaxial nematics*, *J. Chem. Phys.* **128**, 024905 (2008).
- [237] E. Bodenschatz, W. Zimmermann, and L. Kramer, *On electrically driven pattern-forming instabilities in planar nematics*, *J. Phys. France* **49**, 1875 (1988).
- [238] R. G. Larson and H. C. Öttinger, *Effect of molecular elasticity on out-of-plane orientations in shearing flows of liquid-crystalline polymers*, *Macromolecules* **24**, 6270 (1991).
- [239] G. Rienäcker, A. Kröger, and S. Hess, *Chaotic and regular shear-induced orientational dynamics of nematic liquid crystals*, *Physica A* **315**, 537 (2002).
- [240] J. Ding and Y. Yang, *Brownian dynamics simulation of rodlike polymers under shear flow*, *Rheol. Acta* **33**, 405 (1994).
- [241] V. Faraoni, M. Gross, and S. Crescitelli, *The rigid-rod model for nematic polymers: An analysis of the shear flow problem*, *J. Rheol.* **43**, 829 (1999).
- [242] M. Gross, S. Crescitelli, E. Somma, J. Vermant, P. Moldenaers, and P. L. Maffettone, *Prediction and Observation of Sustained Oscillations in a Sheared Liquid Crystalline Polymer*, *Phys. Rev. Lett.* **90**, 098304 (2003).
- [243] Y.-G. Tao, W. K. den Otter, and W. J. Briels, *Kayaking and Wagging of Rods in Shear Flow*, *Phys. Rev. Lett.* **95**, 237802 (2005).
- [244] Y.-G. Tao, W. K. den Otter, and W. J. Briels, *Periodic orientational motions of rigid liquid-crystalline polymers in shear flow*, *J. Chem. Phys.* **124**, 204902 (2006).
- [245] M. Heni and H. Löwen, *Surface Freezing on Patterned Substrates*, *Phys. Rev. Lett.* **85**, 3668 (2000).
- [246] J. P. Hoogenboom, A. K. van Langen-Suurling, J. Romijn, and A. van Blaaderen, *Hard-Sphere Crystals with hcp and Non-Close-Packed Structure Grown by Colloidal Epitaxy*, *Phys. Rev. Lett.* **90**, 138301 (2003).
- [247] J. P. Hoogenboom, A. K. van Langen-Suurling, J. Romijn, and A. van Blaaderen, *Epitaxial growth of a colloidal hard-sphere hcp crystal and the effects of epitaxial mismatch on crystal structure*, *Phys. Rev. E* **69**, 051602 (2004).
- [248] T. Biben, R. Ohnesorge, and H. Löwen, *Crystallization in sedimentation profiles of hard spheres*, *Eur. Phys. Lett.* **28**, 665 (1994).
- [249] M. Marechal and M. Dijkstra, *Crystallization of colloidal hard spheres under gravity*, *Phys. Rev. E* **75**, 061404 (2007).
- [250] S. V. Savenko and M. Dijkstra, *Sedimentation and multiphase equilibria in suspensions of colloidal hard rods*, *Phys. Rev. E* **70**, 051401 (2004).

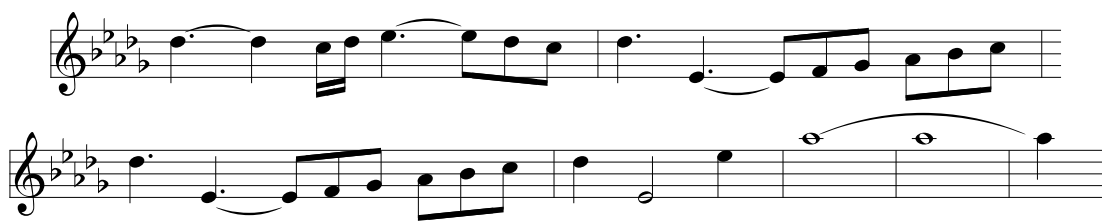
- [251] M. Marechal and M. Dijkstra, *Colloidal hard dumbbells under gravity: structure and crystallization*, Soft Matter **7**, 1397 (2011).
- [252] D. Henderson, J. Quintana, and S. Sokolowski, *A comparison of integral equations and density functional theory versus Monte Carlo for hard dumbbells near a hard wall*, J. Chem. Phys. **102**, 4991 (1995).
- [253] A. Poniewierski and R. Holyst, *Density-Functional Theory for Nematic and Smectic-A Ordering of Hard Spherocylinders*, Phys. Rev. Lett. **61**, 2461 (1988).
- [254] H. Graf and H. Löwen, *Density functional theory for hard spherocylinders: phase transitions in the bulk and in the presence of external fields*, J. Phys.: Condens. Matter **11**, 1435 (1999).
- [255] P. Bolhuis and D. Frenkel, *Tracing the phase boundaries of hard spherocylinders*, J. Chem. Phys. **106**, 666 (1997).
- [256] M. Schmidt, *Density functional theory for colloidal rod-sphere mixtures*, Phys. Rev. E **63**, 050201(R) (2001).
- [257] A. Esztermann, H. Reich, and M. Schmidt, *Density functional theory for colloidal mixtures of hard platelets, rods, and spheres*, Phys. Rev. E **73**, 011409 (2006).
- [258] J. A. Cuesta and Y. Martínez-Ratón, *Fundamental measure theory for mixtures of parallel hard cubes. I. General formalism*, J. Chem. Phys. **107**, 6379 (1997).
- [259] B. Groh and B. Mulder, *A closer look at crystallization of parallel hard cubes*, J. Chem. Phys. **114**, 3653.
- [260] S. Belli, M. Dijkstra, and R. van Roij, *Free minimization of the fundamental measure theory functional: Freezing of parallel hard squares and cubes*, J. Chem. Phys. **137**, 124506 (2012).
- [261] M. Marechal, U. Zimmermann, and H. Löwen, *Freezing of parallel hard cubes with rounded edges*, J. Chem. Phys. **136**, 144506 (2012).
- [262] L. Onsager, *The effects of shape on the interaction of colloidal particles*, Ann. N.Y. Acad. Sci. **51**, 627 (1949).
- [263] A. Isihara, *Theory of High Polymer Solutions (The Dumbbell Model)*, J. Chem. Phys. **19**, 397 (1951).
- [264] S. C. McGrother, D. C. Williamson, and G. Jackson, *A re-examination of the phase diagram of hard spherocylinders*, J. Chem. Phys. **104**, 6755 (1996).
- [265] C. Henning, K. Fujioka, P. Ludwig, A. Piel, A. Melzer, and M. Bonitz, *Existence and Vanishing of the Breathing Mode in Strongly Correlated Finite Systems*, Phys. Rev. Lett. **101**, 045002 (2008).
- [266] H. H. Wensink and G. J. Vroege, *Nematic order of model goethite nanorods in a magnetic field*, Phys. Rev. E **72**, 031708 (2005).
- [267] K. B. Migler and R. B. Meyer, *Solitons and pattern formation in liquid crystals in a rotating magnetic field*, Phys. Rev. Lett. **66**, 1485 (1991).

- [268] T. Frisch, S. Rica, P. Coullet, and J. M. Gilli, *Spiral waves in liquid crystal*, Phys. Rev. Lett. **72**, 1471 (1994).
- [269] S. Nasuno, N. Yoshimo, and S. Kai, *Structural transition and motion of domain walls in liquid crystals under a rotating magnetic field*, Phys. Rev. E **51**, 1598 (1995).
- [270] H. R. Kim, Y. W. Lee, S. J. Kim, D. W. Kim, C. J. Yu, B. Lee, and S. D. Lee, Ferroelectrics **312**, 57 (2004).
- [271] K. Kang and J. K. G. Dhont, *Double-layer polarization induced transitions in suspensions of colloidal rods*, Eur. Phys. Lett. **84**, 14005 (2008).
- [272] K. R. MacKenzie and G. McKay, *Director orientation in Nematic Liquid Crystals Under Orthogonal Magnetic and Electric Fields*, Mol. Cryst. Liq. Cryst. **413**, 197 (2004).
- [273] E. Wandersman, E. Dubois, F. Cousin, V. Dupuis, G. Meriguet, R. Perzynski, and A. Cebers, *Relaxation of the field-induced structural anisotropy in a rotating magnetic fluid*, Eur. Phys. Lett. **86**, 10005 (2009).
- [274] V. Nosenko, A. V. Ivlev, S. K. Zhdanov, M. Fink, and G. E. Morfill, *Rotating electric fields in complex (dusty) plasmas*, Phys. Plasmas **16**, 083708 (2009).
- [275] D. Svenšek and S. Žumer, *Complex backflow dynamics in nematic liquid crystals*, Continuum Mech. Thermodyn. **14**, 231 (2002).
- [276] C. Zheng and R. B. Meyer, *Structure and dynamics of solitons in a nematic liquid crystal in a rotating magnetic field*, Phys. Rev. E **56**, 5553 (1997).
- [277] N.-T. Nguyen and Z. Wu, *Micromixers—a review*, J. Micromech. Microeng. **15**, R1 (2005).
- [278] A. E. Miroshnichenko, E. Brasselet, and Y. S. Kivshar, *All-optical switching and multistability in photonic structures with liquid crystal defects*, Appl. Phys. Lett. **92**, 253306 (2008).
- [279] M. C. Jenkins and S. U. Egelhaaf, *Colloidal suspensions in modulated light fields*, J. Phys.: Condens. Matter **20**, 404220 (2008).
- [280] M. Rex, H. Löwen, and C. N. Likos, *Soft colloids driven and sheared by traveling wave fields*, Phys. Rev. E **72**, 021404 (2005).
- [281] H. Löwen, *Brownian dynamics of hard spherocylinders*, Phys. Rev. E **50**, 1232 (1994).
- [282] H. Löwen, *Anisotropic self-diffusion in colloidal nematic phases*, Phys. Rev. E **59**, 1989 (1999).
- [283] P. M. Johnson, C. M. van Kats, and A. van Blaaderen, *Synthesis of Colloidal Silica Dumbbells*, Langmuir **21**, 11510 (2005).

- [284] E. B. Mock, H. D. Bruyn, B. S. Hawkett, R. G. Gilbert, and C. F. Zukoski, *Synthesis of Anisotropic Nanoparticles by Seeded Emulsion Polymerization*, Langmuir **22**, 4037 (2006).
- [285] S. H. Lee, S. J. Gerbode, B. S. John, A. K. Wolfgang, F. A. Escobedo, I. Cohen, and C. M. Liddell, *Synthesis and assembly of nonspherical hollow silica colloids under confinement*, J. Mater. Chem. **18**, 4912 (2008).
- [286] E. B. Mock and C. F. Zukoski, *Determination of Static Microstructure of Dilute and Concentrated Suspensions of Anisotropic Particles by Ultra-Small-Angle X-ray Scattering*, Langmuir **23**, 8760 (2007).
- [287] S. J. Gerbode, S. H. Lee, C. M. Liddell, and I. Cohen, *Restricted Dislocation Motion in Crystals of Colloidal Dimer Particles*, Phys. Rev. Lett. **101**, 058302 (2008).
- [288] S. J. Gerbode, U. Agarwal, D. C. Ong, C. M. Liddell, F. Escobedo, and I. Cohen, *Glassy Dislocation Dynamics in 2D Colloidal Dimer Crystals*, Phys. Rev. Lett. **105**, 078301 (2010).
- [289] A. F. Demiroörs, P. M. Johnson, C. M. van Kats, A. van Blaaderen, and A. Imhof, *Directed Self-Assembly of Colloidal Dumbbells with an Electric Field*, Langmuir **26**, 14466 (2010).
- [290] C. Vega, E. P. A. Paras, and P. A. Monson, *Solid–fluid equilibria for hard dumbbells via Monte Carlo simulation*, J. Chem. Phys. **96**, 9060 (1992).
- [291] C. Vega, E. P. A. Paras, and P. A. Monson, *On the stability of the plastic crystal phase of hard dumbbell solids*, J. Chem. Phys. **97**, 8543 (1992).
- [292] C. Vega and P. A. Monson, *Plastic crystal phases of hard dumbbells and hard spherocylinders*, J. Chem. Phys. **107**, 2696 (1997).
- [293] C. Vega, L. G. MacDowell, C. McBride, F. J. Blas, A. Galindo, and E. Sanz, *Molecular modeling of flexible molecules. Vapor–liquid and fluid–solid equilibria*, J. Mol. Liq. **113**, 37 (2004).
- [294] M. Marechal and M. Dijkstra, *Stability of orientationally disordered crystal structures of colloidal hard dumbbells*, Phys. Rev. E **77**, 061405 (2008).
- [295] D. Frenkel and B. Smit, *Understanding Molecular Simulation. From Algorithms to Applications, Computational Science Series*, volume 1, Academic Press, 2nd edition (2002).
- [296] W. A. Curtin and N. W. Ashcroft, *Density-Functional Theory and Freezing of Simple Liquids*, Phys. Rev. Lett. **57**, 1192 (1986).
- [297] C. N. Likos, Z. T. Nemeth, and H. Löwen, *Density-functional theory of solid-to-solid isostructural transitions*, J. Phys.: Condens. Matter **6**, 10965 (1994).
- [298] H. Graf and H. Löwen, *Phase diagram of tobacco mosaic virus solutions*, Phys. Rev. E **59**, 1932 (1999).

- [299] V. A. Froltsov and S. H. L. Klapp, *Dielectric response of polar liquids in narrow slit pores*, J. Chem. Phys. **126**, 114703 (2007).
- [300] B. Groh and S. Dietrich, *Crystal structures and freezing of dipolar fluids*, Phys. Rev. E **63**, 021203 (2001).
- [301] J. K. G. Dhont, *An Introduction to Dynamics of Colloids*, Elsevier, Amsterdam (1996).
- [302] M. Bier, L. Harnau, and S. Dietrich, *Surface properties of fluids of charged platelike colloids*, J. Chem. Phys. **125**, 184704 (2006).
- [303] L. Rossi, S. Sacanna, W. T. M. Irvine, P. M. Chaikin, D. J. Pine, and A. P. Philipse, *Cubic crystals from cubic colloids*, Soft Matter **7**, 4139 (2011).
- [304] A. Haji-Akbari, M. Engel, A. S. Keys, X. Zheng, R. G. Petschek, P. Palffy-Muhoray, and S. C. Glotzer, *Disordered, quasicrystalline and crystalline phases of densely packed tetrahedra*, Nature **462**, 773 (2009).
- [305] H. H. Wensink and G. Jackson, *Cholesteric order in systems of helical Yukawa rods*, J. Phys.: Condens. Matter **23**, 194107 (2011).
- [306] A. Chauviere, H. Hatzikirou, I. G. Kevrekidis, J. S. Lowengrub, and V. Cristini, *Dynamic density functional theory of solid tumor growth: Preliminary models*, AIP Adv. **2**, 011210 (2012).
- [307] E. H. Lieb and M. Loss, *Analysis, Graduate Studies in Mathematics*, volume 14, American Mathematical Society, revised second edition (1997).
- [308] H. Fischer and H. Kaul, *Band 3: Variationsrechnung, Differentialgeometrie, Mathematische Grundlagen der Relativitätstheorie, Mathematik für Physiker*, volume 3, Teubner, Wiesbaden, 2nd edition (2006).
- [309] D. R. Smith, *Variational Methods In Optimization*, Prentice-Hill, Inc., Englewood Cliffs, New Jersey (1974).
- [310] D. G. Luenberger, *Optimization by vector space methods*, John Wiley & Sons, Inc., New York, London, Sydney, Toronto (1969).
- [311] J. S. Rowlinson and B. Widom, *Molecular theory of capillarity*, Clarendon Press, Oxford (1982).
- [312] A. González, J. A. White, F. L. Román, and S. Velasco, *Density functional theory of fluids in nanopores: Analysis of the fundamental measures theory in extreme dimensional-crossover situations*, J. Chem. Phys. **125**, 064703 (2006).
- [313] M. Schmidt, *Replica density functional theory: an overview*, J. Phys.: Condens. Matter **17**, S3481 (2005).
- [314] W. H. Press, S. A. Teukolsky, W. T. Vetterling, and B. P. Flannery, *Numerical Recipes in C*, Cambridge University Press, Cambridge New York Port Chester Melbourne Sydney, 2nd edition (1992).

- [315] L. J. D. Frinka and A. G. Salinger, *Two- and Three-Dimensional Nonlocal Density Functional Theory for Inhomogeneous Fluids: I. Algorithms and Parallelization*, *J. Comput. Phys.* **159**, 407 (2000).
- [316] L. J. D. Frinka and A. G. Salinger, *Two- and Three-Dimensional Nonlocal Density Functional Theory for Inhomogeneous Fluids: II. Solvated Polymers as a Benchmark Problem*, *J. Comput. Phys.* **159**, 425 (2000).
- [317] J. R. Henderson and Z. A. Sabeur, *Liquid-state integral equations at high density: On the mathematical origin of infinite-range oscillatory solutions*, *J. Chem. Phys.* **97**, 6750 (1992).
- [318] K.-C. Ng, *Hypernetted chain solutions for the classical one-component plasma up to $\Gamma = 7000$* , *J. Chem. Phys.* **61**, 2680 (1974).
- [319] A. A. Broyles, *Radial Distribution Functions from the Born-Green Integral Equation*, *J. Chem. Phys.* **33**, 456 (1960).
- [320] P. Pulay, *Improved SCF convergence acceleration*, *J. Comput. Chem.* **3**, 556 (1982).
- [321] R. Wagner, *Götterdämmerung (WWV: 86D)*, B. Schott's Söhne, n.d., Mainz (1876), reprinted by Dover Publications, Mineola (1982).
- [322] M. Gregor-Dellin, *Richard Wagner*, Piper München, Schott Mainz, 2nd edition (1995).



[from: *Götterdämmerung* (WWV: 86D), by Richard Wagner (1813-1883), end of act III [321,322]]